Stochastic modelling of textile structures for resin flow analysis

by

Frank Gommer (MEng)

Thesis submitted to the University of Nottingham for the degree of Doctor of Philosophy

March 2013

Abstract

This work addresses the characterisation of the random micro-structure of fibre bundles in reinforcement textiles for composites and its influence on impregnating resin flow in liquid composite moulding (LCM) processes. Random variations in local filament spacing and local permeability result in a non-uniform flow velocity field. This affects the global fibre bundle permeability. In addition, merging flow fronts due to differences in local flow velocities lead to gas entrapment in the matrix phase, which is difficult to detect or predict. This can eventually result in formation of micro-scale defects, which can significantly reduce the matrix-dominated mechanical properties of the finished composite.

An automated image analysis method was developed to precisely determine local filament distributions within complete fibre bundles based on two-dimensional micrographs. Single-layer carbon fibre epoxy composite specimens were characterised statistically by means of nearest neighbour distance and angle distributions at different compression levels. It was observed that the micro-structure becomes more uniform with increasing level of compaction. A micro-structure generator to reconstruct filament arrangements was adapted incorporating these measurement data. Transverse permeabilities derived from numerical simulations of steady-state flow on these automatically discretised model domains were found to be log-normally distributed and show significant scatter. With increasing model size, average values and widths of the distributions decrease, converging to the permeability of a complete fibre bundle. Similarly, average values and scatter decrease with increasing fibre volume fraction i.e. compaction level. The transverse permeability of random filament arrangements was found to be significantly smaller than for uniform filament arrangements.

The void content in a composite was characterised at different compression levels for specimens produced by resin injection along and perpendicular to the fibre bundles with a developed image analysis method to overcome the rudimentary thresholding approaches proposed in the literature. Due to the more uniform micro-structure at increased bundle compaction, a decrease in void content in impregnated fibre bundles was observed in case of transverse resin injection. An opposite trend for the void content as function of the fibre volume fraction was deduced for injection parallel to the fibre bundles. Similar to the steady state simulations a first step towards void content prediction in a fibre bundle by numerical simulation of transient flow through a randomised filament arrangement was made. It was hypothesised that steady state flow results may be used for the prediction of transient flow.

Acknowledgements

Working on this doctoral thesis has been a wonderful and great experience. It would not have been possible without the help and support of the kind people around me.

I would like to thank my principal supervisor Professor Andrew Long for his excellent help, support and patience. The good advice and support of my second supervisor Dr. Andreas Endruweit has been invaluable, for which I am very grateful. Among many others within the Faculty of Engineering I would like to thank Roger Smith for his technical support during this work.

I would also like to thank my colleagues and friends in the Polymer Composites Group for making this work such an enjoyable experience. I thank my friends in Germany, Great Britain, Belgium and elsewhere for their support and encouragement throughout.

Above all, I would like to thank my parents for their personal support and great patience at all times. I dedicate this thesis to my father Johann who always believed in me and who is dearly missed.

Contents

Nomenclature

Symbol	Description	Unit
a	Semi-major diameter of ellipse	m
A	Cross-sectional area	m^2
A_{bundle}	Total fibre bundle cross-sectional area	m^2
A_f	Fabric areal density	g/m^2
A_{fibre}	Cross-sectional area of fibre	m^2
A_v	Void cross-sectional area	m^2
b	Semi-minor diameter of ellipse	m
c	Shape factor (Gebart)	-
C_1	Shape factor (Gebart)	-
Ca^*	Modified capillary number	-
d	Fibre diameter	m
dp	Pressure drop	Pa
d_h	Hydraulic diameter	m
$F_{inertial}$	Inertial forces	N
$F_{viscous}$	Viscous forces	N
h	Height (cavity, specimen)	m
h_i	Mesh element size, including h_0	m
K	Permeability (subscripts i,j for tensor element)	m^2
K_{hex}	Permeability of a hexagonal arrangement	m^2
K_0	Kozeny constant	-
$K_{periodic}$	Permeability of a periodic arrangement	m^2
K_{random}	Permeability of a random arrangement	m^2
$K_\perp$	Transverse permeability	m^2
$K_{\|\|}$	Longitudinal permeability	m^2
l	(Flow) length	m
m	Exponent (for power-ellipse)	-
M_0	Objective (lens) magnification	-
n	Number of filament neighbours	-
n_l	Number of textile layers	-
N_v	Number of voids	-

p	Pressure	Pa
p_{air}	Air pressure	Pa
p_c	Capillary pressure	Pa
p_{in}	Inlet pressure	Pa
p_{inj}	Injection pressure	Pa
p_{out}	Outlet pressure	Pa
p_{resin}	Static resin pressure	Pa
P_i	Point	-
Q	Volumetric output flow rate	m^3/s
r	Fibre radius	m
r_p	Pore radius	m
Re	Reynolds number	-
s	Degree of saturation	-
$\dot{S}$	Time dependent degree of saturation	1/s
t	Time	s
U	Perimeter	m
v	Velocity	m^2/s
v_{avg}	Average velocity	m^2/s
v_{in}	Inlet velocity	m^2/s
v_{max}	Maximum velocity	m^2/s
V	Volume	m^3
V_a	Volume fraction of the gaseous phase	m^3
V_{bundle}	Fibre bundle volume	m^3
V_c	Void content	-
V_f	Fibre volume fraction	-
V_{fibre}	Filament volume	m^3
$V_{f\,max}$	Maximum achievable V_f	-
V_r	Volume fraction of the resin phase	-
w	Width	m
w_g	Gap width	m
x	Cartesian coordinates	-
x_c	Cartesian ellipse centre position	-
y	Cartesian coordinates	-
y_c	Cartesian ellipse centre position	-

Greek symbols

α	Ellipse rotation angle	degrees
γ	Surface tension	N/m

δc	Image pixel spacing	m
δx	Offset in x-direction	m
δy	Offset in y-direction	m
Δp	Pressure drop	Pa
Δh	Filament height underestimation	m
Δl	Finite flow length	m
Δt	Time step	s
Δc	Camera image sensor pixel spacing	m
$\Delta\theta$	Angular resolution	radian
θ	Contact angle	degrees
λ	Courant number	-
λ_{max}	Maximum allowable courant number	-
μ	Distribution mean	-
μ_{air}	Viscosity of air	$Pa \cdot s$
μ_f	Fluid viscosity	$Pa \cdot s$
ρ	Density	kg/m^3
σ	Standard deviation	-
φ	Out of plane ellipse rotation (ratio of ellipse axes)	degrees
Φ	Porosity	-
ψ	Sectioning angle of samples	degrees

Abbreviations

CFD	Computational Fluid Dynamics
CFL	Courant-Friedrich-Lewy condition
CFRP	Carbon Fibre Reinforced Plastic
HCM	Hard Core Model
LCM	Liquid Composite Moulding
micro-CT	X-ray micro Computer Tomography
MRI	Magnetic Resonance Imaging
PISO	Pressure Implicit with Splitting Operators
prepreg	Pre-impregnated fibre reinforcement
PRESTO!	PREssure STaggering Option
RVE	Representative Volume Element
SEM	Scanning Electron Microscopy
UD	Unidirectional
URF	Under Relaxation Factor
VOF	Volume of Fluid

1. Introduction

The new generation of long-range aircrafts entering the market now consume less than three litres of fuel per 100 kilometres per passenger [1]. To a great deal this fuel efficiency is owed to the use of composite materials. Their outstanding strength-to-weight ratio compared to conventional materials such as metals leads to a reduced structural weight [2]. It is demonstrated that the decrease in weight of a vehicle is directly related to its fuel efficiency [3]. In a composite, high strength and stiffness fibres carry the load and are embedded in a matrix which ensures load transfer between fibres and adds toughness to the composite. Complex shaped parts can be produced in a single process step reducing the number of components for a finished product significantly compared to metal forming [4]. To produce composite parts, many manufacturing processes involve infusion of a liquid matrix material into a dry fibre preform. This work sets out to analyse factors affecting the resin flow process and the potential occurrence of defects.

1.1 Liquid composite moulding processes

At present high performance composite parts are often produced with use of pre-impregnated textile reinforcements (prepregs). These are placed in a mould tool and most often consolidated and cured in an autoclave. Especially in the aerospace industry this production method is widely used due to the achievable low resulting void content in the final part. However, due to the generally high investment costs and poor energy efficiency of the production facilities, a lot of research is conducted for "out-of-autoclave" processing [5, 6] which means employing another composite manufacturing process.

A widely used production methods to manufacture composite parts are the liquid composite moulding (LCM) processes such as the resin transfer moulding (RTM) process depicted in Figure 1. Common for all processes in this group of production methods is that a dry fibre preform is placed in a mould, and after mould closure a liquid matrix is injected. After solidification, the part can be demoulded and only little post processing such as deflashing might be necessary. The choice of an LCM process also allows the use of specially tailored

textile preforms, e.g. braided preforms, which can be manufactured with optimised fibre alignments resulting in increased part performance.

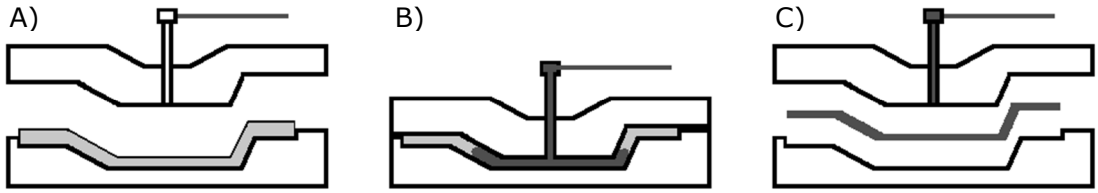

Figure 1: Schematic of an RTM process. A) Dry preform (light grey) loaded into the mould. B) After mould closure a liquid resin (dark grey) is injected. C) The final shaped part is demoulded, after solidification of the resin.

The allowable injection pressures in LCM processes are limited by the tooling rigidity. Therefore, low viscosity liquid resin systems are required for injection which generally limits the matrix material to thermoset resins. Thermoplastic matrices usually exhibit a too high viscosity which would cause mould deflection or deformation of the textile reinforcements during the mould filling process. One solution for the use of thermoplastic materials in LCM processes is in-situ polymerisation [7] which is, however, not yet available on an industrial scale.

This work is focussed on resin flow and resin flow induced effects occurring in LCM processes. Other composite production methods such as press moulding or pultrusion processes for the mass production or hand lay-up for small scale series productions are not in the scope of this work, even though they might be subjected to similar effects.

1.2 Fibre reinforcements

Textile reinforcements utilised in the manufacture of composite components (e.g. uni-directional or woven fabrics) are based on filaments which are usually bundled to yarns and then processed into a fabric for easier handling. This design leads to dual-scale porosities of preforms with gaps formed in-between and within the individual fibre bundles. During a LCM process, both types of pores have to be saturated with resin to guarantee a good load transfer between the solidified matrix and fibres in service.

The flow behaviour of a fluid through textile reinforcements at the macroscopic scale in terms of the permeability is assumed to be uniform for the principal directions. The dual-scale porosity on a smaller scale implies, however, that different types of flow must be present. The flow at the fibre bundle scale is therefore not homogeneous. The larger pores in-between fibre tows will exhibit

less resistance to the pressure driven flow than the smaller pores formed in-between single filaments. In the case of impregnating resin flow into a dry fabric, the pores within the fibre bundles will also be subjected to capillary pressure. The pressure driven inter-bundle flow and the intra-bundle flow assisted by the capillary effects will compete against each other. Optimal production parameters are aimed at balancing these flow types, leading to an even flow front. Fabric manufactures usually apply a surface treatment to the filaments in order to reduce surface tension and increase the wettability of the bundles which will reduce the mismatch of inter- and intra-bundle flow for common processing parameters and materials. Intrinsic variabilities present in the alignment of fibre bundles with respect to each other or the random arrangement of the filaments within the bundles, however, also lead to local flow front variations which can lead to defect formations.

1.3 Defect formation in LCM

While impregnating the dry preform during a LCM process, several types of defects can form. Macroscopic resin-free dry spots on the component scale due to partial mould filling (Figure 2A) will lead to rejection of the part. These dry spots can form due to race tracking of the resin along the sides of the mould or merging flow fronts which result in not wetted areas within the preform. The choice of the injection strategy and the placement of the inlet and vents strongly influence the probability of dry spot formation. Dry spots can also be caused by locally increased fibre volume fraction, V_f, e.g. induced by fabric shear, resulting in different local flow velocities in the fabric. Even though this type of defect will generally lead to immediate wastage, it is relatively easy to predict [8, 9] and avoid.

Microscopic gas entrapment within the reinforcement, however, is much more challenging to identify (Figure 2B-C). These voids, typically the size of a few micrometres up to a few millimetres, can form in between and within fibre bundles, inter- and intra-bundle respectively. Other classifications used are meso- and micro-scale voidage. The occurrence of voids is an intrinsic problem of LCM processes. The detection of these defects is difficult as the resolution of non-destructive evaluation techniques is generally too low at the component scale [10]. Therefore, material samples need to be extracted which can be analysed for the presence of smaller defects [11, 12].

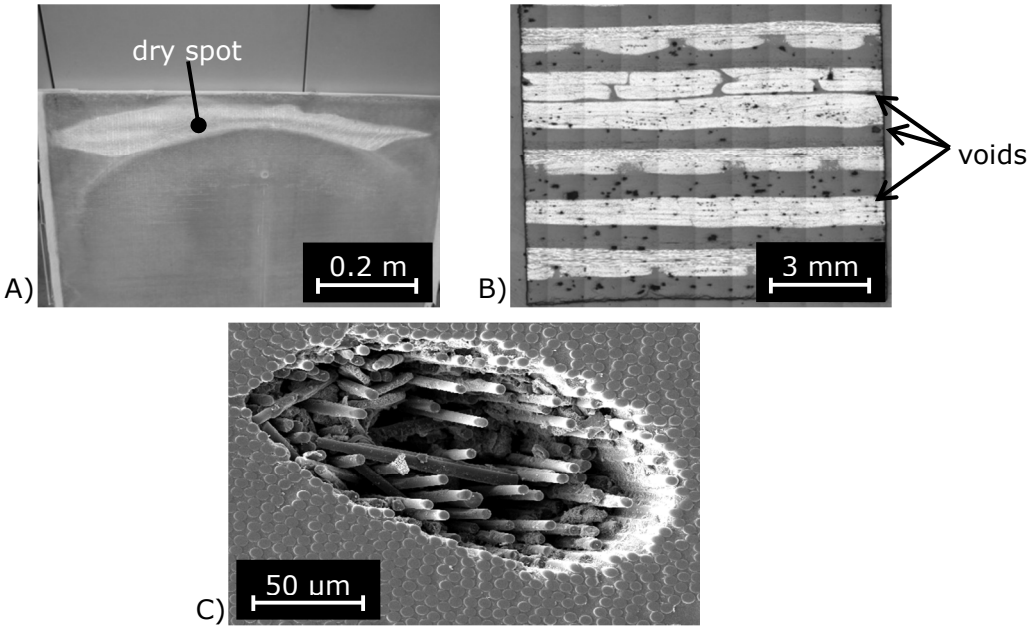

Figure 2: A) Macro-scale dry spot in a triaxial glass composite panel formed during light RTM; B) Micro-scale defects formed within and in between fibre bundles in a glass-carbon hybrid composite produced by vacuum bag infusion (black spots); C) SEM image of a void within a fibre bundle formed during RTM.

Voidage can significantly reduce matrix dominated mechanical properties of a part. Tests have shown, for example, inter-laminar shear strength reductions of 5-15% for every 1% increase of void volume fraction [13, 14]. Therefore, a minimisation of the remaining degree of voidage is necessary during the production of composite parts. Critical void contents below which no reduction of mechanical properties are expected range between 1% and 4% [15]. Chambers et al. [15] argued, however, that the large spread of the reported degradation of mechanical properties as a function of void content indicates that other factors such as the size, shape and physical distribution of voids have a significant influence. The presence of small voids showed little influence, whereas larger voids had a detrimental effect on the mechanical properties of composites. In addition, they were able to relate a larger scatter of test results to an increased probability of larger voids being formed during the production process. Based on image analysis of micrographs, Paciornik and D'Almeida [16] demonstrated that the void content is not equally distributed. Void clustering could lead to void growth and hence have a greater detrimental influence on the mechanical properties.

Huang and Talreja [13] made an attempt to predict the resulting mechanical properties of a composite by incorporating the void morphology into their finite element model. Their simulations showed that size and shape of the voids affect

the stiffness properties differently. The composite properties are dominated by the fibres if aligned in the loading direction whereas the properties transverse to the fibre axis are matrix dominated. Therefore a larger impact of the voidage on the properties transverse to the fibre axis was observed compared to the longitudinal properties. However, due to the use of a periodic volume element approach their results can only give a qualitative idea of the effect of voidage. The influence of the spatial distribution and the presence of different types of voids is ignored. In addition to the reduction of quasi-static mechanical properties, the life-time of parts in service can be significantly reduced due the presence of voids resulting in fatigue failure [17]. For tension-compression fatigue tests it should be mentioned, however, that the test results of Gehrig et al. [17] suggest an improvement of the fatigue life in the presence of voids. They hypothesised reduced interlaminar cracking due to the voidage but failed, however, to present a satisfactory reason for this behaviour.

In LCM, these microscopic dry spots can form due to varying flow velocities of the injected resin in different zones of the fibre reinforcement, e.g. inter- and intra-fibre bundle flow. The inherent heterogeneity and random nature of the filament arrangement within the fibre bundles will enhance this effect. Local fibre arrangements within the yarns determine the local resin flow velocities and therefore also the chance of local gas entrapment and void formation. Zones with low flow velocity or merging flow fronts can lead to local gas entrapment, resulting in voidage.

The formation of volatile products during curing of thermoset resins as result of a chemical reaction can be another cause of micro-scale voids within the final composite product. Even if resin cure does not produce any volatile products, gas could already be entrapped in the neat resin. Therefore, degassing of the resin is often recommended prior to the injection to minimise the void content. A reduction of void content can also be achieved by purging resin through the material after complete mould filling, effectively flushing voids out [14]. It was shown that vacuum assisted impregnation is another possible method to reduce the void content in the final part by reducing the air content in the preform during manufacture [15].

1.4 Thesis overview

The aim of this project was the description of the geometric variabilities present within fibre bundles for the prediction of subsequent properties. The gathered

data is used to describe the resin flow within reconstructed filament arrangements. The modelling of saturated resin flow enables the determination of the origin of scatter in permeability at the micro-scale. This indicates zones which are subjected to low flow velocities. The modelling of transient flow enables the prediction of the effect of local filament arrangement on void formation due to gas entrapment.

Chapter 2 provides a review of the fundamental theory and literature of fluid transport in textile reinforcements used in LCM processes. The equations governing the saturated and unsaturated flow are discussed and different modelling approaches are reviewed. In addition, flow induced void formation mechanisms are analysed.

Chapter 3 presents work addressing the micro-scale description and quantification of the filament arrangement within fibre bundles of reinforcement textiles. The distribution of distances and angles of a filament to its *n*-th nearest neighbour was chosen as a statistical descriptor of the micro-structure. Based on this measurement data, representative models of fibre bundle cross–sections were generated following an adapted approach proposed by Vaughan and McCarthy [18].

Chapter 4 describes the saturated flow behaviour in randomised models employing commercial computational fluid dynamics (CFD) software. Randomised unit cells are analysed as well as models of statistically equivalent filament arrangements generated following the approach outlined in Chapter 3. These models predict the influence of the local filament arrangement on the micro-scale flow behaviour of a resin through fibre-bundles.

Chapter 5 presents results of void content measurements for resin injections transverse and longitudinal to the fibre bundle axis in single layer uni-directional carbon composites. An attempt is made to evaluate the influence of local filament arrangements on the void formation by simulating transient unsaturated flow through a small randomised domain using CFD modelling.

Chapter 6 contains an overall discussion and conclusions of the work described in the previous chapters. In addition, recommendations for future work are presented.

2. Theory and literature review

To achieve good load transfer between the filaments in a composite part, it is necessary that the reinforcement is completely saturated with the polymer matrix. The fibre reinforcement is impregnated during the LCM process. The pores formed in between fibre bundles and within fibre bundles of reinforcement fabrics need to be fully saturated with the liquid resin. This chapter discusses the different types of fluid transport processes present. The basic considerations of fully saturated flow will be discussed in Section 2.1. These equations are then employed in Section 2.2 to describe the fully saturated flow within fibre bundles for periodic and random filament arrangements. The flow impregnating the dry fibre preform and defect formation mechanisms are discussed in Section 2.3. Models predicting the transient flow and probable void formation are then discussed in Section 2.4. A summary of this chapter can be found in Section 2.5.

2.1 Introduction

2.1.1 Steady state flow - Darcy's law

Fibre reinforcements used in LCM processes are subjected to flow of a liquid resin through the pores formed in between and within fibre bundles during the injection step. Darcy was the first to describe such type of flow of a fluid though a porous medium. In his experiments, he analysed the slow flow of water through saturated vertical linear beds of sand and found an empirical relationship of the volumetric output flow rate, Q, of a fluid with the viscosity, μ_f, to the pressure drop, Δp, over the flow length, l, of a cross-sectional area, A [19]. He introduced the permeability, K, as a material constant to fit his measurement data; effectively this describes the resistance of a material to flow through it. His formulation is now widely known as Darcy's law:

$$Q = \frac{KA}{\mu_f l}\Delta p \qquad \text{Eq. 1}$$

Dividing this equation by the cross-sectional area it is possible to normalise the volumetric outflow rate, resulting in the outflow velocity, *v*. The pressure drop is assumed to be linear over the flow length and therefore the output fluid velocity is constant for a material with a constant permeability, using a fluid exhibiting Newtonian behaviour.

Considering the flow length, *l*, as the flow over a small distance *δx* between two points, Darcy's law for the case of one-dimensional flow in the general form can be expressed as:

$$\boldsymbol{v} = \frac{K}{\mu_f}\frac{\delta p}{\delta x} \qquad \text{Eq. 2}$$

The limitations of Darcy's law, derived for linear flow through a homogeneous material only, can be overcome when considering the generalised form in three-dimensional space:

$$\boldsymbol{v} = \frac{\boldsymbol{K}}{\mu_f}\nabla p \qquad \text{Eq. 3}$$

with ***K***, representing the three-dimensional permeability tensor (Eq. 4) and *∇p* the respective three-dimensional pressure gradient.

$$\boldsymbol{K} = \begin{bmatrix} K_{11} & K_{12} & K_{13} \\ K_{21} & K_{22} & K_{23} \\ K_{31} & K_{32} & K_{33} \end{bmatrix} \qquad \text{Eq. 4}$$

Darcy's law applies to laminar flow only which is generally present at low fluid velocities. In order to evaluate the flow regime present during a manufacturing process, the Reynolds number can be calculated (Section 2.1.2).

2.1.2 Reynolds number

Darcy's law is only applicable in the laminar flow regime. In order to identify the type of flow present during fluid flow the dimensionless Reynolds number, *Re*, can be used [19]. It is defined as the ratio between the inertial forces, $F_{inertial}$, and viscous forces, $F_{viscous}$, acting on the fluid (Eq. 5).

$$Re = \frac{F_{inertial}}{F_{viscous}} \qquad \text{Eq. 5}$$

At a low Reynolds number, the fluid motion is characterised by smooth layers of fluid flowing parallel to each other in the flow direction and not mixing with adjacent layers. Considering the fluid flow around a cylinder, the different types of flow as function of the Reynolds number can be visualised. It can be shown that the fluid layers will stay separated from each other in case of laminar flow around a cylinder at low Reynolds number (Figure 3A). After passing the cylinder the fluid layers will return to their original position. If the inertial forces are larger than the viscous forces in between the fluid particles, turbulence will form after passing the cylindrical object (Figure 3B).

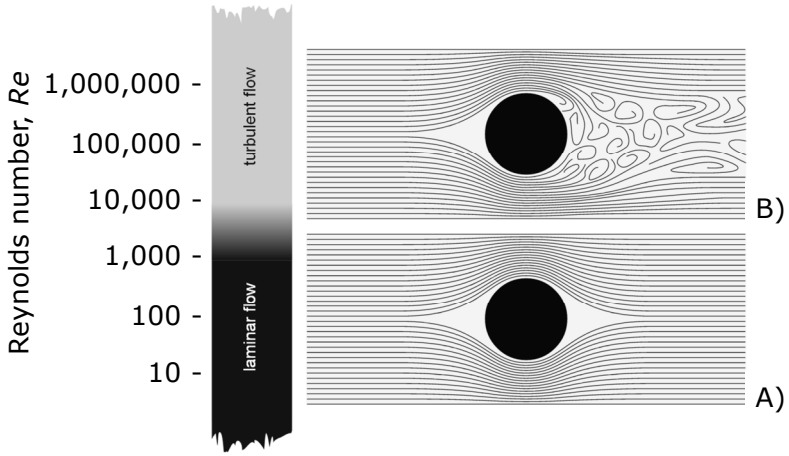

Figure 3: Visualisation of the flow regime as function of the Reynolds number of layers of fluid flowing around a cylinder. A) Flow contours for the laminar and B) turbulent flow regime. Image reprinted from http://physics.info/ with kind permission from Glenn Elert.

For the flow in a tube, the critical Reynolds number under which the laminar flow changes into turbulent flow is 2300 [20]. The flow present in composites manufacturing processes will generally have a Re smaller than 1 [21], hence the laminar flow assumption is valid.

2.1.3 Permeability of textile reinforcements

Fibre preforms for high performance composite parts usually exhibit geometric symmetry due to the construction of the material, e.g. woven or unidirectional. This usually results in orthotropic material properties. Hence, the generalised permeability tensor (Eq. 4) can be simplified by:

$$K_{12} = K_{21},\ K_{13} = K_{31} \text{ and } K_{23} = K_{32} \qquad \text{Eq. 6}$$

For large enough systems, the permeability components should become constant for materials exhibiting random geometrical variabilities [22]. Therefore, a principal coordinate system should exist with a principal permeability tensor

$$\boldsymbol{K} = \begin{bmatrix} K_{11} & 0 & 0 \\ 0 & K_{22} & 0 \\ 0 & 0 & K_{33} \end{bmatrix} \quad \text{Eq. 7}$$

Testing of the material can be reduced to determining the three principal permeability values, K_{11}, K_{22} and K_{33}, accordingly. On the example of a bed of rock it was demonstrated, however, that the permeability tensor can become non-symmetric for imperfect layering [23]. For fibre reinforced composites, the necessary degree of imperfection is, however, unlikely to be present.

The principal permeability tensor (Eq. 7) is assumed to be constant over the macroscopic flow length of textile reinforcements. Hence, one permeability constant in each principal direction is assumed to be able to represent the complete material. The measurement of these material bulk values can be performed for saturated or unsaturated flow. In most LCM processes, unsaturated flow is present when a dry textile preform is impregnated with a liquid resin matrix during the injection process. Saturated flow is present in the textile reinforcement only behind the flow front. It can be measured once the complete preform is wetted by means of the volumetric outflow rate. Generally, the flow resistance is larger in a dry compared to a wetted preform [24]; however, ratios of 0.25 to 4 are reported as ratios of saturated to unsaturated permeabilities in the literature [25]. It was speculated that the unexpected lower unsaturated permeability values might stem from deformations of the fibre bed during the impregnating flow which would have a significant influence on the longitudinal permeability [25]. In addition to permeability tests conducted under saturated or unsaturated flow, the flow behaviour can also be measured at constant inlet pressure or constant flow front velocity.

Usually, measurement set-ups are classified by the number of permeability values determined during a single test:

- One-dimensional
  Linear flow experiments are designed similar to the work originally performed by Darcy. The measurement of the in-plane permeability values does require, however, the prior knowledge of the principal

permeability directions. Three separate experiments are required to determine both in-plane permeability values and their orientation. In textile composites, this method is therefore usually employed to measure the through thickness permeability [26] even though this is not necessarily a principal direction [27].

- Two-dimensional

  A two-dimensional test set-up can measure two in-plane principal permeability values and their orientation in one test [28]. Due to the relative small thickness of many composites parts manufactured compared to the width and length dimensions; the out-of-plane permeability can often be ignored. The data is collected in a closed mould by means of pressure [29] or electrical sensors [30]. In case of a transparent mould tool , the flow front can be captured by optical flow visualisation [31, 32]. The out-of-plane permeability is neglected in this type of measurement method and, if necessary, would have to be measured separately.

- Three-dimensional

  To measure the three-dimensional permeability tensor in one experiment different methods were employed. Weitzenböck et al. [33] tried to employ a number of thermal sensors to measure all three principal permeability values in a single experiment but concluded that the approach is questionable. Several attempts were made using optical sensors embedded in the material [34, 35]. These sensors detect changes of light transmitted through the optical fibres due to local contact with the impregnating fluid. Even though the complete unsaturated permeability tensor of textile reinforcements can be measured in one experiment, the placement of the sensors will distort the material locally and may alter the test results.

In general, permeability measurements with the test set-ups described above are conducted at a single V_f only. For the experimental determination of the saturated permeability a method was suggested enabling the measurement at adjustable V_f [36]. The measurement results may, however, be influenced by lubrication effects during compaction of the saturated reinforcement fabrics.

It was observed that experimentally determined permeability values of fibre reinforcements exhibit large scatter even if the test conditions are not changed [37]. This stems from the intrinsic heterogeneity and variabilities found in the textiles as well as measurement errors. Hoes et al. [38] determined fibre nesting as the main source of permeability variability in their experiments and found that small amounts of shearing can be disregarded. Larger shear angles on the other hand will influence the permeability considerably [39]. Simulations on fibre bundle angle variations [40] or bundle waviness [41] showed a clear influence on the macroscopic permeability and shape of the flow front. Even measurements of the same fibre reinforcement on different test rigs can, however, lead to a large differences in observed permeability values in the order of one magnitude [42]. In practice, however, it appears to be difficult to determine a single major source influencing the variability of textile permeabilities as different sources of variability will be present at the same time. Therefore, Morren et al. [30] proposed the use of a reference specimen to calibrate the test set-up. The specimen manufacture is, however, difficult and expensive and would need adjustment for every test set-up. Repeatability of test results with a scatter of 15% is therefore already assumed to be good [27].

Measurement results for composite properties are commonly expressed in terms of the overall V_f which in turn determines the porosity of the compacted fibre reinforcement in the mould. A frequently used method to relate the V_f of a textile reinforcement to the measured permeability is the Kozeny-Carman equation (Eq. 8) which was originally developed for isotropic homogeneous media with filament radius, r.

$$K = \frac{r^2}{8K_0} \cdot \frac{\left(1 - V_f\right)^3}{V_f^2} \qquad \text{Eq. 8}$$

The shape of the curve is determined by the overall V_f in the mould. The Kozeny constant, K_0, is employed to scale the curve to the measured data. Despite the restrictions of this relation and significant discrepancies of the Kozeny constants reported in the literature [32], this relation is frequently applied and several adaptations are proposed.

2.2 Modelling of saturated flow

In the literature, a large number of models are proposed to predict the steady state flow behaviour of a fluid through saturated fibre reinforcement textiles. These models are developed for different length scales and assume different amounts of homogenisation of the material properties. The fluid flow is driven by an applied pressure gradient and assumed to follow Darcy's law (Eq. 3). The fluid properties are taken into account by the material viscosity. The current work is focused on the micro-scale flow behaviour.

2.2.1 Levels of homogenisations

Composite parts produced by LCM processes (e.g. Figure 4A) are usually composed from several layers of technical textiles. The textile layers used are often based on individual yarns and each yarn consists of a large number of single fibres with a diameter of around 10 μm. For a composite cross-section this implies that up to one million fibres per cm² can be found. In order to calculate the properties of composites, the different length scales introduce several challenges. Currently, different models are used to estimate these properties, generally involving homogenisation of the next lower level reducing the computational effort required. Macro-scale modelling is focused on the part as a whole and the constituent material properties are used as single lump values. Meso-scale modelling is based on the fabric architecture. A unit cell is presumed to be the smallest representative repeating element for a textile structure (Figure 4B). Based on this textile unit cell, the properties of the complete textile layup can be predicted [43].

Employing this meso-scale unit cell approach the textile reinforcement is assumed to exhibit a perfect geometrical arrangement of the tows. This implies that the fibre bundles are equally spaced and are represented as homogeneous solid beams. Some studies tried to incorporate the intrinsic variabilities found in real composites caused by bundle movement or distortion of the fibre arrangement at the micro-scale. Based on micrographic computer tomography (micro-CT) measurements of the yarn shape change Zeng et al. [44] predicted the permeability of a reconstructed 3D textile reinforcement. They presented close permeability prediction in the warp direction compared to experimental data. Permeability predictions in the weft direction, however, still require further improvement.

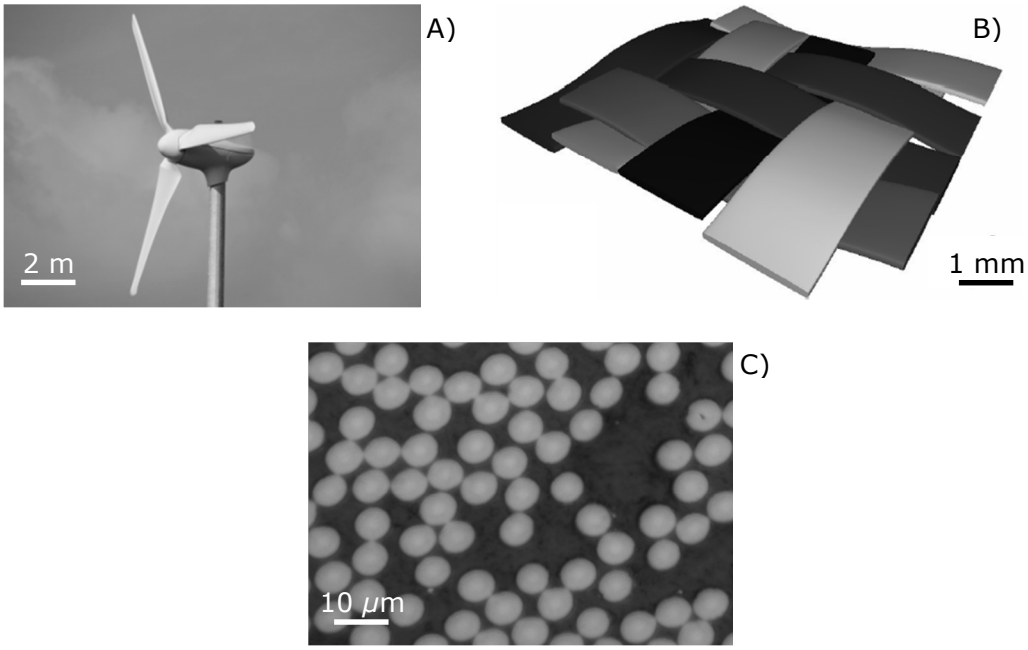

Figure 4: A) Camira C10 wind turbine with composite blades. B) Model of a 2x2 twill weave unit cell generated with TexGen [45]. C) micro-scale filament arrangement in a carbon fibre bundle cross-section.

Zhou et al. [46] attempted to incorporate the fact that fibre bundles are not solid beams and therefore able to change shape under an external force. The yarns are assumed to consist of a limited number of flexible rods, limiting the computational complexity (multi-chain model). During fabric compaction, these rods are able to move individually and thus enable deformation of the overall yarn shape (Figure 5). They found good agreement of their deformed unit cell to experimental data. They were, however, only able to compare their model predictions to visualisation of the top layer of a multi-layer composite material. Applicability of their model to deformations of fabric layers within the composite material still need to be demonstrated. In addition, their approach presumes that a unit cell is representative for the complete material. Variabilities caused by other effects such as handling are ignored.

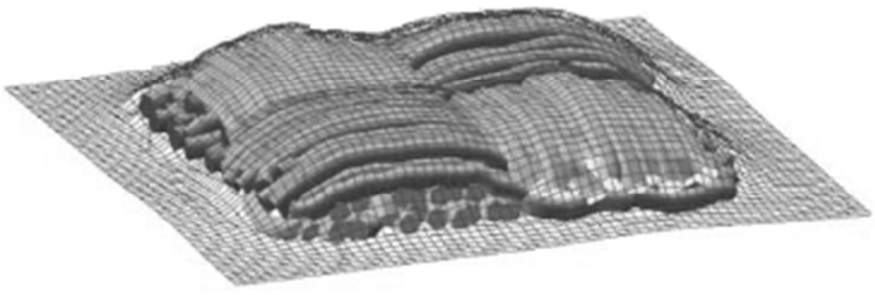

Figure 5: Representation of the multi-chain element model. Yarns consist out of a small number of bars which can move individually under deformation or loading. Adapted from Zhou et al. [46].

Other studies argue, however, that the variability at the unit cell level is negligible for the description of global properties and the variabilities found in fibre bundle waviness on a larger scale are more significant for the reinforcement properties [47]. Endruweit et al. [40] demonstrated variations of the flow front shape resulting from experimentally determined fibre bundle waviness by means of numerical simulations. Glatt et.al [48] simulated the influence of yarn path variability and yarn shape change on the flow and filtration properties of a filter media. These studies, however, ignore the fact that local variations in the flow front can be caused by small local defects which in turn will have a significant influence on subsequent properties such as mechanical fatigue [5]. In addition, the influence of the variability and arrangement of single filaments within the yarns is also neglected.

For the modelling of steady state flow through filament arrangements at the micro-scale several models have been proposed in the literature (Table 1). The most basic modelling approaches assume periodic arrangements of filaments such as hexagonal or square packing (Section 2.2.2), reducing the computational effort. These structures are considered to be representative for all filaments within a fibre bundle or complete composite component. In reality, the filament arrangement in fibre reinforcements is not periodic (Figure 4C). To accommodate the geometric variability found in fibre bundles, several models for randomisation of the filament arrays are proposed in the literature (Section 2.2.3). These arrangements are generally used in models of representative volume elements (RVE). These local representations of the fibre bundle consist of hundreds of single filaments. For the simulation of resin flow, these RVEs are assumed to reflect the real micro-structure of a composite reflecting the intrinsic variabilities. To account for the influence of dual-scale porosity of fibre reinforcements a few multi-scale flow models are proposed, simulating the flow within and in between fibre bundles (Section 2.2.5). For better comparison of different data, it is advantageous to normalise the permeability value by dividing by the fibre radius.

Table 1: Overview of steady state permeability models for transverse and longitudinal flow and the assumed filament arrangements.

$K_\perp$	$K_\parallel$	Author	Arrangement / method
Periodic arrangements (Section 2.2.2)			
✓	✓	Gebart [49]	- Square and hexagonal
✓	✓	Berdichevsky and Cai [50]	- Hexagonal and 'hollow' hex - Square and 'hollow' square
×	✓	Davis and James [51]	- Square (rings) and offset planes (small V_f only!)
✓	✓	Tamayol and Bahrami [52]	- Various ducts ($K_\parallel$); rectangular ($K_\perp$)
✓	×	Hellou et al. [53]	- Triangular (hexagonal)
×	✓	DeValve and Pitchumani [54]	- Rectangular and staggered
Randomisation (Section 2.2.3 and 2.2.4)			
✓	✓	Cai and Berdichevsky [55]	- Randomised square
✓	×	Bechtold and Ye [56]	- Morisita index
✓	×	Yazdchi et al. [57]	- Random disks (hard core model) - Monte Carlo (hard core shaking model) - Energy minimisation - Molecular dynamic
×	✓	Chen and Papathanasiou [58]	- Monte Carlo (hard core shaking model)
✓	×	Hellström et al. [22]	- Voronoi cell
Multi-scale modelling (Section 2.2.5)			
✓	✓	Cai and Berdichevsky [59]	- Cylindrical flow channel (inter-bundle) embedded in homogeneous material (bundle)
✓	✓	Choi et al. [60]	- Regular periodic arrangements
✓	✓	Brennan and Walrath [61]	- Monte Carlo (Hard core shaking model)
✓	✓	Tran et al.[62]	- Ellipsoidal pores in homogeneous material based on semi-empirical measurements

2.2.2 Periodic filament arrangements

The assumption of a periodic filament arrangement in fibre bundles (Figure 6), such as hexagonal or square configurations, enables the simple description and simulation of flow through a fibre bed. Several models were proposed in the literature to describe the longitudinal and transverse flow through a bed of periodically arranged parallel rods. Based on the assumptions made, e.g. type of flow and approximations of the shape of the flow front passing through these cylinders, these models are generally only valid for a certain range of V_f. Formulations proposed for small V_f, e.g. Davis and James [51] for $V_f < 0.02$, are not useful to composite manufacturing processes where significantly larger V_f are targeted. Parallel aligned solid rods of infinite length are assumed to be a good representation of filaments within a fibre bundle. Imperfections such as filament waviness and random arrangement are ignored when employing these models. The filaments are assumed to be non-permeable and the fibre bed does not deform during the flow. These approaches, however, allow a simple analytical expression for the estimation of the permeability of a filament arrangement.

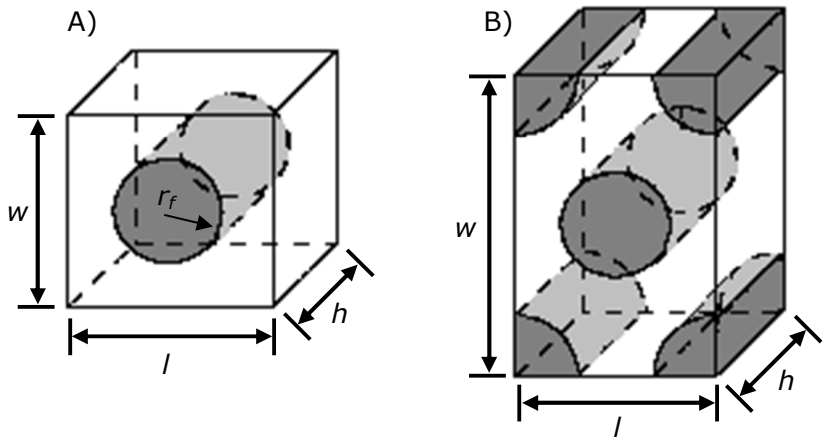

Figure 6: Representation of a A) square and B) hexagonal unit cell.

Gebart [49] proposed a solution for the estimation of the permeability for flow parallel, $K_{\parallel}$, and transverse, $K_{\perp}$, to a periodic arrangement of aligned filaments with an infinite length. He derived his equations based on Navier-Stokes' equation (Appendix A.2) for creeping flow through parallel plates for hexagonal and square filament arrangements.

For the flow parallel to the filament arrangement he derived the following expression:

$$K_{\parallel} = \frac{8r^2}{c}\frac{\left(1-V_f\right)^3}{V_f^2} \qquad \text{Eq. 9}$$

which has the same form as the Kozeny-Carman equation (Eq. 8). For the permeability transverse to the filament arrangement he proposed the following equation:

$$K_{\perp} = C_1\left(\sqrt{\frac{V_{f_{max}}}{V_f}}-1\right)^{\frac{5}{2}}\cdot r^2 \qquad \text{Eq. 10}$$

The permeability in his solution is only dependent on geometrical parameters such as the filament radius, *r*, the effective V_f and the filament arrangement. The parameter, *c*, in longitudinal flow specifies the fibre arrangement. In the case of transverse flow the constant shape factors C_1 and the maximal possible fibre volume fraction, $V_{f_{max}}$ specify the filament arrangement and therefore the geometry of the formed channels in between filaments. For a square arrangement $V_{f_{max}}$ = 0.785 and for hexagonal packing $V_{f_{max}}$ = 0.907 [63]. Normalising the permeability with the fibre radius, curves for the longitudinal and transverse permeability as shown in Figure 7 are produced.

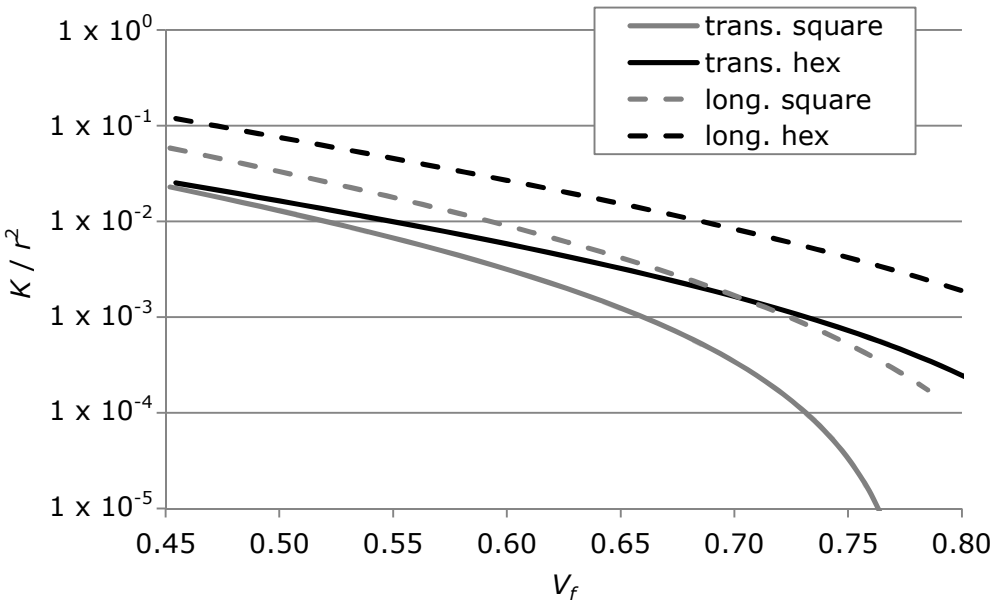

Figure 7: Permeability, *K*, normalised by the fibre radius, *r*, as function of the fibre volume fraction following Gebart's model [49] for longitudinal (long.) and transverse (trans.) flow through square and hexagonal (hex) arrangements.

Due to the assumptions made, the derived equations are only valid for a V_f >0.5 which, in case of composites based on reinforcement textiles, can be presumed. The agreement to experimentally measured permeability values was found to be "less than perfect" which is, considering the scatter and spread of permeabilities found in practice [42], not surprising.

Berdichevsky and Cai [50] developed a model to predict the longitudinal and transverse permeability of various regular filament arrangements including hexagonal and square packing based on the V_f only. They assumed a circular insertion, exhibiting the geometrical properties of a regular arrangement, to be embedded in a homogeneous material. A good agreement of their proposed model with finite element simulations of the same arrangement was found. In addition, they demonstrated a significant variation in permeability predictions at a constant V_f depending on the filament arrangement under investigation. In analogy to the model proposed by Gebart [49], they extended their model to incorporate $V_{f_{max}}$to account for the filament packing. Even though they extended the range of considered regular arrangements compared to other studies, the simplification of assuming a periodic filament arrangement still fails to capture the intrinsic heterogeneity observed in real fibre bundle.

There are more recent attempts to describe the permeability of periodic arrangements, all lacking the simplicity of the solution offered by Gebart [49]. Hellou et al. [53] described the permeability of a triangular filament arrangement, which is effectively a part of a hexagonal arrangement. They demonstrated that variation of the side length of the hexagonal arrangement (*l* and *w* in Figure 6B) leads to varying permeability values at constant V_f. Extending their analytical model approach to an arbitrary arrangement, they presented an approximate solution for the permeability. This solution is based on curve fitting of pre-determined permeability values as a function of the side length aspect ratio *l*/*w*. The need of predetermination of analytical values makes their approach difficult to use in practice.

Tamayol and Bahrami [52] developed an analytical model for the prediction of the transverse permeability of a rectangular filament arrangement. Unlike Gebart [49], who determined the permeability only on the pressure drop in-between the smallest gap of two filaments, they incorporated the velocity profile within the complete unit cell into their model. Their predictions for a square arrangement, however, are similar to the model proposed by Gebart, which does not justify the

much more complicated solution they propose. It should be mentioned, that they also propose a model for the longitudinal permeability prediction of ducts formed in between touching filaments. Their model is, however, only valid for the case of ducts formed in between perfectly touching filament arrangements which are unlikely to be found in composite materials.

In addition to Gebart [49] and others [50-52], DeValve and Pitchumani [54] recently proposed another way of determining the longitudinal permeability of a regular arrangement. They did not only discuss a symmetrical hexagonal and square arrangement but generalised it to a rectangular and staggered arrangement (included angle variations between filaments). Their solution is based on Darcy's law where they derive the average velocity for the considered arrangement from an analytical series solution. Considering the need of up to 10 numerically derived and tabulated coefficients for every V_f and an insignificant difference with the solution proposed by Gebart [49] makes this approach impractical.

All permeability models based on regular micro-structures ignore the intrinsic variability of the filament arrangement as well as filament waviness and undulation. The resulting permeability values can therefore be considered as approximations only. To get a better estimation of the permeability, a model reflecting a more accurate filament arrangement of a fibre bundle is required.

2.2.3 Randomisation of the fibre arrangement

Studies for the prediction of mechanical [64] or flow properties [55, 57, 60] using periodic configurations showed an over-estimation of local properties compared to random filament arrangements. From these results it was concluded that the permeability of a fibre assembly is influenced not only by the V_f or porosity but also by the fibre packing arrangement [50]. In the literature, several methods are proposed for the generation of random filament micro-structures. Similar to the assumptions made for the periodic arrangements, all randomised approaches assume rods which are perfectly aligned parallel to each other. Hence, flow simulations can be reduced to two-dimensional problems which simplifies numerical modelling. This ignores, however, any waviness or twist which is present in the fibre bundle.

The 'hard core model' (HCM) is the most simple method of generating random filament arrangements. Disks, representing fibre cross-sections, are randomly

placed within a specified domain. Most often, a Poisson distribution is assumed and a disk is only placed if it is not overlapping with a previously placed filament [65]. Attempts were also made to incorporate measured fibre diameter distribution into the model, however, the influence on the micro-scale properties was found to be small [66]. A limitation to the HCM is the jamming limit of around 55% V_f [18] which is at the lower end of the local V_f within the fibre bundles used in composite materials. Generation of geometrical models with a larger V_f is not possible using this approach.

To overcome the limitation of the maximum achievable V_f an extension to the HCM, the "hard core shaking model" has been proposed. Here, the area of interest is embedded within a larger domain and the randomly placed disks are subsequently moved a finite distance in a random direction [65] or in the direction of a certain neighbour [67]. The V_f can be increased if the filaments at the domain boundary are only moved inwards. A similar result can be achieved when instead of a random distribution a periodic model is used as the initial arrangement for the shaking or stirring process. After a certain number of iterations, Wongsto and Li [68] used 250, the shaking process is terminated. Bechtold and Ye [56] used varying numbers of iterations in order to achieve different degrees of order. Employing these techniques, artificial filament arrangements with V_f up to the theoretical maximum packing can be generated. These generated filament arrangements are, however, not necessarily representative for the arrangements present within real fibre bundles because they are based on computational considerations only.

All the micro-structure generators described above are entirely based on purely mathematical algorithms. Vaughan and McCarthy [18] proposed a random filament generator based on measured data. They employed experimentally determined nearest neighbour distributions to generate their models. After placing a first filament randomly in the specified domain two additional filaments are placed at a distance to the initially placed filament selected from the nearest neighbour distributions. Subsequently, the focus is set to the next filament and the process is repeated. No further processing step such as stirring is required to achieve the desired V_f. This generated micro-structure is, however, only valid for the analysed material. Yang et al. [69] proposed an update to this procedure based on computational considerations only. However, they only consider a single V_f and fail to overcome a natural jamming limit of this process.

At present, it is not feasible to simulate the behaviour of every single filament within a composite part at the micro-scale. Therefore, it is necessary to limit the domain of interest to a representative size. Consequently, this modelling domain is also known as the "representative volume element" (RVE) or "statistically equivalent representative volume element" (SERVE). Traditionally, square domains of 10 – 100 times the size of the filaments (inclusions) are analysed [70]. Based on micro-mechanical considerations, Trias et al. [64] proposed the following ratio, δ, for an optimal square micro-structure with side length, l, and filament radius, r:

$$\delta = \frac{l}{r} = 50 \qquad \text{Eq. 11}$$

Table 2: Summary of recommended representative volume element (RVE) sizes reported in literature for different materials at specified fibre volume fractions, V_f, represented by the ratio side length, l, to the fibre diameter, d.

Author / Material	V_f	d (μm)	size ($\frac{l}{d}$)	Nr. Fibres	Convergence criteria
Grufman and Ellyin [71] / UD E-glass	0.55	11.6	26	300 - 400	Local V_f
Vaughan and McCarthy [18] / CFRP	0.59	6.6	4 [2)] 10	34 73	Radial distribution function stiffness
Trias et al. [72] / CFRP	0.22	7.0 [1)]	50	700	Stress-strain field
Thomas et al. [73] / UD CFRP	0.55	7.0 [1)]	4 [2)] 14 40 67 87	33 143 1120 3184 5353	Pair correlation function Covariance function Thermal conductivity calculations Local V_f Oriented pair correlation function
Swaminathan et al. [74] / UD steel fibre–epoxy	0.32	3.5	10 [2)] 10 [2)] 10 [2)] 10 [2)] 17 [2)]	50 50 50 50 135	Stiffness convergence Radial distribution function Fibre volume fraction Critical micro-structural variable Pair correlation function
Yazdchi et al. [57] / artificial geometries	0.4	7.0 [1)]	4 [2)] 40	26 800	Pair distribution function Permeability convergence

[1)] Assumed values for the fibre diameter, d.

[2)] The representative domain size is reported as a circle with radius r (here: l=r).

However, numerous other domain sizes are suggested in the literature depending on the material used and the property (including allowable error / residuals) analysed [73, 75]. Table 2 gives a summary of recommended RVE sizes reported in literature. From these examples it is evident, that the model size for a particular problem has to be determined specifically.

2.2.4 Flow through randomised filament arrangements

Cai and Berdichevsky [55] were among the first to investigate the influence of randomisation of the filament arrangements on the resulting permeability. They numerically analysed the flow through a set of square unit cells containing one filament. The filaments were randomly displaced from the centre position or completely removed, ensuring periodicity of the unit cell on the macro-scale while randomising the micro-scale. As discussed in their previous work [50] they related their permeability results to $V_{f_{max}}$ to account for the filament packing geometry which they assumed not to change significantly after bundle manufacturing. Even though the randomisation of their modelling approach is limited by the use of the periodic unit cells they were able to show substantially varying permeability values at the same overall V_f depending on the micro-scale arrangement.

Bechtold and Ye [56] performed manual micrographic analyses for the characterisation of random filament distributions in fibre bundles and described the observed degree of order in the arrangement by the Morisita index. They found indications of filament clustering as a result of increased injection pressures during sample manufacture which suggests movement of filaments and formation of local flow channels. They compared this data to generated micro-structures with varying degrees of order. The general trend of an increasing transverse permeability value with an increasing degree of regularity for the V_f analysed (V_f = 0.52) could be shown. They argued that the systematically higher experimental data found in the literature compared to their model predictions must stem from deformations of the flow channel during the test. The comparison of their micro-structural permeability predictions to macroscopic permeability test results is, however, questionable. The influence of scatter found in permeability tests was ignored (Section 2.1.3). Unfortunately, the validity of their results is limited due to the small domain size used containing 15 filaments only which is considerably smaller than recommended volume element sizes determined in other studies (Table 2). In addition, the

Morisita index only characterises the global filament arrangement; locally varying arrangements or directionality of a filament arrangement are not captured.

The pressure driven transverse flow through random arrays of filaments was also numerically analysed by Yazdchi et al. [57]. Their simulation results suggested that the majority of fluid is transported through a few major flow channels only (Figure 8). They found a power law relationship, similar to Eq. 10, between the permeability values of the complete micro-structural domain and the mean distance of the second nearest neighbour. For the model generation, four different random generator algorithms were employed. All these algorithms produced artificial random filament arrangements which were not correlated to actual micro-structures found in fibre bundles.

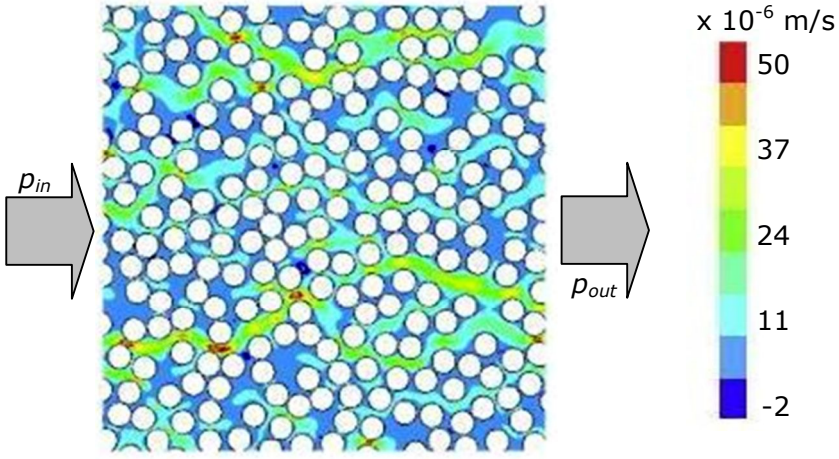

Figure 8: Transverse flow through a random array of filaments. The colour code shows the horizontal velocity field in the pressure driven system. The formation of major flow channels (high flow velocities) is visible. Reprinted from Yazdchi et al. [57] with permission from Elsevier.

A similar approach for the prediction of the axial permeability, $K_{\parallel}$, in a random array of filaments was used by Chen and Papathanasiou [58]. In order to generate the random micro-structure, they employed a method to disturb a regular arrangement (Section 2.2.3). Depending on the number of distortion iterations, they could influence the degree of randomness. They observed a higher average permeability with an increase in heterogeneity of the micro-structure of their models at constant V_f. The random filament arrangement leads to the formation of large pores locally which dominate the flow behaviour. The observed effect therefore contradicts the observations made in transverse permeability simulations. The resulting permeability values could be related to a power law relationship to the average first nearest neighbour distance. Unlike

the equations derived for models with regular filament arrangements (e.g. Eq. 9) the exponent is not constant but a function of the V_f. Due to the nature of the chosen micro-structure generator, employing a Monte Carlo algorithm, the V_f range was limited to 0.10 - 0.55 which is not representative of the V_f found in fibre bundles within a composite part.

In order to reduce the computational effort due to the discretisation of the domain into a large number of finite elements, the Voronoi cell tessellation of the random filament arrangement was proposed [76]. It is estimated that the computational time with the use of VCFEM would be 60-70 times lower than that compared with conventional FEM packages [74]. Therefore, larger systems with more than 1000 fibres could also be modelled as claimed by Hellström et al. [22]. They applied this concept to flow predictions of water through particles of sand in a dam but claimed that it would be equally applicable to fibre reinforced composites. They incorporated flow induced deformations due to drag forces on the particles to their model. From series of simulations they found that small flow induced deformations in their random arrangements always lead to increased permeabilities of the system. This finding is similar to the observations made by Chen and Papathanasiou [58] for longitudinal flow along random filament arrangements. Their numerical analyses suggest that the permeability can be described as a function of the average mean nearest neighbour distance. Based on this consideration an empirical model for the prediction of the longitudinal permeability was proposed based on curve fitting of the simulation results. The consideration of the mean distance between closest nearest neighbours only assumes, however, some sort of homogeneity of the filament arrangements and local variabilities are ignored.

All the discussed models for the prediction of saturated permeability in randomised filament arrangements are based on computational considerations only. Different degrees of randomness are analysed, however, the validation on actual filament arrangements is omitted or only performed with insufficient detail. In addition, these models assume perfect parallel alignment of the filaments. Influence on the flow due to tortuosity in the third dimension is ignored. Despite these limitations, the models clearly demonstrate the effect of filament arrangement on the resulting saturated permeability.

2.2.5 Multi-scale permeability modelling

Studies showed that micro-scale heterogeneities can significantly affect the macroscopic behaviour of composite parts [13, 17, 64]. The behaviour on the macro-scale, however, determines the micro-scale conditions. Therefore, numerous multi-scale models are proposed to incorporate the response of different length scales into one modelling approach [77]. The employed material properties are homogenised to different degrees depending on the length scale considered. Deviations from the global behaviour by a more refined local simulation are then estimated [78].

Embedding a micro-structure (RVE) in a homogenised material exhibiting average material properties is the simplest multi-scale modelling approach [64]. This method enables a simplified analysis of the considered problem and enables the detailed estimation of the influence of the micro-structure locally. Prior knowledge of critical areas within the composite is, however, required to determine the location at which the RVE is evaluated. Therefore this approach is usually limited to elementary problems. To overcome this limitation, hierarchical models are employed where models on different length scales are evaluated. This can be achieved by bottom-up [79] or top-down [76] calculations, starting from the micro- or macro-scale respectively.

For the permeability prediction in composites Cai and Berdichevsky [59] proposed a model for unidirectional reinforcements combining the inter- and intra-bundle flow. They assumed a cylindrical flow channel subjected to Darcy flow as inter bundle space which is surrounded by an annulus of material exhibiting the permeability of a densely packed hexagonal filament arrangement [50] embedded in a homogeneous material. For the transverse permeability of this regular arrangement they found a solution depending on the maximum achievable V_f and the average V_f similar to the work proposed by Gebart [49]. To improve their model, they employed curve and parameter fitting which makes the application of their approach impractical. They found that the transverse permeability for their model is dominated by the gaps in between single filaments. Their estimation of the longitudinal permeability indicates domination of the properties by the inter bundle gap geometry. Therefore, they concluded that without an accurate description of the meso-structure the longitudinal permeability cannot be predicted accurately.

Choi et al. [60] employed the Kozeny-Carman equation (Eq. 8) to predict the longitudinal and transverse permeabilities at different length scales successively. The factor K_0 in the Kozeny-Carman equation was shown to be dependent on the V_f and therefore not presumed to be constant. Their work, however, was based on regular periodic arrangements only. Even though they claimed that their predictions are an improvement compared to single scale permeability predictions, their work failed to predict the variability observed during permeability measurements.

A multi-scale model incorporating micro-scale variabilities was suggested by Brennan and Walrath [61] in order to improve the accuracy of the macroscopic saturated flow analysis. Their model, however, ignores meso-scale structures which result in dual-scale porosities in between and within fibre bundles commonly found in composites. The geometrical micro-scale variability was incorporated based on data from their earlier work of simulated random arrangements [80]. Local geometrical arrangements of the modelled filament structures are replaced by idealised rhombic configurations. To account for the randomness, the actual V_f is fitted with an empirical polynomial function resulting in an adjusted V_f used as input for the model. The average transverse and longitudinal permeability was approximated based on Darcy's law for the resulting equivalent micro-structures. In the case of transverse flow their permeability value is surprisingly higher than the permeability of regular arrangements which contradicts findings reported in the literature [50, 57, 59, 60]. In addition, the applicability of their model to actual composite manufacturing processes is questionable due to the lack of different geometrical scales.

For a uni-directional fibre bundle, Tran et al. [62] developed a model to describe the porous structure formed in between filaments. Based on semi-empirical inter-filament distance distributions, they estimated the shape and spatial distribution of presumed ellipsoidal pores within a homogeneous, non-permeable material. They showed, however, that their micro-scale approach is limited to low V_f only (V_f <0.4) due to the necessary pore connectivity which is not present at higher V_f. Their model is therefore not suitable for the description of flow in fibre bundles used in composites where larger V_f are present. Instead, they applied their pore based modelling approach to the meso-scale, assuming a distribution of ellipsoidal inter-bundle and inter-layer porosities, estimated from measurements on micrographs. These porosities were assumed to be embedded

in a homogeneous material, representing the fibre bundles. The permeability of the yarns on the micro-scale was assumed to be constant and estimated by Gebart's model [49], ignoring micro-scale heterogeneity. Their permeability predictions were lower than their measurements and they argued that stronger pore connectivity must exist. However, the simplifications and assumptions made will add to this effect.

2.3 Impregnating transient flow and void formation

At the macro-scale, the description of the mould filling in a LCM process can be assumed to follow Darcy's law for a homogeneous material (Section 2.1.1). More detailed simulations of the impregnation of dry textile reinforcements with liquid resin are governed by two types of flow. Channels are formed in between fibre bundles which exhibit large pores compared to the gaps present within the yarns. Therefore, the inter bundle flow is expected to be pressure driven only and is often assumed to follow Darcy's law or sometimes the Navier-Stokes equations (Appendix A.2). The impregnation of fibre bundles on the other hand is also affected by capillary effects [19, 81]. Their strength depends on the ratio of capillary pressure, which in turn depends on the local filament spacing, to the applied pressure gradient as discussed e.g. by Kang et al. [82]. It is assumed that the intra-bundle flow can be described by the Navier-Stokes equations (Appendix A.2). These two types of flow are competing during the impregnation process of the dry fibre preform. Effects related to the resin properties, such as change of viscosity during impregnation and outgassing, which may affect the flow behaviour are usually ignored.

Even though movement of fibre bundles can be observed close to injection gates (high pressure) or vents (wash-out) at the macro-scale, filament movement within these bundles during impregnation was not yet reported in the literature. Movement of single filaments during impregnating flow would alter the permeability locally. This would then influence the shape of the flow front and hence affect the probability of air entrapment at the micro-scale. For the case of water flow through sand particles in a dam a significant influence due to particle mobility was shown [22]. However, interactions between filaments in a fibre bundle will restrict possible movements in a composite. Movement of filaments are therefore usually ignored in the modelling of transient flow.

2.3.1 Description of transient flow

During the impregnation process of dry fibre reinforcements the domain is saturated with resin behind the flow front only. For the description of the transient fluid flow into the dry fibre bundles a set of equations is employed. These equations consist of conservation equations, auxiliary relations, initial and boundary conditions [83].

The most important equation of transient fluid flow is the principle of the conservation of mass (Appendix A.1). The mass conservation law states that mass can neither be created nor destroyed and is transported by the fluid velocity, *v*. Considering incompressibility of the fluid, which is generally valid for most fluids, mass conservation reduces to:

$$\nabla \boldsymbol{v} = 0 \qquad \text{Eq. 12}$$

with ∇ representing the differential operator for the fluid velocity vector. It is worth noting that the conservation of mass becomes independent of the fluid properties in Eq. 12.

The time rate change of the fluid motion (velocity) equals the applied forces and is described by the conservation of momentum equations. Simplifications can be made due to the fact that the impregnating fluid velocity in LCM processes is generally low. Therefore, laminar flow assumptions can be applied. The typical Reynolds number (Section 2.1.2) for composite manufacturing process is generally much smaller than one ($Re \ll 1$) which enables the use of further simplifications. Creeping flow assumptions can be made and the conservation of momentum equation reduces to so called Stokes flow:

$$\nabla p = \mu_f \nabla^2 v \qquad \text{Eq. 13}$$

This equation reflects the necessary equilibrium between the applied pressure gradient, ∇p, and the shear stresses present within the fluid, $\mu_f \nabla^2 v$. The velocity term in Eq. 12 and Eq. 13 can be estimated over the permeability of the textile reinforcement and calculated by Darcy's law (Eq. 3). Commonly made assumptions for the simulation of fluid transport in LCM processes are summarised in Table 3.

Table 3: List of assumptions commonly made for simulations of transient impregnating flow in composite production processes based on fibre reinforcements.

Property	Assumptions
Flow type	Laminar (low Re) Creeping ($Re \ll 1$) • viscous forces much stronger than advection
Fluid	Newtonian (μ_f = constant) Homogeneous Incompressible (ρ = constant)
Others	Isothermal (no temperature effects, resin curing etc.) Gravity effects are ignored
Boundary conditions	Model domain • Periodic boundary conditions Filaments: • No-slip boundary conditions (0 fluid velocity at boundaries) • Solid impermeable boundaries
Initial conditions	Pressure gradient applied
Reinforcements	Stationary (no flow induced deformations)

2.3.2 Capillary pressure effects

In LCM process, a liquid resin impregnates the dry fibre reinforcement and replaces the air in the mould. Liquid transport is driven by the applied pressure, pushing the resin into the material. Due to their size, the filling of the pores in between fibre bundles with resin is not only affected by the pressure driven flow but also by capillary effects [19]. The capillary effects can be visualised for the example of the shape of the interface between a liquid and gaseous phase in a small diameter tube (Figure 9A-C). The liquid column is moving upward at the side of the tube, resulting in a concave shaped surface. The pressure difference across the interface of the two immiscible fluids (e.g. air and resin) is called the capillary pressure and stems from the difference in molecular attraction forces (Figure 9D).

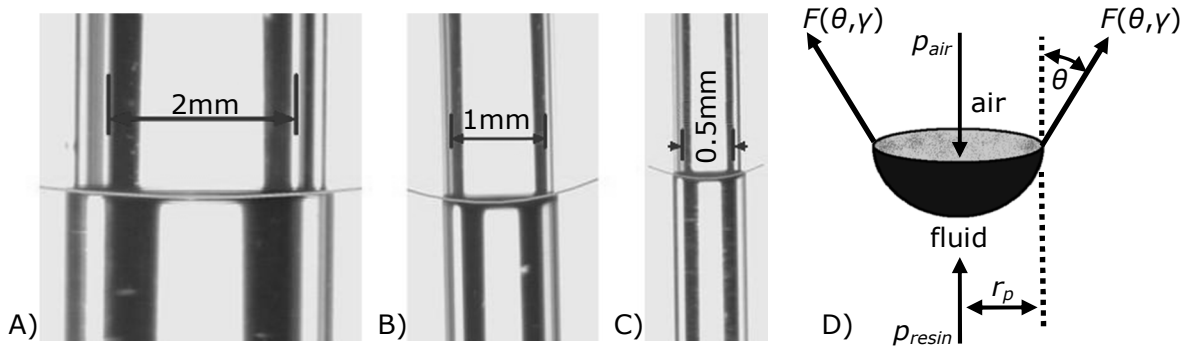

Figure 9: A-C) Examples of concave flow front shapes for contact angle measurements as function of the inner tube diameter. Reprinted from Li et al. [81] with permission from Elsevier. D) Schematic representation of the resulting fluid-air interface due to difference in molecular attraction forces at the wall surface of the air-liquid interface.

Presuming the fluid column to be in static equilibrium, the forces acting on the surface of the water column must be balanced. Thus, the external forces, p_{air} and p_{resin}, acting on the cross-sectional area of the tube with radius, r_p, must be in equilibrium to the forces, F, exerted by the surface tension of the air-resin interface, γ, and the contact angle, θ, defining the wettability of the container circumference (Eq. 14).

$$(p_{air} - p_{resin})\pi r_p^2 = \gamma \cos\theta\left(2\pi r_p\right) \qquad \text{Eq. 14}$$

Defining the capillary pressure, p_c, as the difference in interfacial pressures

$$p_c = p_{air} - p_{resin} \qquad \text{Eq. 15}$$

Eq. 14 can be re-written as:

$$p_c = \frac{2\gamma \cos\theta}{r_p} \qquad \text{Eq. 16}$$

If the resin and fibre reinforcement combination is kept constant, it can be seen from Eq. 16 that the capillary effect will only be determined by the pore structure of the fibre bundle. A reduction of the pore radius, r_p, will result in a larger capillary pressure [84]. This is equivalent to an increase in V_f within the composite. In the case of impregnating pressure driven flow parallel to the filament axis, Li et al. [81] confirmed this behaviour experimentally. They found a significant influence of the capillary pressure as driving force of the impregnating flow within composite materials. For vacuum assisted flow the

opposite effect was observed. It was speculated that the vacuum assisted flow might alter the longitudinal flow channel geometry. This would lead to an increased heterogeneity of the flow channel width which in turn leads to increased permeability due to the presence of larger flow channels dominating the flow. The influence of varying flow channel geometries was, for example, demonstrated in the simulations performed by Chen and Papathanasiou [58]. Presence of larger flow channels in the model domain was shown to dominate the longitudinal flow behaviour. Based on their experimental measurements of the impregnation of fibre bundles Li et al. also concluded that the dynamic capillary pressure is not constant but a function of the velocity of the impregnating fluid (compare with Ca^* in Section 2.3.3). In addition, they concluded that the unsaturated permeability of a fibre bundle depends on the type of pressure applied; pressure driven flow or vacuum assisted flow respectively. As a result they proposed different Kozeny-Carman constants (Eq. 8) to describe the unsaturated permeability of the tested fibre bundles depending on the applied driving pressure. However, the applicability to actual reinforcement materials exhibiting dual scale porosities has still to be proven.

The definition of the capillary pressure is derived for the ideal case of a circular tube. Pore geometries formed in actual fibre bundle micro-structures are, however, more complex. To simplify the calculations and describe arbitrary channel shapes, the concept of the hydraulic diameter, d_h, was developed, e.g. [19]:

$$d_h = \frac{4A}{U} \qquad \text{Eq. 17}$$

Here, A is the cross-sectional area of an arbitrary shaped tube and U its perimeter. The concept of d_h will enable the description of the capillary pressure for an arbitrary channel geometry in analogy to the special case described by Eq. 16. It should be noted that the hydraulic diameter is related to the geometry constant, c, in Eq. 9 which is derived from the channel geometry formed between filaments.

2.3.3 Void formation mechanism

The formation of voids on the micro-scale is known to be dependent on the dimensionless capillary number, *Ca* (Eq. 18) [82]. This number describes the ratio of the viscous forces, $F_{viscous}$, to the forces exerted by the surface tension, $F_{surf.tens}$. The viscous forces are a product of the viscosity, μ_f, of the fluid and the resin velocity, v. The cohesion forces within the fluid are specified in the surface tension, γ.

$$Ca = \frac{F_{viscous}}{F_{surf.tens.}} = \frac{\mu_f v}{\gamma} \qquad \text{Eq. 18}$$

When impregnating fibre reinforcements, the liquid is wetting a solid filament network. Incorporating the adhesive tension of the penetrating liquid in form of the contact angle, θ, to a given reinforcement material leads to the generalised definition of the capillary number, Ca^* (Eq. 19). This expression can be used in the description of LCM processes [14] for the evaluation of the influence of p_c.

$$Ca^* = \frac{\mu_f v}{\gamma \cos\theta} \qquad \text{Eq. 19}$$

With this approach the influence of the mould surface is ignored [85]. This assumption is considered valid for composite production methods due to the limited number of filaments in contact with the mould tool compared to number of fibres in the bulk material.

The formation of voids is a result of local gas entrapment due to merging flow fronts during impregnation [86]. Utilising electrical sensors placed in a mould tool, Bréard et al. [24] related the measurement of electrical conductivity during impregnating fluid flow to the degree of saturation of the non-conductive glass reinforcement. They discovered a parabolic pressure profile, suggesting a partially saturated zone in the textile reinforcement travelling after the flow front. Only after complete mould filling, the pressure profile became linear as suggested by Darcy's law. Employing Magnetic Resonance Imaging (MRI) Endruweit et al. [87] concluded that the partially saturated zone after the fluid flow front has a specific length depending on the fabric geometry. Their voxel resolution was too small to detect micro-scale voidage; however, meso-scale void formation due to gas entrapment could be displayed. The detected voids did not move during the course of the impregnating flow but reduced in size due to the increase in pressure of the fluid. The zone of partial saturation vanished after complete mould filling.

Rohatgi et al. [14] determined the inter- and intra- bundle void formation in a unidirectional stitched fibreglass mat during impregnating flow in a RTM process. The translucent properties of the glass reinforcement used made it possible to visualise the liquid flow front (Figure 10) of different types of oil by shining light through the transparent mould tool. They could visualise the formation of voids, due to air entrapment of merging flow fronts at different injection pressures.

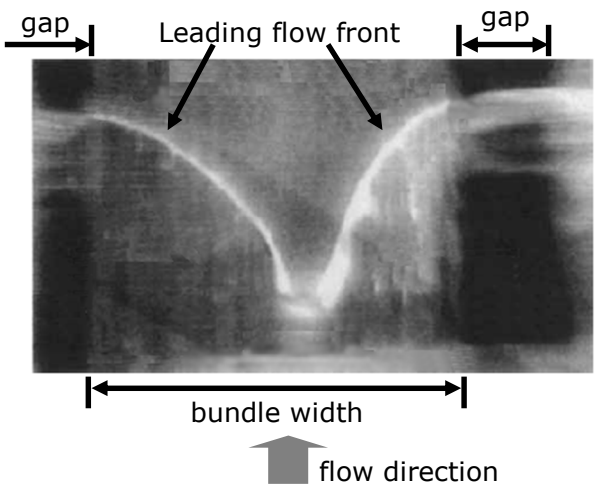

Figure 10: Flow front visualisation within a uni-directional glass fibre bundle. Merging inter-bundle flow fronts lead to air entrapment within the fibre bundle. Adapted from Rohatgi et al. [14] with permission from John Wiley and Sons.

They related the observed void content to the modified capillary number (Eq. 19) and could show that an optimum flow velocity exists, minimising the void content for flow along and transverse to the fibre bundle. At low capillary numbers (corresponding to low fluid velocities), the forces exerted by the surface tension are larger than the viscous forces. The observed flow front within the fibre bundles was therefore faster advancing than the resin flowing through the inter-bundle gaps resulting in an increased void content within the fibre bundles. The opposite effect was observed for a larger modified capillary number. Critical Ca^* for the formation of micro voids were found to be $>10^{-3}$ for axial and $\sim 10^{-4}$ for transverse flow. With regard to composite manufacturing processes these observations imply that it would be advantageous to maintain a constant flow velocity of the fluid flow front within the mould rather than a constant injection pressure. Even though their results are an interesting observation of micro-scale void formation at the flow front, the applicability to other materials has still to be validated. In addition, in case of carbon fibre reinforcements their measurement method will not be applicable due to the non-transparent nature of the material. Furthermore, more complex flow geometries such as found in layered stacks of material might also alter the results.

For practical applications it should be noted that it was found feasible to purge macro-voids with an increased flow rate after complete mould filing [14]. Voids formed within the fibre bundles, however, seemed not to be removable. In addition, the utilisation of vacuum pressure can lead to a minimisation of the micro void content [6]. The remaining voids formed during the impregnation of the fluid into the fabric will reduce in size due to a build-up of the resin pressure after the flow front advances [25]. This effect was, for example, observed experimentally by Endruweit et al. [87] for a meso-scale void.

At the micro-scale, void formation was experimentally visualised for small regular and random arrangements which contained up to 18 filaments by Okabe et al. [88]. They were able to show small entrapments of air when water was impregnating their arrangement of parallel aligned pillars. They used their observations as validation of their numerical transient flow models (Section 2.4.2). Their pillars with a diameter of 200 μm are significantly larger than filaments used in composite materials. They fail to report, however, in how far their choice of materials for their filaments and fluid matches the interaction between fibres and resin used in composites. In particular, the surface tension (Section 2.3.2) may be significantly different.

2.4 Modelling of unsaturated flow

The modelling of impregnating unsaturated flow is usually performed to either describe the variability of the shape of the flow front observed in LCM processes or to simulate the formation of voids [89]. Usually, these models incorporate meso- and micro-scale levels with varying levels of simplification. The global flow is assumed to be governed by Darcy's law (Eq. 3) and the pressure drop is assumed to be linear. In case of fibre preforms exhibiting dual scale porosity it was observed that the pressure drop is not linear due to the presence of a partially saturated region behind the flow front [25]. Other assumptions made are outlined in the following sections.

2.4.1 Shape predictions of the flow front

Tan and Pillai [89] developed a dual-scale transient flow model based on hierarchical simulations. Their approach is based on the assumption that the resin flow front is partially saturated only (Section 2.3.3). Due to the larger permeability of the channels formed in between fibre bundles the impregnation of the filaments only occurs after the bundles are completely surrounded by fluid.

The delayed impregnation of the filament bundles is incorporated by a sink term, $\dot{S}$, in the mass balance equation [25] similar to:

$$\nabla v = \dot{S} \qquad \text{Eq. 20}$$

and with $\dot{S}$, the degree of saturation, defined as function of the mass flow rate, $\frac{\delta s}{\delta t}$, into the intra bundle porosity Φ:

$$\dot{S} = \Phi f \frac{\delta s}{\delta t} \qquad \text{Eq. 21}$$

$\dot{S}$ becomes zero for a fully saturated fibre bundle. The proposed macroscopic flow model is based on flow through meso-scale unit cells and the micro-scale flow is assumed as flow through an array of hexagonal filaments following Gebart's model [49]. They could predict the partially saturated zone in the modelling of a larger composite structure as a function of the resin velocity. They failed, however, to incorporate variability in the preform on the meso- or micro level. The resulting flow front is therefore always symmetric. In addition, the micro-scale flow variation can influence the macro-scale flow behaviour which is not accounted for in top-down modelling schemes [25]. The influence of the fluid velocity on the type of void formed (inter- or intra-bundle) [14] is also not taken into account.

Wong [90] predicted variabilities in permeability derived from simulations of steady-state flow employing different fabric architectures. He found a strong dependence of the permeability on the geometric variability. His simulations, however, were based on periodic variable meso-scale unit-cells only. This implies periodicity on a larger scale.

2.4.2 Models for prediction of void formation

Kang et al. [82] proposed a model to predict the void content formed during a LCM process based on the fluid velocities within and around fibre bundles transverse to the bundle axis. Based on the difference of flow arrival times of the fluid, voids can form either within or in between the fibre bundles (Figure 11). This approach corresponds to the observations made by Rohatgi et al. [14], correlating the type of voidage to the capillary number.

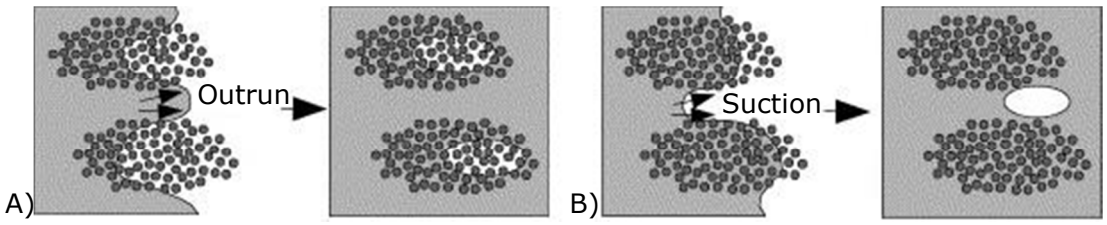

Figure 11: Void formation mechanism within and in between fibre bundles. A) Fluid velocity in between fibre bundles is larger than within the tows which leads to air entrapment in the bundles. B) The flow within the fibre bundles is faster which leads to air entrapment in between fibre bundles. Reprinted from Kang et al. [82] with permission from Elsevier.

The flow in the inter-bundle channels was assumed to be pressure driven only, following Darcy's law (Eq. 3). For the intra-bundle flow capillary pressures were considered additionally:

$$v = \frac{K}{\mu_f} \nabla (p - p_c) \qquad \text{Eq. 22}$$

Their model requires curve fitting of experimental data of the void content as a function of the capillary number assuming an optimal resin velocity minimising the void content. This curve fitting, however, limits the applicability of their approach to a specified material and process only and is strongly affected by the accuracy of the measurements. In addition, it was assumed that only a single void can form either within or in between fibre bundles. This does not conform to experimental observations showing single fibre bundle cross-sections containing a number of voids [86]. The validation of their results to experimental data does therefore show large differences. It should be mentioned, that only relatively large inter-bundle voids were analysed for the validation of their model and intra-bundle voidage was ignored.

This model approach was expanded by Lee et al. [9] incorporating void transport effects. They employed their simulations as a real-time control for a LCM process to minimise the void content based on the optimisation of the fluid velocities within and around fibre bundles. Using curve fitting to experimental data, suggesting an optimal resin velocity resulting in a minimum void content (Section 2.3.3), their model effectively controlled the flow front velocity. The control of the flow velocity was achieved by adjusting the pressure at different inlets or vents as well as the additional placement of vents. They failed, however, to prove a reduction in micro-scale voidage of the final part. Attempts are made

to further refine this approach by relating the permeability and the capillary pressure to the degree of fabric saturation [25], however, additional work is required.

Bréard et al. [24] based their modelling approach on the idea that the permeability during impregnation is not constant due to the presence of capillary effects. They argued that these effects are reflected in the non-linear pressure distribution of the fluid measured during impregnating flow into the dry preform. At full saturation of the preform, the geometrical permeability is identical to the initial material constant. At the flow front and in the zone of partial saturation behind the leading flow front the permeability is assumed to be a function of the degree of fabric saturation, *s*. Hence, Darcy's law is adjusted to:

$$v(s) = \frac{K(s)}{\mu_f} \nabla p \qquad \text{Eq. 23}$$

The local permeability, *K(s)*, is assumed to be based on the degree of saturation and always lower than the fully saturated permeability. Experimental measurement data of the saturated compared to unsaturated permeabilities are, however, inconclusive and show ratios of 0.25 to 4 (Section 2.1.3). This assumption would need therefore to be verified for the analysed fabrics. In addition, they argued that capillary pressures can be ignored due to the very low injection pressures employed, which contradicts experimental results, e.g. Rohatgi [14]. In addition, the validity of the modelling approach for the formation of voidage was not demonstrated experimentally.

Park et al. [8] proposed a model to incorporate, in addition to the inter- and intra-bundle void formation based on the local resin flow arrival times, a void compaction and void migration formulation. Their model could predict some void formation phenomena found in actual textile reinforced composites such as an increased void content at the vent due to void migration and a reduced void content at the inlet due to void compaction as a result of raising fluid pressure. They, however, ignored local heterogeneities which will alter the resin flow locally. Even though capillary flow was considered at the filament (micro)-scale, a periodic filament arrangement following the considerations of Gebart [49] was assumed as input for the permeability in Darcy's law, ignoring the local heterogeneity of the filament arrangement found in real composites.

Transient impregnating flow at the micro-scale was modelled by Okabe et al. [88]. They described the fluid flow by use of the moving particle semi-implicit method for regular and random fibre arrangements. They were able to predict void formation which was validated experimentally on flow through an arrangement of pillars with a diameter of 20 – 30 times larger than actual filaments. The simulation times of several hours up to several days were, however, large compared to their relative small model domain. In addition, their evaluation of formed voids is not straight forward and subjective. Their method seems, however, to be an interesting alternative to classical CFD simulations.

2.5 Summary

Textile reinforcements used in LCM are subjected to two different types of flow during the manufacturing process, saturated and unsaturated respectively (Section 1.2). The governing equations describing these types of fluid transport were elucidated (Section 2.1) and different modelling approaches were discussed (Sections 2.2 and 2.4), focussing on the fibre-scale.

The flow through the fibre network is described by the three-dimensional permeability tensor (Section 2.1.1). Testing and modelling can however be reduced to three principal permeability components only (Section 2.1.3). The permeability longitudinal is significantly larger than the permeability transverse to the fibre bundle axis (Section 2.2.2). Geometric variability in the preform leads to scatter in the determined permeability values. The transverse permeability is significantly reduced with an increase in heterogeneity of the micro-structure (Section 2.2.4). An opposite effect is observed for the flow parallel to the fibre bundle axis. This work focusses on the description of the transverse permeability due to the larger influence of the variability and lower average permeability in this case.

Several models were proposed in the literature, assuming a periodic arrangement of the filaments, resulting in a single permeability value for a specified V_f in the case of saturated flow (Section 2.2.2). Compared to random filament arrangements it was demonstrated that the flow perpendicular to the filament axis of these models gives systematically higher values [60]. In addition, these models fail to explain the intrinsic variability present within fibre bundles, ignoring the fact that not only the porosity but also the packing format influences the permeability [50].

Different methods for the randomisation of the filament arrangement were developed to overcome this limitation (Section 2.2.3). Most of these models are based on artificial algorithms only compared to measurement data of the fibre network geometry. For the generation of statistically equivalent filament arrangements in this work, the micro-structure within fibre bundles has to be quantified accurately (Chapter 3). Based on these measurement data a suitable modelling approach has to be selected or developed. The generated statistically equivalent filament arrangements can then be used for the determination of the permeability of a reinforcement material at different V_f (Chapter 4). This will improve the understanding of the variability in flow properties of reinforcement textiles at the micro-scale.

During transient impregnating flow, defects can form at the flow front (Section 2.3.3). Due to the multi-scale architecture of fibre reinforcements and the random filament arrangement within fibre bundles, different fluid velocities are present. Converging flow fronts can result in local gas entrapment [14] which can, if not flushed out during the course of mould filling, remain as voids in the final solidified part. Most transient flow modelling approaches describe the multi-scale flow in between and within fibre bundles (Section 2.4). The random micro-structure present within the fibre tows is, however, generally ignored. In this work, the generated statistically equivalent filament arrangements of a fibre bundle will be used for the determination of probable void formation (Chapter 5). This data can then be validated with measured void contents on composite samples produced under defined flow conditions.

3. Micro-structural data acquisition and processing

Reinforcement fabrics used in LCM processes need to be fully saturated with resin during the impregnation process. It is necessary that the pores formed in-between fibre bundles and within the individual filaments are fully saturated with the liquid matrix material. It was shown in Chapter 1 that presence of voids within fibre bundles can significantly reduce the mechanical properties of a part in service. These defects are difficult to detect due to their size. They can form due to differences in local flow velocities and merging flow fronts (Section 2.3.3). It was demonstrated that the variability of the filament arrangement at the micro-scale can lead to significant variations of the local flow properties (Section 2.2.4). Filament arrangements employed in the prediction of the micro-scale flow are based usually on computational considerations only due to the lack of suitable micro-structural measurement data. This chapter therefore focuses on the systematic analysis of the micro-structure of a carbon fibre reinforced composite material (Section 3.2). A suitable measurement technique is proposed (Section 3.3) and the measurement data are presented (Section 3.4). The measured distributions are then utilised in an adapted micro-structure generator (Section 3.5).

3.1 Introduction

In order to gather stochastic data about the micro-structure of a composite, a suitable method of examining samples is required. The selected measurement technique needs to ensure a sufficiently high resolution to guarantee the desired level of detail in the image of the composite. In the case of carbon fibres the resolution of the measurement method needs to be sufficiently smaller than their diameter of around 7 μm. Some measurement techniques can, therefore, be disregarded immediately such as conventional ultrasonic analysis where the maximum achievable resolution is far below that required.

A suitable method of determining the micro-structure is x-ray scanning where internal features can be visualized in a non-destructive way. In order to obtain a

three-dimensional image of the object, micro-computer tomography (micro-CT) was developed which takes virtual two-dimensional slices of an object which are then rendered into a volume image in a second step. Different x-ray sources or scanning methods can be used depending on the desired accuracy and sample dimensions [91].

In micro-CT, there are certain limitations on the sample size depending on the required resolution. The main limitation is the distance between the x-ray source and sample which has to be minimized in order to maximize the resolution. Therefore, only small samples can be scanned. A typical dimension would be 1 mm x 1 mm x 10 mm [92, 93] to visualize single fibres within a carbon composite. For meso-scale investigations such as fibre bundle shapes, which require less detail, larger samples e.g. 5 mm x 15 mm x 50 mm can be analysed [94, 95].

The main challenge when examining carbon fibre reinforced composites by means of x-ray analysis is the similar atomic structure of the carbon fibres and the matrix; both consist primarily of a carbon backbone. In addition, the x-ray absorption of this light element is about a thousand times lower than decrement in phase shift when the x-ray beam passes through the material [96]. This limits the analysis method, e.g. synchrotron x-ray micro-CT, with which the material can be scanned. Ring-like artefacts and noise can cause further problems during scans, which needs to be corrected after the scan e.g. [93, 97, 98].

Due to the sample size limitations and availability of micro-CT devices, two-dimensional optical microscopy is often used to analyse material cross-sections. In addition, the achievable resolution of optical microscopy is significantly higher than in any available x-ray inspection method. To a certain limit, it is possible to extract three-dimensional information from single cross-sections. Eberhard and Clarke [99] used confocal laser scanning microscopy, which enabled them to follow a fibre path up to 200 μm into the material. This technique, however, is not applicable to carbon fibres as it requires a semi-transparent material. Davidson et al. [100] generated three dimensional data from scanning parallel cross sections and developed a pattern matching algorithm to determine the fibre orientation. Even though they managed successfully to stitch local images together to generate a high resolution image of a large cross-section, they employed a simple thresholding procedure to their images which leads to a lack of accuracy of the obtained data.

Image acquisition with Scanning Electron Microscopy (SEM) will result in high magnification images compared to optical microscopy and micro-CT (Figure 12). The good depth of field of SEM ensures a large range of distances outside the focal plane in which contours appear sharp (e.g. Figure 2C). This makes it possible to visualize the changing topography of a sample clearly. Rounded edges of fibre cross sections caused by polishing, differences in sample height of the fibres compared to the surrounding matrix due to different abrasive behaviour during polishing and even voids within the samples can be explicitly visualised. The major drawback of this method of image acquisition is the relatively high cost of the instrument. Additionally, some SEM techniques require an additional surface coating due to the non-conductivity of the surface.

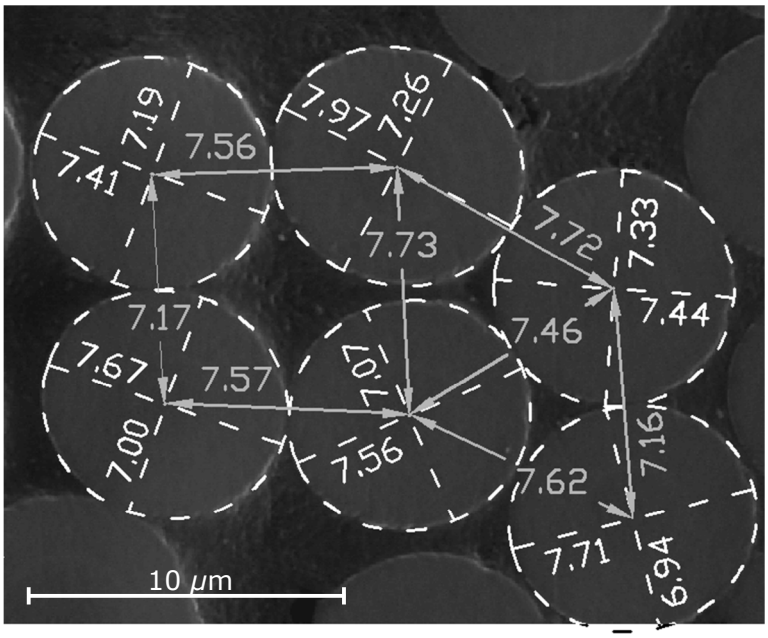

Figure 12: SEM image of carbon fibre cross-sections. The measurements of the inter-filament distances and the radii of manually fitted ellipses are displayed in the image.

Due to the limitations and particular difficulties for the analysis techniques described, it was chosen to use the relatively fast and inexpensive reflective light microscopy in this work. It comes, however, with its own limitations. The theoretical resolution limit for this technique, for example, makes it impossible to detect objects smaller than 0.2 μm [101]. The size of a filament cross-section to be analysed is, however, significantly larger than this limit. In addition, the analysis technique is limited to two dimensions only but it is possible to analyse larger cross-sectional areas compared to the methods discussed [100]. It was decided that this technique offers a sufficiently good balance between the image resolution and the maximum number of images needed to capture full fibre bundle cross-sections containing several thousand single filaments.

3.2 Experimental methodology

Optical microscopy can be an inexpensive alternative compared to other measurement techniques. Together with image stitching of overlapping single images it offers the opportunity to generate a high resolution, large area image of the fibre bundle cross-section which enables larger areas to be studied [99, 100, 102]. A stitching code is implemented in the current work based on fast-Fourier correlations programmed in Matlab [103]. The microscope set-up at the University of Nottingham enables a large area scan of a sample by a computer controlled stage which allows automated x-y positioning as well as automated z-positioning.

In order to obtain morphological data from an image, the colour or grey scale data generally has to be transformed into a binary image. Most often this is done through simple image thresholding [66, 99, 100, 104-106]. This means that colour values below a certain threshold are set to 0 and all values above this threshold are set to 1 representing matrix and fibres respectively. Some researchers use image enhancement techniques before thresholding their images e.g. [66]. The contrast of object edges, for example, can be enhanced by an 'unsharp' mask [107]. After thresholding of the image, the detected objects can be separated manually [104]. Preferably, objects are separated automatically by a segmentation algorithm such as the watershed procedure before or after thresholding. The watershed segmentation assumes the colour or greyscale values of an image to be a topographic surface [108]. Local minima are detected by a flooding simulation (in analogy of raising the water level on an uneven surface), and the separation lines between merging minima correspond to the watershed lines. However, inevitable differences in lighting, local light reflections and shading [109] makes it unfeasible to use one global threshold for an entire image.

Manual image enhancement should, with view on the amount of data, be avoided [105]. Gajdošík et al. [104] for example restored image features manually, however, this was only necessary because of the poor quality of input images used in their work. Furthermore, they only used their processed images to estimate fibre centre positions. The detected filament cross-sections were then replaced with round disks. This approach consequently loses any detailed information about the actual (elliptical) shape of the filament cross-sections.

The assumption that fibres should appear as round disks in composite cross-sections can be made for most grades of glass and carbon fibres. When sectioned under an angle, ψ, they should appear as ellipses (Figure 13). Generally, the filament path within a fibre bundle exhibits undulation and misalignment [92, 110] and therefore the majority of filament cross-sections in a sample should appear elliptical under any sampling angle.

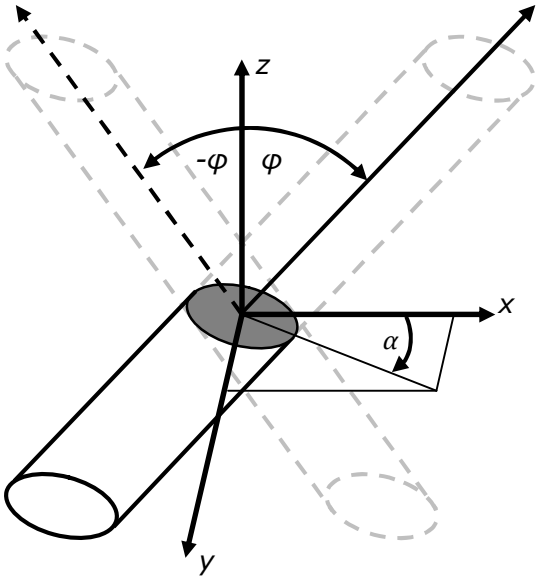

Figure 13: Illustration of the orientation ambiguity of an elliptical filament cross-section (grey shaded area). From the filament cross-section it is not possible to unambiguously determine the filament path into the material (solid lines).

The prior knowledge of the expected fibre cross-sectional geometry can be used to fit a predefined shape through the detected fibre boundary. From a single filament cross-section, it is therefore possible to determine to some extent information about the filament path, φ. Based on the ratio of the minor and major ellipse radii, *a* and *b* of a fitted ellipse (Figure 14) the filament path can be estimated by the following simple relationship (Eq. 9):

$$\cos\varphi = \frac{\mathrm{b}}{\mathrm{a}} \qquad \text{Eq. 24}$$

In case of perfectly aligned filaments, the filament path, φ_i, should be identical to the sectioning angle, ψ, of the sample.

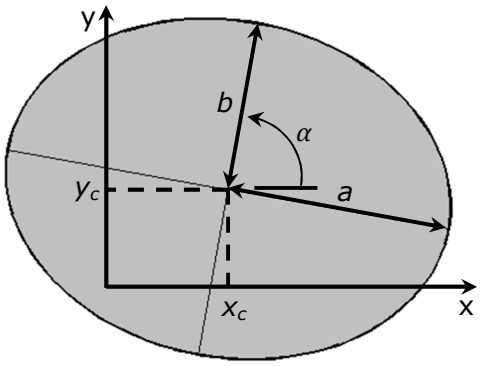

Figure 14: Ellipse in the general position with major and minor semi axis, *a* and *b*, offset to the origin, x_c and y_c, and rotation θ.

From the detected ellipses alone the fibre orientation cannot be unambiguously solved (Figure 13). Several solutions are proposed to section the sample under a defined angle to solve the fibre orientation ambiguity. Kratmann et al. [111] used cross sectional cuts at an angle of around 5° to determine the fibre misalignment. Sectioning the material under 5° was found not to solve the ambiguity problem unequivocally due to the presence of possible fibre bundle undulations. Blanc et al. [106] sectioned their material under about 30° in order to overcome the restriction of fibre orientation ambiguity when detecting an elliptical cross-section. This more pronounced 30° sectioning angle was used in this study which is much larger than any expected fibre bundle waviness and therefore suitable to address the ambiguity problem.

3.3 Image acquisition and processing

3.3.1 Image acquisition

The images were acquired with a Zeiss Axiolab, brightfield reflected light microscope. The objective used was a Zeiss Epiplan 50x/0.7 lens. The microscope is equipped with an automated stage and a 12bit monochrome camera, QICam Fast 1394. The resulting image size is 1392 x 1040 pixels. The pixel spacing δc of 0.093 μm, pixel centre to pixel centre distance, was estimated using the following relationship (Eq. 25):

$$\delta c = \frac{\Delta c}{M_0} \qquad \text{Eq. 25}$$

where Δc is the pixel spacing of the camera image sensor and given as 4.65 μm. M_0 represents the nominal magnification of the objective. The pixel spacing was confirmed on measurements of a calibrated graticule. Measurements of the

graticule in two orthogonal directions showed that that the image pixel spacing is identical horizontally and vertically, validating the assumption of a non-existing geometric distortion [109].

The theoretical resolution of an optical light microscope, i.e. the ability of the system to accurately reproduce the object contrasts within an image, is limited by the wavelength of the light used [109]. This diffraction limit can be determined as about half the wavelength of the light used [101]. In case of visible light, the maximum achievable resolution is therefore about 0.2 μm. It should be noted, however, that several techniques were developed in recent years which enable resolutions up to 20 nm [112]. The resolution limit of 0.2 μm means that it is impossible for edges of touching fibres (Figure 15) to be distinguished clearly.

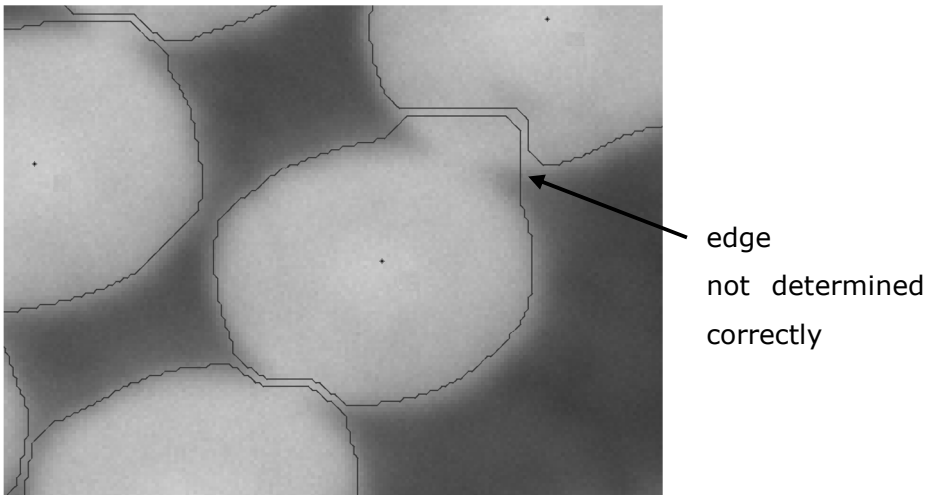

Figure 15: Magnification of fibres with boundaries detected by the watershed algorithm after thresholding.

Unfortunately, the nature of the captured micrographs (Figure 16) and the desired accuracy did not allow a simple thresholding technique to obtain morphological data (data about the form and structure). It is impossible to find 'one' threshold value for a complete image which can easily contain up to 250 fibres. The field of view is affected by inevitable variations in shading which is reflected in differences of local contrast. In addition, this effect is amplified locally by the presence or absence of filament cross-sections within the image. This will therefore result in different greyscale values for the same object. Furthermore, rounding effects of the specimen at the sample edges due to polishing of the specimen leads to fibres in the images appearing darker with less pronounced boundaries. Their greyscale values are therefore lower than in regions of fibre agglomeration.

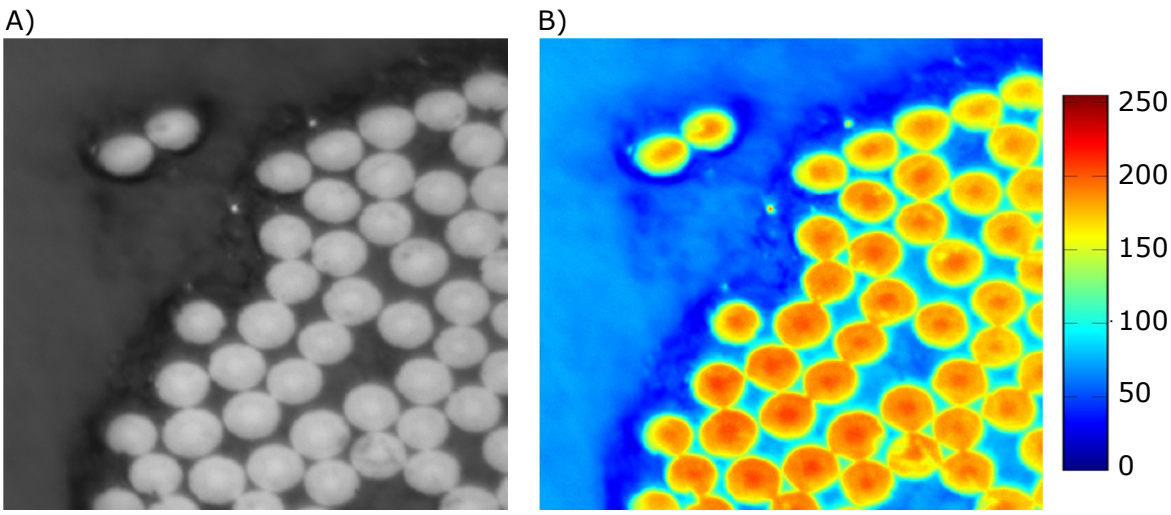

Figure 16: A) Part of a micrograph of a carbon fibre reinforced composite cross section and B) the same image re-coloured to emphasise differences in local colour values. The legend shows the greyscale values of the re-coloured image.

Finally, it is not always possible to separate touching fibres with an object separation algorithm such as watershed separation. Local greyscale differences are too small (Figure 15) due to the diffraction limit. Areas of adjacent fibres can therefore appear to belong to another fibre, leading to erroneous morphological data.

3.3.2 Image processing

In the current work, the simple thresholding technique cannot be applied and therefore a different approach is utilised based on prior knowledge of the expected filament shape. The process developed in this work is implemented in a Matlab® program described below and illustrated Appendix B. In a first step, areas of interest are determined. The contrast of the bright and dark areas, fibres and matrix respectively, is enhanced in the image initially. This is followed by the simple overall thresholding technique and a watershed separation of the remaining objects. Even though it is not possible to extract precise data of every single fibre cross-section, it is possible to determine centre points of areas of interest. These points are used as input of a first approximation of the fibre cross-section centres. A window of defined size is centred on every single position and a local image analysis is carried out.

It is possible to directly detect fibre edges in these local images. A widely used and generally accepted method of edge detection was developed by Canny [107]. This algorithm detects edges by examining neighbourhoods of pixels and evaluates the gradients. If this algorithm is applied to the image of a fibre, it can

be demonstrated that the detected fibre radii are underestimated (Figure 17). The minor ellipse axis, representing the actual fibre diameter, is significantly under predicted (6.48 μm instead of 7.17 μm here). Compared to a set of 29 reference measurements of manually fitted ellipses on high magnification SEM images, it can be shown that the major ellipse axis is underestimated by 1.9% and the minor ellipse axis by 8.4%. This shows that the direct edge fitting approach is not applicable for the obtained micrographs.

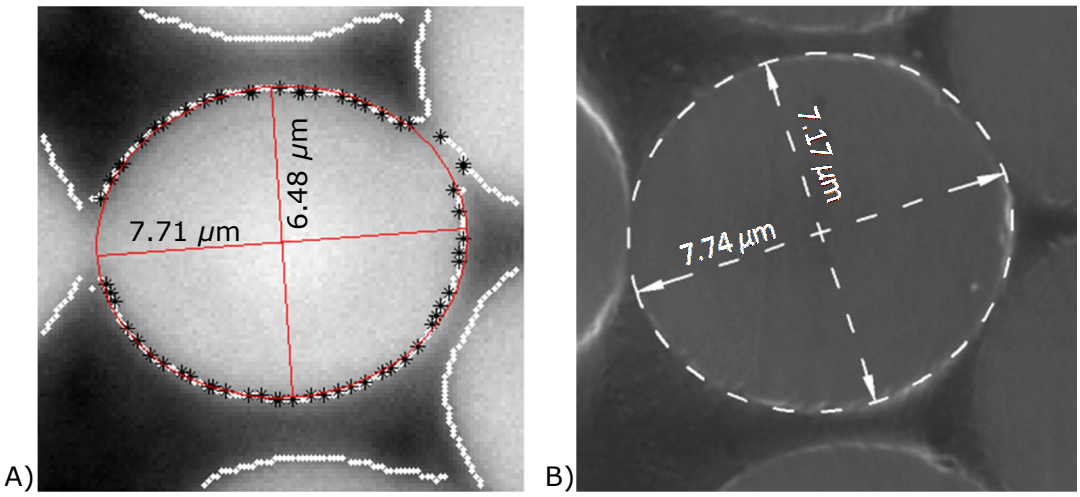

Figure 17: A) Edges detected with Canny algorithm, B) manually fitted ellipse on SEM image

Instead of using the original image, local colour gradients are calculated (Figure 18A) using the Sobel filter [107]. The calculation of colour gradients in these locally confined areas also allows absolute colour values of the image to be neglected. The problem of different levels of contrast or brightness, which depends on the position of the fibre in the overall image, can therefore be overcome.

After smoothing the gradient image, the edges can be determined using Canny's edge detector. The image of the fibre boundary gradients will show two distinct edges (Figure 18B). The inner edge (yellow dots) is present because the gradient of a fibre edge exhibits a greyscale gradient in two directions. The points belonging to the inner edge can be eliminated using a stencil based on a fitted ellipse through the Canny edges determined initially. This leaves just the outer fibre edge of interest and the edges detected from neighbouring fibre cross-sections as noise.

A) 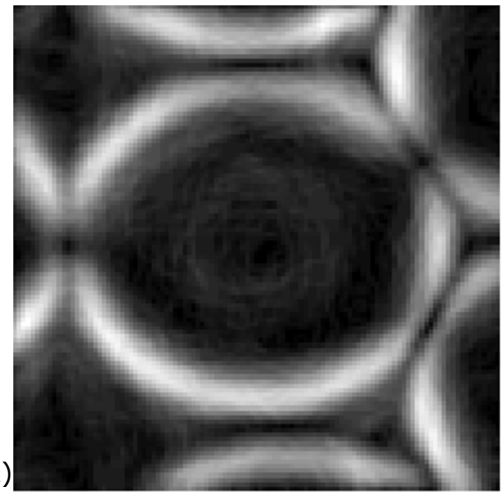 B) 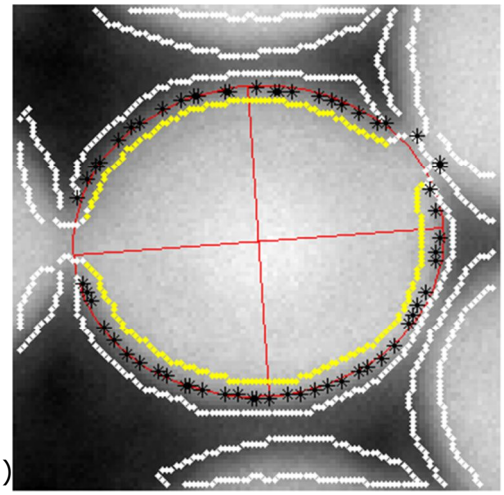

Figure 18: A) Representation of colour gradients of a fibre with parts of touching fibres, B) detected Canny edges of the fibre (black *) and Canny edges of the gradients (white and yellow dots). Canny edges marked yellow are removed.

In order to remove all points not belonging to the actual fibre edge, the distance to the image centre of all points is calculated. Only the points closest for every 5 degrees are selected and an ellipse is fitted through these remaining data points (Figure 19A). Since it cannot be ensured that all data points from adjacent fibre borders are removed the fitted ellipse is used as a new stencil. Points outside this ellipse plus a selected offset are removed iteratively and the ellipse is refitted through the remaining data points. It was identified that an offset of 2 pixels resulted in an optimal detection of the actual filament boundary.

The achieved good fit is shown in Figure 19B. The resulting differences of the major and minor ellipse diameters compared to the manual ellipse fit shown in Figure 12 are 1.6 % and 0.5 %. The good fit of the minor ellipse diameter enables the precise estimation of the fibre diameter distribution within a complete fibre bundle.

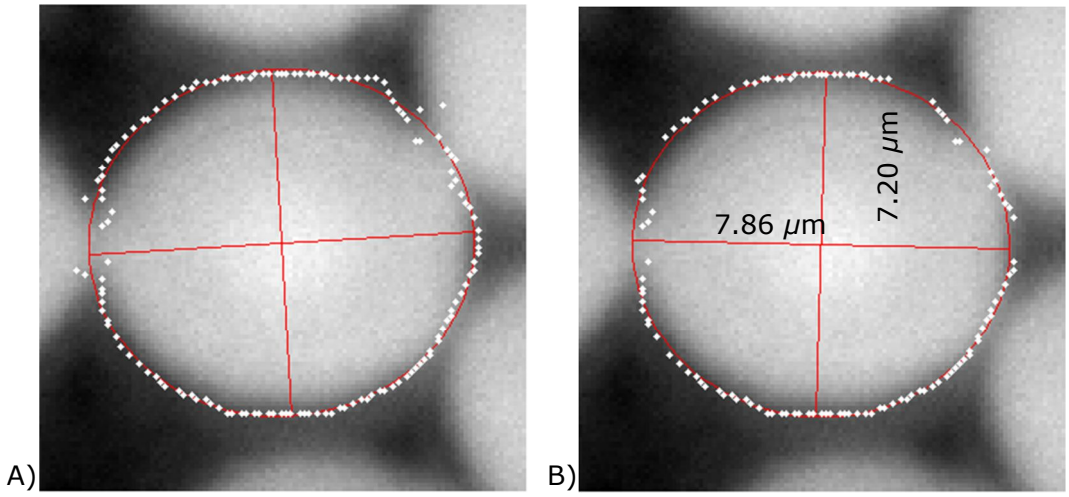

Figure 19: A) Initial ellipse fit of fibre boundary based on the determination of colour gradients. Noise, points belonging to edges of touching fibres are present. B) Final result of the fitted ellipse to the fibre boundary after iteratively removing points outside the first ellipse fit.

Compared to the reference results of manually fitted ellipses, an average overestimation of the major ellipse axis of 4.6% and an underestimation of the minor ellipse axis of 0.8% can be identified. It should be noted, however, that the manual fit of the ellipses is done at a lower magnification than shown in Figure 17B. The results of this manual fibre fit compared to the results determined on the lower magnification reference set (Figure 12) would indicate an underestimate of 2.4% and 1.4% for the major and minor ellipse diameter, respectively. The measurement of 300,000 single filament cross-sections showed a normal distribution of the filament diameter with a mean of 6.97 µm and a standard deviation of 0.39 µm which is in good agreement with the manufacturer's specification. Taking this into consideration, the automatically fitted ellipse does give a small error only.

The developed procedure of image processing implemented in Matlab® (Appendix B) allows the automated analysis of filaments within complete fibre bundles. Problems encountered during conventional image analysis employing simple techniques such as colour thresholding are overcome with the proposed method by analysing colour gradients instead. Fitting a predefined shape to the filament edges allowed the precise determination of filament dimensions. The presumed elliptical fit of the filament boundary may be questionable for the shape of other filament cross-sections such as natural fibre cross-sections. However, the proposed process allows the use of any other shape approximation. This makes the proposed technique a powerful tool to systematically analyse large areas within a composite at high magnification in an automated manner.

3.4 Statistical data for fibre bundles

3.4.1 Materials and processing

To characterise the behaviour of fibre bundles under compression, single layer composite sheets were moulded and cured. Panels with dimensions 125 mm × 60 mm were made from single layer non-crimp carbon fibre fabric (Appendix C.1) and a low viscosity epoxy resin system (Appendix C.2). The fabric consisted of filaments with a filament count of 12K stabilized by thin glass weft yarns coated with a thermoplastic polymer. The specimens were moulded by circumferential injection of the liquid resin into a stiff metallic tool containing the fabric. The tool was closed and the fabric compacted by means of tightening bolts in a cross-wise pattern at the edge of the cavity. Depending on the V_f the injection pressures used were between 1 bar and 4 bar to ensure complete mould filling. The resin viscosity during injection (μ_f ~ 0.025 Pa×s) was controlled via the ambient temperature. Initially, the resin was preheated to 70 °C before the injection pressure was applied. Subsequently the temperature was increased to 130 °C, to further decrease the resin viscosity and initiate the curing process. The mould cavity height, h, i.e. the level of fabric compression, was varied. Three sets of samples with fibre volume fractions of 0.45, 0.60 and 0.74 were produced (mould cavity height of 0.37 mm, 0.28 mm and 0.22 mm respectively). Micrographic analysis of cross-sections of the moulded and cured specimens allowed the filament distribution to be identified (Figure 20).

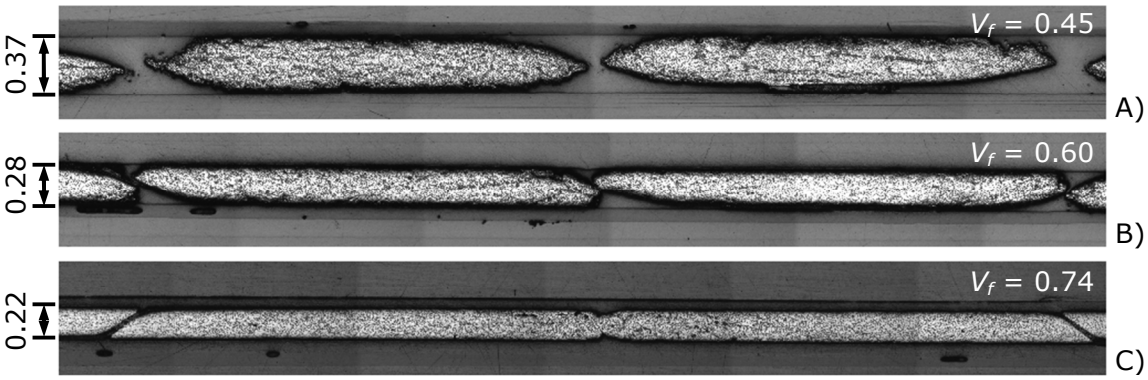

Figure 20: Cross-sections of composite specimens produced by resin transfer moulding at a gauge pressure of p = 4 bar and varying cavity heights specified in the image (0.37 mm, 0.28 mm and 0.22 mm); fibre bundle with 12K carbon fibre filament count.

3.4.2 Sampling data

A total of 11 composite panels were manufactured successfully with the method and conditions outlined in Section 3.4.1. Images of fibre bundles from 5 of these sheets (2 panels of V_f = 0.45, 2 panels of V_f = 0.60 and 1 panel of V_f = 0.74)

were analysed in this work. The samples from the composite panels were taken at an angle of 30° to the bundle axis (Figure 21A) in order to avoid filament orientation ambiguity (Section 3.2). The section cuts were started approximately 10 mm from one end of the panel and did not include the centre locations. From these panel cross-sections a total of 26 complete fibre bundles (9 for V_f = 0.45, 10 for V_f = 0.60 and 7 for V_f = 0.74) were analysed which did exhibit the best conditions for the desired image analysis (e.g. absence of dry spots). These fibre bundles were located at random positions along the sample cut.

The obtained fibre bundle cross-sections (Figure 20) indicate clearly how the overall yarn shape changes with increasing level of fabric compression. Ignoring the localised influence of the fixation thread on the bundle geometry the bundle cross-sectional shape changes from approximately elliptical or lenticular to approximately rectangular. During compaction, the yarn width increases, reducing the gaps between the fibre bundles (V_f = 0.45 to 0.60). If compressed even further (V_f = 0.60 to 0.74), the yarns merge and a distinction between fibre bundles is not possible any longer with the exception of the localised influence of the fixation thread on the bundle geometry.

In order to perform a quantitative analysis, the measurement data has to be rotated into the plane normal to the fibre bundle axis correcting for the sectioning of the samples at an angle. This data projection assumes no significant influence of a partially sectioned weft binder yarn on the measured data with filaments acting as straight solid cylinders over the limited range of inclination within the fibre bundle (Figure 21B).

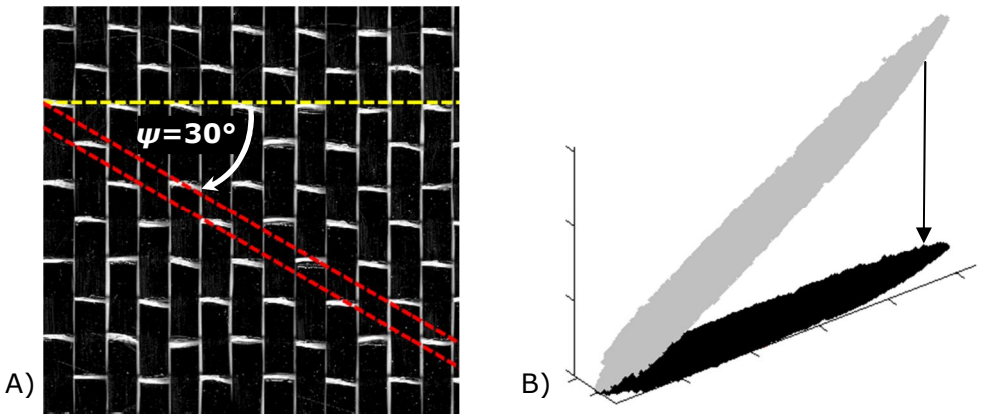

Figure 21: A) Image of the fabric with indication of the cutting angle and B) an example of the projection of the measured data cut at an angle ψ.

The accuracy of the desired sectioning angle, ψ, is limited by the finite precision of the employed sample cutting method. Measurements of filament cross-sections in the cutting plane as described in Section 3.3.2 can be used to determine the direction of the filament path, φ_i, (Eq. 9). The average filament path (Figure 22) should be identical to ψ (Figure 13) and hence it is possible to accurately determine the exact cutting angle.

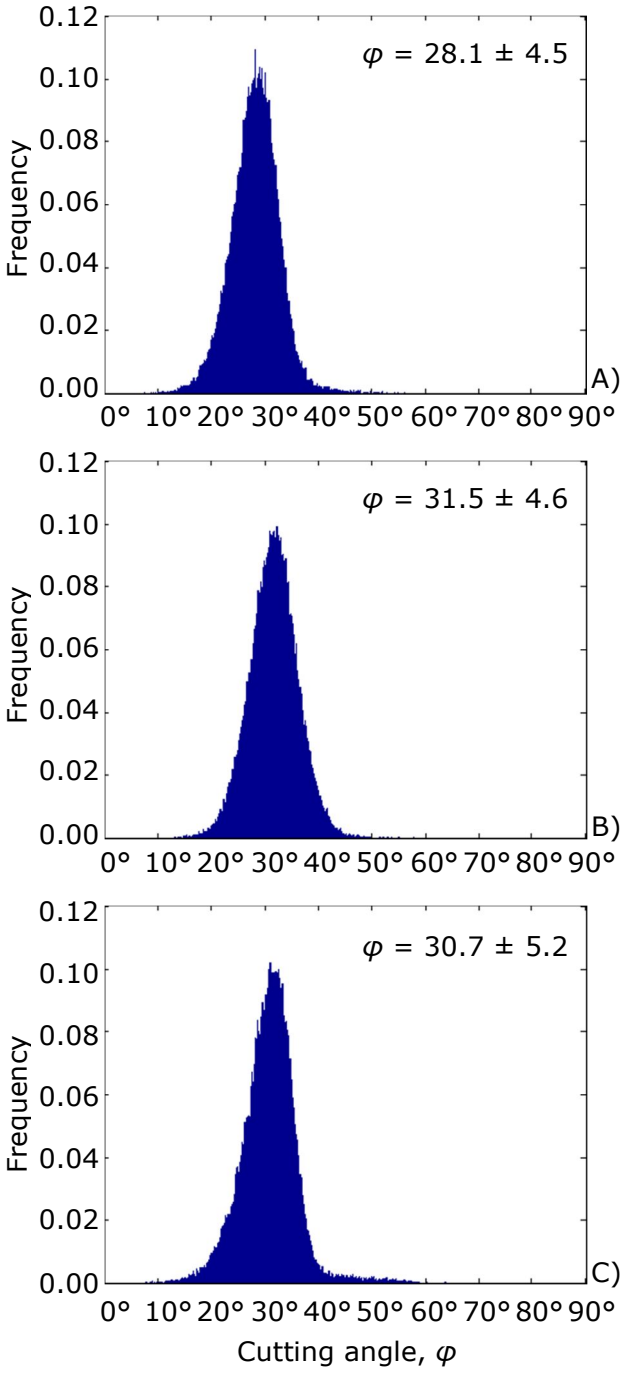

Figure 22: Distribution of filament cut angles, φ based on the ratio of determined ellipse diameters for the samples with A) V_f = 0.45, B) V_f =0.60 and C) V_f =0.74. The mean and standard deviations are indicated.

However, fibre bundle waviness and the accuracy of the detection of fibre dimensions limit the potential of this method. The cutting angle ψ is therefore estimated by manual measurements of the entire sample cross-section and not from Figure 22.

The image analysis of several fibre bundles, containing around 300,000 single fibre cross-sections, was performed. Based on the minor ellipse radius, a normally distributed fibre diameter distribution was measured with a mean of 6.97 μm and a standard deviation of 0.39 μm. Considering the underestimation of the fibre diameter of less than 1% during the image processing, the nominal fibre diameter of 7.0 μm can be confirmed. This measurement accuracy is significantly better than the one reported by Vaughan and McCarthy [18]. They reported a filament diameter of 6.6 μm whereas their statistical descriptors would suggest a mean fibre diameter of about 7.0 μm.

3.4.3 Fibre bundle shape

A method to precisely determine the filament dimensions was described in Section 3.3.2. Based on this information and the exact location of the filaments it is possible to determine the edge of the entire fibre bundle. These edges can be fitted with a suitable shape function describing the fibre bundle boundaries. This enables the quantification of fibre bundle shape changes due to fabric compaction. In the literature, the fibre bundle shape is often assumed to be elliptical only [113]. This assumption, however, does not necessarily lead to a good fit to the overall shape. The extension to a super ellipse (Eq. 26) is therefore a more suitable shape approximation which allows a wider range of bundle like shapes to be fitted with a single function [43]. Whereas the semi major and minor axes, a and b, are given by the maximum width and height of the sample, the exponent will define the bundle shape.

$$\left(\frac{x}{a}\right)^m + \left(\frac{y}{b}\right)^m = 1 \qquad \text{Eq. 26}$$

By varying the exponent, m, it is possible to achieve an elliptical shape (m=2) or a more rectangular shape with rounded edges (m>2). For exponents smaller than 2, diamond or star shapes result (Figure 23A) which are not likely to be found in actual fibre bundles. Therefore a power ellipse, a special case of the super ellipse, was proposed to be used to describe the yarn shape [43]. By omitting the exponent in the first term, a lenticular, elliptical or rectangular shape with rounded edges can be generated (Figure 23B).

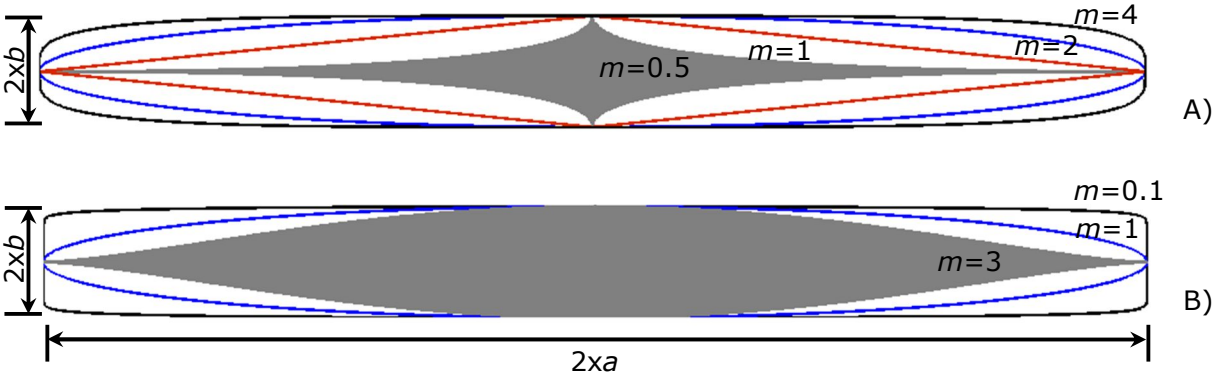

Figure 23: examples of A) super-elliptical and B) power elliptical shapes

The power ellipse function

$$\left(\frac{x}{a}\right)+\left(\frac{y}{b}\right)^{m}=1 \qquad \text{Eq. 27}$$

can be transformed into the form of the algebraic distance (Eq. 28) to avoid the need of solving an exponential equation. This form can then be used to fit a power ellipse to a set of measurement data [114].

$$Q_0(x,y)=\left(\frac{x}{a}\right)+\left(\frac{y}{b}\right)^{m}-1 \qquad \text{Eq. 28}$$

The best fit power ellipse can be found by minimising the sum of squares of the offsets of the data points to the curve, minimising the function $Q_0^2(x,y)$ [114]. To fit the ellipse to a set of arbitrary data, the general form of the power ellipse (Eq. 29) with offset from the origin and a rotation θ can be used:

$$\left(\frac{(x-x_c)\cos\theta-(y-y_c)\cos\theta}{a}\right)+\left(\frac{(y-y_c)\cos\theta-(x-x_c)\cos\theta}{b}\right)^{m}=1 \qquad \text{Eq. 29}$$

Here, the subscript c denotes the centre of the power ellipse. This equation can be converted to the form of the algebraic distance and the power ellipse shape can be fitted to the dataset accordingly (Figure 24).

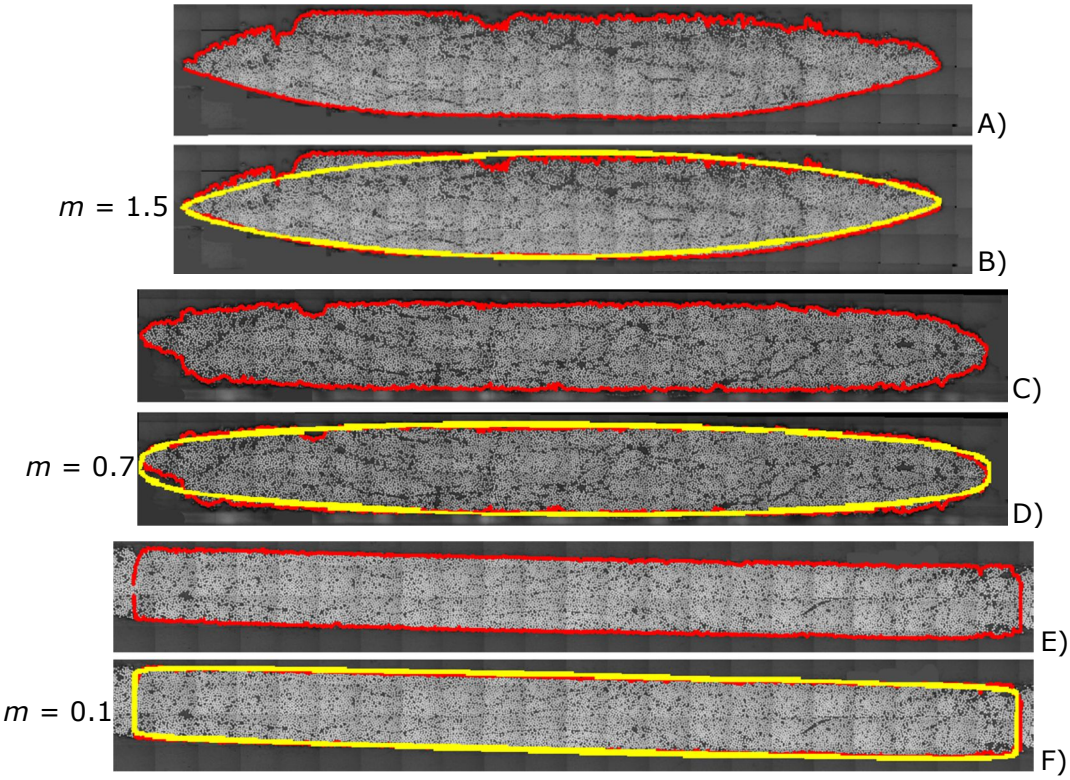

Figure 24: Examples of the detected bundle boundaries (red) and of the fitted power ellipses (yellow) at three different configurations. A and B) gobal V_f = 0.45; C and D) gobal V_f = 0.60 and E and F) gobal V_f = 0.74.

The estimated power ellipse exponents as a function of the V_f are depicted in Figure 25. The exponent, m, defining the shape of the power ellipse decreases almost linearly with increase in global V_f.

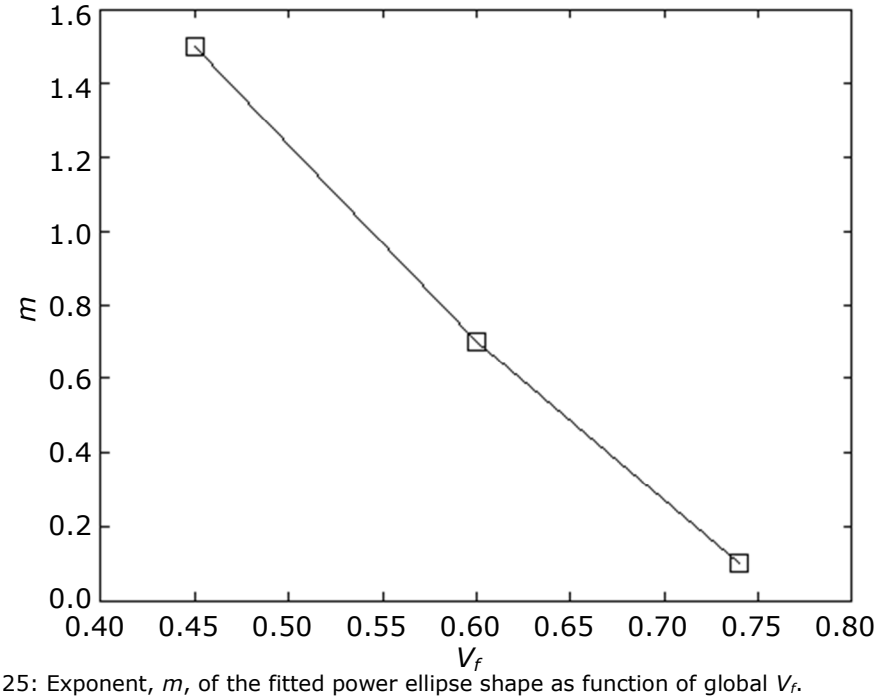

Figure 25: Exponent, m, of the fitted power ellipse shape as function of global V_f.

3.4.4 Bundle width and height

The width of individual bundles, *w*, initially increases with a decrease in *h* (Figure 20A and B). Due to the increase in *w*, adjacent bundles overlap for *h* = 0.28 mm (Figure 20B) and merge for *h* = 0.23 mm (Figure 20C). Only in areas where the fixation thread is present, the yarn remains physically separated (Figure 20C; near left and right edge of image).

The global V_f in the mould cavity with a height, *h*, can be estimated when fabric areal density, A_f, the density of the material, ρ, and the number of layers, n_l, are known (Eq. 30).

$$V_f = \frac{n_l \cdot A_f}{h \cdot \rho} \qquad \text{Eq. 30}$$

This equation demonstrates that a linear variation in V_f can only be achieved with a non-linear change of *h* if the fabric layup is kept constant in the mould tool. This corresponds to the measured data (Figure 26). The change in bundle width, however, exhibits a more distinct non-linear relationship with increasing compaction (Figure 26). The width of the fibre bundle increases significantly when the bundle is compressed initially. This data therefore suggests that the increase in global V_f from 0.45 to about 0.60 is accompanied by a significant shape change of the fibre bundle in the textile layer.

This is also visible in Figure 20. The internal V_f of the fibre bundle should therefore be less affected. Only if the bundle is further compressed (from 0.60 to 0.74 global V_f), V_f within the bundle should significantly increase because the overall change in bundle width is limited. The inter-yarn space as seen in Figure 20A is completely occupied when the bundle is highly compressed (Figure 20C) and the increase in global V_f can only be achieved by compaction of the filaments within the fibre bundle and not by displacement, e.g. bundle widening.

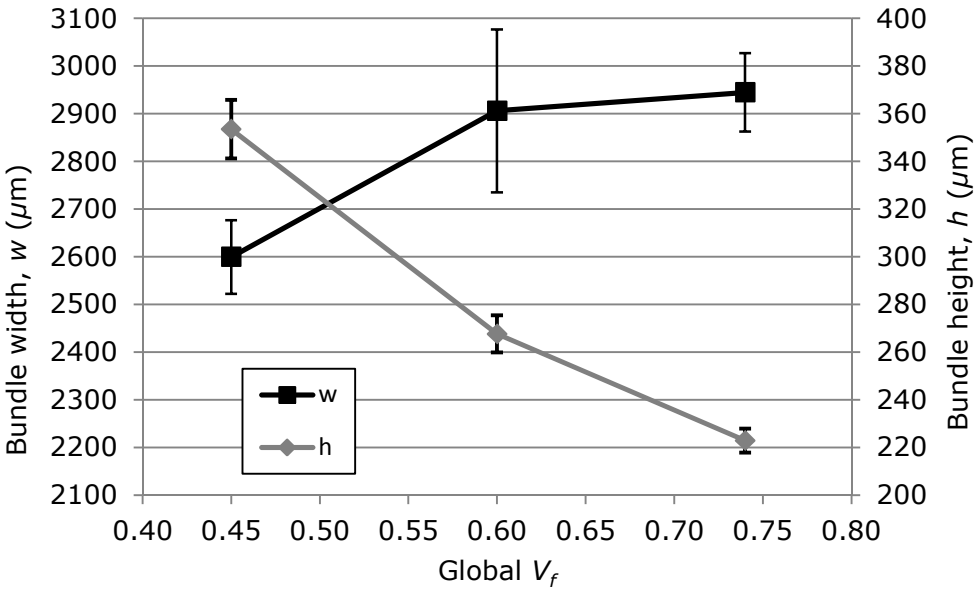

Figure 26: Fibre bundle height, *h*, and width, *w*, as a function of the global fibre volume fraction, V_f. The error bars show the standard deviation of the measurements.

3.4.5 Fibre volume fractions

3.4.5.1 Fibre volume fraction of the tow

The internal V_f of a fibre bundle can be estimated based on the analysis of a two-dimensional cross-sectional area by assuming the following relationship of the volume, *V*, and the cross-sectional area, *A*, of this volume (Eq. 31):

$$V_f = \frac{\sum V_{fibre}}{V_{bundle}} = \frac{\sum A_{fibre}}{A_{bundle}} \qquad \text{Eq. 31}$$

The area of all filament cross-sections of a fibre bundle, $\sum A_{fibre}$, is determined during the image analysis (Section 3.3.2). The total fibre bundle area, A_{bundle}, is defined by the fibre bundle boundary enclosing all filaments in the fibre bundle cross-sections. The location of the maximum and minimum filament edge is determined for the complete bundle width which defines the envelope of the fibre bundle. To avoid sudden changes in the estimated boundary, the maximum and minimum filament locations are determined for a discrete step size. The selected width of this step size is approximately equivalent to the filament diameter.

It can be shown that internal V_f of the fibre bundle increases almost linearly with an increase of the global V_f (Figure 27). In addition, the average V_f within the fibre bundle is higher than the global V_f. The V_f within the bundles and the global

V_f become identical at very high levels of compaction. Considering the meso-scale structure of the fibre reinforcement, consisting of fibre bundles and inter-bundle gaps, this is not surprising. The V_f of the fibre bundle does not change more significantly when compacted from 0.45 to 0.60 global V_f than when compacted from 0.60 to 0.74 global V_f . While the global V_f within the mould is increased by around 30% the internal V_f within the fibre bundle increases only by around 15%. This suggests that the increase in global V_f during compaction of the bundles is equally shared between bundle deformation (reduction of the gaps between the fibre tows) and the internal movement of the filaments. The approximately linear increase of V_f within the fibre bundles with increasing global V_f suggests that the bundle compaction is not only a function of the non-linear change in bundle dimensions, *w* and *h*, as indicated in Figure 26. The change of bundle dimensions is also accompanied by an approximately linear change of the bundle shape as illustrated by the shape factor in Figure 25. This factor suggests that the change in bundle area is more pronounced at increased V_f due to its exponential nature (Eq. 29).

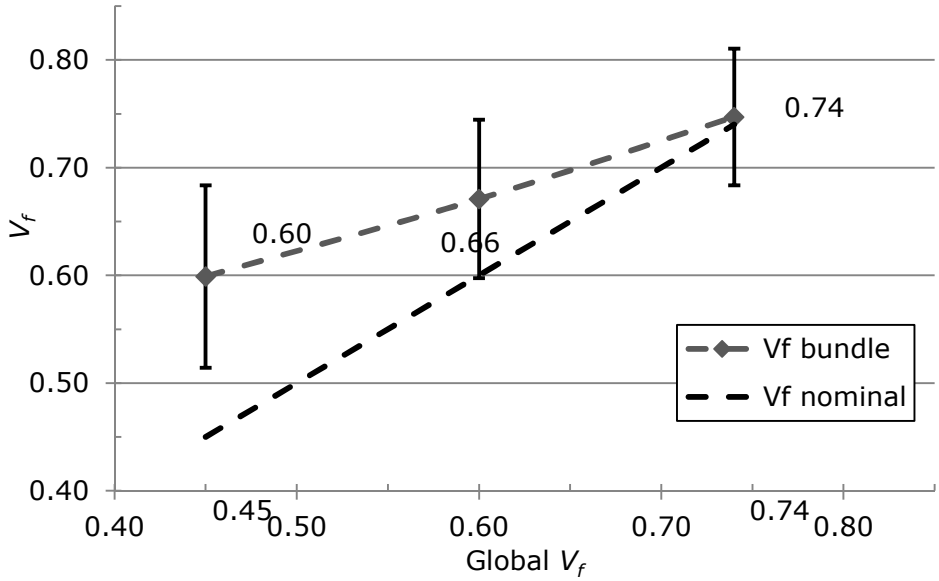

Figure 27: Nominal and internal bundle V_f as function of the global V_f. The error bars indicate the measured standard deviation of the measurement data.

3.4.5.2 Fibre volume fraction based on tow segmentation

Due to the nature of the material, the V_f within the bundle cannot considered to be constant. Analysing greyscale levels in vertical slices of an image of a fibre bundle, Summerscales and Russel [115] reported variations of local filament densities. Their analysis, however, was based on low resolution images and employed a direct thresholding technique which only allows qualitative measures as discussed earlier (Section 3.2).

Employing a similar technique, the spatial distribution of the fibre volume within the fibre bundle can be identified. After processing of all filament cross-sections and detecting the bundle envelope (Figure 28A), the fibre bundle is segmented into a finite number of vertical slices. It can be shown that the absolute number of filaments decreases at the tips of the fibre bundle as one would expect (Figure 28B). If, however, the relative amount of fibres within the yarn boundaries is calculated, the internal fibre volume fraction within the fibre bundle appears to be rather constant over the width of the yarn (Figure 28C). This is different to bundle V_f distributions reported in the literature which suggests a decrease in V_f towards the tips of the yarn [116]. Artefacts, such as separations within the fibre bundle, caused by handling of the dry textile, for example visible on the left side of the yarn in Figure 28A, decrease the absolute number of filaments locally and therefore also reduce the internal V_f in this area.

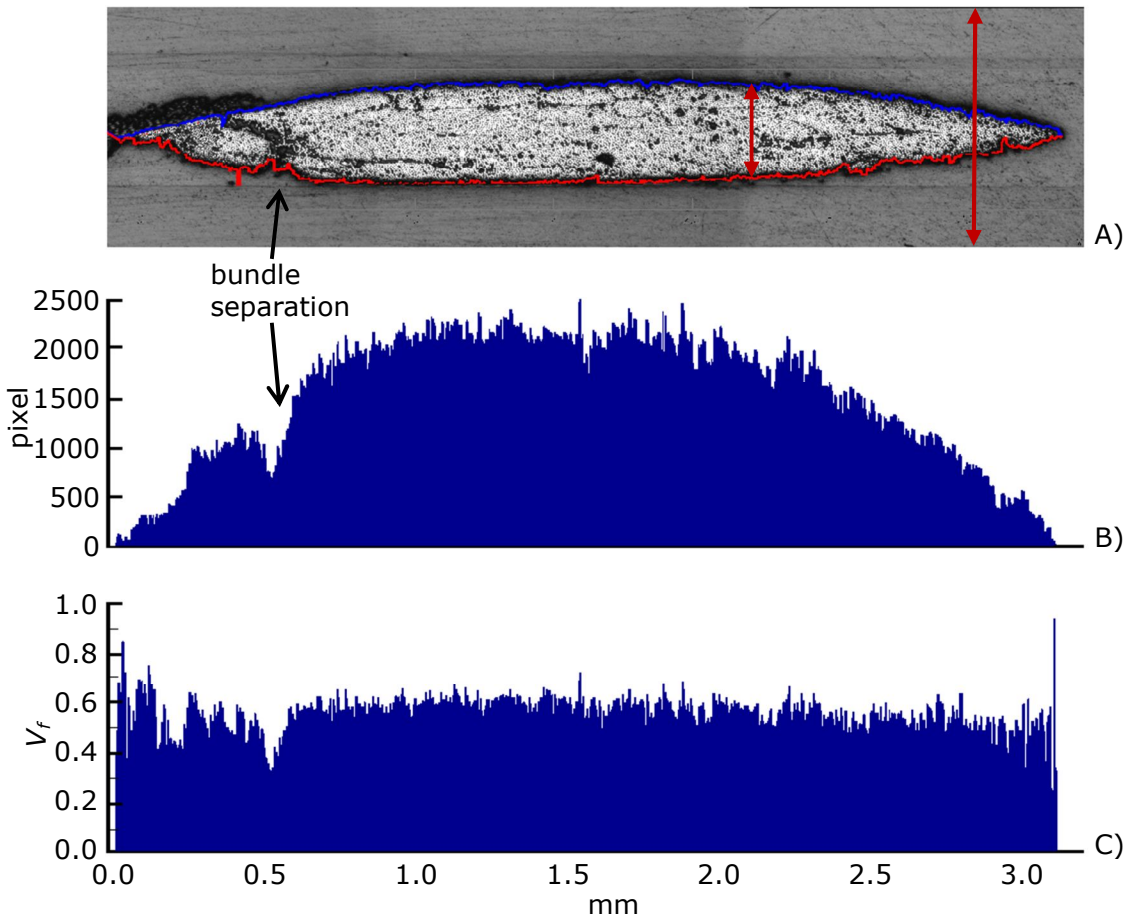

Figure 28: A) Fibre bundle with estimated boundaries; B) Total filament area in pixels within the fibre bundle cross-section estimated for vertical slices of one pixel width (δc = 0.093 μm); C) V_f within the boundaries of the fibre bundle.

3.4.5.3 Bundle discretisation in finite volumes

Another way of analysing the spatial distribution of the V_f within the yarn is by discretisation of the yarn area into windows of finite size. Local V_f can be estimated (Figure 29). The window sizes used in this work were 100, 300 and 500 pixels (0.009 mm, 0.028 mm, 0.047 mm side length). For evaluation of the results, all windows located at the fibre bundle boundary were disregarded. When the data are analysed, it is not possible to find a clear correlation between the V_f in adjacent windows. This suggests that the local V_f, based on the local filament arrangement, does not influence the filament arrangement beyond a certain (small) distance.

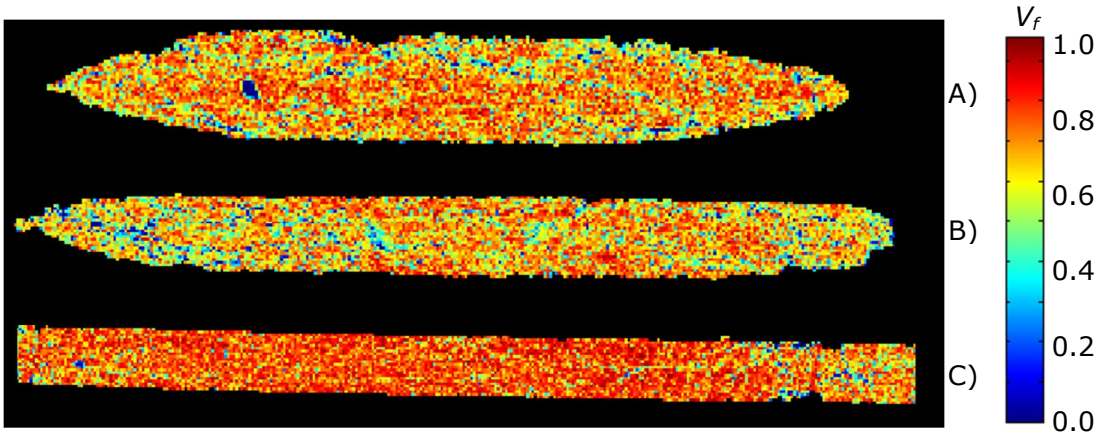

Figure 29: Example of the variation of the local V_f within fibre bundles. Window size used is 100 pixel x 100 pixel for A) V_f = 0.45, B) V_f = 0.60 and C) V_f = 0.74. V_f is averaged over the bundle area.

3.4.5.4 Local Voronoi cell based fibre volume fraction

To analyse the local V_f, the use of Voronoi cells is often suggested [117]. This technique tessellates the domain of interest into Voronoi cells with the knowledge of the fibre centres. Each location in the image is associated to the closest centre point, resulting in a partitioning of the domain into multiple polygons. The ratio of the fibre area to the respective polygon area is then considered to reflect the local V_f. The resulting Voronoi V_f (Figure 30) of the samples analysed in this work gives an almost identical mean compared to the internal V_f as presented earlier (Figure 27). The standard deviation, however, does increase significantly.

A limitation to the concept of Voronoi cell tessellation of a fibre bundle is that the analysis is based only on fibre centre positions and the fibre areas are ignored. Varying fibre diameters of the fibre cross-sections and fibre inclinations, resulting in elliptical fibre cross-sections, are ignored. This will result in an erroneous result. Hellström [22], used an adjusted version of the Voronoi cell tessellation in

their work to generate a two-dimensional model of particles with varying size, considering the actual particle area. This consideration should also be implemented when the Voronoi cell based local V_f is determined.

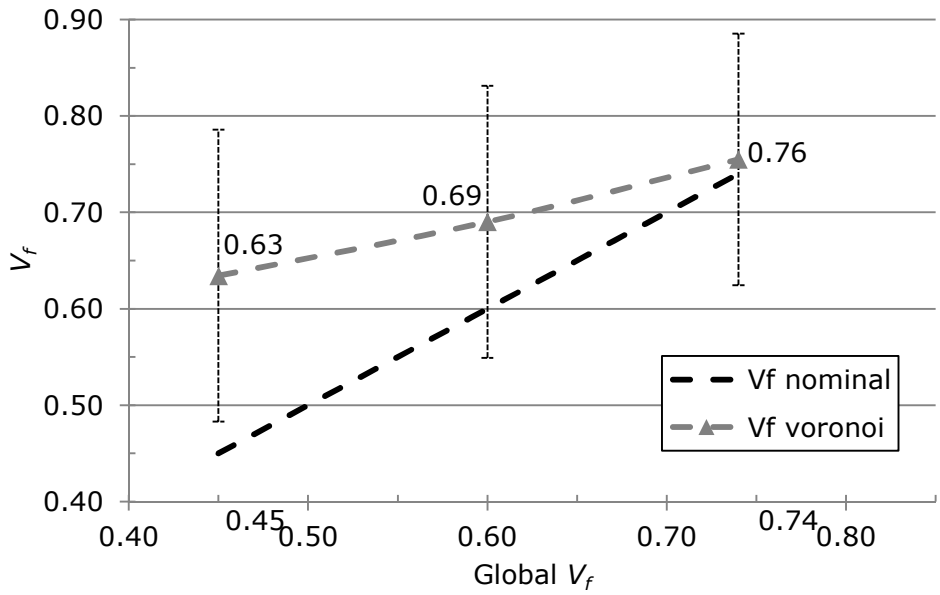

Figure 30: Nominal and local V_f based on Voronoi cell tessellation. The error bars show the standard deviation of the measurement data.

3.4.6 Local filament arrangement

The decomposition of the fibre bundle into Voronoi cells can lead to an insight of the packing configuration of the fibres and therefore, to some extent, also about the regularity of the fibre arrangement [118]. Voronoi polygons sharing a side with each other are considered to represent fibres which are close neighbours. The average number of line segments of the polygons is therefore equivalent to the average nearest neighbour count. For all three V_f considered in this work the average neighbouring filament count is 5.7 (Figure 31). This finding is equivalent to the findings of Paluch [110] and Zangenberg et al. [119] and close to the neighbour count of 6 which would be the result of a perfectly hexagonal arrangement. Even though the differences in the average number of neighbours are small, it seems that there is a tendency to reduce the mean neighbour count with increasing V_f. It will be demonstrated later (Section 3.4.7.3), that a more precise measure of determining the angle distribution will give a better description of the degree of order in the filaments.

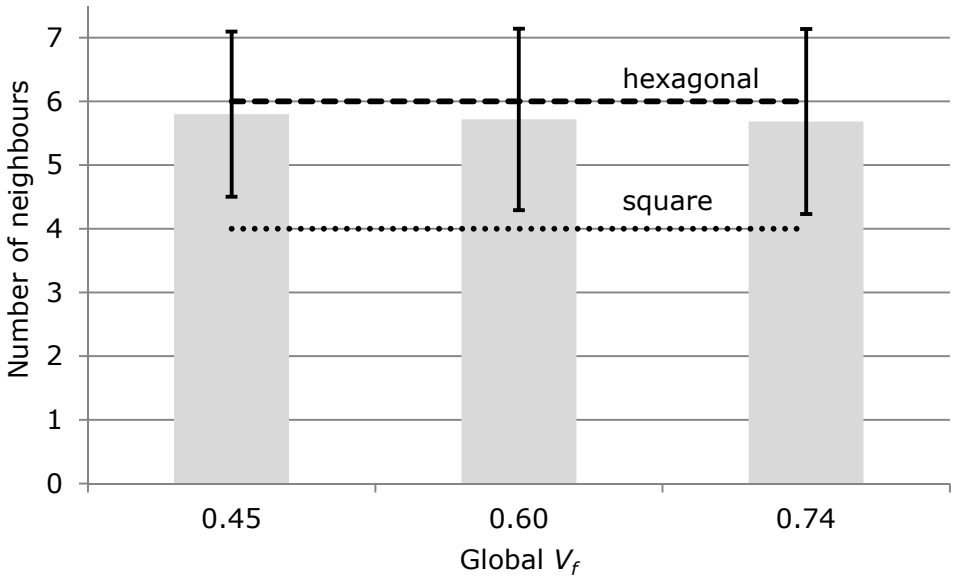

Figure 31: Average number of nearest neighbours based on Voronoi cells sharing an edge as a function of the global V_f. The error bars show the standard deviation of the measurement data.

3.4.7 Nearest neighbours

3.4.7.1 Nearest neighbour distances

Some researchers used the Voronoi cell tessellation for the determination of the nearest neighbour distances [71]. It was argued that this method would limit the number of inter-filament distances to be calculated to the number of edges of the Voronoi cell. Advances in programming languages (vectorisation in Matlab®) made it feasible, however, to determine all possible inter-filament distances with small computational effort only. In this work, the neighbouring distances of a filament to its n-th nearest neighbour are therefore based on the calculation of distances between all filament centroids. The mean distances for the first ten nearest neighbours, measured between the centre points of the filaments, are given for three V_f in Figure 32. The graph clearly shows that the average inter-filament distances decrease with increasing level of compression. For n=1, the closest neighbouring filament, the distance converges to the average filament diameter since the nearest possible distance is achieved when neighbouring filaments are in contact with each other. Furthermore, the decrease in inter-filament distance is more pronounced when the fibre bundle is compacted from 0.60 to 0.74 global V_f within the mould. This indicates that, due to a change in yarn shape, inter-filament distances decrease less significantly when compacted from 0.45 to 0.60 global V_f.

At maximum packing density in perfectly hexagonal packing of identical filaments, the neighbouring distances for the first six neighbours, n = 1 to 6, are identical at a value of the filament diameter, d, for n = 7 to 12 at a value of $d \cdot \sqrt{3}$, for n = 13 to 18 at a value of $2 \cdot d$ etc. With increasing level of bundle compression, the average distance as a function of n tends to this step function, implying that reduction in inter-filament spacing and increasing packing density are related to increasingly uniform filament distributions. This agrees with observations by Potluri and Sagar [120], who report flattening of fibre bundles by micro-scale filament reordering as a fabric compression mechanism.

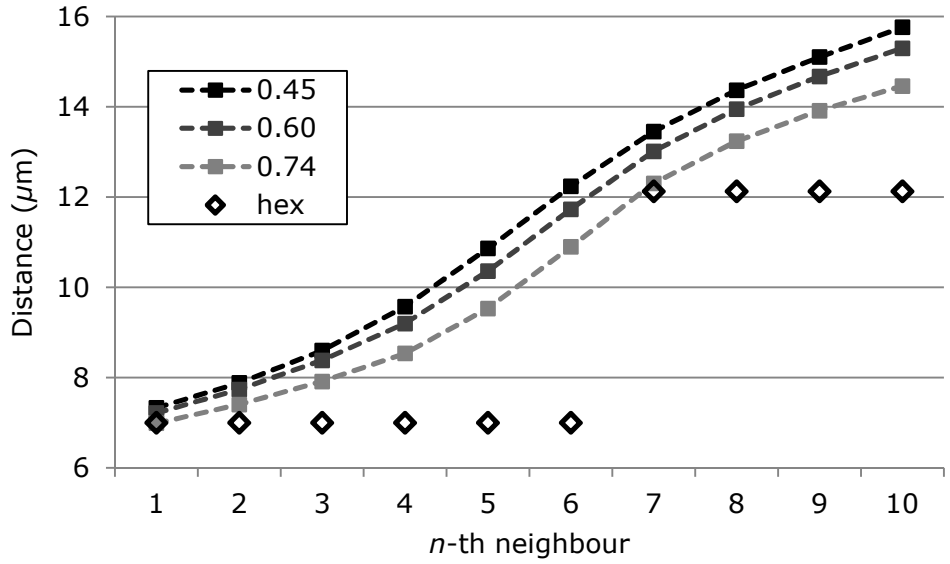

Figure 32: Mean filament distance to first to tenth nearest neighbour for three samples with global V_f = 0.45, 0.60 and 0.74. The filament distances for a hexagonal (hex) arrangement at maximum V_f = 0.91 with d=7.0 μm are shown as diamonds.

3.4.7.2 Nearest neighbour distance distributions

The inter-filament distances for the n-th nearest neighbour show right-tailed distributions. With an increasing number, n, of the neighbour distance this positive skew gets more pronounced (until approximately n = 6). The distributions also exhibit a lower truncation limit on the left hand side due to the fact that two fibres cannot interpenetrate one another. The minimum possible inter-filament distance is therefore equivalent to the sum of their radii.

The measured data could be approximated by a log-normal distribution (Figure 33). For the first nearest neighbour, n=1, the distribution is narrow with its maximum at around 7 μm. This is equivalent to the nominal fibre diameter of the carbon fibres used in the fabrics, indicating that the first nearest neighbours are

most probably touching filaments. With an increase in n the distribution is widened, indicating a higher spread in neighbour distances. Additionally, the sample mean becomes larger. The occurrence of touching fibres is less probable.

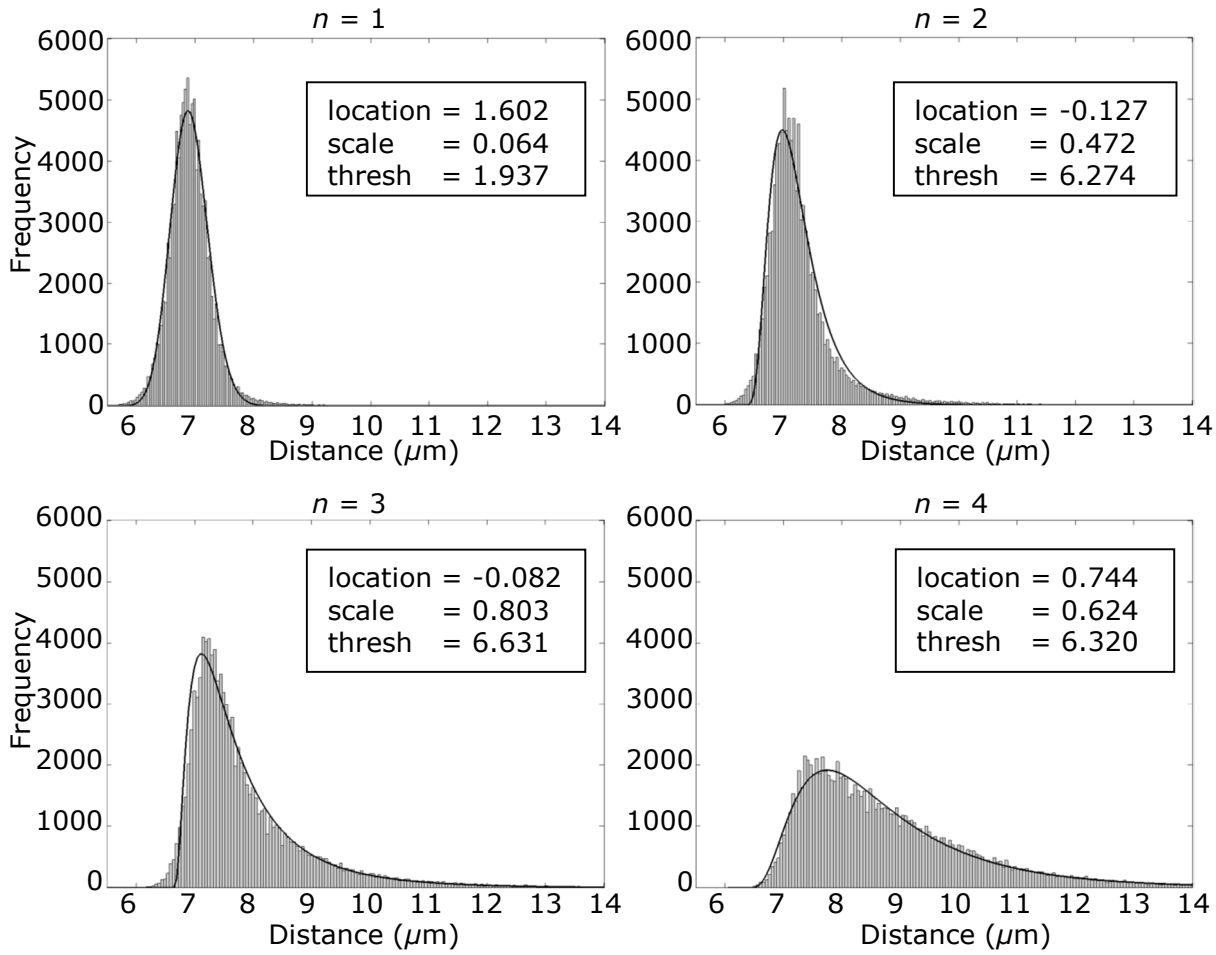

Figure 33: Example distributions of the first four nearest neighbour distances (n=1 to 4) for V_f = 0.45. The fitted log-normal distributions and distribution parameters are indicated in the graphs.

For better comparison of different samples, it is advantageous to normalise the inter-filament distances by the average filament diameter of the sample. For the first nearest neighbour, all three fibre volume fractions show a similar distribution (Figure 34A). Only a slight reduction of the mean value is observed when the V_f is increased. The peak value close to 1 indicates that the most probable distance between filaments is one fibre diameter, indicating that neighbouring fibres are touching. The fact that the peak value is slightly below 1, especially for the highest V_f (0.74), suggests that the majority of filaments are closer together than the average fibre diameter. This can be explained by the fact that double counts between filaments are not avoided. Thus, smaller filaments are likely to be the closest neighbour to more than one filament.

When compacting the fibre bundles within the mould, increasing the V_f, the fibres have to move closer to each other, reducing the spacing between them and the material becomes more uniform. This behaviour is quite distinct in the second, third and fourth nearest neighbour distance distributions. An increase in V_f leads to a decrease in the distribution (Appendix D.4) location and scale parameter (Figure 34B-C).

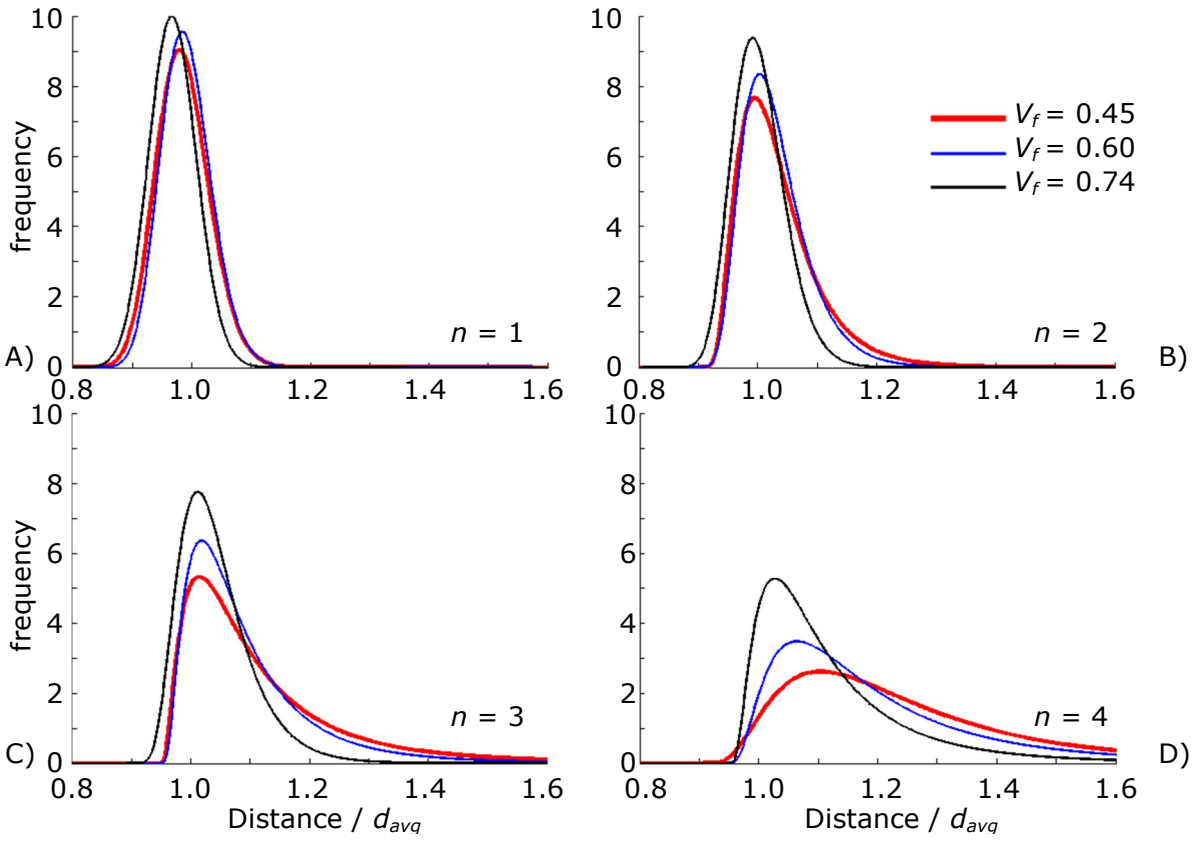

Figure 34: Distance distribution of the n-th nearest neighbour normalised by the measured average filament diameter, d_{avg}.

3.4.7.3 Nearest neighbour angle distributions

The distance to the n-th nearest neighbour (Figure 32) indicates that with an increase in compaction of the fibre bundle, the inter-filament distance converges to the hexagonal closest packing. The angle, under which the n-th neighbouring filament is located, should also reflect this increased degree of order within the fibre bundle. For the analysis of the samples, the 0° direction was chosen to be aligned with the width of the fibre bundle and hence, ±90° represents the direction of the sample thickness.

It can be demonstrated that the distribution of angles under which the n-th nearest neighbours are located changes significantly with increasing fabric

compaction. With minimal fabric compaction, the distribution of angles is almost uniform (Figure 35A). A minor preference of the closest neighbour in direction of the bundle width (0° / 180°) can be observed. This could stem from the fabric production process when the fibre tow is flattened by pulling through various loops before being processed into the textile reinforcement and/or the fabric storage in the form of a tightly wound bobbin.

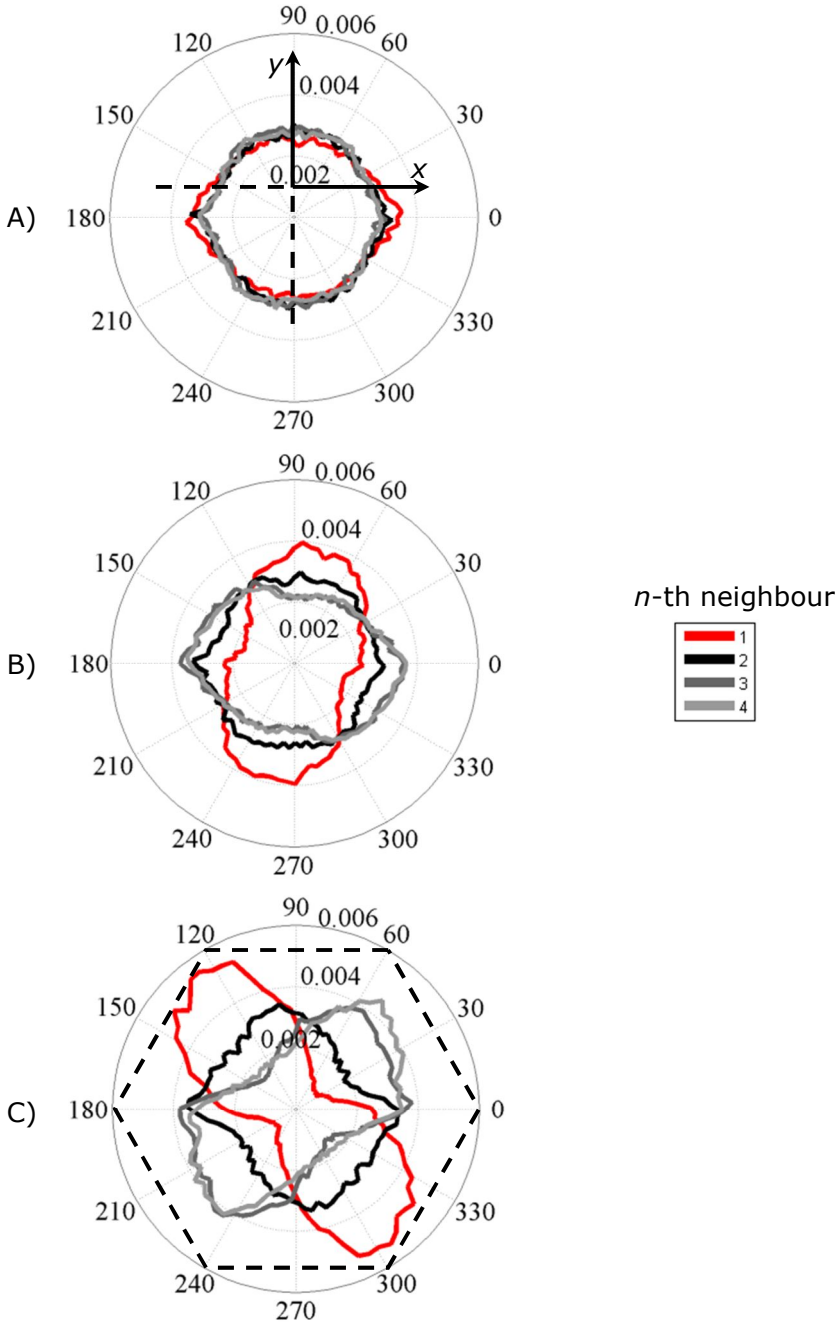

Figure 35: Histogram of the measured angle distributions for A) V_f = 0.45, B) V_f = 0.60, C) V_f = 0.74 within fibre bundles compacted in thickness, *y*-direction. A perfectly hexagonal arrangement is indicated in C). The numbers in the legend correspond to the data of the *n*-th nearest neighbour.

With an increase in compaction of the fibre bundle, the probability of the closest filament to be found in the compaction direction (±90°) is significantly increased (Figure 35B). During the reduction in cavity height, the filament arrangement is compressed as a result of the compaction force. Filaments are pressed against each other in the compaction direction, reflected in the increased probability of finding the closest neighbour in the ±90° direction. The effect of yarn widening can also be observed from this data. Filaments are pushed in the direction normal to the compaction force. An increased probability of the third and fourth neighbour to be located in the direction of the bundle width results. If the cavity height is further decreased, filaments in vertical contact (in bundle thickness direction) have to move normal to the compaction direction due to the reduced available space. Since the filament arrangement is already rather closely packed, further increase in bundle width is limited (Figure 26). Hence, the filament arrangement is compacted more and tends to hexagonal close packing (Figure 35C). An increased probability of the location of a filaments *n*-th neighbour in the 0°, 60°, 120°, 180°, 240° and 300° directions can be observed.

A misaligned of the angle distributions with respect to the direction of the bundle width and height can be observed. This effect is more distinct in the measured angle distribution of the sample with maximum compaction (Figure 35C). The most probable location of the first neighbouring filament is at an angle of 120° or 300° respectively. It is assumed that the onset of this preference of the angles stems from the mould closure. A slight misalignment of the upper and lower mould tool would lead to slightly misaligned compaction planes. This effect can be further pronounced when physically compacting the fibre reinforcement in the mould by means of tightening bolts around the mould cavity. Even though care was taken that all bolts where fastened equally (tightening bolts in a cross-wise pattern), an increased compaction force could have been introduced from one side of the mould initially. This would explain the preference of a preferred angle for the first nearest neighbour in Figure 35.

As input for simulations, it is advantageous to describe the measured distributions in Figure 35 in a closed form. Due to the fact that the filaments can be each other's *n*-th nearest neighbour, the distributions are symmetric. This consideration can be utilised to simplify the measurement data. Employing reflectional symmetries, filaments located on opposite sides of a virtual horizontal line are treated equally (Figure 36). Therefore, the range of angles can be reduced to 0° - 180°.

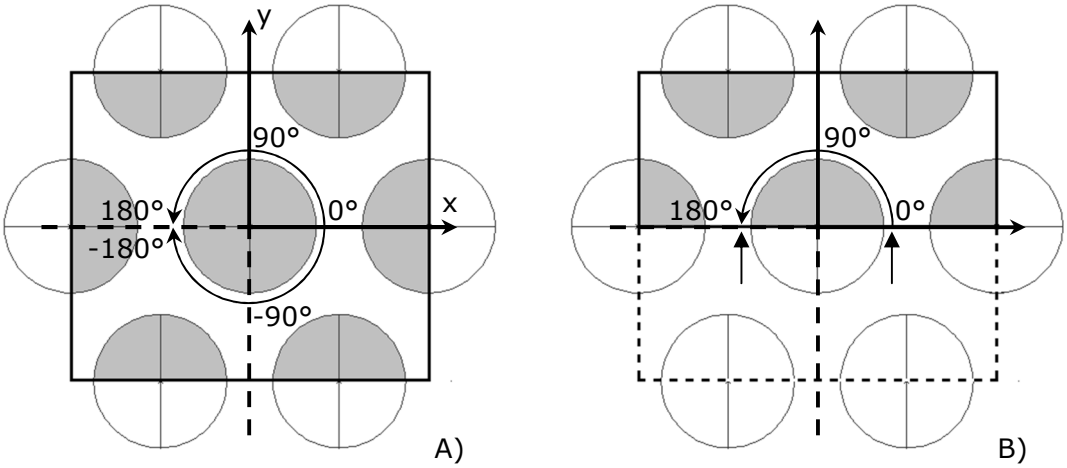

Figure 36: Reduction of the range of angles by employing symmetry considerations on the example of a hexagonal arrangement. A) Full 360° angle range. B) Employing horizontal symmetry, reducing the angle range to 180°.

The measured distributions in Figure 35 are not necessarily symmetric along the bundle width direction (*x*-axis). The determination of the symmetry angle (Figure 37A), however, enables the reduction of the angle distribution to 180° (Figure 37B) for an arbitrary symmetry. A description of these reduced distributions with a combination of two nested truncated normal distributions was found to give the best approximation of the data (Appendix D.1 to D.3).

The description of the probability density functions of the fitted curves shown in Figure 37B, requires a total input of seven variables (mean and standard deviation for each of the two nested distributions, upper and lower distribution limits as well as the mixing probability). These input parameters are determined automatically after analysis of the micro-structure (Section 3.3.2). In future, it would be advantageous to reduce the amount of input variables. For the fibre placement algorithm described in Section 3.5, all seven input variables were used.

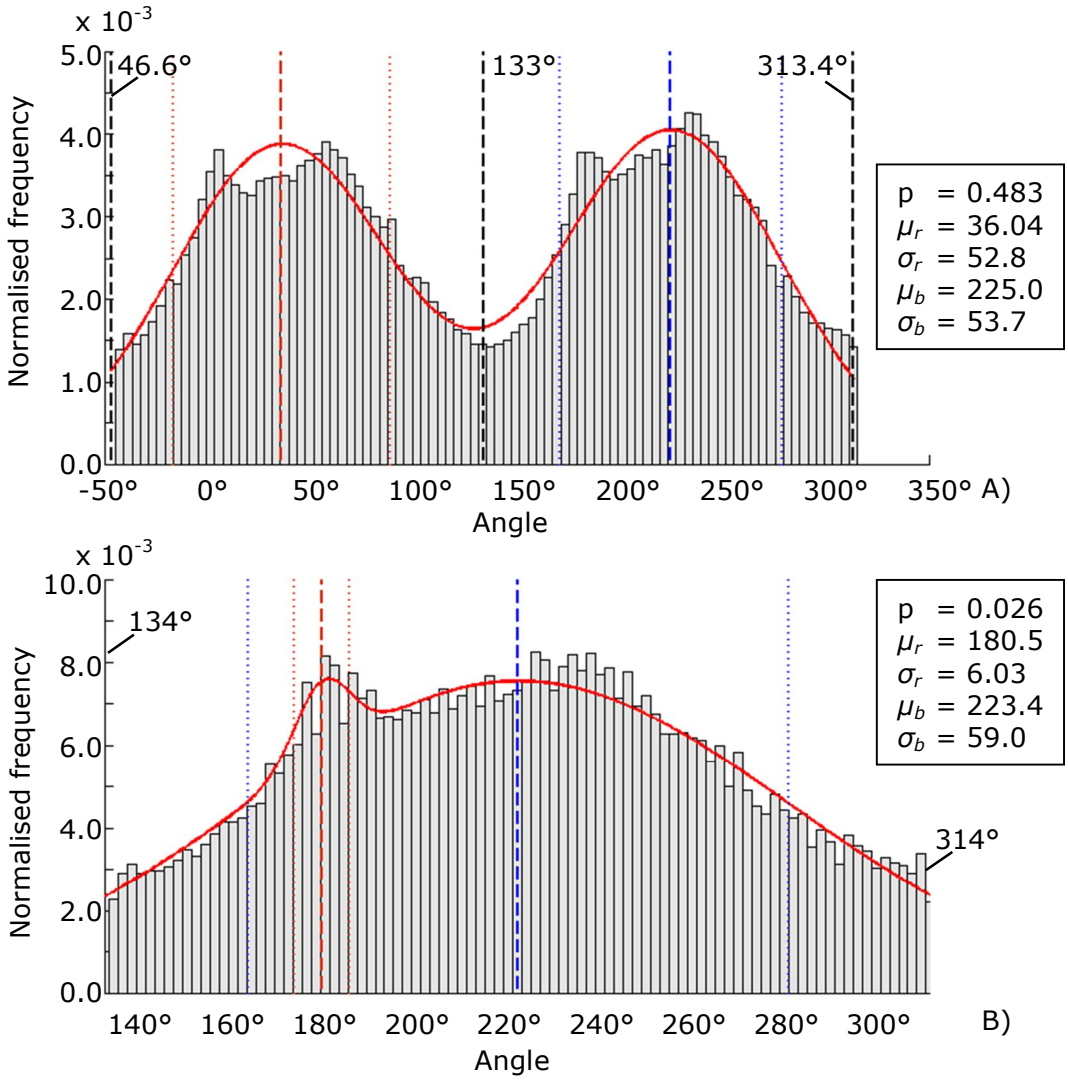

Figure 37: Example angle reduction from 360° to 180° for the third neighbour of V_f = 0.74 samples. Two nested truncated normal distributions are fitted to the data with upper and lower limit indicated in the graphs. The distribution frequencies are normalised to 1 for the area under the fitted curve. The mixing probabilities, p, distribution mean values, μ_r and μ_b and standard deviations, σ_r and σ_b are shown in the figure. The subscripts *r* and *b* indicate the colour red or blue respectively. A) Original distribution with the symmetry angle indicated. B) Distribution reduced to 180°.

3.5 Statistically equivalent geometry generation

For input in numerical simulations, several generators have been proposed to create random filament arrangements (Section 2.2.3). The statistically equivalent two-dimensional micro-structure in this work was generated following an adapted version of the procedure described by Vaughan and McCarthy [18] by means of measured distributions of distances between neighbouring filaments (Figure 34). This overcomes the limitation of the models described in Section 2.2.3 such as the jamming limit at low V_f or the lack of correlation of the generated micro-structure to actual filament arrangements.

In the original model [18], a pre-determined number of filaments are placed at given distances, which are picked randomly from the measured distributions, and in random directions relative to a randomly placed starting filament. After the last filament is placed, the starting point is set to the first newly placed filament, and the process is repeated. These steps are repeated until the specified domain is filled with filaments, and no additional filament can be placed. The adjustment of the nearest neighbour distributions, avoiding double counts of filament distances which are each other's *n*-th nearest neighbour, effectively leading to a widening of the distributions, was omitted in this work. This, however, does reflect the reality where two filaments within one yarn cross-section can be each others' *n*-th nearest neighbour. To accommodate the change in procedure the first four nearest neighbour distributions were used for the filament placement procedure.

For the assumption of a periodic hexagonal packing, the maximum $V_f = 0.91$ is achieved if the nearest neighbour distance is equal to the constant filament diameter. An identical nearest neighbour distance is present in the case of a square arrangement exhibiting maximum $V_f = 0.79$ for the first four nearest neighbours. It can be demonstrated, however, that the procedure described by Vaughan and McCarthy, has a natural jamming limit of $V_f \sim 0.70$ (Figure 38) if these neighbour distances are used in the reconstruction for the filament arrangement (Figure 39A). This limit can be explained by the fact that whilst the neighbouring filament distance is picked from a measured distribution, the neighbouring filament angle is randomly assigned. This introduces an unintended assumption about arrangement which does not necessarily reflect the actual filament configuration.

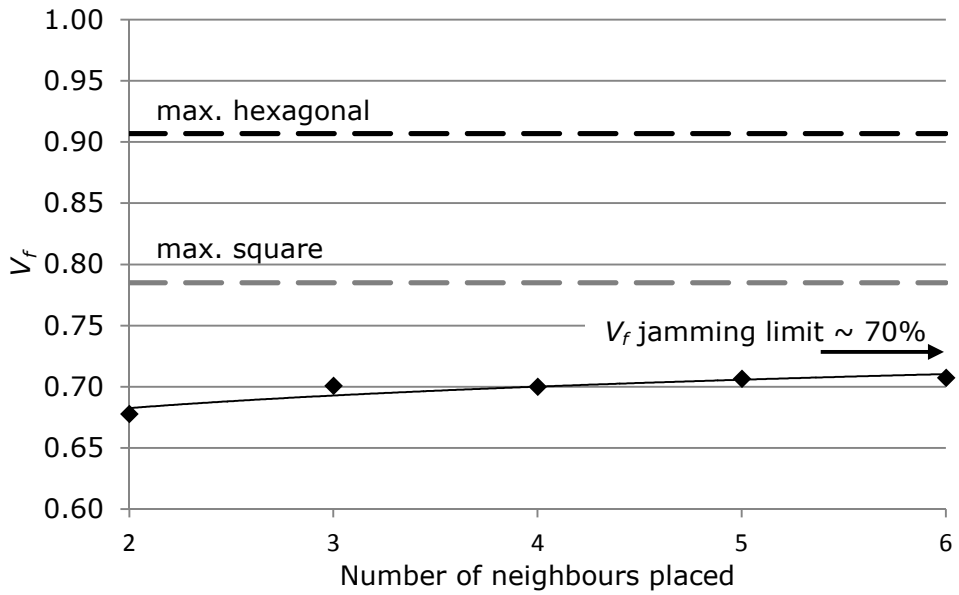

Figure 38: Jamming limit of the V_f utilising the model generator proposed by Vaughan and McCarthy [18] when used with the input data of touching filaments as present in hexagonal or square arrangements at maximum (max) V_f.

As indicated in Figure 32, the filament distances seem to converge to the hexagonal arrangement when the fibre bundle is compacted. This compaction introduces some regularity which is also reflected in the neighbour angle distribution (Figure 35). Therefore, it is necessary to take the actual angle distributions into account at which a probable *n*-th nearest filament is located instead of using a randomly assigned angle. Incorporating this consideration into the procedure proposed by Vaughan and McCarthy a statistically equivalent filament arrangement can be generated. Utilising the filament distance and angle distributions for a periodic hexagonal packing with maximum V_f = 0.91 as previously, the actual filament arrangement can be reconstructed (Figure 39B).The jamming limit of the fibre placement algorithm as shown in Figure 38 and Figure 39A can be overcome. Depending on the provided input data it is now possible to generate any achievable V_f.

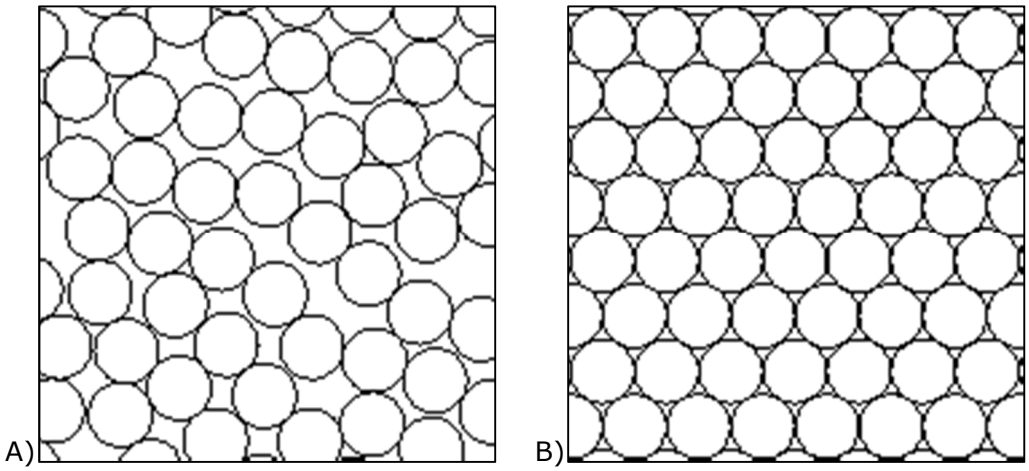

Figure 39: A) Reconstructed random filament arrangement (V_f ~ 0.70) following the procedure described by Vaughan and McCarthy [18] with neighbour distance distribution employed equal to the filament diameter. B) Filament arrangement (V_f = 0.91) achieved after additionally incorporating the angle distribution of a hexagonal configuration in the adapted model generator.

The generated V_f distribution for the micro-structure is similar to the distribution measured on cross-sectional samples of fibre bundles. In case of a global V_f of 0.60, the average V_f within the fibre bundle was estimated as V_f = 0.67 ± 0.07 whereas the reconstructed V_f was determined to be V_f = 0.66 ± 0.01 over a large number of realisations. The mean V_f is slightly lower than the measured data and the distribution is more narrow. This narrow distribution is also clearly visible in the neighbour distribution data (Figure 40). The measured neighbour distances are well within the confidence interval of one (log-normal) standard deviation.

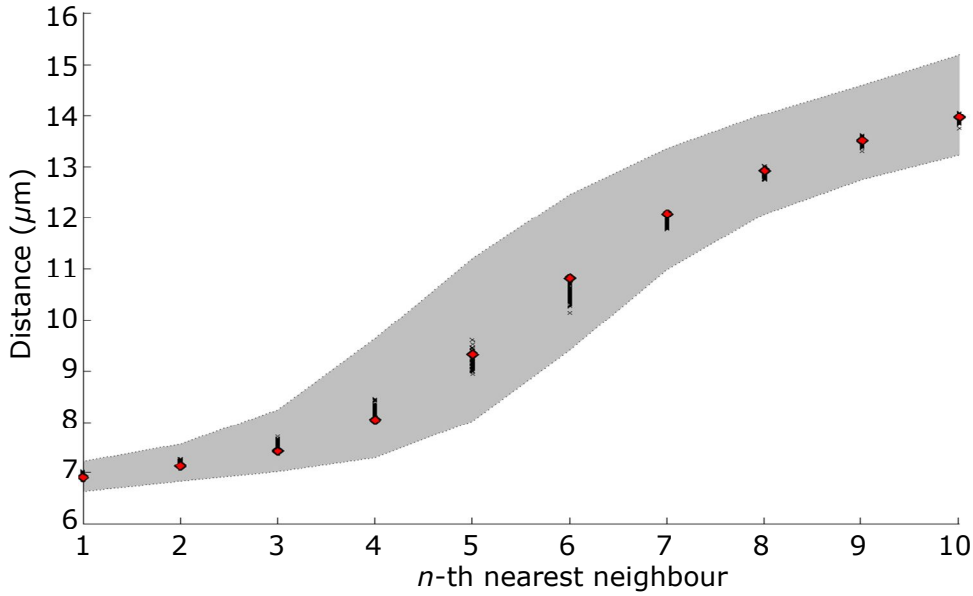

Figure 40: Measured n-th nearest neighbour distances (black x) of generated RVEs with a V_f = 0.66 compared to the distributions mean (red diamond). The log-normal standard deviation is marked as grey shaded area.

3.6 Summary

It was shown that the filament arrangement at the micro-scale will affect the permeability (Chapter 2). This chapter addressed the quantification and description of the filament arrangement within fibre bundles of composites on the micro-scale. Single layer uni-directional carbon fibre reinforcements (12K filament count) were moulded at different cavity heights, effectively varying the fibre volume fraction, V_f, of the resulting samples (Section 3.4.1). The manufacture of single layer composite samples made it possible to analyse the influence of compaction for single fibre bundles. Other factors present in multi-layered composite samples such as fibre bundle nesting are eliminated. The moulded and cured specimens were analysed by means of micrographs of polished cross-sections (Section 3.4.2). This allowed the micro-structure to be determined over a large area and at a high resolution (Section 3.3). The developed method of automated analysis of stitched images in Matlab® allows the analysis of much higher resolution images compared to examples reported in the literature [119]. This enables the systematic analysis of a large number of samples. Other imaging techniques, such as micro-CT [92], were identified to have an inferior resolution (Section 3.1).

To gain morphological data from the acquired images, a simple colour thresholding technique is often employed [104]. Inevitable differences in lighting, local light reflections and shading [109] make it, however, unfeasible to use one global threshold. An automated image analysis process was developed in this work, based on the edge detection of local colour gradients to overcome these issues (Section 3.3.2). The detected filament outlines are approximated with an ellipse. Kratmann et al. [111] pointed out that this method is sensitive to irregular shapes and time consuming. With the automated detection method developed in this work, the analysis time is relatively small and for the case of carbon fibres the shape assumption was concluded to be a good fit.

Compared to a set of manually fitted ellipses, an average underestimation of the minor ellipse axis of 0.8% could be identified (Section 3.3.2). The measurement of 300,000 single filament cross-sections showed a normal distribution of the filament diameter with a mean of 6.97 μm and a standard deviation of 0.39 μm which is in good agreement with the manufacturer's specification. It was concluded that the developed automated measurement technique for systematic analysis of micrograph cross-sections delivers superior results compared to measurement data presented in the literature e.g. [18, 106, 115].

Different statistical descriptors can be employed for the random arrangement of filaments within a fibre bundle. The distance of a filament to its *n*-th nearest neighbour was selected to describe the spatial arrangement of the filaments (Section 3.4.7). It was shown that these distances to nearest neighbours decrease with increasing fibre bundle compaction. In the literature, the increasing degree of order of the filament arrangement, reflected in the angle distribution under which the *n*-th nearest neighbour is located, is always disregarded. An almost perfectly random arrangement of the filaments is present when the bundle is not compacted (Figure 35A), which is reflected in uniform angle distributions. The angle distributions become less uniform, however, with increasing compaction (Figure 35B and C), i.e. increasing degree of order of the filament arrangement. The description of the degree of order in the arrangement by means of nearest neighbour angle distributions has not yet been reported in the literature. The analysis of the angle distribution in this work was only made possible because of the developed automated measurement technique allowing a systematic analysis with high precision of a large number of images.

To generate statistically equivalent micro-structures, the fibre placement algorithm proposed by Vaughan and McCarthy [18] was further developed to utilise the presented measurement data (Section 3.5). In particular the incorporation of the angle distribution of nearest neighbours guaranteed a statistically equivalent model. This also eliminated the jamming limit ($V_f \sim= 0.70$) of this model generation approach. It is now possible to generate any possible V_f depending on the provided input data. The generated micro-structures were validated with the same statistical descriptors as employed for the measurement of the filament distributions within fibre bundles. The micro-structures will be used for the predictions of fluid transport on the micro-scale in the following chapters (Chapter 4 and 5).

4. Saturated transverse micro-scale flow

Reinforcement fabrics used during a LCM process are saturated with resin behind the flow front. It is possible, however, that small amounts of air are entrapped in the liquid resin. After complete mould filling, purging of resin is therefore often employed in an attempt to flush out this remaining voidage. The saturated permeability of a reinforcement textile describes its behaviour during this type of flow (Section 2.1.1). Variability in the fibre preforms (e.g. fibre bundle spacing and nesting) can lead to significantly different permeability values at the component scale [38, 42]. In addition, random arrangement of filaments at the micro-scale will lead to fluctuations in the fluid velocity within fibre bundles (Section 2.2.4). These variabilities can lead to gas inclusions at the flow front (Section 2.3.3) and impede void transport in the fully saturated fibre bundles at the micro-scale. Numerical simulations of fluid transport within random filament arrangement are analysed in this work. The model domains were generated following an adapted version of the method proposed by Vaughan and McCarthy [18] as described in Section 2.2.3. Measured distributions of the filament arrangement in non-crimp carbon fibre reinforced composite samples as described in Section 3.4 were used to generate statistically equivalent micro-structures. The results presented in this chapter describe fully saturated steady-state flow.

4.1 Numerical modelling of saturated transverse micro-scale flow

The flow simulations in this work are governed by the Navier-Stokes equations, describing conservation of mass and momentum (Chapter 2.3.1). These equations are solved on specified model geometries utilising the commercial software Ansys Fluent® for steady state laminar flow (Appendix E) implying a low Reynolds number (Chapter 2.1.2). It is assumed that the fluid is incompressible and exhibits Newtonian behaviour. Transverse flow with respect to infinite long parallel filaments in varying arrangements was assumed. The simplification of the flow domain to two-dimensions is therefore possible. The momentum and pressure-based continuity equations were solved on discretised flow domains employing an unstructured triangular mesh (Section 4.1.2). The results describe laminar steady-state flow, as in a fully saturated fibre bundle.

4.1.1 Model boundary conditions

For the numerical modelling of the flow through a random filament arrangement, suitable boundary conditions are required. Regardless of the choice, the selected boundary conditions will imply an assumption on the flow. A selection of these boundary conditions is, however, without alternative.

All filament boundaries within the flow domain were treated as impermeable no-slip walls (Figure 41). Pressure gradients are applied across the model as boundary condition to simulate transverse flow. The model boundaries parallel to the applied pressure gradient were assumed to behave as impermeable frictionless walls. Boundary conditions for the model domain are a necessity for the numerical simulations. In reality, however, these boundary conditions will not exist as specified in Figure 41. The fluid flow through the filament arrangement before entering the model domain is likely to lead to varying flow velocities at the inlet boundary. The assumption of a constant inlet pressure could therefore be challenged. The use of periodic boundaries would address this problem. The random filament arrangement would then, however, need modification to ensure geometrical symmetry. This would imply an additional assumption on the flow problem. The error induced by the choice of the inlet and outlet boundaries on the total net flow in a non-symmetrical filament arrangement was considered to be small, in particular for large models. In addition, the impermeable frictionless walls do not allow flux through the horizontal edges. In reality, flow in this direction might also be present. Again, the error induced due the choice of this boundary condition is assumed to be small for larger models.

Pressure inlet and outlet boundary conditions were applied to induce a pressure gradient across the flow domain. It was shown that the selected pressure drop does not affect the resulting permeability of the filament arrangement (Appendix F). Nodes at the model boundaries were not matching (see Section 4.1.2) because geometrical symmetry at the model edges was not enforced (see Section 4.3.1). Periodic boundary conditions could therefore not be applied.

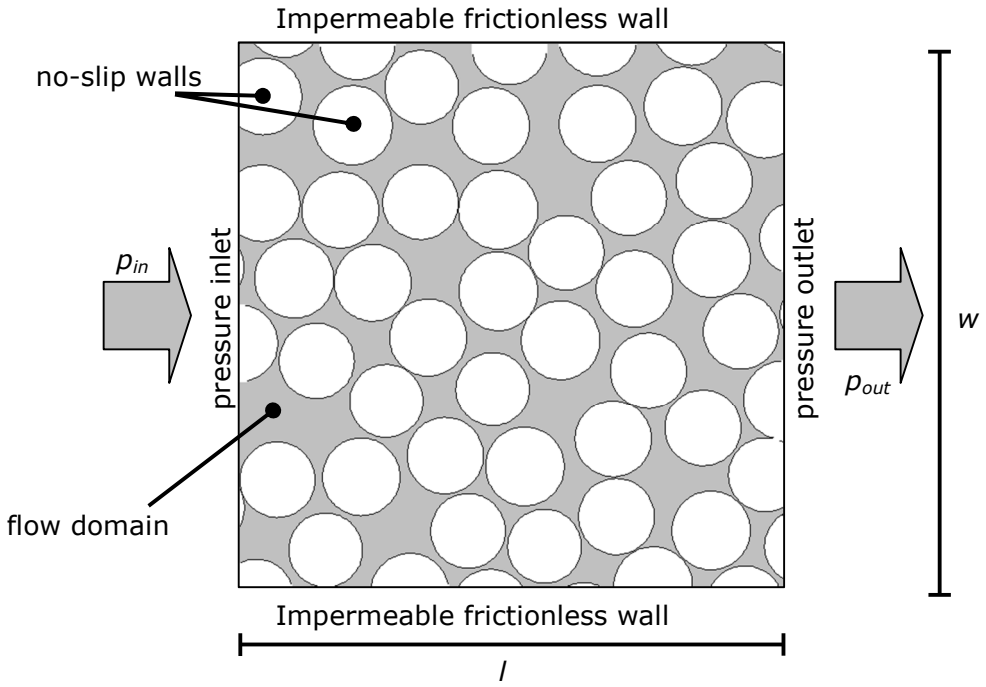

Figure 41: Applied boundary conditions for the analysis of steady-state flow through a random filament network in a model domain with side length, *l*, and width, *w*.

The impact of different types of boundary conditions was analysed based on simulations of hexagonal filament arrangements. Periodic versus pressure inlet and outlet boundary conditions were compared for flow through model domains discretised following the optimal parameters determined during the mesh sensitivity study employing local mesh refinement (Section 4.1.3). The results were then compared to the analytical and numerical predictions presented by Gebart [49]. His numerical simulation results, employing periodic boundary conditions, were in very good agreement to his analytical model. It could be demonstrated that the choice of pressure inlet-outlet boundary conditions here is in better agreement to Gebart's model compared to applied periodicity at identical V_f (Figure 42). This contradicts Gebart's results, but the difference was considered to be small.

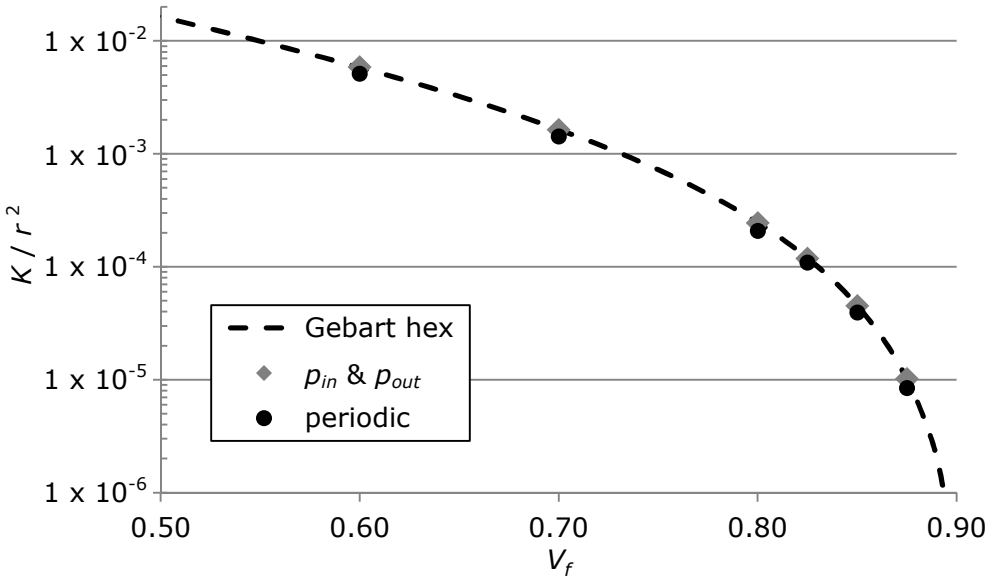

Figure 42: Effect of the boundary condition, pressure inlet and outlet condition (p_{in} & p_{out}) and periodicity (periodic) on the resulting permeability of a hexagonal (hex) unit cell filament arrangement compared to the analytical solution resulting from Gebart's model [49].

4.1.2 Model domain discretisation

For the numerical solution of the fluid transport through the generated random filament arrangement, the model domain is discretised into finite elements. It is necessary to have a sufficiently fine discretisation of the mesh locally, to reproduce the non-linear flow profile correctly. Especially in small gaps this requires small elements. The mesh generator mesh2d [121] in Matlab® is employed in this work. This code automatically generates an unstructured locally refined triangular mesh based on a Delaunay algorithm. This section describes the procedures which were developed to apply this mesh generator for automatic discretisation of generated random filament arrangements as described in Section 3.5. In addition, new rules are developed and implemented to automatically apply local mesh refinement in small gaps between filaments.

For the description of the flow domain, it is not necessary to discretise the impermeable cross-sections of the filaments (Figure 41). The mesh generator assumes piecewise linear geometries for these object edges. The circles, representing the filament cross sections, are therefore expressed as sets of lines with finite length. These lines are defined by generated nodal positions and their connectivity. The accuracy of the approximation of the circle curvature by straight lines is defined by their finite length. The angular resolution, $\Delta\theta$, of the circle division has to be selected in such a way that it does not interfere with the laminar flow. For filaments only located partially within the domain, the

intersection points with the domain boundaries have to be determined additionally. This is achieved following the procedure outlined in Appendix G and ensures the correct representation of the filaments.

The discretisation procedure is based on an initially generated background mesh which stores the finite element size data according to the specified finite element size. The mesh is then refined by iterative smoothing operations updating node locations and mesh topology. Nodes are added or removed during every iteration in order to achieve the required mesh quality. Due to the iterative smoothing process, the boundary nodes of opposite model edges do not necessarily match. The initial background seeding process is independent of the specified boundaries. Areas which are not intended to be discretised are initially included in the background mesh.

In order to achieve a sufficiently fine discretisation of small gaps between two filaments a large number of elements is required. Limiting the total number of elements typically requires local mesh refinement due to the difference in scale between domain size and gap size. This is achieved by applying a specified seed size in selected areas. The areas subjected to mesh refinement should be minimised in order to limit the memory required due to the applied background seeding process. Therefore, a rectangle intersecting with the filament boundaries is determined, containing the smallest gap between two filaments (Figure 43A). This rectangular area is then subjected to mesh refinement ensuring a minimum number of finite elements at the smallest inter-filament distance by specifying a predefined element size, h_0 (Section 4.1.3). This element size specifies the characteristic edge length of the triangular mesh. It should be mentioned; however, that the user defined finite element size is only applied if it is smaller than the automatically determined mesh size. This method of local mesh refinement was implemented as user specified function in the mesh generator mesh2d [121] written in Matlab®. This allows the generation of a locally refined mesh between filament pairs automatically.

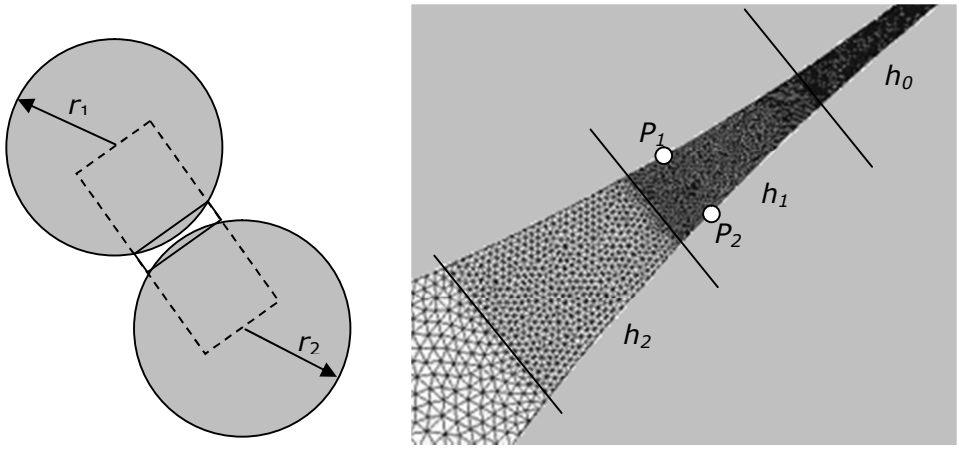

Figure 43: A) Area subjected to the user defined mesh refinement between two filaments (rectangle with solid lines). B) Applied local mesh refinement as function of the distance between the filament boundaries.

The curvatures of the filament boundaries imply a gradual change in gap width. The number of user defined seeds and consequently the number of generated finite volumes will increase with increasing distance between filament boundaries if the finite volume size is kept constant. Hence it is advantageous to gradually change the element size, maintaining at least the minimum required mesh resolution locally (Figure 43B). This is achieved by a gradual increase of the specified finite volume size in the area subjected to mesh refinement depending on the local gap width. For a given distance between two points, P_1 and P_2, on opposite filament boundaries, the minimum necessary finite volume size is determined. A rule has been implemented in this work, adjusting the local discretisation if the minimum required volume size, h_i, could be twice as large as the previously applied minimum volume element size. This method limits the total number of finite volumes in the complete model domain and reduces the computational cost. If the minimum gap width between two filaments is not limited, very small volume elements are needed in order to sufficiently discretise these areas. With the current settings, a minimum volume size of about 4.5 x 10^{-27} unit length can be realised. Smaller gaps will not be discretised accurately and filaments are considered to be touching. These small distances, however, are very unlikely to occur and are much smaller than the accuracy of the employed numerical solver. The flux through these gaps does not have a major influence on the overall steady-state result but will be more critical in impregnating transient flow simulations (Chapter 5). The described method has been implemented in a Matlab® program for the automatic discretisation of generated RVE structures.

4.1.3 Mesh sensitivity

For an accurate simulation of fluid flow, the finite volume mesh needs to be fine enough to reproduce the expected theoretical parabolic velocity profiles in inter-filament channels. To estimate the necessary resolution of the mesh flow through unit cells of a hexagonal filament arrangement (Figure 44) at different V_f was simulated for different mesh densities. Evaluating the resulting convergence of the permeability results made it feasible to determine the optimal mesh resolution.

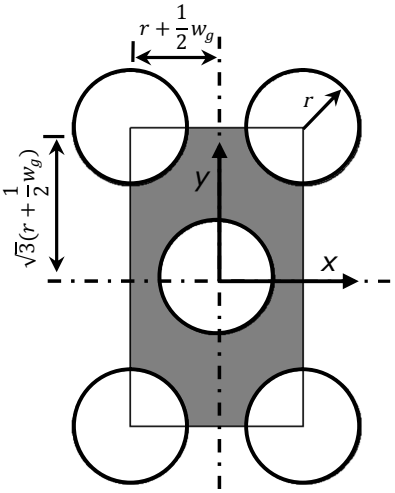

Figure 44: Unit cell of hexagonal filament arrangement. The cell dimensions as function of the gap width, w_g, are shown in the figure.

In addition, the boundaries of the filaments are assumed to be piecewise linear (Section 4.1.2). The angular resolution of the filament boundaries determines the precision of the approximation of the curvature. The choice of angular resolution of the filament boundaries in combination with the maximum allowable finite volume size also defines the degree of discretisation of the model domain. A number of different mesh densities were assigned in small gaps between filaments with width, w_g, in order to determine the necessary level of discretisation

The optimal angular resolution, $\Delta\theta$, could be identified by evaluating the convergence of the resulting permeability value of a set of models with different V_f and varying constant finite volume sizes in the gaps between filaments. An optimal trade-off between the total number of volumes in the model and the conversion of the results for all V_f studied was achieved with $\Delta\theta$ = 0.004 (Figure 45). This resulted in approximately 500 nodes per filament boundary (2π / $\Delta\theta$). The results are presented as percentage difference compared to the corresponding permeability value predicted by Gebart's model [49] for transverse flow through a hexagonal filament arrangement.

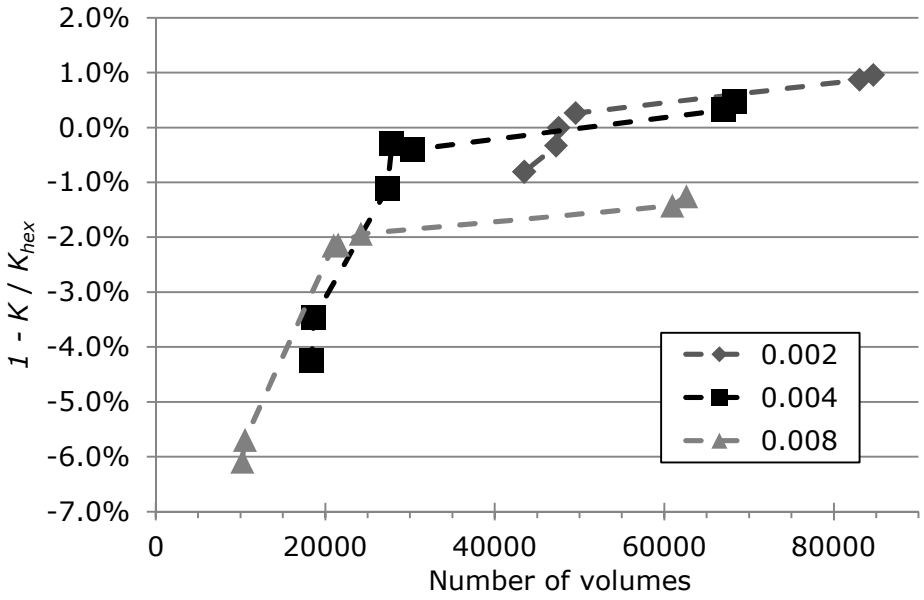

Figure 45: Example of the mesh sensitivity study of three different angular resolutions ($\Delta\theta$ = 2, 4 and 8 x10^{-3}) of a hexagonal unit cell (V_f = 0.875). The simulation results are presented in terms of percentage difference between the resulting transverse permeability, K, and the results predicted by Gebart's model for a hexagonal arrangement [49].

The selection of the optimal angular resolution allowed estimation of the required mesh density in small gaps between filaments. The local mesh density is defined by the corresponding finite volume size, described by the characteristic edge length, h_0, of the finite volumes. The required discretisation was determined by evaluation of permeability values calculated for different inter-filament gaps at different mesh densities. Again, the permeability is expressed as percentage difference to the predictions by Gebart's model [49] for transverse steady-state flow through a hexagonal filament arrangement with a corresponding V_f. The obtained results show that the relative change of the permeability values decreases with an increase in the total number of elements (Figure 46). With a large number of elements, the change in permeability values significantly decreased and the solution converges to a limit value (indicated by arrows). To limit the number of elements, a solution was considered convergent when it came to within ±1 % of this limit value of the permeability as a function of the total number of volumes (red labelled data points in Figure 46).

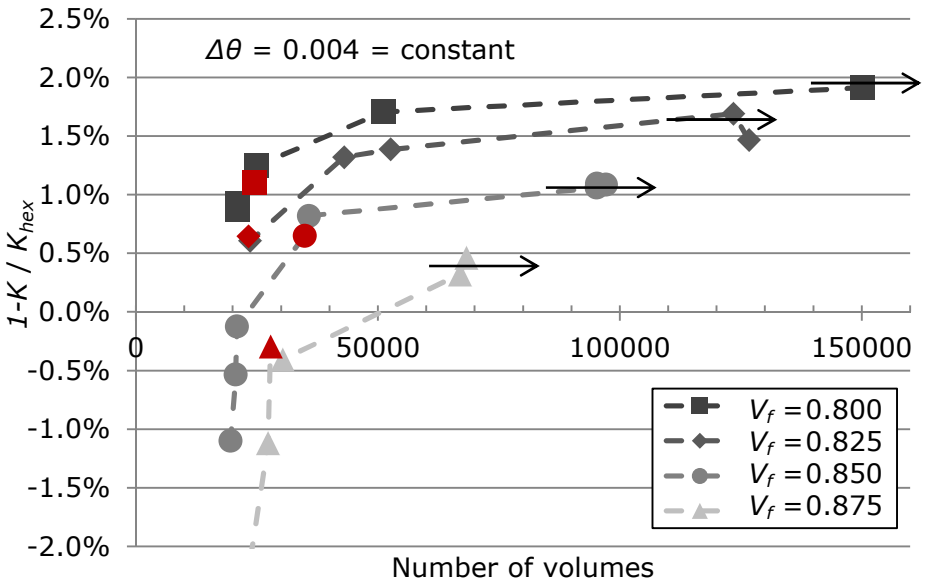

Figure 46: Mesh convergence calculations for steady-state flow through hexagonal unit cells with a constant angular resolution of the filaments ($\Delta\theta$ = 0.004) for different fibre volume fractions, V_f. The resulting permeability values are expressed as the percentage difference to the predictions by Gebart's model [49]. The data represent varying user defined volume size within the smallest gaps between filaments. The points marked in red are considered to be within ±1 % of the limit value.

The diagram of the finite volume size h_0 as a function of the gap width, w_g, in Figure 47 indicates that approximately 15 rows of volumes are required across the gap width to obtain convergent solutions according to the selected criterion. This is significantly more than determined by Yazdchi et al. [57] who employed 10 rows of finite volumes for the discretisation of small gaps in RVEs. Compared to the approach employed in this work, an underestimation of the permeability of up to 5% is anticipated based on steady state flow simulations on hexagonal unit cells. These errors are, however, likely to accumulate in larger models containing multiple inter-filament gaps.

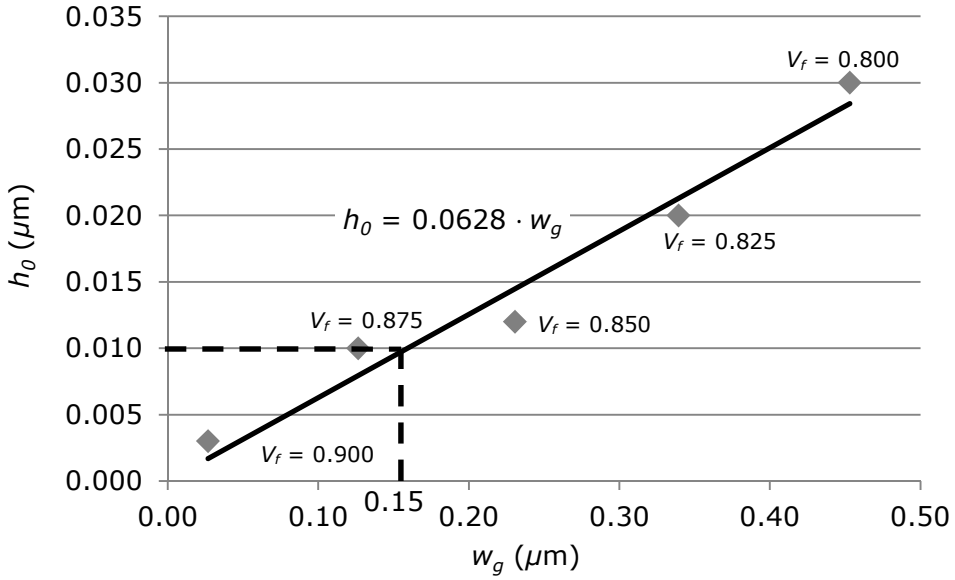

Figure 47: Maximum size of triangular finite volumes, in terms of characteristic edge length, h_0, for which convergence of the numerical solution for flux through an ideal hexagonal filament arrangement was obtained, as function of the inter-filament gap width, w_g; data is approximated by a linear trend line.

The determined correlation between gap width and minimum required element size ensures sufficient discretisation of small gaps between filaments. This level of discretisation minimises the error of the steady-state flow simulations. The relationship of the element size as a function of the gap width between filaments was implemented in the automated local mesh refinement approach described in Section 4.1.2.

4.2 Micro-scale permeability predictions

Gebart [49] suggested that the permeability of a fibre bundle can be described by a periodic unit cell and is only dependent on geometrical parameters. The permeability can therefore be described as a function of the fibre arrangement, V_f and fibre radius only (Section 2.2.2). This, however, ignores the random filament arrangement and the variation in local fibre volume fractions.

4.2.1 Permeability of randomised hexagonal unit cells

As a measure for the randomness of the flow behaviour, transverse permeability values can be derived for non-uniform filament arrangements. In the unit cell of an originally regular hexagonal filament arrangement (Figure 44), which is the smallest configuration allowing randomisation [122], different V_f can be realised by adjusting the geometry parameter w_g. This parameter corresponds to the gap width between two filaments and is defined as:

$$w_g = 2\left(\sqrt{\frac{\pi}{2\sqrt{3}V_f}} - 1\right)r \qquad \text{Eq. 32}$$

Randomisation is achieved by shifting the centre filament horizontally by a distance δx and vertically by a distance δy. For a number of randomised unit cells with the centre filament shifted to arbitrary positions (x, y), transverse flow was simulated numerically as described in Section 4.1. Permeability values were generated from the imposed pressure gradient, Δp, and the calculated average horizontal flow velocity (weighted by the respective finite volume dimensions), v_{avg}, according to

$$K = \frac{(2r + w_g)\mu_f v_{avg}}{\Delta p} \qquad \text{Eq. 33}$$

The randomised permeability values are, however, only random and valid for the domain size of a single unit cell. Periodic boundary conditions of this domain may be assumed but the global arrangement would then be considered periodic again as well. The use of just a single unit cell domain with non-periodic boundary conditions can therefore be considered as the smallest randomised filament arrangement.

Maps of the flow velocity (Figure 48) indicate that for shift of the centre filament along the x-axis, the permeability decreases with increasing distance of the filament from its original position (Figure 48C). This coincides with decreasing width, w_{gi}, of either of the two horizontal flow channels formed in the top and bottom halves of the unit cell, which are in series. This illustrates that the cell permeability is dominated by flux through the narrower channel. For shift along the y-axis, the permeability increases with increasing width of either of the two flow channels which are in parallel, since the permeability is dominated by flux through the wider channel (Figure 48B).

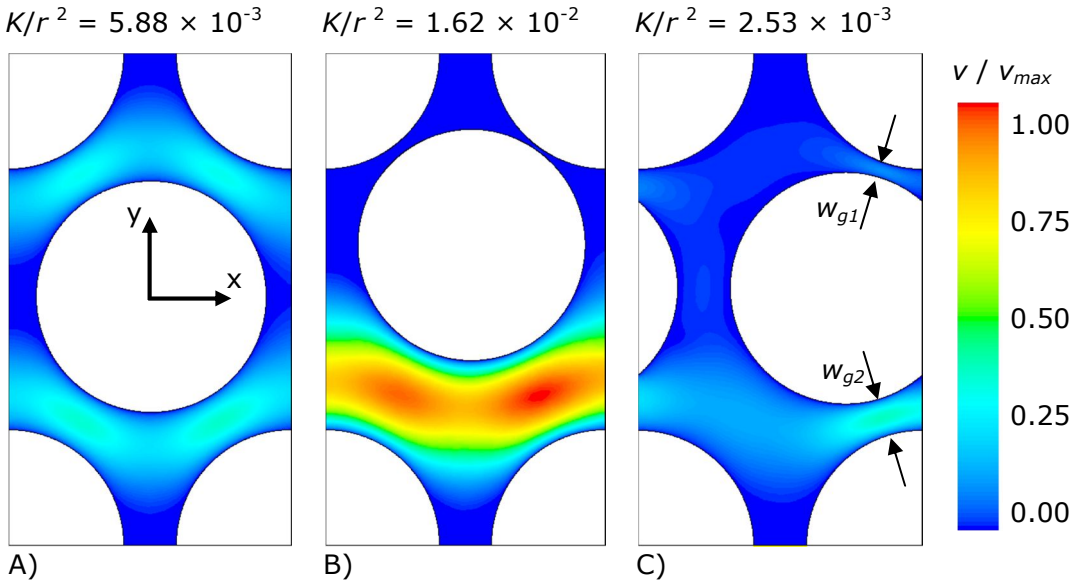

Figure 48: Maps of the magnitude of the flow velocity, v, normalised by the maximum observed velocity, v_{max}, for transverse flow (pressure gradient from left to right) through randomised hexagonal unit cells at V_f = 0.60; analytical transverse permeability for ideal hexagonal unit cell is K/r^2 = 5.82 × 10^{-3} m^2 [49].

Results for the permeability as a function of the centre filament position of 100 realisations for V_f = 0.60 are plotted in Figure 49. For x = 0 and y = 0, the calculated result is in good agreement with the solutions given by Gebart [49].

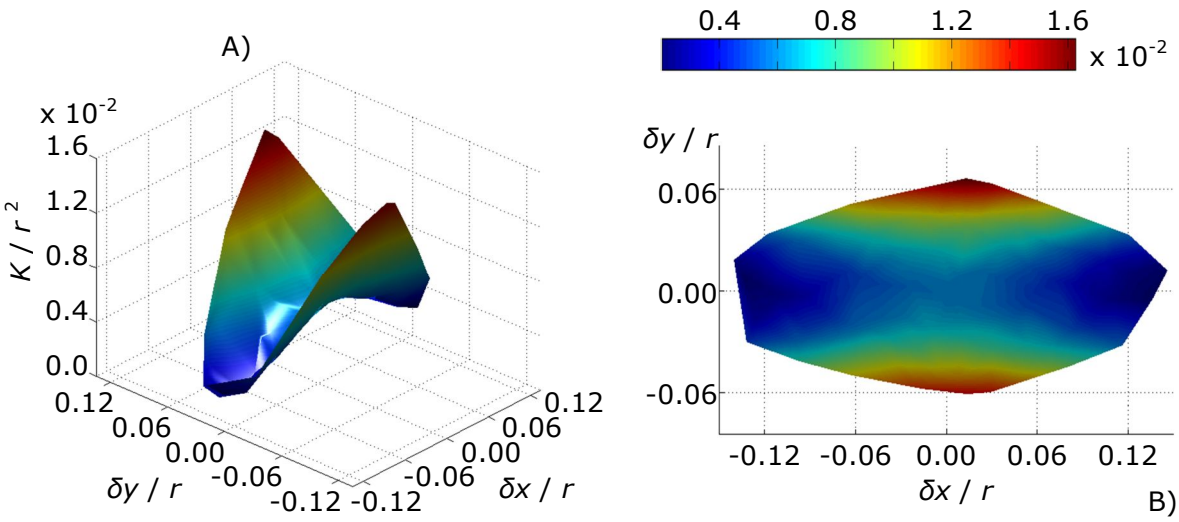

Figure 49: Numerical results for the transverse permeability, K, of a randomised hexagonal unit cell (V_f = 0.60) for 100 realisations as a function of the position of the centre filament along the x- and y-axes, normalised by the filament radius, r. A) Three-dimensional representation of the saddle shaped permeability profile and B) the top view on this saddle shape.

The randomisation was achieved with the use of the pseudo-random number generator in Matlab®. Random positions (x, y) of the centre filament were generated within the specified domain. Positions which lead to an overlap with the corner filaments were disregarded. The distributions of permeability values derived from simulations at different fibre volume fractions illustrate that the permeability of a randomised unit cell can be either higher or lower than the permeability of a regular unit cell (Figure 50). The mobility of the centre filament is limited by the fixed positions of the corner filaments in the unit cell. This results in different ranges for δx and δy at different V_f. Even though the orders of magnitude for the relative spread of the values increases, the scatter of absolute permeability values decreases with increasing V_f.

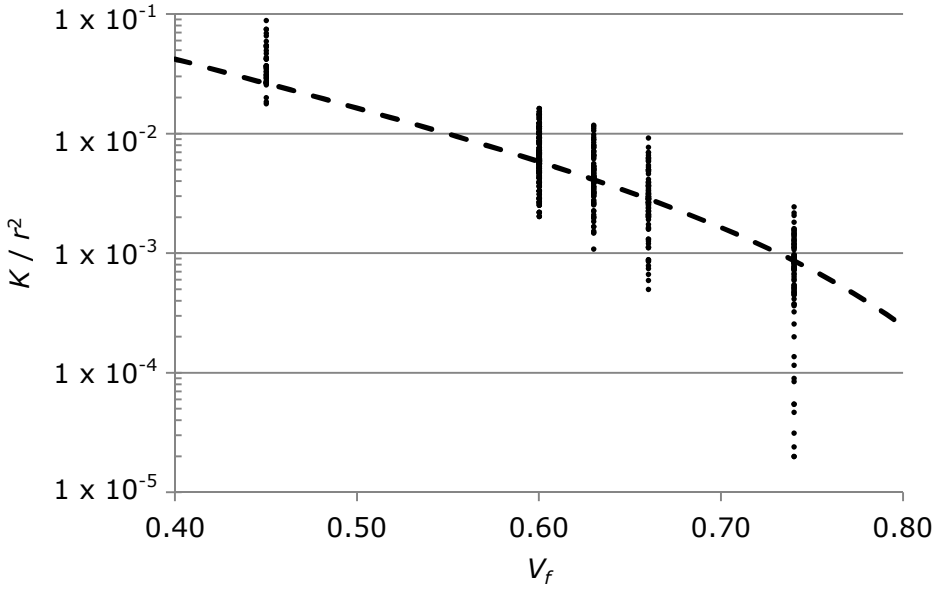

Figure 50: Numerical results (dots) for the transverse permeability, K, of a randomised hexagonal unit cell as a function of the fibre volume fraction, V_f, normalised by the fibre radius, r, (100 realisations per V_f) compared to analytical solution (dashed line) based on Gebart's equations [49].

4.2.2 Flow channels connected in series

It was demonstrated on the example of randomised hexagonal unit cells (Section 4.2.1) that the transverse permeability is strongly dependent on dimensions of the flow channel. A reduction in width of the flow channel (i.e. centre filament is moved horizontally in flow direction) leads to significantly reduced flux through the filament arrangement at constant V_f. Filaments in reinforcement textiles are arranged randomly, creating wide distributions of inter-filament gaps. Assuming transverse flow and parallel alignment of the filaments, these arrangements form flow channels connected in series (Figure 51).

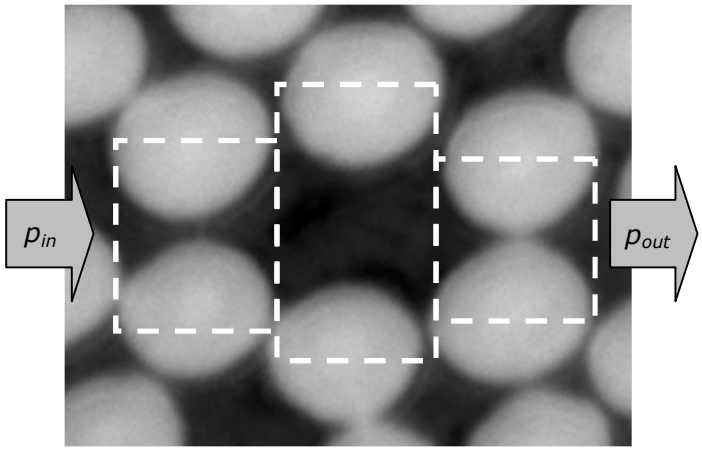

Figure 51: Unidirectional carbon fibre composite cross-section, showing a flow channel formed by filaments in close contact. The filament arrangement is assumed to be an arrangement of quadratic unit cells connected in series.

Transverse flow through filament arrangements as shown in Figure 51 can be considered to behave like (quadratic) unit cells connected in series. Assuming these cells exhibit no net flux through the horizontal model boundaries, the permeability of the arrangement becomes equal to sum of all pressure drops. In contrast to a periodic arrangement at an identical V_f the pressure drops in the random cells are not constant. Due to the non-linear relationship of the permeability as a function of the gaps formed between two fibres (V_f in Eq. 10) the smaller gaps will have a larger effect on the behaviour of the entire arrangement. It can therefore be demonstrated that the overall permeability of a random arrangement is dominated by the filament pair with the smallest gap (Appendix H for the case of two cells). An example of transverse flow over a series of three quadratic unit cells at identical V_f = 0.39 is depicted in Figure 52. For the analytical determination of the permeability of the arrangements the same assumptions as described above and in Appendix H, such as constant fluid flow is through the vertical cell edges only, are made.

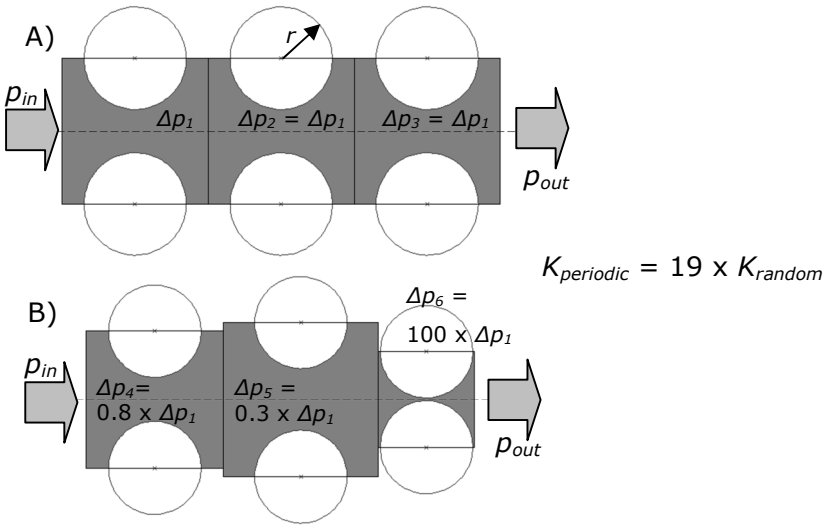

Figure 52: Permeability, K, of transverse steady state flow over a series of three unit cells with a V_f of 0.39 with no flux through the horizontal cell boundaries. A) Periodic square arrangement of filaments; B) varying filament distances. The pressure drop following Gebart's model [49] is displayed in the corresponding cells.

The pressure drop is identical ($\Delta p_1 = \Delta p_2 = \Delta p_3$) for flow through three unit cells connected in series exhibiting constant filament distances (Figure 52A). Introducing geometrical variability (Figure 52B), the pressure drops also become variable. The pressure drop of the first two unit cells (Δp_4 and Δp_5) is in the same order of magnitude as the pressure drop in the periodic example. The width of the gap formed between the filaments in the third unit cell is very small compared to the other gaps shown in the example of Figure 52. This results in a pressure drop more than 100 times larger than the periodic example (Δp_6). As a result, the transverse permeability of this random arrangement was determined to be 19 times lower than the periodic arrangement at identical V_f. This example also suggests that the transverse permeability of randomly sized flow channels connected in series should always be lower than predicted by an analytical model based on a periodic arrangement (e.g. [49]) at equal V_f (Appendix H) Keeping in mind the extensive assumptions made (e.g. no flux through horizontal cell edges), this simple example demonstrates clearly the limitations of a unit cell approach by disregarding random filament arrangements. The permeability of a fibre bundle is a result of the varying gaps formed between randomly arranged filaments. Therefore representative volume elements (RVE) need to be employed for the numerical determination of micro-scale properties instead of unit cells. It should be kept in mind, however, that in practise geometrical variabilities in the longitudinal direction of the filaments such as undulations and twist exist [92] which are also not captured by employing RVEs.

The local blockage of flow channels can also explain significant differences in transverse permeability found at identical V_f for flow through random filament arrangements (see Section 4.3.1). Gaps with varying widths form between filaments, affecting the fluid transport differently. The two examples illustrated in Figure 53 are both characterised by V_f = 0.64. The resulting permeability values, however, vary by two orders of magnitude. The larger permeability of the RVE shown in Figure 53B can be explained by the formation of a major flow channel, enabling a continuous fluid flow from the pressure inlet to the pressure outlet. In comparison, the smaller transverse permeability of the model shown in Figure 53A is a result of flow blockage due to narrow gaps between filaments. Although the V_f is low in the right half of the RVE, the average flow velocity in the model is low due to the small flow channels formed in between the filaments. While these domains are two-dimensional only, flow in the third dimension might circumvent the blockage of the transverse flow.

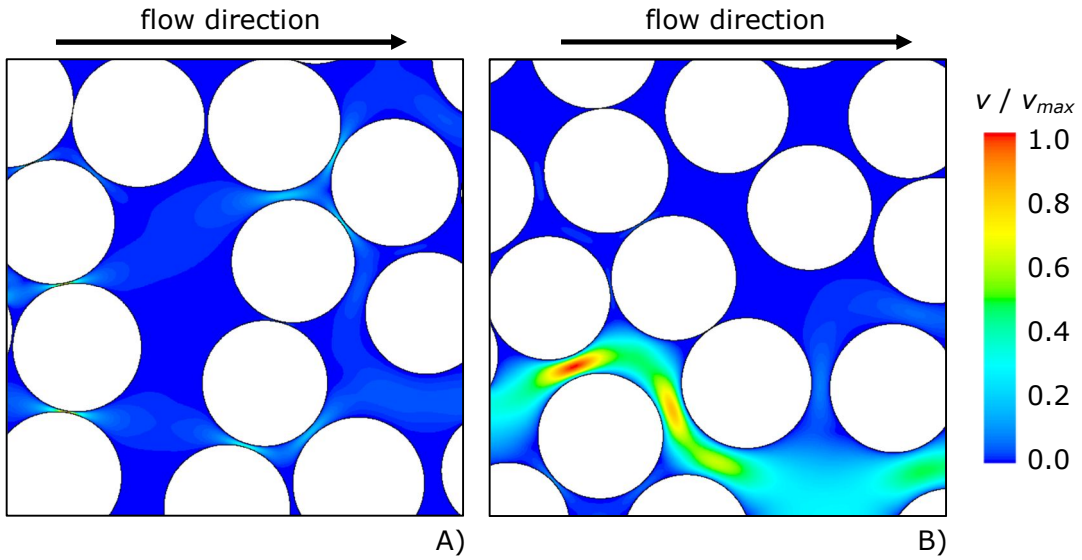

Figure 53: Maps of velocity distributions for transverse flow through random filament arrangements at V_f = 0.64. A) Flow is blocked by a fibre cluster; $K / r^2 = 1.56 \times 10^{-5}$. B) Formation of a flow channel over which the majority of fluid is transported; $K / r^2 = 2.49 \times 10^{-3}$.

4.3 Permeability of randomised filament arrangements

4.3.1 Generation of statistically equivalent micro-structures

The utilisation of a unit cell approach fails to represent the random filament arrangement found in fibre bundles (Figure 54A). Even though regular filament configurations (such as square or hexagonal) can be present within yarn cross-sections locally, it is evident that these periodic arrangements do not reflect the actual micro-structure. The filament density within the micro-structure varies depending on the position. Effects, such as local filament clustering or the

formation of flow channels (outlines indicated with lines in Figure 54), can be predicted utilising reconstructed filament arrangements (Figure 54B) generated following the procedure discussed in Section 3.5. These reconstructed structures represent the original filament arrangement but are are not intended to reproduce the exact arrangements as measured. Whilst, the filament arrangements in Figure 54A and B do not look identical, they do exhibit a similar statistical filament distribution.

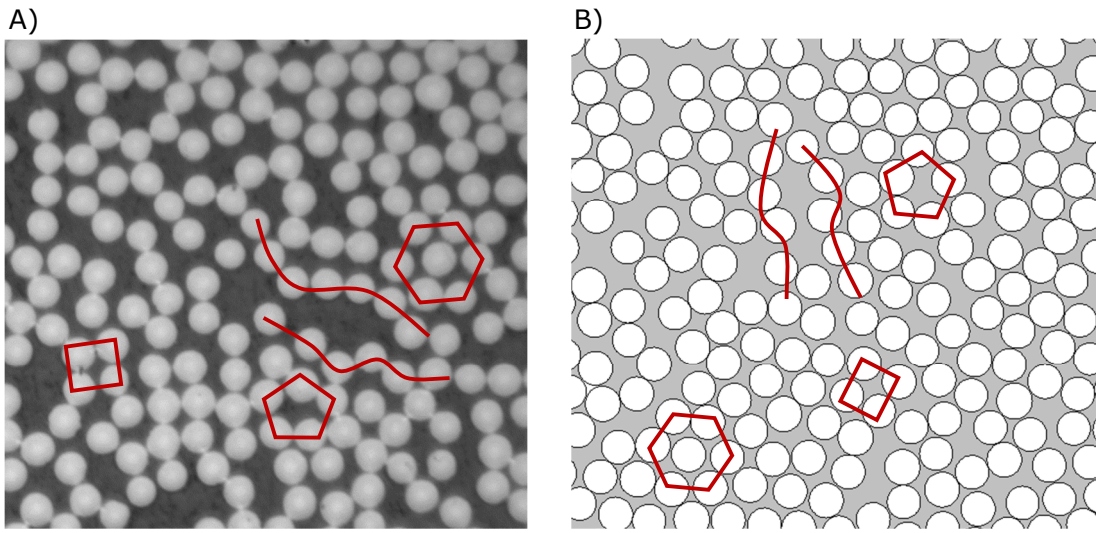

Figure 54: A) Micrograph of a unidirectional carbon fibre bundle cross-section showing a random arrangement of filaments. B) Reconstructed filament micro-structure. Typical fibre arrangements are marked in the images.

It is assumed that the filaments have an infinitive length and are aligned parallel to each other. Therefore, it is not necessary to analyse transverse flow through a three-dimensional network and the simulation of the micro-structure can be reduced to a two-dimensional problem only (Figure 55). In reality these filaments would, however, exhibit undulation and twist along the filament axis [92, 110].

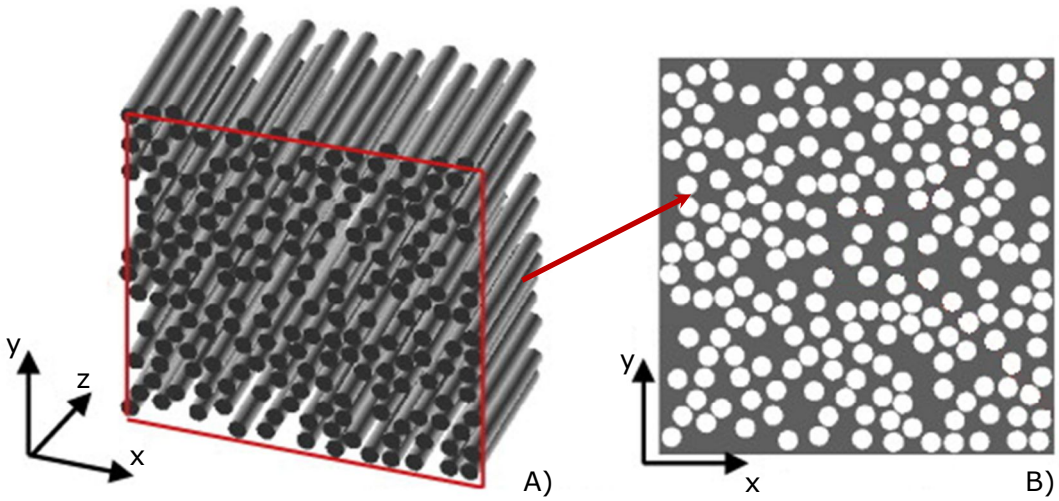

Figure 55: A) Three-dimensional random arrangement of continuous filaments aligned in parallel. B) Two dimensional reduction of the three dimensional filament network. Reprinted from Yadzchi et al. [57] with permission from Elsevier.

The statistically equivalent micro structures in this work were generated following an adapted version of the method proposed by Vaughan and McCarty [18] as discussed in Section 3.5. In this approach, a predefined two-dimensional domain is populated with filament cross-sections, represented by circles (Figure 56). The utilised distance and angle distributions for the model generation at which the *n*-th nearest neighbours are located were presented in Section 3.4 and determined on specimens exhibiting three global V_f (0.45, 0.60 and 0.74).

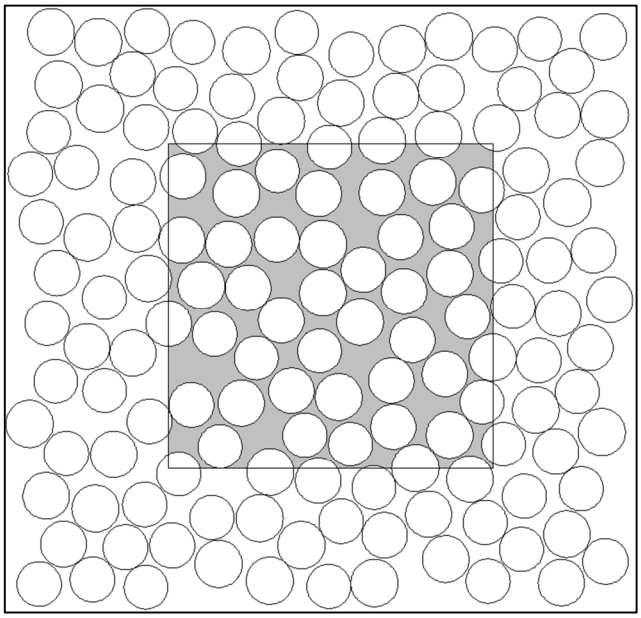

Figure 56: The target model domain, shaded in grey is embedded in an initial larger domain, to ensure complete population of the area with filaments.

The initially selected model dimensions are larger than the target area (grey shaded area in Figure 56) to ensure a complete population of the modelling domain with filaments. The offset was selected to have a width of approximately three filament diameters and was kept constant for all model sizes. After completion of the filament placement procedure, all fibres outside the area of interest are removed and only the filaments which are at least partially located within the target area remain. The resulting opposite model boundaries are not symmetric regarding intersections with filament boundaries. In the literature, different methods have been proposed to achieve geometrical symmetry of an RVE. Trias et al. [64] only used filaments which were completely located within the specified domain. The model boundaries do therefore exhibit symmetry and periodicity considerations can be applied. Vaughan and McCarthy [18] employed a procedure during the filament placement process allowing fibre segments to remain within the model while ensuring model symmetry. Their approach enforces the placement of a complementing fibre on the opposite edge if a placed filament is only partially located within the model domain. In the present model, geometrical symmetry is not enforced at the boundaries to avoid another assumption implied on the filament arrangement. Symmetrical boundary conditions can therefore not be employed. It was shown, however, that suitable alternative boundary conditions can be applied (Section 4.1.1).

4.3.2 Flow through randomised filament arrangements

In this study, larger models exhibiting random filament arrangements (Section 4.3.1) containing up to approximately 160 filaments were analysed applying the same numerical procedure as described previously (Section 4.1). The transverse permeability was determined from CFD flow simulations for square-shaped random models of different sizes at different V_f. The target V_f were chosen based on the determined local V_f (section 3.4.5.2). The number of simulations employed to generate each data point are presented in Table 4.

Table 4: Number of simulations for three intra bundle V_f at different model sizes given as ratio of model side length, *l*, to average filament radius, *r*.

l / r	V_f = 0.63	V_f = 0.66	V_f = 0.74
4.3	281	192	228
7.1	143	256	99
14.3	62	54	8
21.4	95	62	12
28.6	23	12	--

The results depicted in Figure 57 are based on a total of 1527 simulations. The results indicate that the average permeability decreases with increasing V_f. The increased filament density leads to a decrease of the width of the flow channels formed in between the filaments. The very small differences in permeability observed between the results for V_f = 0.63 and V_f = 0.66 are a result of the very small difference between the actual V_f. The results show that the average permeability tends to decrease with increasing size of the models. Based on the simulation of rectangular model domains it will be demonstrated later that this effect is related to the probability of locally blocked flow channels being formed within the filament network.

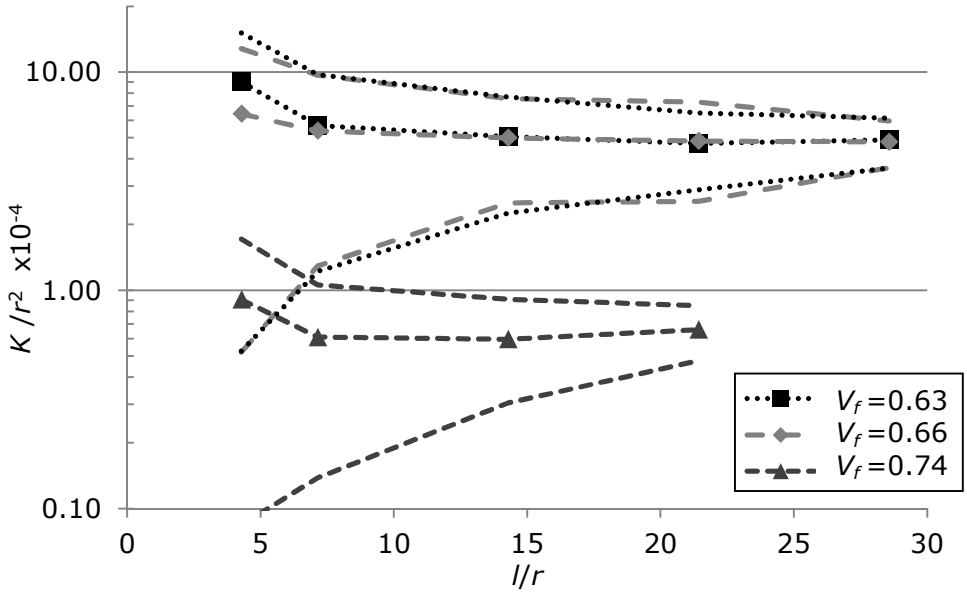

Figure 57: Permeability of random filament arrangements for three V_f, measured within fibre bundles at different levels of bundle compaction, as function of the model size expressed as model length, l, normalized by the average filament radius, r. The dashed lines represent the standard deviation of the simulated results.

The permeability values were found to be log-normally distributed. For illustration, the histogram of a distribution of K, for visualisation normalised by the permeability of an ideal hexagonal filament arrangement at the same fibre volume fraction, K_{hex}, is plotted in Figure 58. The width of the distribution of $\ln(K/K_{hex})$ decreases with increasing model size, i.e. ratio of model edge length, l, and filament radius, r (Figure 57). Since, with increasing model size, the flux through an increasing number of local inter-filament flow channels is averaged, the scatter in permeability is significantly reduced.

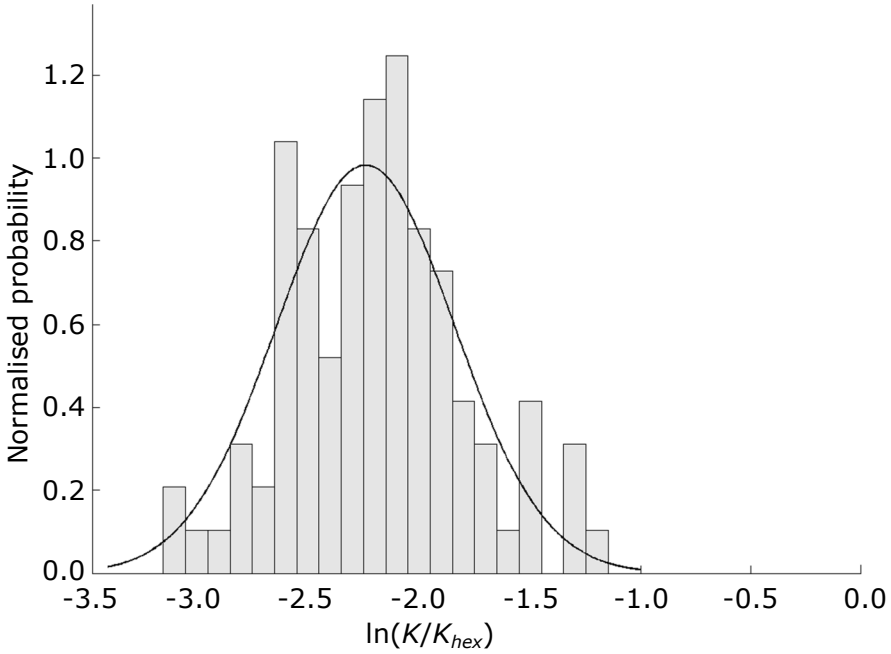

Figure 58: Log-normally distributed permeability values derived from CFD flow simulations of transverse flow through 95 random filament arrangement (l/r = 21.4) at constant V_f =0.63 ± 0.02 normalised with the value of the hexagonal permeability predictions by Gebart [49]. The fitted normal distribution with mean and standard deviation -2.25 ± 0.41 is shown for comparison. The distribution is normalised so that the area under the curve is equal to 1.

Figure 59 shows that the average values of $\ln(K/K_{hex})$ converge to a value of approximately -1.7 to -2.3 depending on V_f (compare with Table 5). Convergence of the permeability in this case was assumed when the relative change between values is less than 5%. This reflects the convergence of K to the permeability of a complete fibre bundle. Models with a ratio l/r above a critical value, for which convergence is achieved, can be considered statistically equivalent to a complete bundle, implying that they can be expected to exhibit the same properties. This can be utilised to reduce the computational effort for numerical analyses of the bundle behaviour by minimising the domain for analysis to a size characterised by the critical ratio. Here, the resin flow through a fibre bundle can be represented by models with edge lengths of 100 μm or more, i.e. for ratios l/r greater than approximately 30. The reduction of the observed scatter in permeability with increasing models size is attributed to the more homogeneous micro-structure.

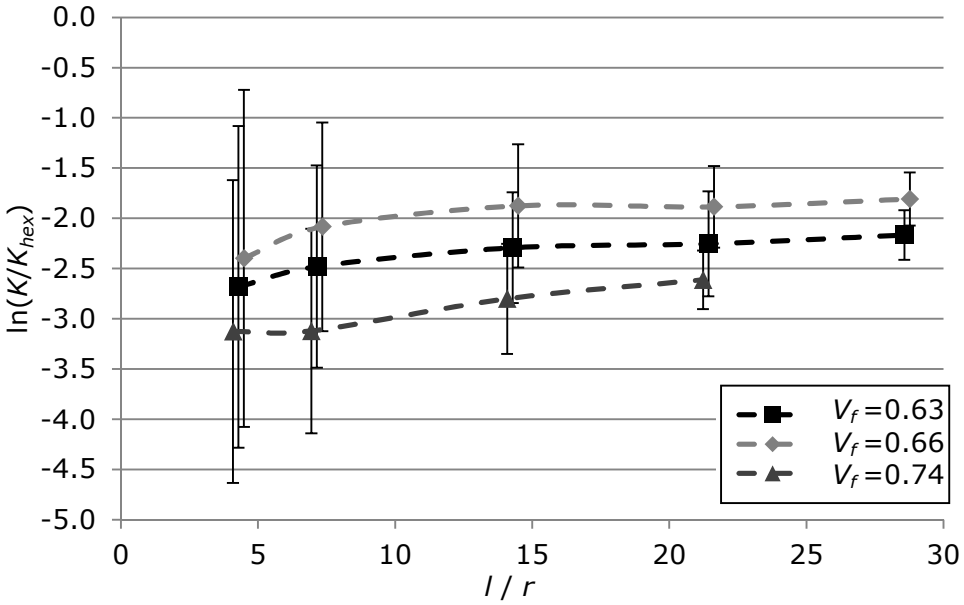

Figure 59: Permeability values from CFD simulations on random filament arrangements, normalised by the analytical prediction for an hexagonal filament arrangement following Gebart's model [49] . For improved visualisation, the permeability values at V_f = 0.66 and V_f = 0.74 are staggered off the values shown for V_f = 0.63.

In terms of absolute values, the predicted average permeability is about 6 to 10 times lower than the numerical or analytical model predictions of a periodic hexagonal arrangement (Table 5). This implies that the often employed flow predictions based on a simple unit cell approach will give systematically different results. Flow predictions based on these models will result in erroneous process predictions for the LCM process, and hence the deduced process parameters used in practise will not be optimal.

Table 5: Converged permeability values based on CFD flow simulations of random filament arrangements.

V_f	0.63	0.66	0.74
Converged K/r^2 (x 10^{-3})	0.51	0.50	0.09
K_{hex}/r^2 (x 10^{-3})	4.12	2.84	0.87
Converged $\ln(K/K_{hex})$	-2.10	-1.74	-2.29
K/K_{hex}	0.12	0.18	0.10

Based on different schemes for characterisation of the minimum size for a statistically equivalent model domain, critical ratios between 4 and 200 were reported in the literature (Section 2.2.3). This demonstrated that the model size depends not only on the filament arrangement in a bundle, but also on the method for its definition. Yazdchi et al. [57] reported a minimum l/r ratio of 80

for a converged solution of steady state flow transverse to the filament axis which is significantly larger than the value observed here. This may result from the fact that only artificial micro-structures were analysed in their work and a minimum remaining gap distance was enforced between two neighbouring filaments. In addition, a significantly higher mesh resolution between small inter-filament distances was employed here, which will improve the accuracy of the solution especially in very small gaps (Section 4.1.3).

Numerical simulation domains employing random filament arrangements are usually square shaped. The effects of rectangular shaped model domains with ratios of flow length to model width, l/w, of 0.5 and 2.0 at constant V_f on the resulting permeability was analysed here (Figure 60). In analogy to the basic examples of filament variability and the formation of flow channels discussed in Section 4.2.2, the permeability of random filament arrangements is influenced by the probability of flow channel formation. An increased flow length is accompanied by an increased probability that a flow channel will be blocked locally by filaments in close contact, reducing the resulting permeability. A varying model width should therefore show a contrary effect. The probability of a flow path be formed increases with increasing model width and the permeability should increase accordingly.

The difference in permeability for random filament arrangements in square-shaped domains for different flow directions (horizontal and vertical) was found to be insignificant (Table 6). For the rectangular models, the permeability decreases with increasing flow length, i.e. vertical (Figure 60A) compared to horizontal (Figure 60B) flow. The probability of a blocked flow channel is increased with increased flow length, resulting in a lower average permeability. The larger permeability of the rectangular model compared to the square model domain with identical l/r ratio is a result of the increased model width. The probability of a flow channel without blockage increases with increasing model width. In quadratic model domains, the l/w ratios are constant ($l/w = 1$). The probability of formation and blockage of flow channels with increasing model size is balanced, resulting in convergence of the permeability values and a reduction in scatter (Figure 59). A single permeability value as a function of the converged l/r ratio can describe the permeability of the structure in any direction of the flow, assuming a random filament arrangement.

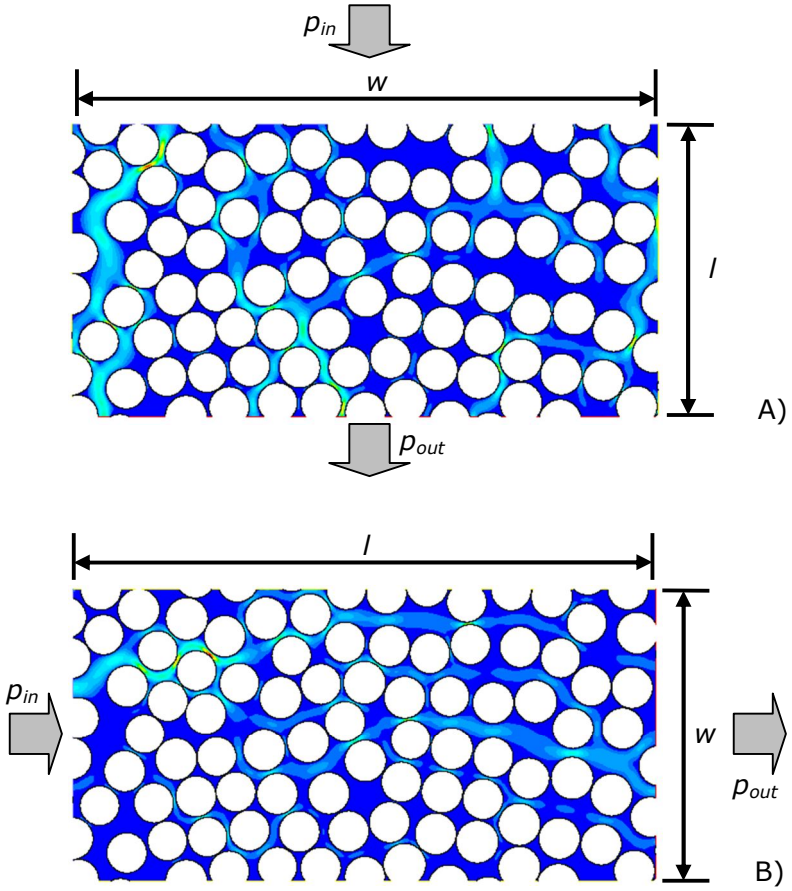

Figure 60: Maps of fluid velocities for A) vertical and B) horizontal flow transverse to a random filament arrangement (V_f = 0.63) in a rectangular flow channel with *l*/*r* ratios of 14 and 29 and *l*/*w* ratios of 0.5 and 2.

Table 6: Average permeability values of 17 rectangular and 41 square-shaped models with random filament arrangements. The absolute permeability is given as well as the log-normal mean and standard deviation.

Model shape	Flow direction	*l* / *w*	*l* / *r*	$K_\perp$ / r^2 x 10^{-4}	ln(K/K_{hex})
square	horizontal	1.0	14	6.6	-1.90 ± 0.43
	vertical	1.0	14	6.7	-1.86 ± 0.31
rectangular	horizontal	2.0	29	6.1	-1.72 ± 0.29
	vertical	0.5	14	7.7	-1.93 ± 0.24

Fibre bundles used in reinforcement fabrics usually exhibit a large width to height ratio. The simulation results of flow through random filament arrangements employing rectangular models suggest that the probability of formation of local flow channels depends on the flow length and width. In the case of a complete fibre bundle these results imply higher bundle permeability in

the through thickness direction compared to the in-plane transverse permeability. Figure 61 illustrates that, due to the reduction of the filament mobility, the scatter in absolute permeability values at a given model size decreases significantly with increasing V_f. Unlike in Figure 50, the permeability values are predominantly smaller than Gebart's model predictions [49] for ideal uniform filament arrangements. The horizontal scatter in Figure 61 is a result of the micro-structure generation process (Section 3.5). A deviation from the target V_f is inevitable due to the scatter of V_f observed (Section 3.4.5) and for the model generation a scatter of ±1% was allowed. With increasing model size scatter decreases. This indicates that in a model with multiple randomly arranged filaments, which can be described as a network of flow channels in series and in parallel, the characteristics of flow channels in series always dominate. This is in contrast to a randomised hexagonal unit cell, where flow channels in parallel can also dominate the fluid transport (Section 4.2.1). These results suggest that the local permeability cannot be estimated based on the V_f only and the actual filament arrangement has to be taken into account.

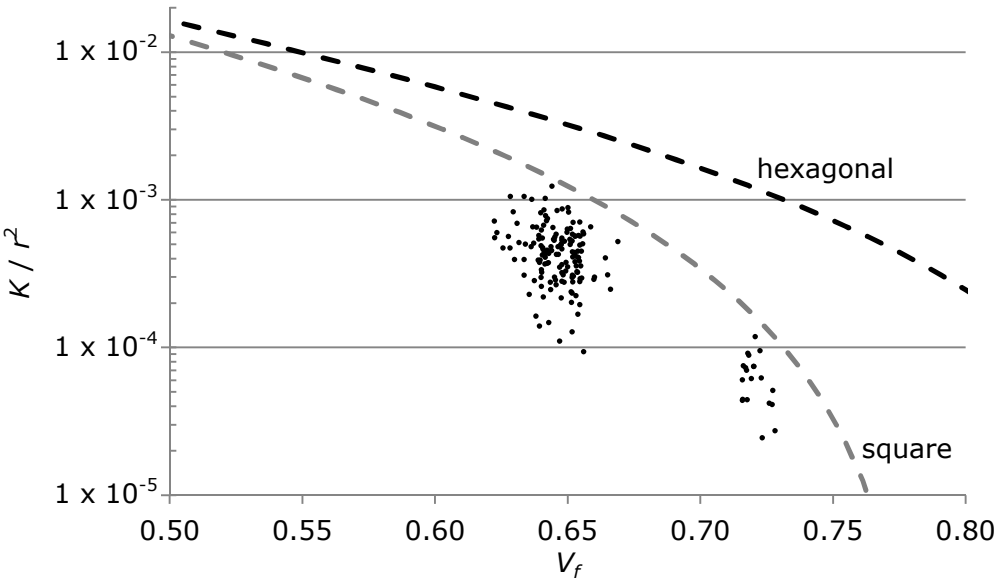

Figure 61: Numerical results (dots) for the transverse permeability, K, of a model with random filament arrangement (dimensions l/r = 21) as a function of the fibre volume fraction, V_f. The values are normalised by the fibre radius, r and compared to the analytical solution (dashed lines) based on Gebart's equations for a hexagonal and square filament arrangement.

4.3.3 Local flow velocity distribution

The results for steady state flow suggest that low flow velocities could indicate probable zones for dry spot formation in transient unsaturated flow. From the evaluation of the maps of flow velocity magnitudes, e.g. Figure 48 and Figure 53, it can be seen that the highest flow velocities during steady-state (saturated) flow are present in channels formed in between filament clusters. Outside these channels the flow velocity is low, suggesting that only a small amount of fluid transport is happening in these zones.

In order to quantify these observations, the simulated local flow velocity fields were analysed for the models with non-uniform filament arrangements. Since unstructured meshes with local refinement are used for the simulations (Section 4.1.2), the areas of the triangular 2D finite volumes are heterogeneous. Therefore, the velocity calculated for each finite volume was weighted by the respective area for generation of the velocity distribution. The typically very wide distributions of the local flow velocities were plotted logarithmically for improved clarity. In addition, the histograms in Figure 62 and Figure 63 were normalised by the total model area to obtain probabilities, which are independent of the model size or the number of finite volumes in each velocity interval.

Figure 62 shows velocity distributions for three different randomised hexagonal unit cells at V_f = 0.60 as discussed in Section 4.2.1. The filament arrangement Figure 62A is almost perfectly hexagonal and has a permeability close to the ideal theoretical value, whereas Figure 62B and Figure 62C show examples of arrangements with higher and lower effective permeability, respectively (compare with Figure 48). For the almost ideal hexagonal arrangement, the resulting velocity distribution shows one major peak. A second minor peak at lower velocities is thought to be related to reduced velocity near the stagnation points on both sides of the filament and the applied no-slip boundary conditions on the filament boundaries. Presence of a single peak in the distribution indicates that the flow velocity is identical in both (horizontal) flow channels in the unit cell. Since there is no preferential flow path, the probability for void formation in impregnating flow is considered marginal.

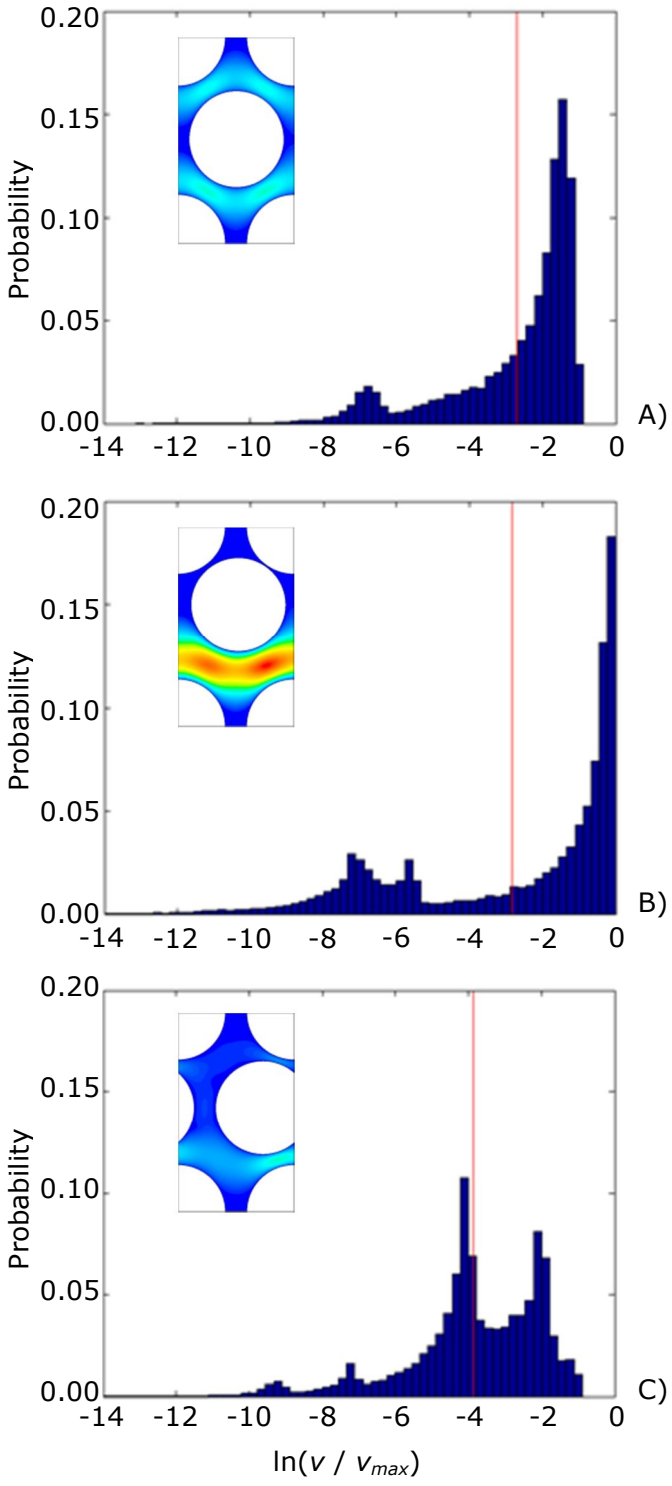

Figure 62: Histograms for the distributions of the flow velocity, v, normalised by the maximum observed velocity, v_{max}, for transverse flow (pressure gradient from left to right) through randomised hexagonal unit cells at V_f = 0.60, expressed as $\ln(v/v_{max})$.

The permeability for the arrangement in Figure 62B is significantly higher than for a perfectly hexagonal arrangement. The centre filament is displaced mainly along the *y*-direction. As a result, the width of one of the flow channels which are in parallel is increased significantly, while the width of the other channel is reduced. Flow through the filament arrangement is dominated by the wider of the two parallel channels, which results in a lower resistance to transverse flow compared to the case in Figure 62A. However, the uneven distribution of flow through the two channels results in the presence of two peaks in the velocity distribution. The low flow velocity zone in the upper half of the cell is suspected to indicate an area of probable void formation during impregnation.

In the example in Figure 62C the centre filament is displaced mainly along the *x*-direction, resulting in a reduced width of both parallel flow channels and in a reduced permeability compared to the ideal case. The flow velocity distribution shows two distinct peaks, reflecting flow at different velocity through the two major flow channels. The fact that these two peaks are relatively close to each other, suggests however, that the probability for void formation during impregnation is reduced compared to the case in Figure 62B.

Analysis of the local flow velocity field in larger models with random filament arrangements (Figure 53) indicates that most of the fluid flows through a few major flow channels which are formed in between densely packed clusters of filaments. Outside of these channels, the flow velocity is generally very low, suggesting that, during impregnation, hardly any fluid flows into the filament clusters. Similarly, voids may form in zones of low filament density, if they are cut off from flow channels by chains of filaments (as in Figure 53A) with low permeability perpendicular to the local chain axis. In summary, the probability for void formation is thought to be related to differences in local filament density between clusters and channels, and is not only dependent on the average fibre volume fraction, which can correspond to a variety of different filament configurations and permeabilities. For more detailed analysis, distributions of local flow velocities were determined at different effective permeabilities (at given example model size 25 μm × 25 μm). The model in Figure 63A has higher permeability, which is mainly a result of the presence of a major flow channel. In addition, a large filament cluster with low flow velocity is present, suggesting that the probability for void formation in this zone is high. As in the examples in Figure 62B and Figure 62C, the corresponding flow velocity distribution shows distinct peaks, reflecting the presence of zones with different flow behaviour.

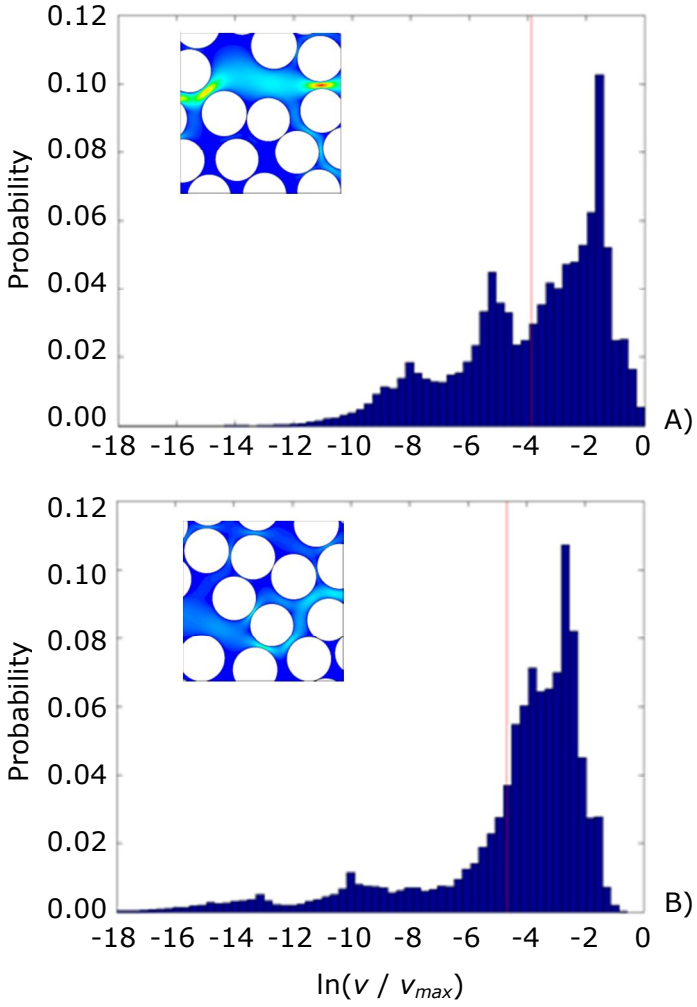

Figure 63: Histograms for the distributions of the flow velocity, v, normalised by the maximum observed velocity, v_{max}, for transverse flow (pressure gradient from left to right) through random filament arrangements at V_f = 0.63 ± 0.03, model size 25 μm × 25 μm, expressed as ln(v/v_{max}).

The model in Figure 63B has lower permeability. The majority of local fluid velocities are more evenly distributed, resulting in one major peak in the velocity distribution. However, the distribution is wider than that for Figure 63A, and there are two minor peaks at lower velocities. It can be speculated that the width of the distributions reflects differences in local inter-filament gap width and is an indicator for the probable void content. If a distribution is narrow, the flow velocity is similar in all inter-filament gaps in the model, and the probability for void formation is low, even if the velocities are consistently low. For a wide distribution, local flow velocities differ significantly, and the low velocity tail of the distribution might indicate the propensity for void formation. The width of the distribution alone, however, is not necessarily the primary indicator for void prediction. The occurrence of peaks and their relative distance from each other may be equally important, since the height of the peaks in the distributions is

related to the size of the zone with the respective flow behaviour (Section 5.4.4). This would lead to the conclusion that for the case in Figure 63A, occurrence of large voids in two zones can be expected, while Figure 63B would show small voids in two zones. An increase of the model domain will lead to an increase in the number of peaks (Appendix I) and eventually the distributions will convergence similar to the permeability values (Section 4.3.2).

4.3.4 Influence of filament clustering

The RVEs employed in this work for the analysis of transverse flow through random filament arrangements were generated based on the method described in Section 3.5. The utilisation of measured inter-filament distance distributions to the *n*-th nearest neighbour (Section 3.4.7.2) and corresponding angle distributions under which this neighbour is located (Section 3.4.7.3) made it feasible to reconstruct actual fibre bundle micro-structures. Changes in the micro-structure based on different amounts of compaction of the fibre bundles (increase in V_f) were reflected in changing distributions. Systematic modification of these distributions at constant V_f results in smaller or wider gaps between closest filaments. This is equivalent to an increase or decrease in filament clustering. This fibre clustering may occur during the injection process due to filament movement. Large injection pressures can lead to bundle movement which will also lead to filament rearrangement. Larger flow channels can form, leading to an increase in permeability.

Keeping the location and threshold parameters of the measured log-normal distributions constant (Figure 64), a variation of the scale factor leads to a change of the distribution height (Appendix D.4). This effect is similar to a variation of standard deviation in a normal distribution. The scale parameter for the first four closest neighbour distributions was changed by adding or subtracting 20 % of the originally observed value. For enhanced visualisation, the distribution values are normalised with the average measured filament diameter, d_{avg}, of the analysed sample.

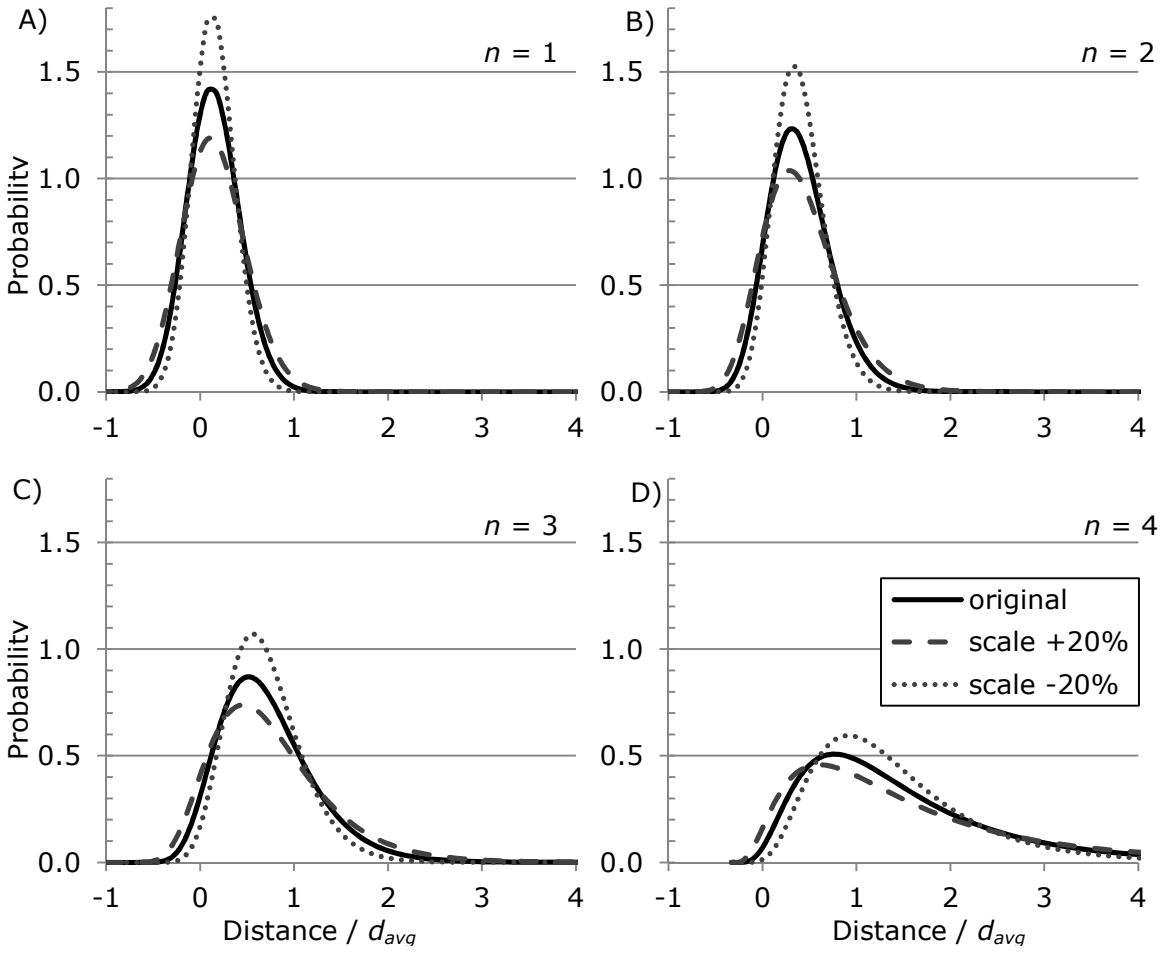

Figure 64: Influence of the scale factor variation on the lognormal distribution of the *n*-th neighbour distances at constant V_f = 0.63. The originally measured distributions are shown with solid lines and the distributions with an adjusted scale factor by ±20% are shown as dotted lines.

With a reduction of the scale factor, the distribution's peak value increases and the positive skewness (right sided tail) is reduced. The distribution becomes narrower. This implies that the scatter in distances between neighbouring filaments is decreased. This reduces the probability of larger inter-filament gaps which results in a reduced average permeability compared to the original distributions as shown in Figure 65. An increase in scale factor widens the neighbour distance distributions. The probability of larger channels being formed in between filaments locally is increased. This results in an increased permeability of the micro-structure.

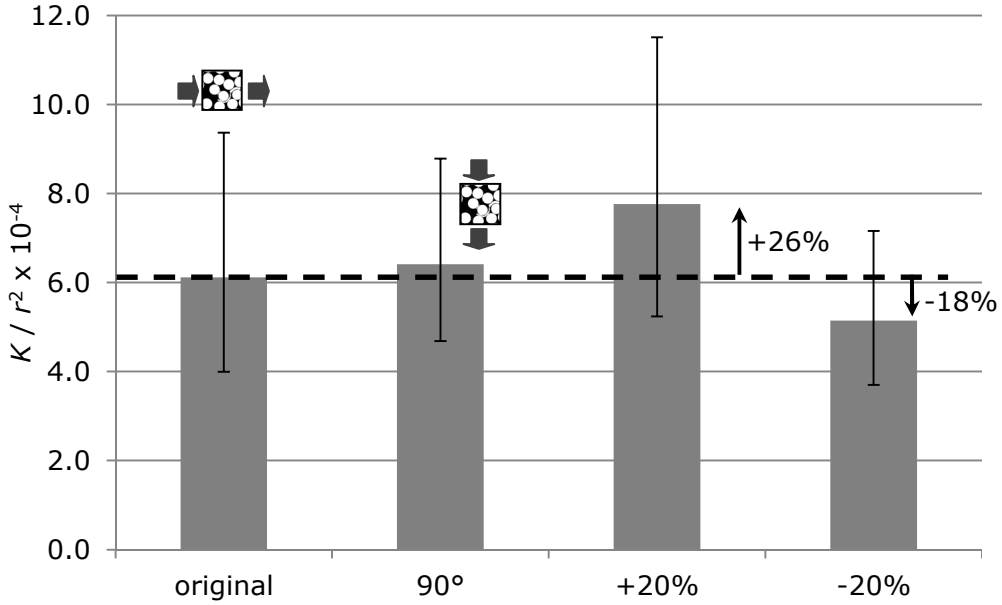

Figure 65: Influence of varying neighbour distributions on the permeability for 30 to 40 models of random filament arrangements at constant V_f = 0.63. The pressure gradient over the square shaped models was applied from left to right. For the original dataset, the permeability was also determined for flow in models with the boundary conditions rotated by 90°.

The filament arrangements studied were generated following the procedure described in Section 3.5. It was shown from the measured angle distributions (Section 3.4.7.3) that data of the analysed V_f = 0.63 exhibited almost perfect randomness. The minor differences present in the average permeability values of the original flow simulations (applied pressure drop from left to right as shown in Figure 41) compared to the simulation result with boundary conditions rotated by 90° (applied pressure drop between top and bottom boundary) are a result of the slight preference for the closest neighbours to be located in the horizontal direction. Effects of systematic variations of the angle distributions were not analysed in this work.

The scatter of the resulting permeability decreases with decreasing scale factor of the distributions. The narrower filament distance distributions result in a more homogenous filament arrangement. The probability of flow channel formation is similar in the generated filament arrangements and therefore the scatter of predicted permeabilities is reduced. This more homogenous filament arrangement does, however, also lead to a decreased average permeability.

The increased scatter in combination with the increased average permeability for filament arrangements generated with a larger log-normal standard deviation of the nearest neighbour distances (scale +20 %) is a result of the wider

distribution of neighbour distances. The probability of larger distances between the filaments results in a higher probability of larger flow channels being formed in the random filament arrangement. This leads to a larger average permeability but also to a larger scatter in observed permeability values.

The systematic variation of nearest neighbour distance distributions enables the estimation of the effects of varying filament arrangements on the resulting permeability. These varying configurations may be present in one composite part within different fibre bundles at identical V_f. These results also suggest that a more homogeneous filament arrangement (reduced scale factor of the distributions in Figure 64) will reduce the scatter present in local permeability values. This results in a more homogeneous velocity field which would be advantageous for the case of impregnating flow in LCM processes. Differences in local flow velocities can lead to air entrapment due to merging flow fronts (Section 2.3.3). A more homogeneous velocity profile within the fibre reinforcement would reduce the probability of void formation. Therefore, it would be advantageous to homogenise the filament arrangement as reflected in the nearest neighbour distance distributions. The more difficult injection as a result of the decreased permeability would be compensated by a decrease in the probability of void formation.

4.4 Conclusions

The permeability transverse to the fibre axis was identified to be more affected by variability in the filament arrangement than the longitudinal permeability (Chapter 2). Therefore the flow transverse to statistically equivalent micro-structures (Chapter 3) was modelled numerically in this chapter. It was demonstrated that the selected inlet - outlet boundary conditions to generate a pressure gradient between opposite model edges were suitable (Section 4.1). The discretisation of the flow domain was implemented in a Matlab® program using an unstructured triangular mesh of finite volumes (Section 4.1.2). The optimal mesh refinement as a function of the gap distance in between filament pairs was identified (Section 4.1.3). It was concluded that a minimum of 15 rows of volumes in small gaps is necessary to result a converged solution. This is substantially more than reported in the literature [57]. Unit cells fail to represent the variability of the random filament arrangement found within fibre bundles and therefore fail to predict the micro-structure permeability (Section 4.2). The observed permeability values for the randomised filament arrangements in RVEs were systematically lower than the analytical predictions based on regular

filament arrangements (Section 4.3). The differences in permeability were up to an order of magnitude. This implies that employing a computational inexpensive regular filament arrangement for the estimation of fibre bundle permeability will result in predicted values that are systematically too high.

Convergence studies of different model sizes, characterised by the ratio of model side length, l, to average filament radius, r, were performed. It was concluded that a l/r ratio of 30 leads to a converged permeability of the micro-structure (Section 4.3.2). This value is significantly smaller than 80 as reported by Yazdchi et al. [57] for transverse flow through artificially created RVEs. The improved discretisation employed in this thesis is thought to be one of the reasons for this significantly reduced model dimension for convergence of the permeability. Their choice to enforce a minimum gap between nearest filaments might be an additional reason for the necessity of larger model dimensions. A similar effect is visible in the increased standard deviation of the simulated permeability values (Figure 65) in the case of an increased skewness (increase in scale factor). This leads to an increase of the distance between closest filaments and therefore to an increased probability of flow channels being formed.

The convergence of the permeability with increasing model size was related to the probability of flow channel formation and the probability that these flow channels are blocked locally by filaments in close contact (Section 4.2.2). This observation was confirmed by flow simulations on rectangular flow domains with varying aspect ratio of the flow length, l, to model width, w (Section 4.3.2). For future work a further reduction of the number of models to be analysed for the prediction of the permeability could be achieved by employing sets of randomised RVEs [70].

The simulation results presented in this chapter describe the fully saturated flow in random filament arrangements. In LCM processes, this type of flow is present behind the flow front. The random filament arrangement will lead to local differences in fluid flow velocities. These varying flow velocities will lead to a variation in the flow front progression for the fluid impregnating the dry reinforcement. It was shown that merging flow fronts can lead to air entrapment and void formation (Section 2.3.3). The voidage formed as a function of the fibre bundle compaction will be analysed in Chapter 5. In addition, the behaviour of the fluid impregnating a dry filament arrangement will be analysed, and the probability of local gas entrapment will be discussed.

5. Simulation and implications of impregnating flow

The presence of micro-scale voids in composite materials has a detrimental influence on the matrix dominated mechanical properties of a part in service (Section 1.3). These voids form due to gas entrapment as a result of varying flow velocities and merging flow fronts in the textile reinforcements during injection of the resin in a LCM process [14]. The differences of local resin flow velocities stem from the fibre preform architecture employed in the manufacture process. Fibre bundles have a relatively low permeability compared to channels formed in between these bundles, resulting in a difference in flow velocities. This effect is amplified by presence of variability in fibre bundle arrangement (e.g. bundle waviness and nesting) [38, 41] and filament arrangement (Section 2.2.4). Capillary effects within fibre bundles present in impregnating flow will have an additional influence on the resin transport [81]. It was hypothesised that results from steady-state flow analysis (Section 4.3.3) could indicate effects which should be expected in the case of impregnating flow.

At the micro-scale, the influence of non-uniformity of the filament distribution on axial and transverse flow is likely to be very different due to the fundamentally different geometry of the flow channels [57, 58]. Therefore, specimens produced by resin injection along either fabric direction were analysed separately to quantify the void content and estimate the influence of the filament arrangement on void formation. The focus in this work is on voidage formed within the fibre bundles only. This type of defect is directly affected by the filament arrangement. Similar to the models analysed in Section 4.3.2 for the case of steady state flow, an attempt is made to simulate the formation of air inclusions by use of numerical CFD analysis in a randomised filament arrangement. These transient flow simulations are then compared to the computational less expensive steady-state flow predictions presented in Section 4.3.3. It is demonstrated that these steady state predictions can deliver information about the transient flow behaviour.

5.1 Specimen and material data

Single layer non-crimp fibre reinforced composite sheets were manufactured employing the same manufacturing process as described in Section 3.4.1. The stiff metallic tool containing the fabric was closed by means of tightening bolts around the mould cavity. The injection strategy was chosen to be linear ensuring the start of injection over the full fabric width at one end of the tool. During the injection process the fabric (Appendix C.1) was saturated with the liquid polymer matrix (Appendix C.2). Air within the fabric was replaced by the resin used for the manufacture of the samples. For analysis of the void content, specimens were produced by axial or transverse resin injection at different global V_f and different injection pressure. The void content was estimated based on the analysis of micrographs following the procedure outlined in Section 5.2.1.

Based on estimated experimental mould filling times, the average resin flow velocity could be approximated as 4.5×10^{-5} m/s for flow transverse to the fibre bundle axis. The corresponding modified capillary number (Section 2.3.3) is therefore about $Ca^* = 2.2 \times 10^{-4}$. This value is in the range of the critical capillary number at which a minimum micro-scale voidage was observed as reported by Rohatgi et al. [14]. Therefore, a low void content was expected to be present within the fibre bundles.

The resin viscosity, μ_f, during injection was estimated from the datasheet based on the ambient temperature (Appendix C.2) and assumed to be constant. The viscosity increase during mould filing at elevated temperature due to the initiated resin solidification process is ignored. For the air viscosity, μ_{air}, the value at room temperature was assumed in the fluid transport simulations (Table 7).

Table 7: Viscosities, μ, surface tension, γ and the contact angle, θ, of the resin used and air present in the manufacture of the unidirectional carbon fibre reinforced composite samples.

μ_f	0.1 Pa·s
μ_{air}	1.79×10^{-5} Pa·s
γ	0.042 N/m
θ	61°

The temperature dependence of the air viscosity is small compared to the change in resin viscosity and therefore ignored in this work. The surface tension, γ, of the air-resin interface (Section 2.3.2) was selected as 0.042 N/m which is in good agreement with values presented in the literature [123]. Contact angles, θ, of 61° to 66° are reported in the literature for the carbon – epoxy interface [124, 125]. The minimum value of 61° was used in this work. These contact angles are similar to the value of 57° as reported for an epoxy E-glass interface [123]. For other resin systems this contact angle can be significantly different [87]. For the transient flow simulations in this work, immiscibility between the resin and gas phase was assumed.

5.2 Void content

5.2.1 Measurement technique

For analysis of the specimens, micrographs of complete fibre bundle cross-sections were taken with the same method described in Section 3.3.1 at predetermined positions to be representative of the entire specimen. The samples were cut transverse to the fibre bundle path over the entire width or length of the specimen. From the casted and polished samples, micrographs of every third fibre bundle were captured and analysed at a magnification of 20x. A total of 8 different composite sheets were manufactured from which a total of 111 fibre bundle specimens were analysed. Due to the three-dimensional geometry of voids, accurate determination of the volumetric void content of a composite from two-dimensional micrographs is not straightforward [86]. In the analysed images, the ratio of resin free area (identified as black areas in Figure 66) and total bundle cross-sectional area is used as the descriptor for the void content. Assuming voidage is randomly distributed throughout the specimen, the measured areal void content will reflect the volumetric void content, V_c, of the entire specimen.

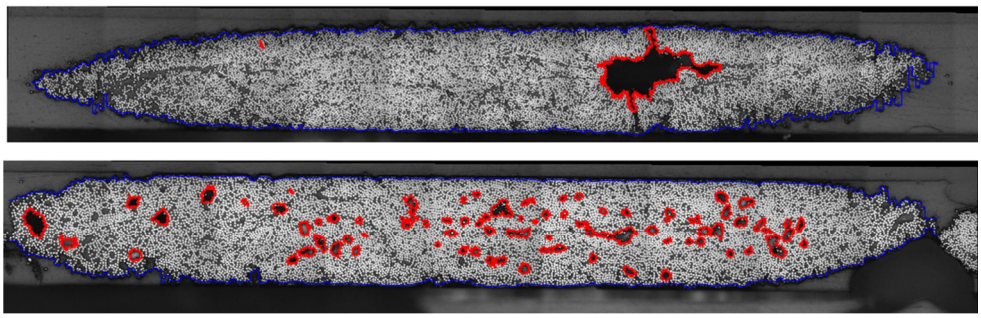

Figure 66: Voidage in transverse flow examples. Depending on the filaments, the fibre bundle boundary marked in blue is determined and the detected voidage is outlined in red. A) One large void formed within fibre bundle and B) a large number of small voids formed.

The resolution of the captured images for the void content analysis in terms of the pixel spacing was estimated to be 0.23 μm for a 20x objective (Eq. 25). Stitching of images made it feasible to analyse complete fibre bundle cross-sections. Rounding effects of the sample edges due to the polishing process resulted in dark shadows around the fibre bundle specimens. These dark boundaries were determined by a simple thresholding operation of the image, initially subjected to image enhancement. This effect lead to an underestimation of the bundle cross-sectional dimensions compared to manual measurements on the specimens. An underestimation of the fibre bundle height, Δh, of 20 μm – 60 μm was determined for the samples analysed in this work (Table 8).

Having identified the sample boundaries, more detailed analysis of the fibre-bundle cross-sections was conducted. On the original image, the contrast was enhanced and speckle noise removed. Voids cannot reflect light and they appear as black areas in micrographs (Figure 67A). Accumulation of debris, remaining filaments in the resin free areas or shallow voids can, however, lead to slight light reflections (Figure 67B). Simple thresholding techniques as proposed in the literature [16] can, therefore not be employed for the automated identification of voidage. It was observed, however, that all these objects exhibit a distinct dark perimeter enclosing the void area. Exploiting this observation, objects exhibiting a distinctive dark boundary were identified as voids.

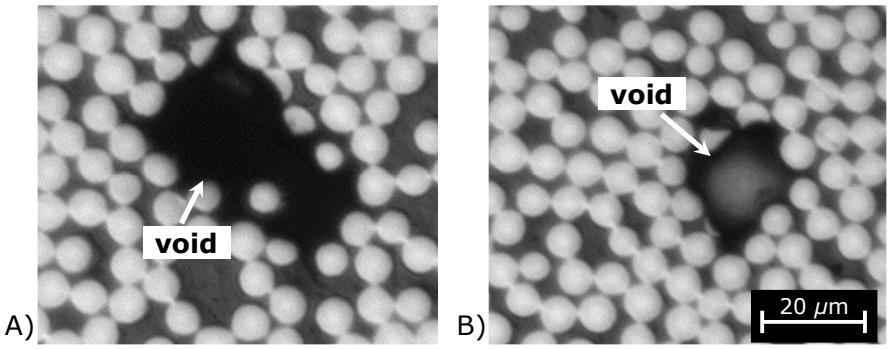

Figure 67: Micrographic examples of intra-bundle voidage. A) Void appearing as black area in the image. B) Void showing bright centre area enclosed by a dark boundary.

The procedure described above was implemented in a Matlab® code, allowing automated analysis of the void content (Appendix J). For the 111 analysed fibre bundles, a total number of 2314 voids could be identified. The exact quantification of this voidage allowed further detailed analysis.

5.2.2 Void content analysis

Image processing of the captured micrographs enabled the quantification of the void content of the analysed specimens. The results are listed in Table 8. Samples were produced at different injection pressures, p_{inj} = 1 bar to 3 bar, effectively varying the resin velocity. The fabric was aligned so that the resin flow was parallel or perpendicular to the fibre bundle axis (longitudinal or transverse). Sealant was applied to prevent flow along the edges of the tool (race tracking).

Table 8: Void content in fibre bundles (sheets impregnated in uni-directional flow parallel or transverse to fibre bundle axis); global fibre volume fraction, V_f, based on the measured specimen thickness, h, underestimation of image processing, Δh, injection pressure, p_{inj}, number of voids per fibre bundle, N_v, average size of voids (characterised by area in cross-section), A_v, void content, V_c, in terms of percentage of bundle cross-sectional area.

	V_f	h sample mm	Δh mm	p_{inj} bar	N_v	A_v x10^{-4} mm^2	V_c
transverse	0.45	0.37	0.06	1	24	5.56	2.7 %
	0.46	0.36	0.04	2	19	12.34	2.9 %
	0.51	0.33	0.01	2	12	30.61	1.7 %
	0.52	0.32	0.03	3	10	2.58	0.2 %
	0.62	0.27	0.02	2	93	2.61	4.0 %
longitudinal	0.44	0.38	0.05	2	1	8.15	0.2 %
	0.45	0.37	0.06	1	18	8.67	1.9 %
	0.62	0.27	0.02	2	34	2.72	1.6 %

The V_f of the composite sheets was controlled by adjusting the cavity height, h. The measured thickness of the manufactured plaques was used to calculate the effective V_f following (Eq. 30). It was observed that the void content increased towards the vents of the moulded specimen as predicted by Park et al. [8]. However, a residual void content was found in all specimens independent of the sampling position and the differences were not significant. It was found that the measured data are not normally distributed but positively skewed (Appendix K). The results of the measured V_c and N_v as function of V_f are plotted in Figure 68. The data for the transverse flow experiments are depicted as diamonds and the results for injections along the fibre bundle axis are displayed as circles. Different injection pressures employed are represented by different shades of grey. A total of 8 categories with varying production parameters (V_f and p_{inj}) were analysed containing 111 specimens.

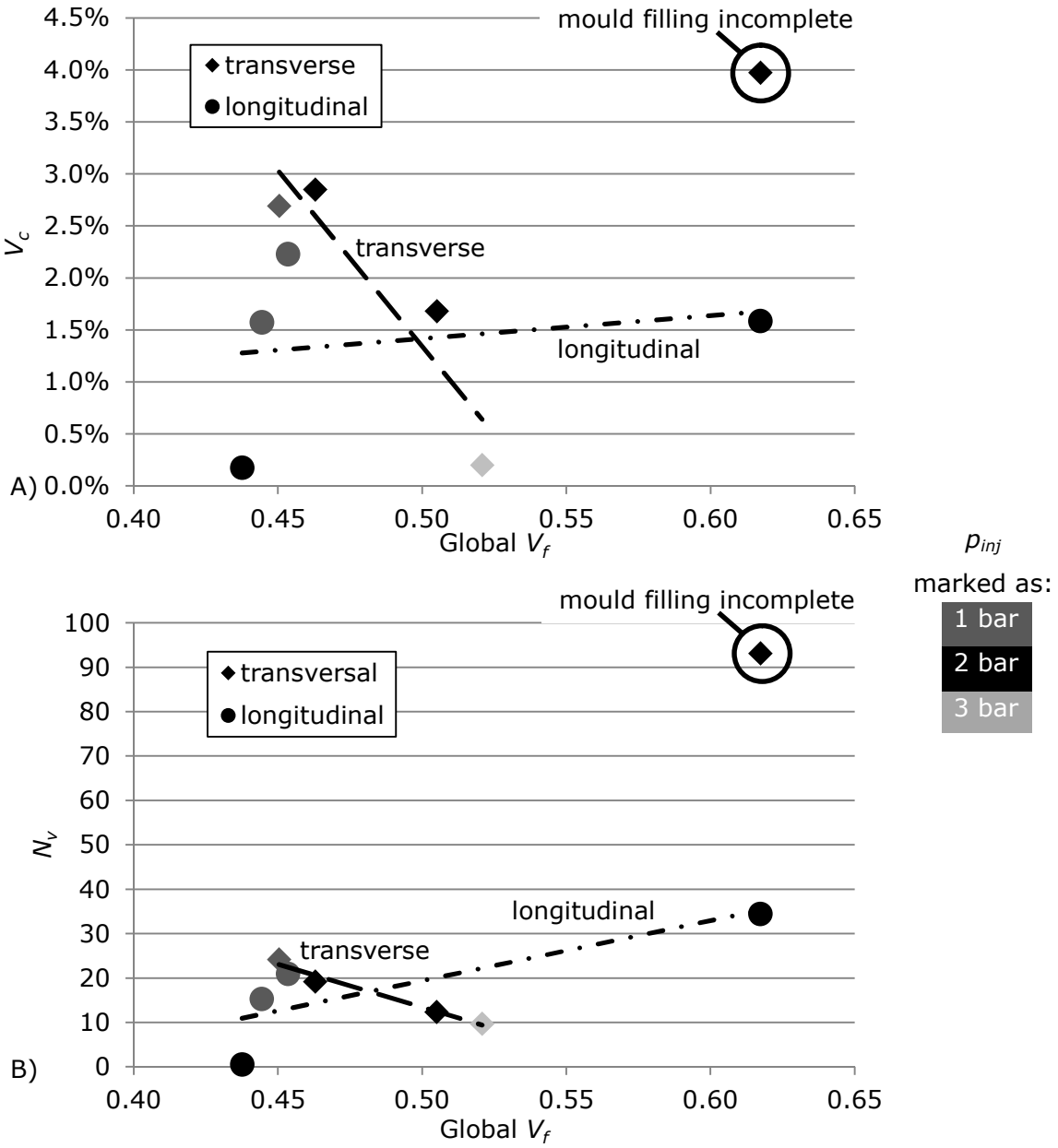

Figure 68: A) Void content, V_c, and B) the number of voids, N_v, as function of the fibre volume fraction, V_f. The data points are coloured in greyscales according to the injection pressure used. Trends are visualised with straight dashed and dash-dotted lines, fitting the transverse and longitudinal measurement data respectively, disregarding p_{inj} and the outlier marked in the graph for transverse flow.

The number of analysed samples was limited and produced under varying processing conditions, e.g. varying injection pressures. Therefore it is unfeasible to derive generally applicable trends and conclusions of the effects of compaction on void formation. The analysis of the data will provide therefore more of a qualitative idea about probable trends. To gain more confidence in the conclusions drawn further investigation is required.

For the transverse flow experiments a linear decrease of the resulting V_c with increasing V_f can be observed, regardless of injection pressures and ignoring the outlier at V_f = 0.62 and V_c = 4.0%. This outlier is a result of a partial mould (approximately 30 %) filling during injection due to the relatively high V_f within the mould and the low transverse permeability of the fibre bundles. This suggests, that the effect of the partially saturated region present behind the flow front [24, 87] has been measured in this case and, therefore, this value is ignored.

The resulting trend suggests that in transverse flow, the decrease in void content is caused by a more homogeneous micro-structure at increased V_f. This observation is supported by the decrease in the number of voids with increasing V_f (Figure 68B). The increase in order of the filament arrangement with increasing compaction of the fibre bundles is supported by the analysis of the micro-structure in terms of nearest neighbour distances (Section 3.4.7.1) and angles at which these neighbours are located (Section 3.4.7.3). There is an increase in the average void area, A_v with decreasing V_f (increasing h), reflecting the more significant non-uniformity within a fibre bundle at a lower V_f (Table 8). If the fibre bundle is compacted, the filament arrangement becomes more uniform and the average void area decreases. The linear trend of the measured data of the V_c suggests that a critical $V_f \sim 0.55$ exists eliminating the voids formed in transverse flow completely. This decrease coincides with an overall decreased permeability which makes complete mould filling more challenging. Manufacture of samples in transverse flow at high V_f with the employed production parameters was therefore not possible in this work. The influence of the injection pressure on the void formation in transverse flow is not apparent from the limited amount of samples studied. Additional transverse flow experiments need to be conducted to confirm these deduced trends.

In longitudinal flow, V_c and N_v decrease with decreasing V_f (Figure 68). The typical void size increases (Table 8), which suggests merging of micro-scale gas inclusions during the injection process. This observation was made for experiments at constant p_{inj}. V_c and N_v increase with decreasing p_{inj} at nearly constant V_f ($\sim$ 0.45) while the average void size is approximately constant. An opposite effect would have been expected if dual-scale flow in between and within fibre bundles had a major effect at the given V_f and injection pressures. It was suggested that a reduction in flow velocity (decrease of p_{inj}) should improve the flow within fibre bundles due to the increasing influence of capillary

pressures (Section 2.3.3). This would lead to a reduction of intra bundle voidage which is not the case in the analysed samples. The obtained data suggest that the increased permeability of the filament arrangement at a decreased V_f outweighs the effects the more heterogeneous filament arrangement. This leads to a decreased V_c compared to samples produced at higher V_f. The increased order of the filament arrangement within the fibre bundles at higher V_f (Sections 3.4.7.1 and 3.4.7.3) will result in a more homogeneous velocity field of the impregnating resin which reduces the probability of air entrapment. This, however, coincides with a reduced permeability of the filament arrangement resulting in an increased V_c. As for the transverse flow experiments, additional experiments are required in order to verify and generalise the observed trends.

At low V_f a tendency to obtain lower V_c can be observed for longitudinally aligned fibres compared to transversely aligned fibres due to the increased permeability. The trend lines fitted to the measurements in Figure 68 indicate that experimental results from longitudinal flow are contrary to the results of transverse flow. A decrease in permeability with increasing V_f leads to a larger void content in flow parallel to the filament axis. For flow perpendicular to the filament axis the decrease in permeability is accompanied by a more homogeneous micro-structure resulting in lower void content at increased V_f. Since the number of analysed combinations of parameters was limited to a total of 8 containing 111 specimens, further investigation is required to gain more confidence in the measured data and the deduced trends.

5.3 Transient flow model set-up

During a LCM process, the liquid polymer matrix impregnates the fibre reinforcement. The position, shape and advancement of the resin flow front depends on the time, t. Employing CFD simulations, these mould filling processes can be simulated. The key concept of CFD is the discretisation of the governing equations over all finite control volumes of the flow domain (Section 4.1.2). Integrating these discretised equations will ensure compliance with the mass and momentum conservation principles [126]. For numerical simulation of the fluid transport, an explicit or implicit time integration scheme can be utilised. Based on the initial conditions given at t_0, both schemes estimate the solution at any time, t_i, employing different techniques.

5.3.1 Model selection and solution method

The explicit scheme calculates the state of the system, u, at time, t_{i+1} based on the current time, t_i, only (Eq. 34). A set of linear equations, f, for each time step has to be solved based on known quantities from the previous time step, simplifying the solution [127]. The time step, Δt, has to be chosen to be small enough to guarantee a stable solution which, however, can mean that a large number of time steps are required.

$$u(t_{i+1}) = u(t_i) + \Delta t \cdot f(u(t_i)) \quad \text{Eq. 34}$$

The stability of the solution solving the partial differential equations for modelling of transient fluid transport can be evaluated by analysing the dimensionless courant number, λ:

$$\lambda = v\frac{\Delta t}{\Delta l} \quad \text{Eq. 35}$$

In the case of transient flow simulation, this number describes the ratio of the distance of fluid propagation per time step, Δt, to the finite flow length, Δl, at a given velocity, v. When employing a discretisation of the model domain, this number will give information about the number of volumes or elements the fluid is transported per time step. For the evaluation of explicit modelling schemes, the Courant-Friedrich-Lewy condition (CFL) is employed as a stability criterion for the choice of the time step (Eq. 36). Usually the maximum allowable λ_{max}, is selected as 1 for achieving a stable solution [127]. Employing a fixed grid, the time step has to be adjusted to satisfy this condition accordingly.

$$0 \leq \lambda \leq \lambda_{max} \quad \text{Eq. 36}$$

The implicit scheme determines the solution, taking the current and a future time into account (Eq. 37). A set of coupled linear equations, f, has to be solved, approximating the solution for the future time step including unknown function values. This set of equations can be quite large compared to the single step explicit scheme [127]. However, many implicit schemes are unconditionally stable and the solution can be achieved in fewer time steps (λ_{max}>1). The limiting factor for the choice of the constant arbitrary Δt are the associated truncation errors only [127]. In the current work, explicit and implicit schemes have been compared.

$$u(t_{i+1}) = u(t_i) + \Delta t \cdot f(u(t_{i+1})) \qquad \text{Eq. 37}$$

Transient flow simulations of explicit or implicit time advancing schemes of two immiscible fluids are offered by available CFD software packages. Tracking of the liquid-gas interface at the micro-scale should enable the prediction of micro-scale void formation. During the progression of the resin flow front, the pressure and velocity field are approximated at every time step. The method to solve the discretised non-linear equations by means of CFD is achieved by iterations and linearization considerations following the following steps [127]:

Step 1: Estimate the current best approximation (e.g. initial conditions) for the velocity and pressure field.

Step 2: Solve the discretised linearised momentum equation iteratively for the approximation of the intermediate velocity field.

Step 3: Estimate the new pressure field based on the intermediate velocity field.

Step 4: Update the velocity field by the new pressure field.

Step 5: Check convergence of the mass and momentum conversation equations and repeat at Step 1 if necessary.

Steps 1 to 5 are repeated for every time step until the necessary accuracy of the solution is achieved. For the start of the simulations initial conditions are specified for Step 1. Updated values are subsequently used after each iteration. Step 2 involves the solution of the discretised and linearised Navier-Stokes equations (Appendix A.2) on the model domain. An intermediate velocity is estimated, however, incompressibility considerations are not satisfied because the pressure field adjusts instantaneously to any change [127]. The pressure field is updated in Step 3 which in turn is used to update the velocity field in Step 4. The convergence of the solution is finally checked (Step 5) and if the desired accuracy is not achieved, the process is repeated at Step 1. The fluid progression of the different phases present in the model is determined by the flow velocities at the flow front. This consideration enables the prediction of the exact shape of the flow front. The iterations of Step 1 to 5 are solved in the so called outer loop. In addition, every single step can involve iterations for the estimation of a specific term. These iterations are solved in inner loops.

The progress of the liquid resin penetrating the filament arrangement is simulated here employing the commercial CFD software Ansys Fluent®. An overview of the employed methods can be found in Table 9 and Appendix L. The choice of the Volume of Fluid (VOF) modelling approach [128] enables the solution of transient flow of two immiscible phases.

Table 9: Transient model settings used in Ansys Fluent®

Model:	pressure -based multiphase (VOF)
Pressure and velocity solver:	PISO
Spatial discretisation:	Green-Gauss Cell based gradient
	Pressure: PRESTO!
	Momentum: 2nd order
	Volume fraction: Compressive

The segregated solver for the pressure and velocity coupling PISO (Pressure Implicit with Splitting Operators) was utilised [128]. This solver ensures the conservation of mass while estimating the current state of the pressure field of the system in Step 3. The pressure field is approximated by simplifications of unknown functions in the system of linearised equations. The PISO scheme adjusts for these simplifications by employing corrector steps. A detailed description can be found in the literature, e.g. [126, 127].

The pressure discretisation is achieved by the PRESTO! (PREssure STaggering Option) scheme. This scheme solves the pressure equation on a virtual staggered grid to avoid numerical anomalies which can be present when solving the velocity and pressure at the same nodal points [126]. Figure 69 illustrates an example of a quadrilateral staggered grid. Scalar values (e.g. pressure) are evaluated at the cell nodes of the staggered grid, marked as dots. Vectors such as velocity are solved on the cell faces of the original volume elements marked as grey square. The use of this virtual (co-located) mesh does imply the need of larger computational power. For larger domains an increased amount of memory would need to be provided. In this work 16MB of memory were found to be sufficient.

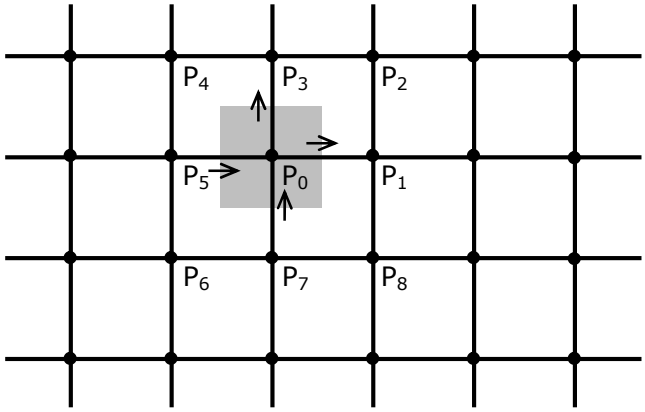

Figure 69: Example of a regular quadrilateral volume mesh with nodes P_i indicated. A volume cell is shown as grey shaded area. In numerical CFD simulations scalars are estimated at the nodes of the staggered grid (circles) whereas cell velocities (vectors) are evaluated at the cell faces of the initial volume elements indicated by arrows.

The iteration values for every iteration step are stored at the cell centres of the discretised domain. For the determination of interactions between neighbouring cells (e.g. mass convection), knowledge of the cell face values is required [128]. The Second Order Upwind scheme is selected in this work to estimate the cell face values on the basis of the stored cell centre value. The Upwind approximation interpolates the data in the direction of flow (upstream) [127].

Connectivity between the discretised volumes is determined by the selected gradient scheme. Here the Green-Gauss cell based scheme is chosen, specifying the relation of the control volume faces to the complete volume. Employing this scheme determines the face value as the simple arithmetic average between the values of neighbouring cell centres [128]. The geometrical shape of the flow front is determined by the Compressive Spatial Discretisation scheme for the volume fraction. This scheme ensures balancing of the convection terms at the cell faces with the cell value of the volume, specified at the cell centre [128].

The pressure and velocity equations to be solved during the numerical flow analysis are nonlinear. Therefore, large changes can be present depending on the selected time step. Under relaxation factors (URF) are introduced for different variables and equations, limiting the maximum change of the function or term during every iteration [127]. This reduces the probability of possible numerical artefact formation such as oscillation. The simulation is stabilised by minimising the allowable maximum change during every iteration which leads to a converged solution [128].

5.3.2 Boundary and initial conditions

For the fluid transport simulations through a reconstructed filament arrangement (Section 3.5), the material properties listed in Table 7 were used. The flow domain is initially assumed to be filled with the gaseous phase only (Figure 70). Hence, the volume fraction of the air, V_a, is set to 1 and the volume fraction of the resin, V_r, is 0 for each finite volume in the model domain at t_0.

Boundary conditions as shown in Figure 70 were applied. As inlet condition, a constant flow velocity was selected for the fluid entering the domain. The inlet velocity, v_{in}, was estimated from average mould filling times of transient flow experiments (Section 5.1). The outlet boundary was chosen as pressure outlet. The selected outlet pressure, p_{out}, of 0 guaranties a pressure gradient over the flow length, l, and ensures fluid transport through the model. The walls parallel to the main flow direction were selected as impermeable frictionless walls similar to the conditions used in the steady state case (Section 4.1.1). The filaments were assumed to be impermeable and no-slip boundary conditions were applied.

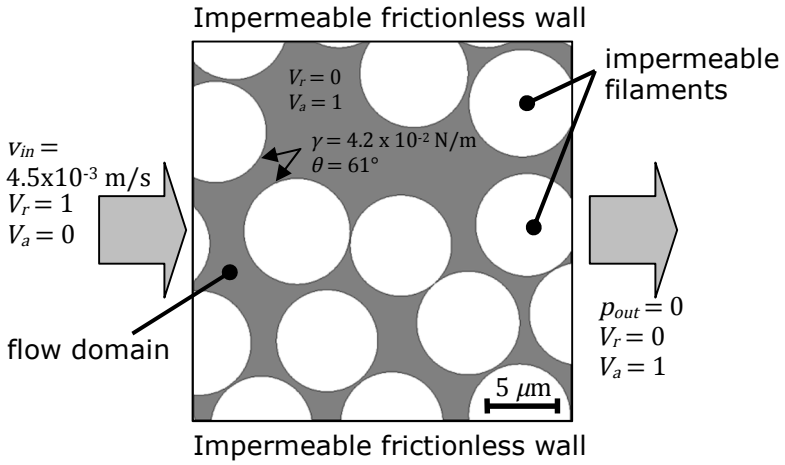

Figure 70: Boundary and initial conditions of transient impregnating resin flow into a filament micro-structure. A velocity, v_{in}, is specified as inlet boundary condition and the pressure at the outlet, P_{out} is assumed to be 0. The volume fraction of the fluid, V_r, is set to 1 at this boundary, whereas the model domain and the exit boundary condition are filled with air, V_a = 1. The specified surface tension and contact angles are indicated for one filament pair.

Capillary effects have to be considered in the model due to the small Ca^* present (Section 2.3.3). These effects are treated as additional stresses at the wall surfaces and are added to the momentum equation (Appendix A.2) in Step 3 (Section 5.3.1) by the CFD software Ansys Fluent®. Due to the technique of determining pressure gradients in case of surface tension the use of a quadrilateral mesh is required [128]. Therefore it was chosen to disregard the

locally refined triangular mesh employed for steady state analyses (Section 4.1.2). The flow domain was discretised using an unstructured quadrilateral grid utilising Abaqus CAE®. The use of an unstructured grid enables local refinement of the mesh. The numerical solution becomes, however, more difficult compared to a mesh with constant element size [127]. In analogy to the steady-state simulations discretisation of the impermeable filaments was not necessary. The filament arrangements employed in the transient flow simulation were generated following the procedure described in Section 3.5 and 4.3.1.

5.4 Transient modelling results

5.4.1 Channel flow

The validity of the selected methods for the simulation of transient fluid flow was initially tested on a simplified model geometry. This model consisted of a single filament located in a rectangular channel as depicted in Figure 71. This simple model geometry was discretised using approximately 2000 equally sized quadrilateral elements, resulting in 11 elements present at the smallest gap between the filament and the model boundaries. Based on the mesh sensitivity study conducted for the case of steady-state flow (Section 4.1.3) this number of elements was initially selected. In future work it is necessary, however, to repeat the mesh sensitivity study for the case of transient flow. The shape of the flow front was evaluated to validate the selected model settings. Initially, the flow front progressed in a straight line before touching the filament. The impermeable frictionless boundaries parallel to the flow direction did not interfere with the shape of the flow front. After the fluid made contact with the filament, a parabolic flow profile developed.

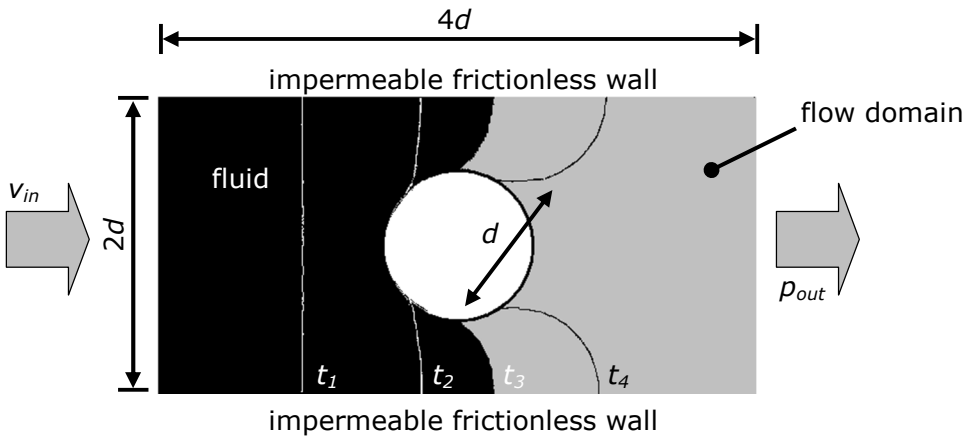

Figure 71: Transient flow in a channel with a single filament located in the centre. A pressure gradient is applied from left to right as driving force. The horizontal boundaries are no-slip symmetry boundary conditions with the explicit modelling scheme applied. The fluid is depicted in black and the flow domain is shaded in grey. The flow front positions are indicated at different times, t_i.

The shape of the flow front developed as expected for this model [49]. It was therefore concluded that the selected model settings are applicable. Employing these settings, transient impregnating flow through a network of filaments can be modelled employing the selected numerical CFD analysis.

5.4.2 Flow in randomised filament arrangement

In the simulation of transient impregnating micro-scale flow, the densities of the two phases were considered to be constant due to the low flow velocities involved. The pressure field in the entire flow domain adjusts instantaneously to any local change in pressure [127]. Capillary forces are treated as pressure discontinuities across the fluid flow front [128]. This leads to an increased number of iterations to satisfy the convergence criteria for the outer and inner loops (Section 5.3.1). The shape of the flow front near the filament boundaries is adjusted according to the contact angle specified.

The influence of capillary effects during impregnation can be evaluated by analysing the resulting shape of the flow front in between a filament pair. Figure 72 illustrates the pressure driven transient flow simulation of a fluid through a gap with width, w_g, formed in between two filaments with radii r_1 and r_2 at different times, t_i. With decreasing local channel width between the filaments the hydraulic diameter (Section 2.3.2) reduces and the capillary pressure increases. The flow front shape in the gap between two filaments is concave as a result of the surface tension at the fluid-gas interface (Figure 72A-C). The shape of the flow front becomes convex after passing through the small gap formed between the filaments illustrating the limited influence of the surface tension (Figure 72D).

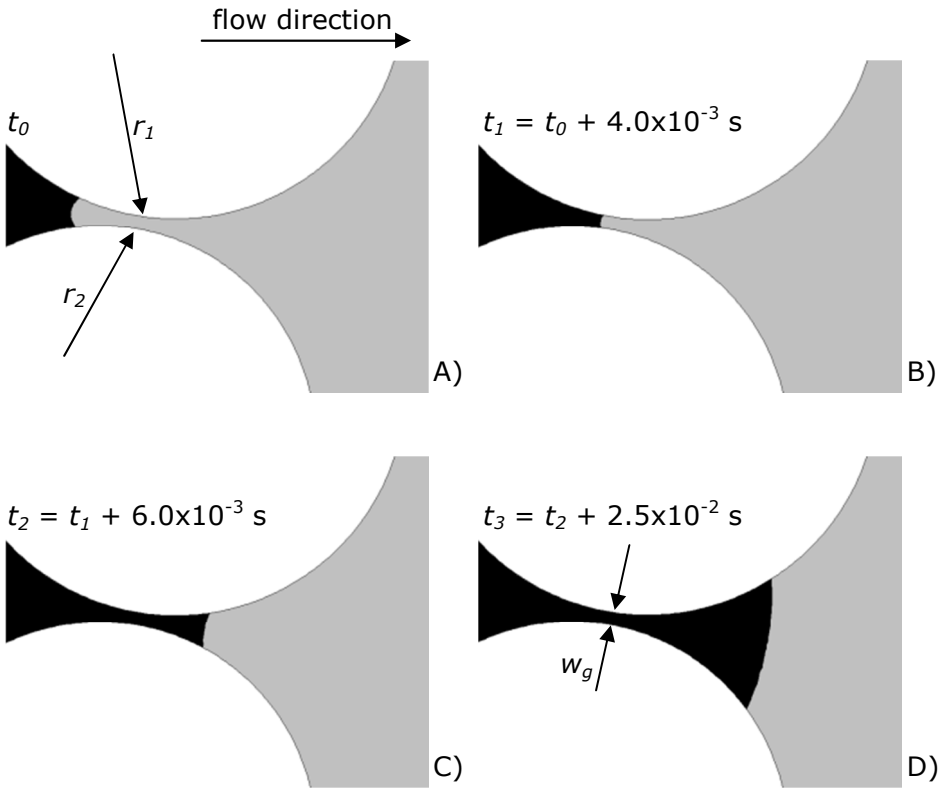

Figure 72: Effect of surface tension on the impregnating flow at constant inlet velocity though a small gap, w_g, in between two filaments with radius r_1 and r_2 at different time steps, t_i. The area occupied by the fluid is marked in black and the space in between the filaments is shaded in grey. A-C) Capillary effects dominate the flow between the filament pair, visible as concave shaped flow front. D) The driving pressure defines the shape of the convex flow front.

The quadrilateral mesh used in the transient flow simulations for the example shown in Figure 70 consisted of approximately 117000 volume elements with similar size. The number of elements was determined by the need of a sufficiently fine discretisation in the majority of the flow domain. Local mesh refinement, as used previously to reduce the total number of elements (Chapter 4), could be implemented in future work after demonstrating the applicability of the CFD analysis.

The iterative solution was considered convergent if the imbalance of the conservation equation (residuals) due to the discretisation procedure for the velocity and volume fraction was less than 1×10^{-3} [128]. For the implicit modelling scheme, a fixed time step of 1×10^{-6} s was selected (Table 10). This time step was small enough to satisfy the selected convergence criterion of the simulation over a limited number of iterations. For the explicit modelling scheme, the time step was selected to be variable, according to the CFL condition (Eq. 36). Initially, v_{max} was set to 1, and after a number of iterations it was changed to

2 in order to decrease simulation times. The increase of the CFL condition is, however, associated with a larger error and potential simulation instability. The necessity of including capillary effects increased the simulation times significantly compared to models ignoring this effect. For the explicit and implicit modelling approach this lead to calculation times of 74 and 77 days for the simulation of one second of flow utilising a quadratic model with a flow length of 25 μm on a computing cluster employing 8 CPUs.

Table 10: Employed settings for the under relaxation factors (URF) and time step, Δt, of the transient impregnating flow simulations utilising the explicit and implicit modelling scheme.

	Explicit	Implicit
URF:	Pressure = 0.6	Pressure = 0.6
	Momentum = 0.6	Momentum = 0.6
Δt:	Variable based on CFL condition (λ_{max} = 2)	1 x 10^{-6} s

It was found that during the numerical simulation of the fluid transport numerical anomalies were created for the implicit and explicit modelling scheme. Zones completely occupied by fluid (Figure 73A) exhibit gas inclusions at a later time step (Figure 73B). These bubbles do not stem from air entrapment as result of merging flow fronts and it could be identified that these inclusions are numerical anomalies only. A number of reasons could cause these phenomena. Poor convergence of the solution during the iterative process could result in these artefacts. Even though the time step was chosen to be small for the implicit model, a further reduction might be necessary. The explicit time step was selected to be variable, ensuring the CFL condition to be valid. The time steps determined automatically were in a similar range as the selected implicit time step. Considering the larger time step possible for the implicit modelling scheme indicated that the selected constant time step was justified.

It was observed that the fluid transport in small gaps in between filaments occasionally lead to flow front separation and the formation of numerical artefacts. The limited mesh resolution could explain this effect in small gaps between filament pairs. The numerical artefacts were, however, also discovered in areas exhibiting sufficiently fine discretisation. Local mesh refinement in future analysis may eliminate this effect.

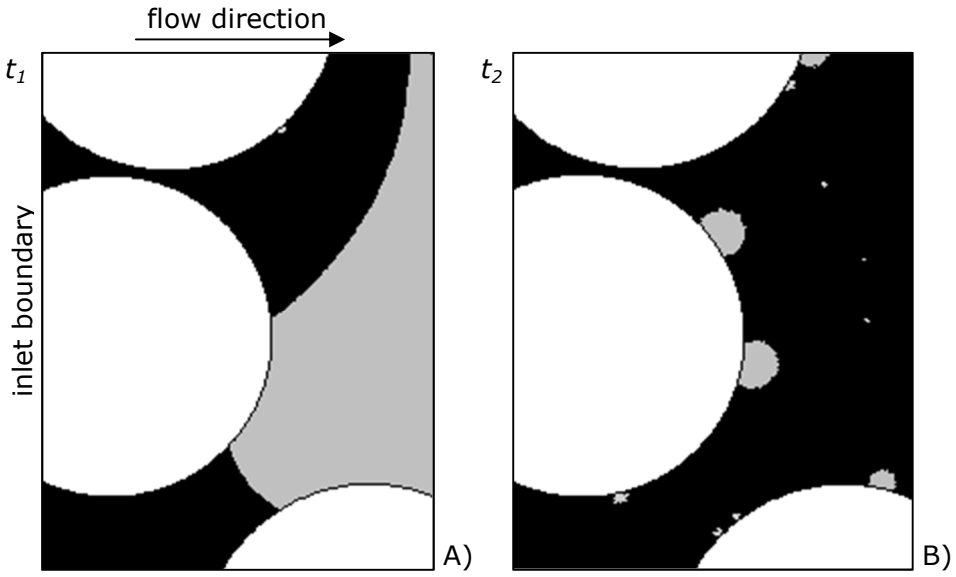

Figure 73: Example of numerical anomalies formed during transient flow simulations at different time steps t_i. A) The fluid (black) enters the modelling domain from the inlet boundary on the left edge, no gas inclusions are present. B) Gas inclusions (grey) are present at locations which were previously completely saturated by fluid.

The resulting transient flow simulations of the filling process are inaccurate due to the formation of these numerical artefacts. The results are not suitable for quantification of the amount of gas entrapment. These results might, however, still be used to give a qualitative idea of flow front progression and defect formation. Figure 74 shows the flow front progression of the explicit and implicit modelling scheme at different time steps. Initially, no numerical artefacts were present; their number and size, however, increased during the simulation. It was observed that the number of numerical artefacts during flow front progression was lower for the implicit scheme compared to the explicit simulations. This reflects the more stable solution of the implicit modelling scheme. The CFL condition employed might, however, be another reason for the observed differences in the number of numerical artefacts.

No substantial differences between the implicit and explicit modelling scheme (t_1 until t_4) were observed for the shape of the flow front. Towards the end of the simulation, no fluid outflow was observed, indicating that the outlet boundary condition needs further adjustment in future work (e.g. Region 5 in Figure 74). The final time step (t_5) of the transient modelling scheme is therefore considered not to be meaningful.

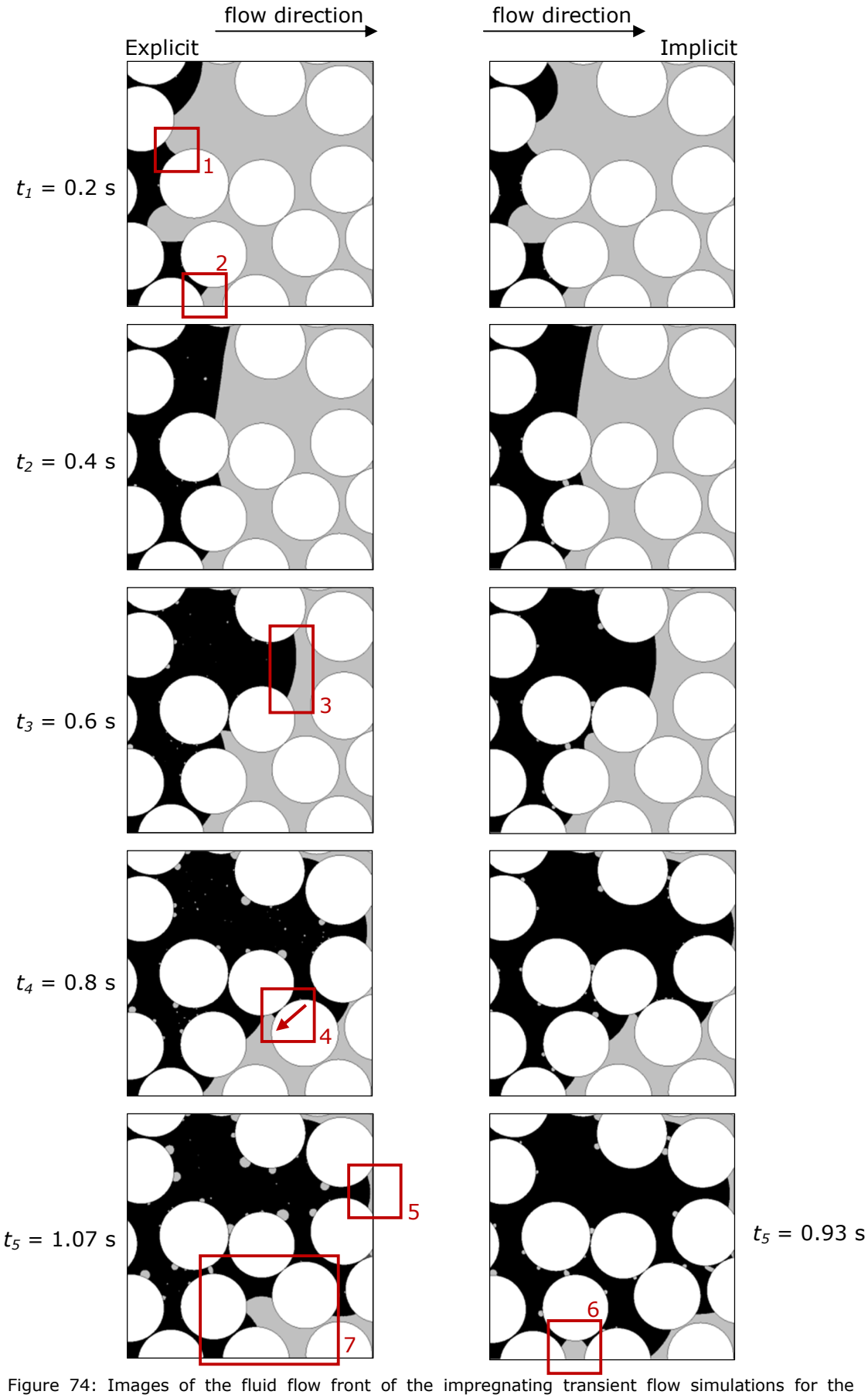

Figure 74: Images of the fluid flow front of the impregnating transient flow simulations for the explicit and implicit modelling scheme at different time steps, t_i. A constant inlet velocity of the fluid was assumed. Regions of interest are marked with rectangles.

Despite the presence of numerical anomalies the flow front in this larger model has the expected shape. In relatively small gaps between filaments, the flow is dominated by capillary effects as expected (Section 2.3.2). As a result the shape of the flow front is concave (e.g. Region 1 at t_1), which is similar to the example shown in Figure 72. The flow front exhibits a convex shape in areas where the distance between filaments is large (e.g. Region 3 at t_3), indicating a limited influence of the capillary pressure and reflecting the result of the no-slip wall conditions of the filaments. It was observed that the direction of local fluid flow does not necessarily coincide with the global flow direction. In the example given at t_4 (Region 4 indicated with an arrow), capillary effects cause flow in the opposite direction with respect to the inlet flow condition. A potential area of gas entrapment (Region 7 at t_5) due to the faster advancing flow front in the upper half of the RVE in Figure 74 is saturated with resin due to presence of capillary effects. If considering undulation and twist of the fibres in the model (Section 3.4.2) then flow in the third dimension may, however, alter these results.

It appears that the fluid is prohibited from exiting the model domain (Region 5 at t_5). The final state of the transient simulation is therefore thought not to be meaningful and no final conclusion can be drawn about the probability of void formation. To improve the accuracy of the transient modelling approach, the simulation and discretisation method will need to be adjusted in future work. Considering the large amount of calculation time needed to solve this relatively small model with the use of the commercial CFD software Ansys Fluent®, successful application for larger models is, however, not possible at present.

5.4.3 Disregarding capillary effects

It can be demonstrated that disregarding capillary effects for the case of transient flow at the micro-scale will result in flow front shapes which are considered to be not physically correct. Flow front positions based on simulations which neglect surface tension and contact angles for the example shown in Figure 74 are presented in Figure 75. Employing the implicit modelling scheme in Ansys Fluent®, the flow front positions are evaluated for the fluid (black) which impregnates the filament network and replaces the air phase (grey). The flow front shape in Figure 75 is significantly different compared to the results described in Section 5.4.2. The shape of the flow front is pressure driven only which can be observed at the convex flow front shape (e.g. Region 1 at t_1 in Figure 75). The faster advancing flow front in the case of capillary driven flow (Region 2 in Figure 74) is not observed in this case. Over the width of the model,

the flow front advances at a similar speed (t_1 to t_3). Only at an advanced time (t_4), the fluid flows faster in the upper half of the model domain as a result of the larger flow channel.

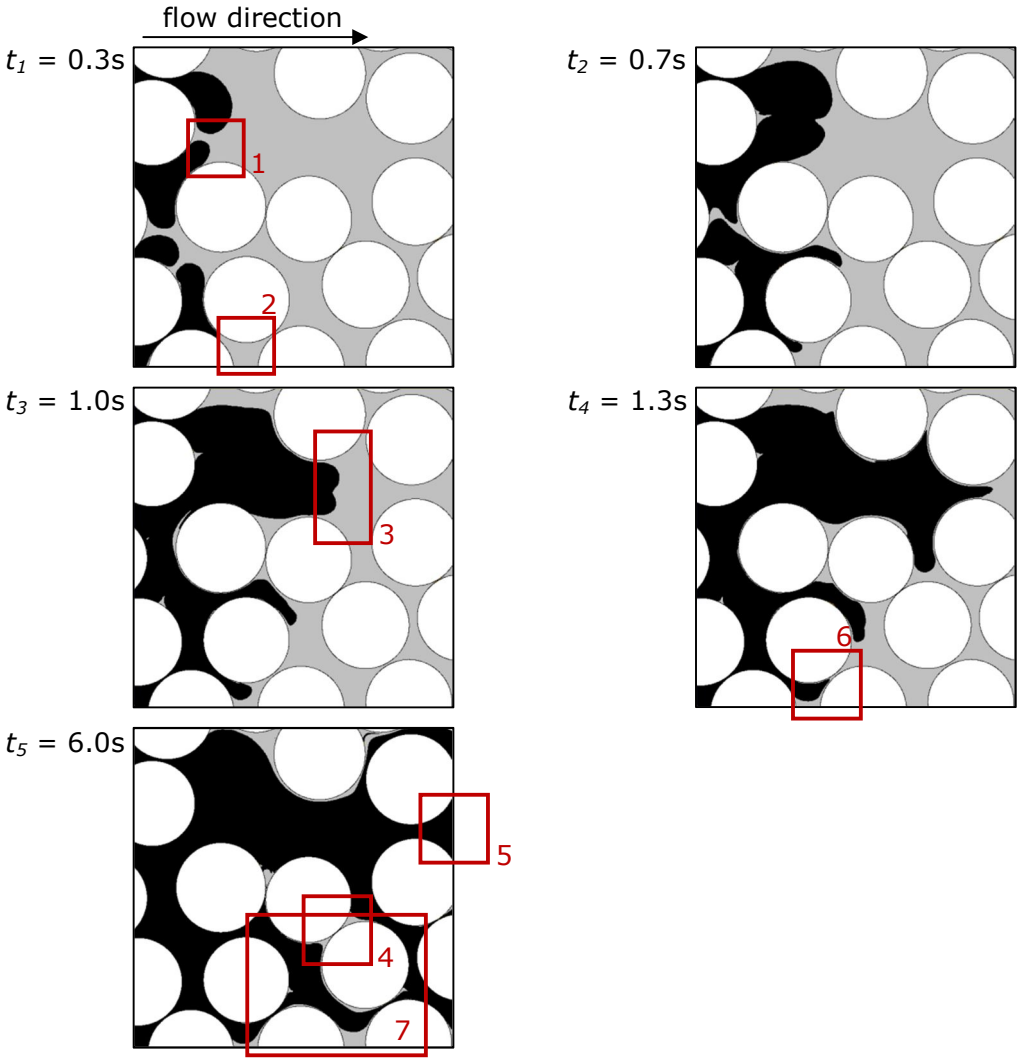

Figure 75: Images of the fluid flow front of the transient flow simulations for the implicit modelling scheme at different time steps, t_i. The fluid (black) impregnates the filament network and replaces the air phase (grey). A constant inlet velocity was assumed and surface tension was not considered.

Flow fronts remain partially separated after merging (e.g. Region 3 at t_3) and do not form a continuous flow front due to the absence of interface reactions. In addition, the absence of capillary effects does inhibit local fluid flow in opposite direction of the global flow direction (Region 4). The small gap formed in between the filaments is not saturated with fluid throughout the simulation. The faster advancing flow in the upper half of the RVE suggests a potential area of gas entrapment in the bottom half of the model domain (e.g. Region 7 at t_5). This area is, however, completely saturated by the pressure driven flow in the absence of capillary effects. The applied boundary conditions lead to small areas

at the model edge which are not saturated with resin during the course of the simulation (e.g. Region 6 at t_4). These can be considered to be numerical artefacts only and do not indicate an increased probability of void formation. In contrast to the simulations presented in Figure 74, the fluid is not prohibited from exiting the model domain (Region 5 at t_5) which indicates a successful transient flow simulation. The necessity of incorporating capillary pressures as suggested by the low capillary number can be confirmed by the evaluation of the observed fluid flow front shape.

5.4.4 Transient vs. steady-state flow

The results from the steady-state analyses in Section 4.3 illustrate the differences of flow velocities present in different areas of the RVE. It was speculated that regions with a low flow velocity may indicate areas with an increased probability of gas entrapment in case of impregnating flow. For the transient flow example depicted in Figure 74 the steady-state simulation result is shown in Figure 76. Areas of similar flow velocities in the RVE corresponding to the three peaks in the histogram of the normalised flow velocities are accentuated by different colours.

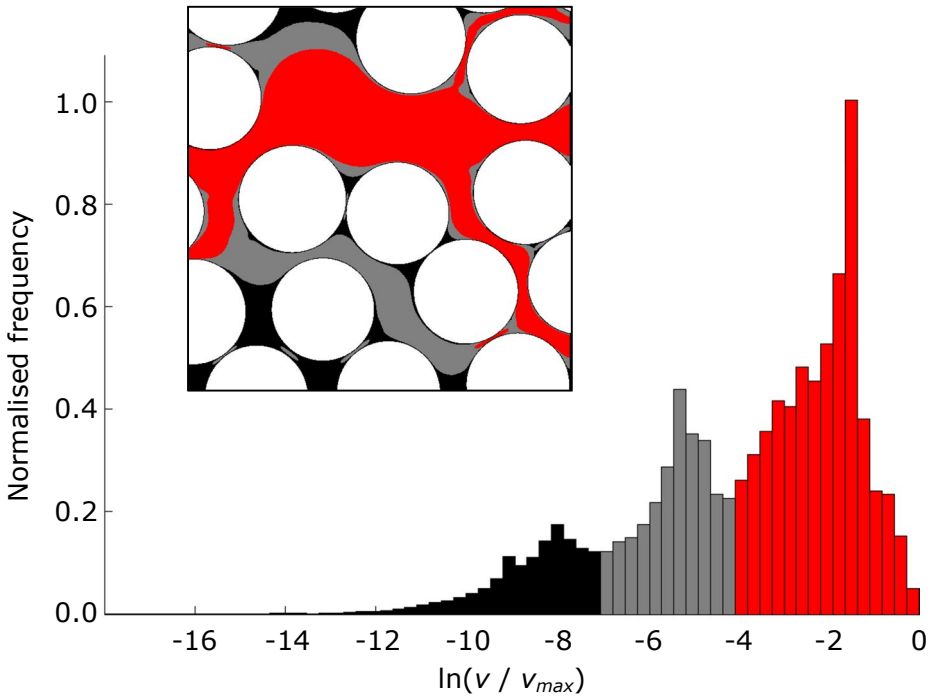

Figure 76: Histogram for the distribution of the flow velocity, v, normalised by the maximum observed velocity, v_{max} for transverse flow through a random filament arrangement with V_f = 0.63 (pressure gradient from left to right). Corresponding areas of flow velocity are highlighted using the same colours in the histogram and model domain. The frequencies are normalised by the maximum observed value.

From the steady-state flow simulations it was hypothesised that zones with high flow velocities would saturate fastest in the case of impregnating flow. Areas exhibiting low flow velocities would therefore have a larger probability of void formation due to gas entrapment as a result of merging flow fronts. In the example of Figure 76, the bottom left of the RVE experiences very low flow velocities. This would suggest a probable zone of void formation. The start of the transient flow simulations (t_1 in Figure 74) indicates, however, that the impregnation advances fastest in this area. Small gaps between filaments (Region 2 in Figure 74) are saturated with fluid due to capillary effects. After saturation of this region, the flow front does, however, not advance significantly throughout the course of the simulation. This indicates that the influence of capillary effects is limited to small areas were filaments are very close together. The curvature of the filament boundaries implies a local change of the distance between filaments which leads to a reduced influence of the capillary pressure on the flow front progression once this small gap is saturated.

The channel with the highest fluid velocity in the case of steady-state flow (Figure 76) does result in a faster advancement of the flow front in case of transient flow (Region 3 in Figure 74). At t_4 =0.8 s the transient flow simulations suggest that this channel is almost entirely saturated. The zone exhibiting a low flow velocity due to the presence of filament clustering appears to be an area of probable void formation. The transient flow simulation did not finish successfully and the results for the final stage (t_5) are surmised not to be physically meaningful. Based on the examples shown in Figure 74 and Figure 76 it is concluded that steady-state flow results could yield limited information about the expected transient flow. Peak values of different velocity zones in the case of steady-state flow alone do not, however, always reflect zones of probable void formation. Other factors will need to be evaluated in addition. Based on the example presented it is hypothesised that channels with high flow velocities in the case of steady-state flow (first pronounced peak in the histogram) are also channels with the fastest advancing flow front in the case of impregnating flow. Zones experiencing low flow velocities adjacent to these channels are saturated with fluid from these channels during impregnating flow. Therefore, it is concluded that the physical distance between zones of different flow velocities in the RVE could indicate zones of probable gas entrapment during impregnating flow.

Whilst steady-state solutions do not reflect the transient flow, indications are found that the steady-state simulation can give information about zones of probable void formation. The comparison of zones exhibiting different steady-state flow velocities could identify areas of probable void formation. The size of these zones and the distance between them could be used to predict the probability of saturation during transient flow, effectively taking capillary effects into account. An improved transient flow simulation in conjunction with a larger analysed model sizes might substantiate this claim. If the hypothesis could be confirmed, computationally intensive transient flow simulations could be replaced with rudimentary steady-state simulations'.

5.5 Conclusions

Voids in composite materials form at the flow front during impregnation in a LCM process (Section 2.3.3). The flow through fibre bundles parallel or perpendicular to the filaments is significantly different due to the difference in permeability (Chapter 2). To measure the void content in the material utilised in this work (Section 3.4.1), single layer samples were produced with flow transverse and longitudinal to the filament axis. Cross-sectional images of complete fibre bundles were taken and analysed. A code was implemented in Matlab® which enabled the systematic and automatic analysis and quantification of the void content (Section 5.2.2).

The void content and the number of voids were presented as a function of fabric compaction represented by the fibre volume fraction (Section 5.2.2). A decrease in void content in the case of transverse flow was observed with increasing compaction of the fibre bundle. The increase in bundle compaction results in a more homogeneous arrangement of the filaments within a fibre bundle as presented in Section 3.4.7. This leads to a more homogeneous velocity distribution of the resin impregnating the random filament arrangement and decreases the probability of gas entrapment due to merging flow fronts. This results in a decreased void content and a reduction in the number of voids. The decreased permeability of the fibre bundles (Section 4.3.2), however, makes the impregnation much more difficult. Mould filling in transverse flow was prevented for high fibre volume fraction with the production technique employed in this work.

The results for the void content analysis of the longitudinal flow experiments showed an opposite trend compared to the data obtained from transverse flow experiments (Figure 68). The effect of the decreased permeability exceeds the effect of a more homogeneous filament arrangement. An increase in fibre bundle compaction results in an increase in void content and number of voids.

An influence of the employed injection pressures could not be observed for the samples analysed. To gain more confidence in the observed trends, more analysis would be necessary in future. In real LCM applications, several layers of textile preforms are subjected to resin flow and transverse and longitudinal flow occur simultaneously which will affect the measurement results.

The simulation of void formation is usually performed on the meso—scale only. Flow in between and within fibre bundles is predicted and usually rudimentary approaches are implemented (Section 2.4). The impregnating flow in fibre bundles in these models is often simplified by lump sink terms or periodic arrangements. An attempt was made here to simulate the transient flow through a random filament arrangement perpendicular to the filament axis (Section 5.4.2). The filaments were assumed to be perfectly parallel and probable undulation and twist of the filament paths (Section 3.4.2) are disregarded. The flow model was therefore reduced to a two-dimensional problem only. Possible blockage of flow within the arrangement can however, be circumvent by flow in the third dimension if the filament path is taken into account.

The model settings using Ansys Fluent® were selected following best practise recommendations [128] and further adjusted after extensive discussions with the Ansys support team (Section 5.3). It was concluded that the flow front shape during the transient flow was as expected. The occurrence of numerical artefacts, however, made the quantification of the model results impossible. In addition, the numerical solution time is inordinately large. Until the issues of necessary simulation time and formation of numerical artefacts can be solved, the use of numerical CFD simulation for flow through random filament arrangements is inhibited.

6. Discussions and conclusions

6.1 Introduction

In LCM processes, the reinforcement textiles used to manufacture composite parts need to be completely saturated with resin during the impregnation phase. The spaces in between fibre bundles and the pores formed in between filaments need to be completely saturated with resin to ensure the desired mechanical properties. This study set out to analyse the influence of variabilities present within fibre bundles on the resin flow behaviour. During impregnation, the reinforcements are subject to different types of flow. At the flow front, the resin wets the dry fabric and displaces air in the reinforcement. Local differences in flow velocities lead to merging flow fronts resulting in air entrapment. Dry spots formed in the material lead to a reduction of the matrix dominated mechanical properties and have a detrimental effect on the life time of a part in service. The area behind the flow front is saturated with resin. The progression of the flow front is ensured by fluid transport through the saturated fabric. After complete mould filling, saturated flow within the preform may enable transport of voids. Both types of flow, saturated (Chapter 4) and unsaturated (Chapter 5), are investigated in this work at the micro-scale.

Differences in flow velocities are a result of the hierarchical fabric structure in textiles. The presence of geometrical variabilities exacerbates local differences in flow velocities. Therefore it was concluded that accurate quantification of the random filament arrangement within fibre bundles is necessary. A number of studies made attempts to quantitatively characterise the micro-structures formed in composite materials. These studies usually lack the necessary spatial resolution for detailed analysis or are not able to analyse large samples. Therefore, extensive work was conducted to systematically characterise the filament arrangement (Section 3.3) within fibre bundles at different levels of compaction. The distributions found for the filament arrangements (Section 3.4) were then used to reconstruct statistically equivalent two-dimensional filament arrangements (Section 2.2.3). On these model domains, saturated fluid flow was simulated (Chapter 4). In addition, the formation of voids was analysed for samples produced by transverse and longitudinal flow (Section 5.2). An attempt

was made to predict the probable void formation on the micro-scale at the fluid flow front based on transient flow simulations (Section 5.4).

6.2 General discussion

The random arrangement of filaments within a fibre bundle was determined in this work based on the analysis of two-dimensional fibre bundle cross-sections (Section 3.3). Unlike in other studies e.g. [99, 102], single layer composite sheets were produced and investigated (Section 3.4.1). This enabled the systematic analysis of the effect of compaction on the filament arrangement within fibre bundles while eliminating effects of bundle nesting. To gain morphological data from acquired micrographic images, a simple colour thresholding technique is often employed. However, inevitable differences in lighting, local light reflections and shading make it unfeasible to use one global threshold (Section 3.3). An automated image analysis process based on the edge detection of local colour gradients was developed in this work to overcome these issues (Section 3.3.2). The detected filament outlines are approximated with ellipses. Compared to a set of manually fitted ellipses, an average underestimation of the minor ellipse axis of 0.8 % could be identified. The developed code made it feasible to analyse a large amount of filaments at high magnification. The measurement of 300,000 individual filament cross-sections showed a normal distribution of the filament diameter with a mean of 6.97 μm and a standard deviation of 0.39 μm. This is in good agreement with the manufacturer's specification (Appendix C.1). Vaughan and McCarthy [18] reported a filament diameter of 6.6 μm for a similar carbon fibre reinforcement. The difference to the observed value in this work probably stems from the rudimentary image analysis process employed in their work. This clearly demonstrates the benefit of the developed technique to automatically analyse filament arrangements within micrographs.

The distance of a filament to its n-th nearest neighbour was chosen to describe the spatial arrangement of the filaments (Section 3.4.7.1). As expected, a decrease of the distances to nearest neighbours with increasing level of fibre bundle compression was observed. This decrease was accompanied with a change of the fibre bundle shape (Section 3.4.4). The decrease in measured inter-filament distances was more distinct when fibre bundles were touching. Therefore, a linear decrease in cavity height resulted in a non-linear decrease of inter-filament distances. The filament distribution within the fibre bundles becomes more uniform, which is related to the reduction in inter-filament

spacing and increasing packing density. The increasing degree of order of the filament arrangement is also reflected in the distribution of angles at which the *n*-th nearest neighbour is located (Section 3.4.7.3). The quantification of the observed order is disregarded in the literature [18, 68] or only indicated by global statistical descriptors. An almost perfectly random arrangement of the filaments was observed when the bundle is not compacted, reflected in uniform angle distributions. The angle distributions were found to become less uniform with an increasing level of compaction. It could therefore be concluded that the degree of heterogeneity in the filament arrangement decreases with increasing amount of compaction. The filament arrangement becomes more regular, approximating the hexagonal configuration.

For the simulation of micro-structural properties, the measurements imply that a random filament arrangement can be expected at low fibre volume fraction and an increased regularity of micro-structures might be assumed at high fibre volume fraction. Reconstructed filament arrangements were generated in this work (Section 3.5). The fibre placement algorithm proposed by Vaughan and McCarty [18] was further developed to utilise the presented measurement data. Incorporating angle distributions during the filament placement procedure made it feasible to generate any possible fibre volume fraction. Jamming limits which can be encountered when utilising other micro-structure generators are avoided [18]. The generated filament arrangements were validated utilising the same statistical descriptors as employed earlier, reflecting the orthotropy resulting from the bundle compaction. The micro-structures were used for micro-scale flow predictions (Chapter 4 and 5) and the results were compared to simulations for an entirely random micro-structure presented in the literature.

Several studies [49, 52, 59] suggested the use of regular filament arrangements to describe the micro-structure within fibre bundles (Section 2.2.2). These models are computational inexpensive but fail to capture the intrinsic variabilities present in real fibre bundles. Steady-state flow simulation on the reconstructed filament arrangements (Section 4.3.2) showed that regular periodic micro-structures overestimate the transverse permeability of the random filament arrangements by up to an order of magnitude. While this effect was already known [22], previous observations were made based on artificially generated random filament arrangements only. As for regular arrangements, the average permeability of a random filament micro-structure decreases with increasing V_f. Unlike for periodic unit cells, a significant scatter in permeability values was

observed for the RVEs as a result of the geometric variabilities present. It was observed that maximum velocities occur for a limited number of flow channels in the model domain. With increasing flow length, the probability of local blockage of these flow channels is increased, whereas the probability of channel formation is increased with increasing width (Section 4.3.2). In case of a complete fibre bundle with a large width to height ratio, this implies that two different permeability values need to be considered.

Convergence of the simulated permeabilities for every fibre volume fraction considered was observed with increasing model size. The convergence flow length determined for the square models in this work was estimated as $l/r = 30$ (Section 4.3.2). This is significantly smaller than the value $l/r = 80$ for steady state flow through a random filament arrangements reported in the literature [57]. The significantly finer discretisation of the gaps in between filaments was thought to be the main reason for this effect (Section 4.1.2). It was shown that for a single filament pair, the difference due to the more detailed discretisation was up to 5 % (Section 4.1.3). This error was thought to compound when utilising larger model domains. Due to the improved discretisation procedure implemented in this work, it was not necessary to restrict the gap distance between filaments as is usually the case in simulations of filament micro-structures [57, 64]. In addition, this work employed reconstructed random filament arrangements (Section 3.5) instead of purely artificially generated random arrangements. The simulations describe therefore the flow in carbon fibre bundles as employed in the composite materials analysed and are not merely approximations.

The distributions of fluid velocities in the case of steady-state flow were analysed (Section 4.3.3). It was hypothesised that peaks in these distributions indicate probabilities for void formation. Qualitative evaluation of a transient flow simulation indicated that flow channels formed in between filaments, which exhibit a high flow velocity in the case of steady-state flow, are also the major channels of fluid transport (Section 5.4.4). Zones exhibiting low flow velocities appear to be saturated from these major flow channels if they are located in close proximity. Due to problems encountered for transient flow simulations (Section 5.4.2), the results cannot be evaluated quantitatively. The presence of numerical artefacts does render the simulation results questionable. Further adjustment of the simulation settings and model domain discretisation is required. Successful simulation of larger model domains will then also enable

validation of the flow predictions with the void content measured in this work (Section 5.2.2). For the void content measurement, the limitations of often employed rudimentary image analysis techniques such as thresholding are overcome. The developed morphological image analysis technique in this work was implemented in a Matlab® code which made automated detailed void content analysis possible. The void content was found to be a function of the fibre volume fraction. For flow transverse to the fibre bundle axis the void content was found to decrease with increasing bundle compaction. The more uniform filament arrangement (Section 3.4.7) leads to a more uniform flow velocity in the fibre bundles which overcompensates for the reduction in permeability. An opposite effect was observed for flow along the fibre bundle axis. To gain more confidence in the obtained values and trends, more tests are needed in future work.

6.3 Recommendations for future work

The developed micro-structure generator (Section 3.5) can be employed for generation of numerical models for the prediction of micro-mechanical properties of composites. This code was therefore already made available for interested researchers. The measured micro-structural rearrangement of the filaments in response to external deformation (Section 3.4) will be included in a compaction model for textile reinforcements by the author. This will increase the understanding of fibre bundle deformation mechanism in textile reinforcements undergoing compaction, e.g. explaining the effect of nesting and bundle deformation. The precise prediction of these phenomena will help to explain the influence of the bundle micro-structure on global component properties.

The precise prediction of transverse flow through a filament network is especially interesting at LCM processes with a high fibre volume fraction to avoid defect formation (Section 1.3). In the case of a homogenised meso-structure, for example a reduced number of inter-bundle channels by use of spread tows, the transverse flow through filaments will also dominate the global flow behaviour. The ability to predict the variability in flow behaviour (Section 2.3.3) will therefore enable to take measures to reduce manufacture induced defects. Especially, the possible prediction of micro-scale defects (Section 2.4 and Chapter 5) which are not apparent after part manufacture is desirable.

The predicted steady-state permeabilities can be employed in multi-scale flow models (Section 2.4). The fibre bundle permeability would not need to be

estimated by periodic arrangements but could be identified with the simulation results presented in this work (Section 4.3.2). It should, however, be verified that the micro-structural data utilised in the model generation is also applicable for other material configurations. In the current description of the random filament arrangements within fibre bundles, single layer composite materials have been manufactured at different levels of compaction (Section 3.4.1). The mould surface was solid and assumed not to deform during compaction. The response of the filaments to compaction during mould closure in multi-layer composites needs therefore to be investigated. Deformable fibre bundles are compacted against each other and the resulting bundle deformations are expected to be different. It is hypothesised, however, that results of filament rearrangement will be similar within each fibre bundle.

The determined convergence of the steady-state permeability predictions to the model size (Section 4.3.2) can be utilised in meso- and macro-scale modelling approaches. It can assist in the choice of a suitable discretisation size. A discretisation which is larger than the converged model size determined on the micro-scale can be considered to exhibit a uniform average permeability behaviour. A smaller discretisation will need to incorporate the determined permeability distributions (Figure 61). This will then include the scatter of permeability due to local effects such as local blockage of flow (Section 4.2.2).

Another attempt to predict the transient flow behaviour (Section 5.4) should be endeavoured. A finer discretisation should be employed and the solution technique adjusted to avoid numerical artefacts. If the computation time can be significantly reduced, a larger model domain should be analysed and the probable gas entrapment visualised. This would enable to validate the hypothesised relationship between steady-state flow predictions and transient flow (Section 5.4.4). The computational resources required for the prediction of steady-state flow are significantly smaller and would make this a simple but valuable simulation technique for the prediction of micro-scale voidage. Reduction of the flow problem to two-dimensions in the simulations ignores, however, that filaments in actual fibre bundles show some degree of tortuosity [92, 129]. Probable flow in the third axial dimension is neglected. For the assumption of perfectly parallel aligned filaments, longitudinal flow could be predicted with the models utilised in this work. Inter-filament gaps may, however, vary along the tow axis; therefore, the validity of this simplification has to be confirmed.

The observed void content (Section 5.2) could be correlated to the local filament arrangements present in the fibre bundle. These data could then be used to validate transient flow predictions. Additional analyses of the shape and local distribution of the formed voids would be desirable. For the systematic analysis of the effect of the filament arrangement on void formation, single layer composite samples have been produced. The deduced trends of void formation for the case of longitudinal and transverse flow (Section 5.2.2) would need to be confirmed on multi-layered composite materials. Other effects such as bundle nesting may influence the results [38]. The developed code to automatically analyse the void content within fibre bundles (Section 5.2.1) will reduce the necessary time and effort in future studies.

6.4 Conclusions

Filament arrangements in composite samples were analysed statistically.

- A novel automated image analysis technique for detection of filament boundaries in two-dimensional micrographs at high magnification was developed and implemented.
- To exclude effects such as bundle nesting, single layer carbon fibre epoxy composites were characterised systematically at different levels of compaction. An increase in uniformity of the filament arrangement was observed for an increase in bundle compaction.

Computational models were generated for simulation of flow through non-uniform filament arrangements.

- A method proposed in the literature to reconstruct random filament arrangements was adapted to incorporate the measured distributions of nearest neighbour distances and angles and to overcome the observed jamming limit.
- Numerical analysis of a large number of models was made feasible by automation of discretisation using an unstructured locally refined triangular mesh.
- The need for applying a minimum gap distance between neighbouring filaments was overcome by development and implementation of automated local mesh refinement, ensuring minimisation of the total number of elements required.

Transverse steady-state resin flow was simulated numerically.

- For transverse flow through the reconstructed filament arrangements significantly smaller permeability values were observed than for regular filament arrangements. The majority of fluid flow was found to be in a limited number of flow channels only.
- Convergence of the log-normally distributed permeability values was found at a ratio between flow length and filament radius of approximately 30 for all analysed fibre volume fractions. This is significantly smaller than reported in the literature for a similar analysis.

Defect formation during fibre bundle impregnation was related to the non-uniformity of filament arrangements.

- Automated detailed void content analysis was made possible by development and implementation of a morphological image analysis technique overcoming the limitations of rudimentary thresholding approaches used in the literature.
- For flow transverse to the fibre bundle axis, the void content was found to decrease with increasing fibre volume fraction. This was attributed to the decrease in non-uniformity of the micro-structure, which overcompensated the decrease in permeability. An opposite effect was observed for flow along the fibre bundle axis.

Transient simulations of flow through a random filament network were run.

- Quantitative evaluation was not possible at the current state of the simulation procedures and the available computational power. Indications were found, however, that the steady-state flow simulations can give information about the transient flow behaviour.

Even though the transient flow simulations require further development, this work successfully demonstrated the effects of random filament arrangements on the resin flow behaviour in fibre bundles.

References

[1] Airbus. "The perfect flight"; www.airbus.com/innovation/eco-efficiency/, (last accessed: 15 March 2013).

[2] R. Stewart, "Automotive composites offer lighter solutions", *Reinforced Plastics*, no. March/April, pp. 22-28, 2010.

[3] A. Beukers, and E. van Hinte, *Flying lightness: Promises for structural elegance*, Rotterdam: 010 publishers, 2005.

[4] Willems, and v. d. Wildenberg. "Technologies for carbon fibre reinforced modular automotive body structures (TECABS)"; www.mtm.kuleuven.be/Onderzoek/Composites/, (last accessed: 17 Jan. 2013).

[5] C. Garschke, C. Weimer, P. P. Parlevliet, and B. L. Fox, "Out-of-autoclave cure cycle study of a resin film infusion process using in situ process monitoring", *Composites Part A: Applied Science and Manufacturing,* vol. 43, no. 6, pp. 935-944, 2012.

[6] J. Kay, L. Fahrang, K. Hsiao, and G. Fernlund, "Effect of process conditions on porosity in out-of-autoclave prepreg laminates", in 18th International Conference on Composite Materials (ICCM18), Jeju South Korea, 2011.

[7] Z. A. Mohd Ishak, Y. W. Leong, M. Steeg, and J. Karger-Kocsis, "Mechanical properties of woven glass fabric reinforced in situ polymerized poly(butylene terephthalate) composites", *Composites Science and Technology,* vol. 67, no. 3-4, pp. 390-398, 2007.

[8] C. H. Park, A. Lebel, A. Saouab, J. Bréard, and W. I. Lee, "Modeling and simulation of voids and saturation in liquid composite molding processes", *Composites Part A: Applied Science and Manufacturing,* vol. 42, no. 6, pp. 658-668, 2011.

[9] D. H. Lee, W. I. Lee, and M. K. Kang, "Analysis and minimization of void formation during resin transfer molding process", *Composites Science and Technology,* vol. 66, no. 16, pp. 3281-3289, 2006.

[10] R. A. Smith, L. J. Nelson, M. J. Mienczakowski, and R. E. Challis, "Automated Non-Destructive Analysis and Advanced 3D Defect Characterisation from Ultrasonic Scans of Composites", in 17th

International Conference on Composite Materials (ICCM17), Edinburgh, 2009.

[11] H. Bale, M. Blacklock, M. R. Begley, D. B. Marshall, B. N. Cox, and R. O. Ritchie, "Characterizing Three-Dimensional Textile Ceramic Composites Using Synchrotron X-Ray Micro-Computed-Tomography", *Journal of the American Ceramic Society,* vol. 95, no. 1, pp. 392-402, 2011.

[12] A. Delarue, and D. Jeulin, "3D morpholgical analysis of composite materials with aggregates of spherical inclusions", *Image Analysis and Stereology,* vol. 22, pp. 153-161, 20.10.2003, 2003.

[13] H. Huang, and R. Talreja, "Effects of void geometry on elastic properties of unidirectional fiber reinforced composites", *Composites Science and Technology,* vol. 65, no. 13, pp. 1964-1981, 2005.

[14] V. Rohatgi, N. Patel, and L. J. Lee, "Experimental investigation of flow-induced microvoids during impregnation of unidirectional stitched fiberglass mat", *Polymer Composites,* vol. 17, no. 2, pp. 161-170, 1996.

[15] A. R. Chambers, J. S. Earl, C. A. Squires, and M. A. Suhot, "The effect of voids on the flexural fatigue performance of unidirectional carbon fibre composites developed for wind turbine applications", *International Journal of Fatigue,* vol. 28, pp. 1389-1398, 2006.

[16] S. Paciornik, and J. R. M. D'Almeida, "Measurement of Void Content and Distribution in Composite Materials through Digital Microscopy", *Journal of Composite Materials,* vol. 43, no. 2, pp. 101-112, 2009.

[17] F. Gehrig, E. Mannov, and K. Schulte, "Degradation of NCF-Epoxy Composites containing Voids", in 17th International Conference on Composite Materials (ICCM17), Edinburgh, UK, 2009.

[18] T. J. Vaughan, and C. T. McCarthy, "A combined experimental-numerical approach for generating statistically equivalent fibre distributions for high strength laminated composite materials", *Composites Science and Technology,* vol. 70, no. 2, pp. 291-297, 2009.

[19] C. Kleinstreuer, *Modern fluid dynamics: Basic theory and selected applications in macro- and micro-fluidics*, 2010.

[20] Y. A. Çengel, and J. M. Cimbala, *Fluid Mechanics: Fundamentals and Applications*, 2nd ed., NewYork: McGraw-Hill, 2010.

[21] C. D. Rudd, A. C. Long, K. N. Kendall, and C. G. E. Mangin, *Liquid moulding technologies*: Woodhead Publishing Limited, 1997.

[22] J. G. I. Hellström, V. Frishfelds, and T. S. Lundström, "Mechanisms of flow-induced deformation of porous media", *Journal of Fluid Mechanics,* vol. 664, pp. 220-237, 2010.

[23] W. Zijl, and J. M. T. Stam, "Modeling permeability in imperfectly layered porous media. I. Derivation of block-scale permeability tensor for thin grid-blocks", *Mathematical Geology,* vol. 24, no. 8, pp. 865-883, 1992.

[24] J. Bréard, A. Saouab, and G. Bouquet, "Numerical simulation of void formation in LCM", *Composites Part A: Applied Science and Manufacturing,* vol. 34, no. 6, pp. 517-523, 2003.

[25] C. H. Park, and I. L. Woo, "Modeling void formation and unsaturated flow in liquid composite molding processes: a survey and review", *Journal of Reinforced Plastics and Composites,* vol. 30, no. 11, pp. 957-977, June 1, 2011, 2012.

[26] S. Drapier, J. Monatte, O. Elbouazzaoui, and P. Henrat, "Characterization of transient through-thickness permeabilities of Non Crimp New Concept (NC2) multiaxial fabrics", *Composites Part A: Applied Science and Manufacturing,* vol. 36, no. 7, pp. 877-892, 2005.

[27] R. S. Parnas, J. G. Howard, T. L. Luce, and S. G. Advani, "Permeability characterization. Part 1: A proposed standard reference fabric for permeability", *Polymer Composites,* vol. 16, no. 6, pp. 429-445, 1995.

[28] J. R. Weitzenböck, R. A. Shenoi, and P. A. Wilson, "Radial flow permeability measurement. Part A: Theory", *Composites Part A: Applied Science and Manufacturing,* vol. 30, no. 6, pp. 781-796, 1999.

[29] Q. Liu, R. S. Parnas, and H. S. Giffard, "New set-up for in-plane permeability measurement", *Composites Part A: Applied Science and Manufacturing,* vol. 38, no. 3, pp. 954-962, 2007.

[30] G. Morren, M. Bottiglieri, S. Bossuyt, H. Sol, D. Lecompte, B. Verleye, and S. V. Lomov, "A reference specimen for permeability measurements of fibrous reinforcements for RTM", *Composites Part A: Applied Science and Manufacturing,* vol. 40, no. 3, pp. 244-250, 2009.

[31] Y. Luo, I. Verpoest, K. Hoes, M. Vanheule, H. Sol, and A. Cardon, "Permeability measurement of textile reinforcements with several test fluids", *Composites Part A: Applied Science and Manufacturing,* vol. 32, no. 10, pp. 1497-1504, 2001.

[32] R. Loendersloot, "The structure-permeability relation of textile reinforcements", PhD thesis, Engineering Technology (CTW), University of Twente, Enschede, 2006.

[33] J. R. Weitzenböck, R. A. Shenoi, and P. A. Wilson, "Measurement of three-dimensional permeability", *Composites Part A: Applied Science and Manufacturing,* vol. 29, no. 1-2, pp. 159-169, 1998.

[34] S. Comas-Cardona, C. Binetruy, and P. Krawczak, "Unidirectional

compression of fibre reinforcements. Part 2: A continuous permeability tensor measurement", *Composites Science and Technology,* vol. 67, no. 3-4, pp. 638-645, 2007.

[35] S. H. Ahn, W. I. Lee, and G. S. Springer, "Measurement of the Three-Dimensional Permeability of Fiber Preforms Using Embedded Fiber Optic Sensors", *Journal of Composite Materials,* vol. 29, no. 6, pp. 714-733, April 1, 1995, 1995.

[36] H. C. Stadtfeld, M. Erninger, S. Bickerton, and S. G. Advani, "An Experimental Method to Continuously Measure Permeability of Fiber Preforms as a Function of Fiber Volume Fraction", *Journal of Reinforced Plastics and Composites,* vol. 21, no. 10, pp. 879-899, July 1, 2002, 2002.

[37] R. S. Parnas, *Liquid Composite Molding*: Hanser Gardner Publications, Inc., 2000.

[38] K. Hoes, D. Dinescu, H. Sol, R. S. Parnas, and S. Lomov, "Study of nesting induced scatter of permeability values in layered reinforcement fabrics", *Composites Part A: Applied Science and Manufacturing,* vol. 35, no. 12, pp. 1407-1418, 2004.

[39] P. Smith, C. D. Rudd, and A. C. Long, "The effect of shear deformation on the processing and mechanical properties of aligned reinforcements", *Composites Science and Technology,* vol. 57, no. 3, pp. 327-344, 1997.

[40] A. Endruweit, A. C. Long, F. Robitaille, and C. D. Rudd, "Influence of stochastic fibre angle variations on the permeability of bi-directional textile fabrics", *Composites Part A: Applied Science and Manufacturing,* vol. 37, no. 1, pp. 122-132, 2006.

[41] A. Endruweit, and A. C. Long, "Influence of stochastic variations in the fibre spacing on the permeability of bi-directional textile fabrics", *Composites Part A: Applied Science and Manufacturing,* vol. 37, no. 5, pp. 679-694, 2006.

[42] R. Arbter, J. M. Beraud, C. Binetruy, L. Bizet, J. Bréard, S. Comas-Cardona, C. Demaria, A. Endruweit, P. Ermanni, F. Gommer, S. Hasanovic, P. Henrat, F. Klunker, B. Laine, S. Lavanchy, S. V. Lomov, A. Long, V. Michaud, G. Morren, E. Ruiz, H. Sol, F. Trochu, B. Verleye, M. Wietgrefe, W. Wu, and G. Ziegmann, "Experimental determination of the permeability of textiles: A benchmark exercise", *Composites Part A: Applied Science and Manufacturing,* vol. 42, no. 9, pp. 1157-1168, 2011.

[43] M. Sherburn, "Geometric and Mechanical Modelling of Textiles", PhD thesis, School of Mechanical, Materials and Manufacturing Engineering, University of Nottingham, PhD Thesis, 2007.

[44] X. S. Zeng, A. C. Long, F. Gommer, A. Endruweit, and M. Clifford, "Modelling compaction effect on permeability of 3D carbon reinforcements", in 18th International Conference on Composite Materials (ICCM18), Jeju Island, South Korea, 2011.

[45] U. o. Nottingham. "TexGen"; http://texgen.sourceforge.net/, (last accessed: 17 Jan. 2013).

[46] E. Zhou, D. Mollenhauer, and E. Iarve, "A realistic 3-D textile geometric model", in 17th International Conference on Composite Materials (ICCM17), Edinburgh, 2009.

[47] A. A. Skordos, and M. P. F. Sutcliffe, "Stochastic simulation of woven composites forming", *Composites Science and Technology,* vol. 68, no. 1, pp. 283-296, 2008.

[48] E. Glatt, S. Rief, A. Wiegmann, M. Knefel, and E. Wegenke, *Structure and pressure drop of real and virtual metal wire meshes*, vol. 157, 2009.

[49] B. R. Gebart, "Permeability of unidirectional reinforcements for RTM", *Journal of Composite Materials,* vol. 26, no. 8, pp. 1100-1133, 1992.

[50] A. L. Berdichevsky, and Z. Cai, "Preform permeability predictions by self-consistent method and finite element simulation", *Polymer Composites,* vol. 14, no. 2, pp. 132-143, 1993.

[51] A. M. J. Davis, and D. F. James, "Slow flow through a model fibrous porous medium", *International Journal of Multiphase Flow,* vol. 22, no. 5, pp. 969-989, 1996.

[52] A. Tamayol, and M. Bahrami, "Analytical determination of viscous permeability of fibrous porous media", *International Journal of Heat and Mass Transfer,* vol. 52, no. 9-10, pp. 2407-2414, 2009.

[53] M. Hellou, J. Martinez, and M. El Yazidi, "Stokes flow through microstructural model of fibrous media", *Mechanics Research Communications,* vol. 31, no. 1, pp. 97-103, 2004.

[54] C. DeValve, and R. Pitchumani, "An analytical model for the longitudinal permeability of aligned fibrous media", *Composites Science and Technology,* vol. 72, no. 13, pp. 1500-1507, 2012.

[55] Z. Cai, and A. L. Berdichevsky, "Numerical simulation on the permeability variations of a fiber assembly", *Polymer Composites,* vol. 14, no. 6, pp. 529-539, 1993.

[56] G. Bechtold, and L. Ye, "Influence of fibre distribution on the transverse flow permeability in fibre bundles", *Composites Science and Technology,* vol. 63, no. 14, pp. 2069-2079, 2003.

[57] K. Yazdchi, S. Srivastava, and S. Luding, "Micro-macro relations for flow

through random arrays of cylinders", *Composites Part A: Applied Science and Manufacturing,* vol. 43, no. 11, pp. 2007-2020, 2012.

[58] X. Chen, and T. D. Papathanasiou, "Micro-scale modeling of axial flow through unidirectional disordered fiber arrays", *Composites Science and Technology,* vol. 67, no. 7-8, pp. 1286-1293, 2007.

[59] Z. Cai, and A. L. Berdichevsky, "An improved self-consistent method for estimating the permeability of a fiber assembly", *Polymer Composites,* vol. 14, no. 4, pp. 314-323, 1993.

[60] M. A. Choi, M. H. Lee, J. Chang, and S. J. Lee, "Permeability modeling of fibrous media in composite processing", *Journal of Non-Newtonian Fluid Mechanics,* vol. 79, pp. 585-598, 1998.

[61] K. P. Brennan, and D. E. Walrath, "Macroscale simulation of fiber bed impregnation utilizing microscale material properties", *Journal of Reinforced Plastics and Composites,* vol. 29, no. 8, pp. 1248-1266, April 1, 2010, 2010.

[62] T. Tran, S. Comas-Cardona, N.-E. Abriak, and C. Binetruy, "Unified microporomechanical approach for mechanical behavior and permeability of misaligned unidirectional fiber reinforcement", *Composites Science and Technology,* vol. In Press, Accepted Manuscript, 2010.

[63] H. Altenbach, J. Altenbach, and W. Kissing, *Mechanics of composite structural elements*: Springer-Verlag, 2004.

[64] D. Trias, J. Costa, J. A. Mayugo, and J. E. Hurtado, "Random models versus periodic models for fibre reinforced composites", *Computational Materials Science,* vol. 38, no. 2, pp. 316-324, 2006.

[65] V. A. Buryachenko, N. J. Pagano, R. Y. Kim, and J. E. Spowart, "Quantitative description and numerical simulation of random microstructures of composites and their effective elastic moduli", *International Journal of Solids and Structures,* vol. 40, no. 1, pp. 47-72, 2003.

[66] A. A. Gusev, P. J. Hine, and I. M. Ward, "Fiber packing and elastic properties of a transversely random unidirectional glass/epoxy composite", *Composites Science and Technology,* vol. 60, no. 4, pp. 535-541, 2000.

[67] A. R. Melro, P. P. Camanho, and S. T. Pinho, "Generation of random distribution of fibres in long-fibre reinforced composites", *Composites Science and Technology,* vol. 68, no. 9, pp. 2092-2102, 2008.

[68] A. Wongsto, and S. Li, "Micromechanical FE analysis of UD fibre-reinforced composites with fibres distributed at random over the transverse cross-section", *Composites Part A: Applied Science and*

Manufacturing, vol. 36, no. 9, pp. 1246-1266, 2005.

[69] L. Yang, Y. Yan, Z. Ran, and Y. Liu, "A new method for generating random fibre distributions for fibre reinforced composites", *Composites Science and Technology,* vol. 76, no. 0, pp. 14-20.

[70] S. R. Niezgoda, D. M. Turner, D. T. Fullwood, and S. R. Kalidindi, "Optimized structure based representative volume element sets reflecting the ensemble-averaged 2-point statistics", *Acta Materialia,* vol. 58, no. 13, pp. 4432-4445, 2010.

[71] C. Grufman, and F. Ellyin, "Determining a representative volume element capturing the morphology of fibre reinforced polymer composites", *Composites Science and Technology,* vol. 67, no. 3-4, pp. 766-775, 2007.

[72] D. Trias, J. Costa, A. Turon, and J. E. Hurtado, "Determination of the critical size of a statistical representative volume element (SRVE) for carbon reinforced polymers", *Acta Materialia,* vol. 54, no. 13, pp. 3471-3484, 2006.

[73] M. Thomas, N. Boyard, L. Perez, Y. Jarny, and D. Delaunay, "Representative volume element of anisotropic unidirectional carbon-epoxy composite with high-fibre volume fraction", *Composites Science and Technology,* vol. 68, no. 15-16, pp. 3184-3192, 2008.

[74] S. Swaminathan, S. Ghosh, and N. J. Pagano, "Statistically Equivalent Representative Volume Elements for Unidirectional Composite Microstructures: Part I - Without Damage", *Journal of Composite Materials,* vol. 40, no. 7, pp. 583-604, 2006.

[75] V. V. Silberschmidt, "Account for Random Microstructure in multiscale models", *Multiscale modeling and simulation of composite materials and structures*, Y. W. Kwon, D. H. Allen and R. R. Talreja, eds., pp. 1-35, 2008.

[76] S. Ghosh, "Adaptive concurrent multilevel model for multiscale analysis of composite materials including damage", *Multiscale modeling and simulation of composite materials and structures*, Y. W. Kwon, D. H. Allen and R. R. Talreja, eds., pp. 83-164, 2008.

[77] S. Sriramula, and M. K. Chryssanthopoulos, "Quantification of uncertainty modelling in stochastic analysis of FRP composites", *Composites Part A: Applied Science and Manufacturing,* vol. 40, no. 11, pp. 1673-1684, 2009.

[78] F. Costanzo, and G. L. Gray, "A micromechanics-based notion of stress for use in the determination of continuum-level mechanical properties via molecular dynamics", *Multiscale modeling and simulation of composite materials and structures*, Y. W. Kwon, D. H. Allen and R. R. Talreja, eds., pp. 203-234, 2008.

[79] R. Haj-Ali, "Nested Nonlinear Multiscale Frameworks for the Analysis of Thick-Section Composite Materials and Structures ", *Multiscale modeling and simulation of composite materials and structures*, Y. W. Kwon, D. H. Allen and R. R. Talreja, eds., pp. 317-358, 2008.

[80] K. P. Brennan, and D. E. Walrath, "Analysis of underlying organization in randomized fiber arrays", *Journal of Composite Materials,* vol. 43, no. 21, pp. 2441-2453, October 1, 2009, 2009.

[81] M. Li, S. Wang, Y. Gu, Z. Zhang, Y. Li, and K. Potter, "Dynamic capillary impact on longitudinal micro-flow in vacuum assisted impregnation and the unsaturated permeability of inner fiber tows", *Composites Science and Technology,* vol. 70, no. 11, pp. 1628-1636, 2010.

[82] M. K. Kang, W. I. Lee, and H. T. Hahn, "Formation of microvoids during resin-transfer molding process", *Composites Science and Technology,* vol. 60, pp. 2427-2434, 2000.

[83] G. Emanuel, *Analytical fluid dynamics*, 2nd ed., Boca Raton: CRC Press LLC, 2001.

[84] C. M. Pastore, and P. Kiekens, *Surface characteristics of fibers and textiles*, New York: Marcel Dekker, inc., 2001.

[85] S. G. Advani, and Z. Dimitrovova, "Role of capillary driven flow in composite manufacturing", *Surface and Interfacial Tension: Measurement, Theory, and Applications*, Surfactant Science Series: CRC Press, 2004.

[86] T. S. Lundström, and B. R. Gebart, "Influence from process parameters on void formation in resin transfer molding", *Polymer Composites,* vol. 15, no. 1, pp. 25-33, 1994.

[87] A. Endruweit, P. Glover, K. Head, and A. C. Long, "Mapping of the fluid distribution in impregnated reinforcement textiles using Magnetic Resonance Imaging: Application and discussion", *Composites Part A: Applied Science and Manufacturing,* vol. 42, no. 10, pp. 1369-1379, 2011.

[88] T. Okabe, H. Matsutani, T. Honda, and S. Yashiro, "Numerical simulation of microscopic flow in a fiber bundle using the moving particle semi-implicit method", *Composites Part A: Applied Science and Manufacturing,* vol. 43, no. 10, pp. 1765-1774, 2012.

[89] H. Tan, and K. M. Pillai, "Fast liquid composite molding simulation of unsaturated flow in dual-scale fibre mats using the imbition characteristics of a fabric-based unit cell", *Polymer Composites,* vol. 31, no. 10, pp. 1790-1807, 2010.

[90] C. C. Wong, "Modelling the effects of textile preform architecture on permeability", PhD tesis, University of Nottingham, Nottingham, 2006.

[91] L. Salvo, P. Cloetens, E. Maire, S. Zabler, J. J. Blandin, J. Y. Buffière, W. Ludwig, E. Boller, D. Bellet, and C. Josserond, "X-ray micro-tomography an attractive characterisation technique in materials science", *Nuclear Instruments and Methods in Physics Research Section B: Beam Interactions with Materials and Atoms,* vol. 200, pp. 273-286, 2003.

[92] G. Requena, G. Fiedler, B. Seiser, P. Degischer, M. Di Michiel, and T. Buslaps, "3D-Quantification of the distribution of continuous fibres in unidirectionally reinforced composites", *Composites Part A: Applied Science and Manufacturing,* vol. 40, no. 2, pp. 152-163, 2009.

[93] M. Rodríguez Hortalá, G. Requena, B. Seiser, P. Degischer, M. Di Michiel, and T. Buslaps, "3D-characterisation of continuous fibre reinforced composites (ICCM17)", in 17th International Conference on Composite Materials, Edinburgh, 2009.

[94] P. Badel, E. Vidal-Sallé, E. Maire, and P. Boisse, "Simulation and tomography analysis of textile composite reinforcement deformation at the mesoscopic scale", *Composites Science and Technology,* vol. 68, no. 12, pp. 2433-2440, 2008.

[95] Y. Mahadik, and S. R. Hallet, "Characterisation of 3d woven composite internal architecture and effect of compaction", in 17th International Conference on Composite Materials (ICCM17), Edinburgh, 2009.

[96] P. Spanne, C. Raven, I. Snigireva, and A. Snigirev, "In-line holography and phase-contrast microtomography with high energy x-rays", *Physics in Medicine and Biology,* vol. 44, no. 3, pp. 741, 1999.

[97] C. Antoine, P. Nygård, Ø. W. Gregersen, R. Holmstad, T. Weitkamp, and C. Rau, "3D images of paper obtained by phase-contrast X-ray microtomography: image quality and binarisation", *Nuclear Instruments and Methods in Physics Research Section A: Accelerators, Spectrometers, Detectors and Associated Equipment,* vol. 490, no. 1-2, pp. 392-402, 2002.

[98] F. Malmberg, J. Lindbad, C. Östlund, K. M. Almgren, and E. K. Gamstedt, "Measuring fibre-fibre contact in 3D images of fibrous materials", Centre for image analysis, Swedish University of Agricultural Sciences, Uppsala.

[99] C. Eberhardt, and A. Clarke, "Fibre-orientation measurements in short-glass-fibre composites. Part I: automated, high-angular-resolution measurement by confocal microscopy", *Composites Science and Technology,* vol. 61, no. 10, pp. 1389-1400, 2001.

[100] N. C. Davidson, A. R. Clarke, and G. Archenhold, "Large-area, high-resolution image analysis of composite materials", *Journal of Microscopy,*

vol. 185, no. 2, pp. 233-242, 1997.

[101] K. R. Castleman, and I. T. Young, "Fundamentals of Microscopy", *Microscope Image Processing*, Q. Wu, F. A. Merchant and K. R. Castleman, eds., pp. 11-24, 2008.

[102] S. J. Jhaveri "Improving an automated mosaicing algorithm for wide-field microscopy ", Master thesis, Drexel University 2010.

[103] B. Luong. "FFT-based convolution"; www.mathworks.co.uk/matlabcentral/fileexchange/24504-fft-based-convolution, (last accessed: 15.April 2013).

[104] J. Gajdosík, J. Zeman, and M. Sejnoha, "Qualitative analysis of fiber composite microstructure: Influence of boundary conditions", *Probabilistic Engineering Mechanics,* vol. 21, no. 4, pp. 317-329, 2006.

[105] C. Redon, L. Chermant, J.-L. Chermant, and M. Coster, "Automatic image analysis and morphology of fibre reinforced concrete", *Cement and Concrete Composites,* vol. 21, no. 5-6, pp. 403-412, 1999.

[106] R. Blanc, C. Germain, J. P. D. costa, P. Baylou, and M. Cataldi, "Fiber orientation measurements in composite materials", *Composites Part A: Applied Science and Manufacturing,* vol. 37, no. 2, pp. 197-206, 2006.

[107] J. C. Russ, *The Image Processing Handbook Fifth Edition*, 2007.

[108] R. A. Lotufo, R. Audigier, A. V. Saúde, and R. C. Machado, "Morphological Image Processing", *Microscope Image Processing*, Q. Wu, F. A. Merchant and K. R. Castleman, eds., pp. 113 - 157: Elsevier Inc., 2008.

[109] K. R. Castleman, "Image Digitization", *Microscope Image processing*, Q. Wu, F. A. Merchant and K. R. Castleman, eds., pp. 27-37, 2008.

[110] B. Paluch, "Analysis of geometric imperfections affecting the fibers in unidirectional composites", *Journal of Composite Materials,* vol. 30, no. 4, pp. 454-485, 1996.

[111] K. K. Kratmann, M. P. F. Sutcliffe, L. T. Lilleheden, R. Pyrz, and O. T. Thomsen, "A novel image analysis procedure for measuring fibre misalignment in unidirectional fibre composites", *Composites Science and Technology,* vol. 69, no. 2, pp. 228-238, 2009.

[112] I. Smolyaninov, "Optical microscopy beyond the diffraction limit", *HFSP journal,* vol. 2, no. 3, pp. 129-131, 2008.

[113] M. Olave, A. Vanaerschot, S. V. Lomov, and D. Vandepitte, "Internal geometry variability of two woven composites and related variability of the stiffness", *Polymer Composites,* vol. 33, no. 8, pp. 1335-1350, 2012.

[114] X. Zhang, and P. L. Rosin, "Superellipse fitting to partial data", *Pattern Recognition,* vol. 36, no. 3, pp. 743-752, 2003.

[115] J. Summerscales, and P. M. Russel, "Observations on the fibre distribution and fibre strain in a woven fabric reinforcement", *Advanced Composites Letters,* vol. 13, no. 3, 2004.

[116] Y. Nakanishi, K. y. Matsumoto, T. Kurashiki, and M. Zako, "Multiscale analysis of material damping properties for textile composites", in 13th European Conference on Composite Materials (ECCM13), Stockholm, 2008.

[117] A. Okabe, B. Boots, and K. Sugihara, *Spatial Tessellations. Concepts and Applications of Voronoi Diagrams.*: J. Wiley and Sons, 1992.

[118] T. Pietsch, N. Gindy, and A. Fahmi, "Nano- and micro-sized honeycomb patterns through hierarchical self-assembly of metal-loaded diblock copolymer vesicles", *Soft Matter,* vol. 5, pp. 2188-2197, 2008.

[119] J. Zangenberg, J. B. Larsen, R. C. Østergaard, and P. Brøndsted, "Methodology for characterisation of glass fibre composite architecture", *Plastics, Rubber and Composites,* vol. 41, no. 4-5, pp. 187-193, 2012.

[120] P. Potluri, and T. V. Sagar, "Compaction modelling of textile preforms for composite structures", *Composite Structures,* vol. 86, no. 1-3, pp. 177-185, 2008.

[121] D. Engwirda. "Mesh 2D version 24: 2D unstructured mesh generation for polygonal geometry. Matlab Toolbox, available on The MathworksTM file exchange";
http://www.mathworks.com/matlabcentral/fileexchange/25555-mesh2d-automatic-mesh-generation, (last accessed: January 2011, 2011).

[122] Y. Fujita, T. Kurashiki, H. Yamatsuka, and M. Zako, "A proposal of FE modeling of unidirectional composite considering uncertain micro structure", in 18th International Conference on Composite Materials (ICCM18), Jeju Island, South Korea, 2011.

[123] S. Amico, and C. Lekakou, "An experimental study of the permeability and capillary pressure in resin-transfer moulding", *Composites Science and Technology,* vol. 61, no. 13, pp. 1945-1959, 2001.

[124] J. Lee, and L. T. Drzal, "Surface characterization and adhesion of carbon fibers to epoxy and polycarbonate", *International Journal of Adhesion and Adhesives,* vol. 25, no. 5, pp. 389-394, 2005.

[125] L. Yao, M. Li, Q. Wu, Z. Dai, Y. Gu, Y. Li, and Z. Zhang, "Comparison of sizing effect of T700 grade carbon fiber on interfacial properties of fiber/BMI and fiber/epoxy", *Applied Surface Science,* vol. 263, pp. 326-333, 2012.

[126] H. K. Versteeg, and W. Malalasekera, *An introduction to computational*

fluid dynamics - The finit volume method, 2nd ed., Harlow, UK: Pearson Eduction Ltd., 2007.

[127] O. Zikanov, *Essential computational fluid dynamics*, Hoboken, New Jersey: John Wiley & Sons, Inc, 2010.

[128] Fluent. "Ansys Fluent 12.0/12.1 Documentation"; www.sharcnet.ca/Software/Fluent12/index.htm, (last accessed: 2013).

[129] P. Latil, L. Orgéas, C. Geindreau, P. J. J. Dumont, and S. Rolland du Roscoat, "Towards the 3D in situ characterisation of deformation micro-mechanisms within a compressed bundle of fibres", *Composites Science and Technology,* vol. 71, no. 4, pp. 480-488, 2011.

[130] O. Gal. "Fit ellipse"; www.mathworks.com/matlabcentral/fileexchange/3215-fitellipse, (last accessed: 10 March 2013).

Appendix

A. Equations governing the fluid flow

A.1 Conservation of mass principle

A.1.1 General conservation of mass theorem

The mass conservation law states that mass can neither be created nor destroyed. Hence, the net mass change, *dm*, of a system during a time interval, *dt*, is equal to the difference in flow rates, $\dot{m}$, entering and leaving the system (subscripts *in* and *out* respectively) [20].

$$\frac{dm}{dt} = \dot{m}_{in} - \dot{m}_{out} \qquad \text{Eq. 38}$$

The mass of the fluid in the system moves with the liquid velocity [83]. The differential mass flow rate over the complete surface areas, *A*, of the inlets and outlets becomes therefore:

$$\dot{m}_{in} - \dot{m}_{out} = \int \rho v \, dA \qquad \text{Eq. 39}$$

It should be kept in mind that the fluid velocity, *v*, is the velocity normal to the surface area. The density of the fluid, *ρ*, does not have to be constant, implying that a conservation of volume theorem does not exist. The change of the amount of mass in the system with a volume, *V*, over a defined time interval is:

$$\frac{dm}{dt} = \frac{d}{dt}\int \rho dV \qquad \text{Eq. 40}$$

Rearranging Eq. 38 and inserting Eq. 39 and Eq. 40 will yield the general law for the conservation of mass:

$$\frac{d}{dt}\int \rho dV + \int \rho v \, dA = 0 \qquad \text{Eq. 41}$$

Considering that the surface area of the system is enclosing its complete volume, the 'divergence theorem' (Gauss's theorem) can be applied:

$$\iint_A v\, dA = \iiint_V \nabla v\; dV \qquad \text{Eq. 42}$$

with ∇ as differential operator for the fluid velocity vector. Hence the conservation of mass equation (Eq. 41) can be written as:

$$\int \left(\frac{d\rho}{dt} + \rho \nabla v\right) dV = 0 \qquad \text{Eq. 43}$$

The volume, V, is of arbitrary shape and size and, employing the 'proof of contradiction', it can only be satisfied if the term in the round brackets is zero. Therefore, the conservation of mass statement can be further simplified to:

$$\frac{d\rho}{dt} + \rho \nabla v = 0 \qquad \text{Eq. 44}$$

This equation is also referred to as the 'continuity equation'.

A.1.2 Steady state flow

For a steady-state case, the mass of the fluid in the system is constant.

$$\frac{dm}{dt} = 0 \qquad \text{Eq. 45}$$

The flow rate into, $\dot{m}_{in}$, and out, $\dot{m}_{out}$, of the system is therefore equal.

A.1.3 Incompressible fluid flow

With the assumption of an incompressible fluid, the density becomes a scalar. The conservation of mass (Eq. 44) simplifies therefore to:

$$\nabla v = 0 \qquad \text{Eq. 46}$$

The conservation of mass becomes independent of the fluid properties and is completely determined by the fluid velocity which is transporting the mass.

A.2 Conservation of momentum (Navier-Stokes)

The conservation of momentum is based on Newton's second law [20], stating that the force, *F*, is a product of the mass of an object, *m*, and its acceleration, a_c.

$$F = ma_c \qquad \text{Eq. 47}$$

The forces acting on the fluid during flow are pressure, gravity and viscous forces within the fluid (identified by the subscripts). The mass of the fluid in case of transient flow are the acceleration (subscript unsteady) and convection acceleration (subscript convection). Newton's second law can therefore be written as:

$$F_{pressure} + F_{viscous} + F_{gravity} = m \cdot \left(a_{unsteady} + a_{convection}\right) \qquad \text{Eq. 48}$$

For the flow considered in this work, forces exerted on the fluid by gravity are ignored. Because the velocities are considered to be small, fluid and gas incompressibility can be assumed. In addition, isothermal flow is assumed. Newton's second law can therefore be expressed in the form of the Navier-Stokes equation:

$$\underbrace{-\nabla p}_{F_{pressure}} + \underbrace{\mu \nabla^2 v}_{F_{viscous}} = \rho \left(\underbrace{\frac{dv}{dt}}_{F_{acceleration}} + \underbrace{v \nabla v}_{F_{convection}}\right) \qquad \text{Eq. 49}$$

For the assumption of strain rate independence of the fluid viscosity, μ_f = constant, (Newtonian fluid), the viscous forces, $F_{viscous}$, are linearly proportional to the viscosity.

$$\underbrace{\rho(v \nabla v)}_{F_{convection}} = \underbrace{-\nabla p}_{F_{pressure}} + \underbrace{\mu \nabla^2 v}_{F_{viscous}} \qquad \text{Eq. 50}$$

Eq. 50 clearly shows that the Navier-Stokes equation is a function of both, fluid pressure and fluid velocity. In contrast, Darcy's law (Section 2.1.1) is only a function of the applied pressure. For very small Reynold's number, $Re \ll 1$, (Section 2.1.2) creeping flow can be assumed. Convection between single fluid layers can be neglected and the Navier-Stokes equation reduces to the so called Stokes flow:

$$\nabla p = \mu \nabla^2 v \qquad \text{Eq. 51}$$

B. Image processing in Matlab

The image processing described in Section 3.3 was implemented in Matlab®. The following description illustrates the layout of the code and the modules employed.

Retile images

The captured micrographs have a varying overlap due to the finite accuracy and eccentricity of the stepping motors of the automated stage. Images following the known capturing raster are loaded. The overlap between two adjacent images is determined using the fast Fourier transform (FFT) based convolution [103]. Manual overwrite of these positions is enabled. After determining the exact overlap the image tiles are assembled (Figure 77). New sub-tiles are created from the complete set of images with a constant overlap. This enables to analyse a large area by means of analysing small sub-domains. This overcomes memory constrains which might be encountered.

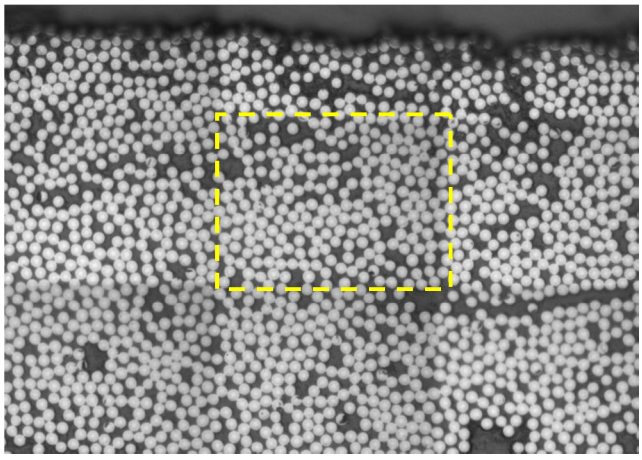

Figure 77: Example of tiled micrographs. The area of a single micrograph is outlined within the image. The different micrographs are assembled and blind together to guarantee a smooth transition between the images.

Image pre-filter

The retiled images are loaded subsequently. The rough filament positions are then determined by:

1) Image enhancement
   - Apply image blur
   - Greyscale erosion and dilation

2) Determine objects
   - Thresholding with empirical threshold
   - Watershed remaining objects
   - Remove noise
   - Clear objects from the image boundary (Figure 78A)
   - Determine object centres (Figure 78B)

A) B)

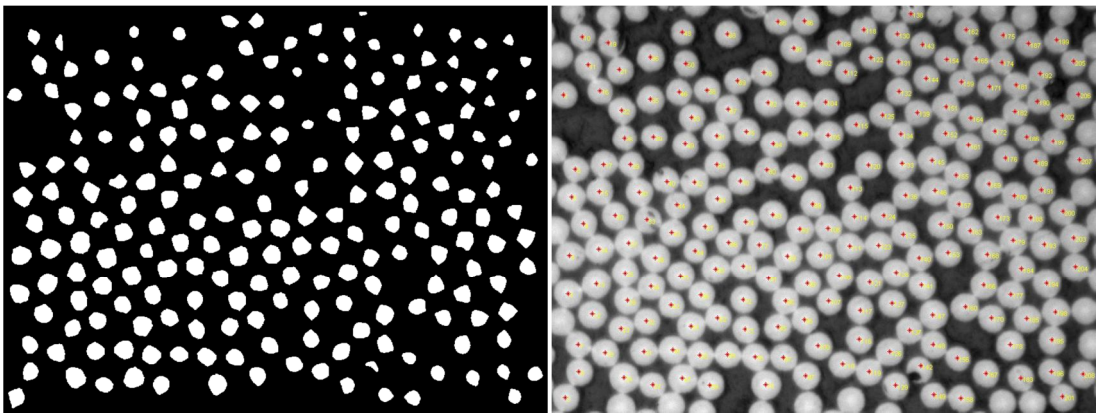

Figure 78: Detection of areas of interest. A) Detected areas of filaments. B) The corresponding centre points marked on the original image.

Analyse single filaments

Loop through all determined objects by placing a stencil centred on the determined positions. Analyse these areas as outlined in Section 3.3.2:

1) Image convolution
2) Average filter
3) Determine canny edges on the enhanced image
4) Fit ellipse [130] to the canny edge
5) Calculate the colour gradients of the image after step 2
6) Remove edges located within the fibre cross-section using the ellipse determined in step 4
7) Determine the distance of the remaining points of the edge
8) Determine the closest edge points for every 5 degrees and remove all others (only closest edges to image centre remain)
9) Fit ellipse [130] to the remaining data points
10) Iteratively remove outliers

Assemble data

The location of the detailed filament geometries is determined for the every sub-tile (Figure 79). This enables the analysis of the exact spatial position of every single filament in the complete fibre bundle. Based on the image analysis, a false detection of less than 2 % was estimated.

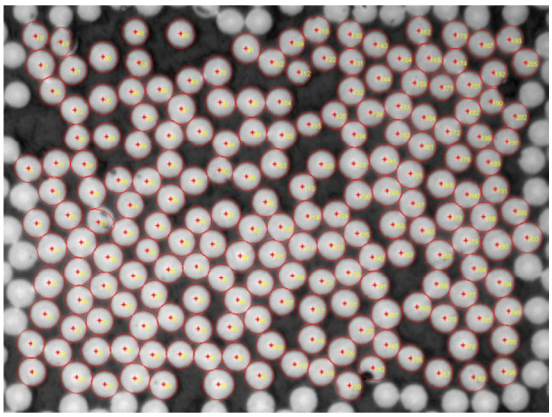

Figure 79: Assembly of all detected filament boundaries overlaid on the original input image.

C. Material data

C.1 Fibre reinforcement

Producer :	Sigmatex
Product Code :	PC2510600
Areal density :	300 g/m^2 confirmed by measurements on specimens
Weave style :	Plain weave with minimum crimp in the warp yarn (non-crimp fabric)
Warp	
Warp yarns :	T700SC 12K 50C
Ends / 10cm :	34 ± 2.5
Filaments diameter :	7 μm
Density :	1.80 g/cm^3 ± 0.04
Weft	
Weft yarns :	Fusible combi-yarn (225Dtex glass+)
Picks / 10cm :	30 ± 2.5

References

Fabric data provided by:

Sigmatex (UK) Limited (www.sigmatex.com)

Filament data extracted from datasheet Toroyca:

www.toraycfa.com/pdfs/T700SDataSheet.pdf

(last visited 08 March 2013)

C.2 Resin

Producer : Advanced Composites Group (ACG)

Product name : MVR 444

Catalyst : One component, pre-catalysed epoxy resin

Degassing : Degassing recommended, but not mandatory because resin is blended under full vacuum

Resin gelation : 130 min @ 130 °C

Viscosity :

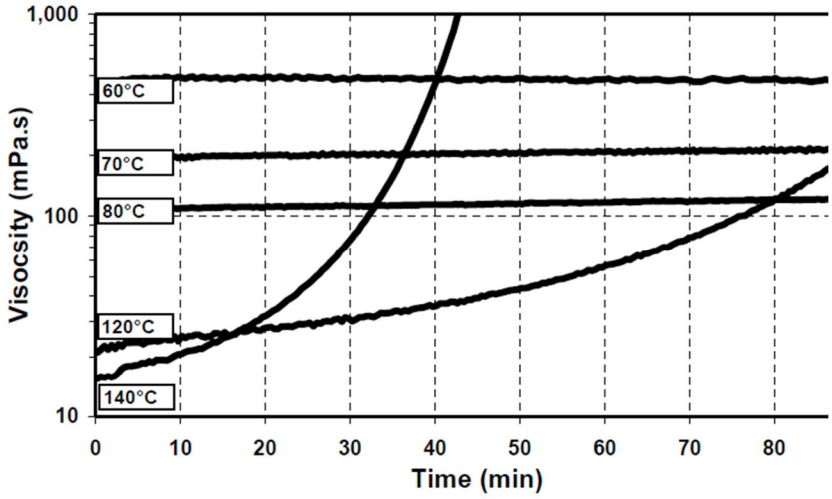

Reference

Data extracted from datasheet:

http://www.advanced-composites.co.uk/data_catalogue/catalogue%20files/pds/PDS1190_MVR444_Issue1a.pdf

(last visited 08 March 2013)

D. Statistical distributions

D.1 Normal distribution

For the description of a dataset, the normal distribution is often used:

$$f_{(x)}^{normal} = \frac{1}{\sigma\sqrt{2\pi}} e^{-\frac{1}{2}\left(\frac{x-\mu}{\sigma}\right)^2} \quad \text{Eq. 52}$$

The resulting bell shaped curve of the probability density function (Figure 80) of a random variable x, is fully described by the distribution mean, μ, and standard deviation, σ.

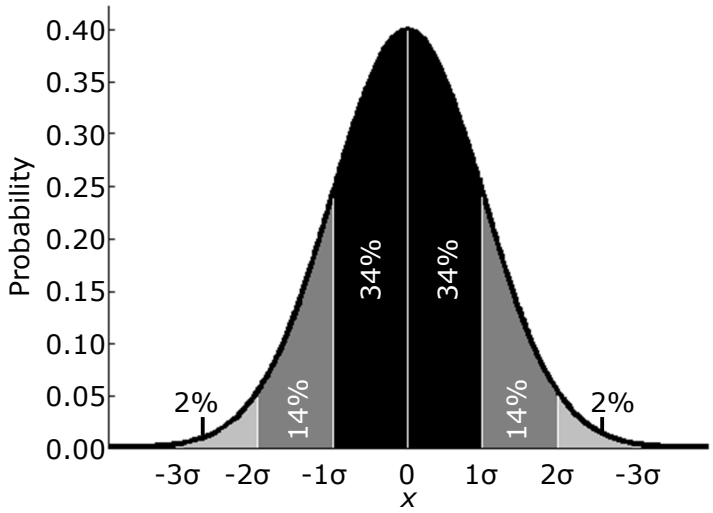

Figure 80: Gaussian normal distribution with a mean, μ=0 and standard deviation, σ.

With

$$\xi = \frac{x - \mu}{\sigma} \quad \text{Eq. 53}$$

this function can be written as

$$f_{(\xi)}^{normal} = \frac{1}{\sigma\sqrt{2\pi}} e^{-\frac{1}{2}(\xi)^2} \quad \text{Eq. 54}$$

The probability that a random number x will fall into an interval -∞ to x is given by the cumulative distribution function Eq. 55. This function (Figure 81) represents the area under the curve of Figure 80.

$$F_{(x)}^{normal} = \int f_{(x)}^{normal}\, dx \quad \text{Eq. 55}$$

In order to simulate a random number from this distribution, the cumulative distribution function can be inverted Eq. 56. The advantage of this representation is that if a uniformly distributed random number, *u*, between 0 and 1 can be generated a corresponding normally distributed value can be determined. Hence,

$$x = F_{(u)}^{-1} \qquad \text{Eq. 56}$$

will generate a random number, *x*, based on a uniformly distributed random number *u*. The resulting data will look like Figure 81.

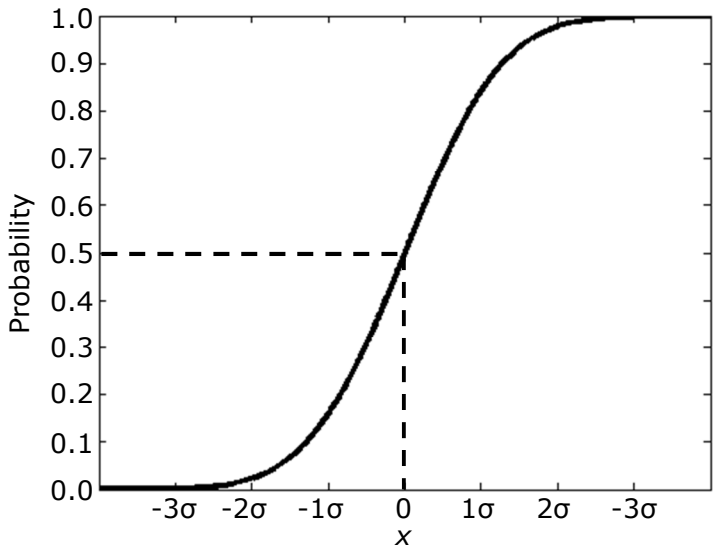

Figure 81: Cumulative distribution function of a normal distribution

D.2 Truncated normal distribution

When the data set exhibits natural lower and upper truncation limits, *a* and *b*, the normal distribution can be adjusted accordingly. Of course, this assumes that the remaining data points are normally distributed. Introducing the following notation:

$$\alpha = \frac{a - \mu}{\sigma} \qquad \text{Eq. 57}$$

$$\beta = \frac{b - \mu}{\sigma} \qquad \text{Eq. 58}$$

The corresponding area of the cumulative distribution function, enclosed by these truncation limits is:

$$Z = F_{(\beta)}^{normal} - F_{(\alpha)}^{normal} \qquad \text{Eq. 59}$$

The probability density function of the normal distribution can now be adjusted, incorporating the upper and lower truncation limits. The distribution will be renormalized by Z so that $\int f_{(x)}^{trunc} = 1$. Hence, the two sided truncated normal distribution can be expressed as

$$f_{(x)}^{trunc} = \frac{1}{\sigma Z} f_{(\xi)}^{normal} \quad \text{Eq. 60}$$

This expression reduces to Eq. 9 with the convention that

$$f_{(\beta)}^{normal} = 1 \quad \text{for} \quad b = \infty \quad \text{Eq. 61}$$

and

$$f_{(\alpha)}^{normal} = 0 \quad \text{for} \quad \mathrm{a} = -\infty \quad \text{Eq. 62}$$

Accordingly, the distribution can be truncated on one side only, if one truncation limit, *a* or *b*, is defined and the other is set to ±∞ respectively.

The cumulative distribution function in this case can be expressed as

$$F_{(x)}^{trunc} = \frac{1}{Z}\left(F_{(\xi)}^{normal} - F_{(\alpha)}^{normal}\right) \quad \text{Eq. 63}$$

Due to the normalisation by Z, the same concept of generating a random truncated normally distributed number can be employed as explained previously. The inverse cumulative distribution function is now defined as:

$$x = \mu + \sigma F_{(u)}^{-1}\left[F_{(\alpha)}^{normal} + u \cdot Z\right] \quad \text{Eq. 64}$$

D.3 Mixture of two nested truncated normal distributions

It is possible that the histogram of measured data exhibits more than one peak. These distributions might be fitted with several nested distributions. These multivariate distributions have to be weighted by a mixture probability in such a way that the sum of the weights is equal to 1. In case of two distinct peaks a bivariate distribution might be a good approximation of the dataset. In case of employing the mixture of two nested truncated distributions the following probability density function would result:

$$f_{(x)}^{2trunc} = p \cdot f_{1(x)}^{trunc} + (1-p) \cdot f_{2(x)}^{trunc} \quad \text{Eq. 65}$$

Where f_1 and f_2 represent truncated normal distributions with each exhibiting their own mean and standard deviation. The mixture probability, p, blends these two functions into each other. Resulting probability density function can therefore look like Figure 82. Depending on the factor p, the function peaks can be more or less pronounced.

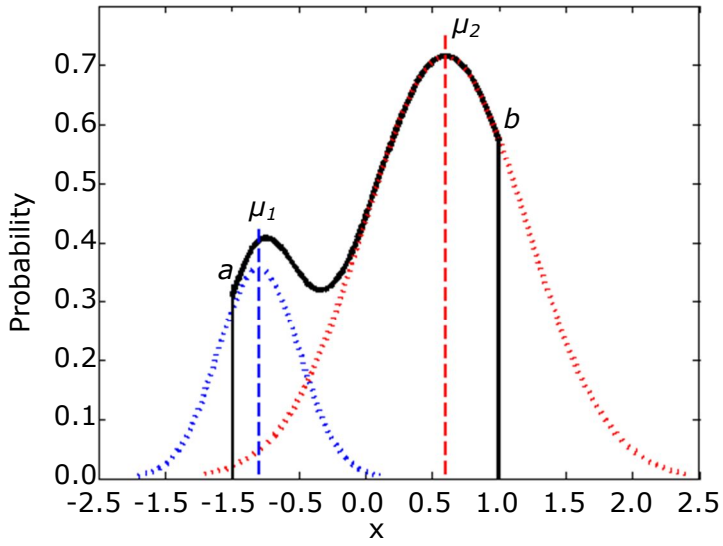

Figure 82: Example of a mixture of two truncated normal distributions (black). The normal distributions f_1 and f_2 (blue and red) have the following mean, μ, and standard deviations, σ: μ_1=-0.8, σ_1=0.3, μ_2=0.6, σ_2=0.6. The lower and upper truncation points, a and b, are -1 and 1 respectively and the mixture probability, p=0.2

Accordingly, the cumulative distribution function can be expressed as:

$$F_{(x)}^{2trunc} = \int \left(p \cdot f_{1(x)}^{trunc} + (1-p) \cdot f_{2(x)}^{trunc}\right) dx \quad \text{Eq. 66}$$

which can be interpreted as

$$F_{(x)}^{2trunc} = p \cdot F_{1(x)}^{trunc} + (1-p) \cdot F_{2(x)}^{trunc} \quad \text{Eq. 67}$$

In order to generate a random number, x, based on a uniformly distributed number between 0 and 1, it is advantageous not to invert Eq. 67 but to employ Eq. 64 instead. The generation of a random number x is then substituted by generating two random numbers, x_1 and x_2, based on the inverse cumulative distribution function of each distribution. A third uniformly distributed number will then be utilised to choose which generated number will be used based on the mixture probability factor p. This approach can then be extended easily to a multivariate distribution.

D.4 Log-normal distribution

If it is possible that data distributed as shown in Figure 83 can be transformed to a form such as shown in Figure 80 by plotting the data on the abscissa in a logarithmic scale, then this distribution is called a log-normal distribution.

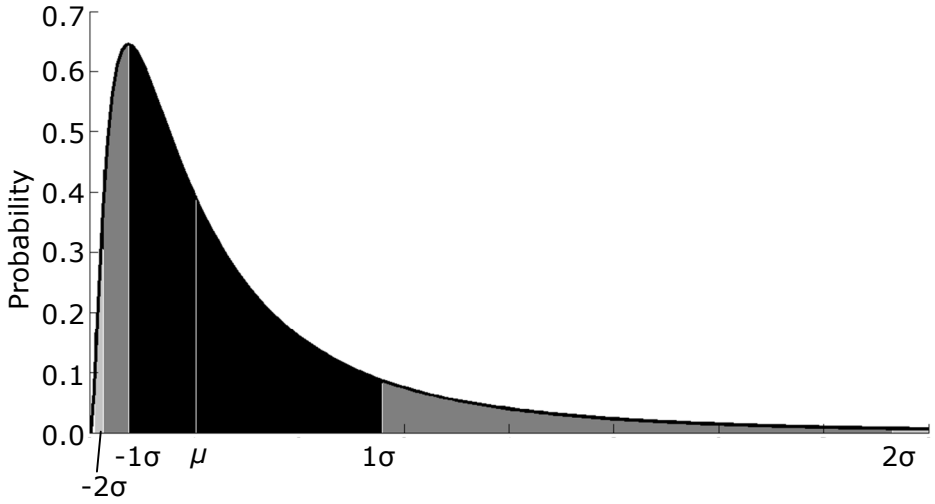

Figure 83: Example log-normal distribution with the location parameter μ and the scale parameter σ.

The distribution mean, μ, is called the location parameter in a log-normal distribution and the standard deviation, σ, is the scale parameter. This two parameter log-normal distribution can be extended to a three parameter distribution if necessary. A threshold can be employed which is subtracted from the measurement data before it is transformed into a logarithmic scale.

E. Steady state Fluent® journal file

The data below is a typical Fluent® journal file (.jou) used in the analysis of steady state flow in Chapter 4. Loading and executing the file enables automated analysis of a two-dimensional model domain.

The following denotations are used:

- wall-1 = inlet (left) boundary
- wall-2 = outlet (right) boundary
- wall-3 and wall-4 = symmetry (top and bottom) boundaries
- As pressure drop in this example 2000 Pa is selected

The journal file:

```
;start fluent journal file
;*************************************************************
;read mesh
file import nastran bulkdata "Folder\FileName.bdf" yes
;*************************************************************
;scale to μm and smooth mesh
mesh scale 1e-006 1e-006
mesh swap-mesh-facesmesh smooth-mesh "skewness" 4 0.4
;*************************************************************
;define materials:
define materials copy fluid water-liquid
;set fluid cell zone condition to water:
define boundary-conditions modify-zones zone-type 1 fluid
define boundary-conditions fluid , yes water-liquid , , , , , , ,
;*************************************************************
;define boundary conditions:
mesh modify-zones zone-type wall-1 pressure-inlet
mesh modify-zones zone-type wall-2 pressure-outlet
mesh modify-zones zone-type wall-4 symmetry
mesh modify-zones zone-type wall-3 symmetry
mesh modify-zones zone-name symmetry-3 wall-3 ,
mesh modify-zones zone-name symmetry-4 wall-4 ,
mesh modify-zones zone-name pressure-outlet-2 wall-2 ,
mesh modify-zones zone-name pressure-inlet-1 wall-1 ,
```

```
define boundary-conditions pressure-inlet wall-1 yes no 2000 no 0 no yes
define boundary-conditions pressure-outlet wall-2 no 0 no yes no
;*****************************************************************
;set pressure-velocity scheme:
solve set p-v-coupling 24
solve set gradient-scheme yes
solve set discretization-scheme pressure 12
solve set discretization-scheme mom 1
;*****************************************************************
;set monitor convergence criteria:
solve monitors residual convergence-criteria 0.0001 0.0001 0.0001
;*****************************************************************
;start solution initialization with 200 Pa gauge pressure:
solve initialize set-defaults pressure 200
solve initialize initialize-flow
;run calculation with 3000 iterations:
solve iterate 3000
;*****************************************************************
;safe case data:
file write-case-data "FileName"
;write report of the areas occupied by the boundaries:
report surface-integrals area wall-1 wall-2 wall-4 wall-3 , yes "FileName.txt" yes
;write report of average flow velocities weighted by the element area:
report surface-integrals area-weighted-avg wall-1 wall-2 wall-4 wall-3 , x-velocity yes "FileName.txt" yes
;write report of the area occupied by the fluid:
report volume-integrals volume solid-5 , yes "FileName.txt" yes
;*****************************************************************
;end of journal file
```

F. Pressure drop and resulting velocity in steady state

The permeability is according to Darcy's law (Eq. 3) a material constant. The transverse flow through a hexagonal unit cell was simulated numerically to confirm that the inlet pressure does not affect the simulated value. Analysing a range of different input pressure gradients with several orders of magnitude difference showed a linear relationship with the predicted model output velocity using Ansys Fluent® (Figure 84). From this linear relationship it can be concluded that the permeability is a constant. The insensitivity of the applied pressure gradient on the resulting permeability is therefore confirmed. For the numerical simulation, any pressure gradient in the analysed range can be used to determine the permeability of a filament arrangement.

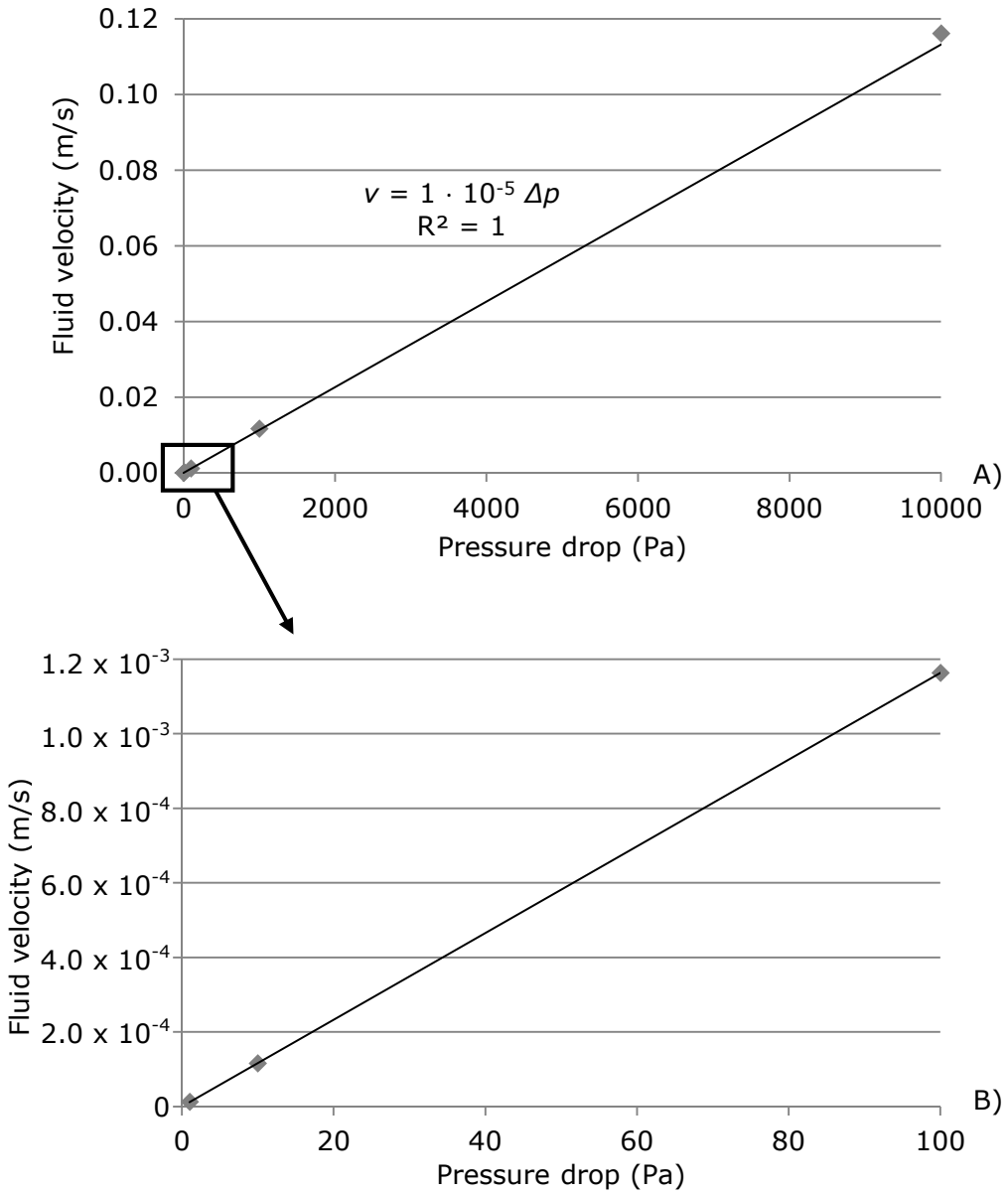

Figure 84: Resulting steady-state flow velocity for a hexagonal unit cell simulated in Ansys Fluent® at varying pressure gradients. A) A linear relationship is observed for the resulting velocity value as function of the applied pressure gradient. B) A magnification for small applied pressure gradients.

G. Circle intersections with boundaries

During generation of the statistically equivalent micro-structure, some of the circles will only be partially located within the domain of interest. The intersections of these circles with the domain boundaries need to be determined. These will form nodal points for the connectivity matrix during the meshing process. The intersections of the circles with the boundaries can be determined by applying the following procedure. The intersection of a line

$$y = mx + b \qquad \text{Eq. 68}$$

with a circle

$$(x - x_0)^2 + (y - y_0)^2 = r^2 \qquad \text{Eq. 69}$$

can be solved by substituting y in Eq. 69 with Eq. 68. After rearranging this Equation, the following expression (Eq. 70) can be derived

$$\underbrace{(m^2 + 1)}_{A}x^2 + \underbrace{(2mb - 2y_0m - 2y_0)}_{B}x + \underbrace{(y_0^2 - 2y_0b + x_0^2 - r^2 + b^2)}_{C} = 0 \qquad \text{Eq. 70}$$

which is the form a simple quadratic equation. Substituting the terms in the brackets with *A*, *B* and *C* the *x* coordinates of the intersections can be found by evaluating Eq. 71.

$$x_{1/2} = \frac{-B \pm \sqrt{B^2 - 4AC}}{2A} \qquad \text{Eq. 71}$$

Evaluating the term of the square root will give information about the number of expected intersections of the circle with the domain boundaries Eq. 72:

$$D = B^2 - 4AC \qquad \text{Eq. 72}$$

Two intersections are found for $D > 0$ and one intersection for $D = 1$.

H. Pressure drop in sequence of unit cells

It can be demonstrated that in the case of a sequence of unit cells connected in series (Section 4.2.2), the permeability is dominated by the smallest gap width, w_g. It can therefore be proven that the permeability in a sequence of filament pairs forming a flow channel is always lower than the permeability predicted by a periodic arrangement.

The permeability depends on the pressure drop which is a result of the minimum inter-filament distance in the case of transverse steady-state flow through filaments in a single unit cell. Gebart [49] determined the pressure drop Δp in this case as:

$$\Delta p = -\frac{1}{C1} \cdot \frac{\mu q}{r^2} \cdot \left(\frac{w_g}{r}\right)^{-2.5} \quad \text{Eq. 73}$$

For unit cells with varying dimensions and all other parameters kept constant, the pressure drop reduces to:

$$\Delta p = k\left(w_g\right)^{-2.5} \quad \text{Eq. 74}$$

The factor k represents in this case all constant parameters. Assuming n unit cells to be connected in series with no net flux through the horizontal model boundaries at constant V_f the Δp of the arrangement becomes equal to sum of all pressure drops:

$$\Delta p_i = k \sum_{i=1}^{n} \left(w_g\right)^{-2.5} \quad \text{Eq. 75}$$

Assuming this statement is valid for unit cells of different sizes connected in series, it can be demonstrated that for the case of two square shaped unit cells (n = 2) the permeability of the random arrangement (Figure 85B) will always be lower than regular arrangement with constant dimensions (Figure 85A). For these arrangements with constant filament radius, r, the V_f is defined as:

$$V_f = \frac{n \cdot \pi r^2}{\sum_{i=1}^{n} a_i^2} \quad \text{Eq. 76}$$

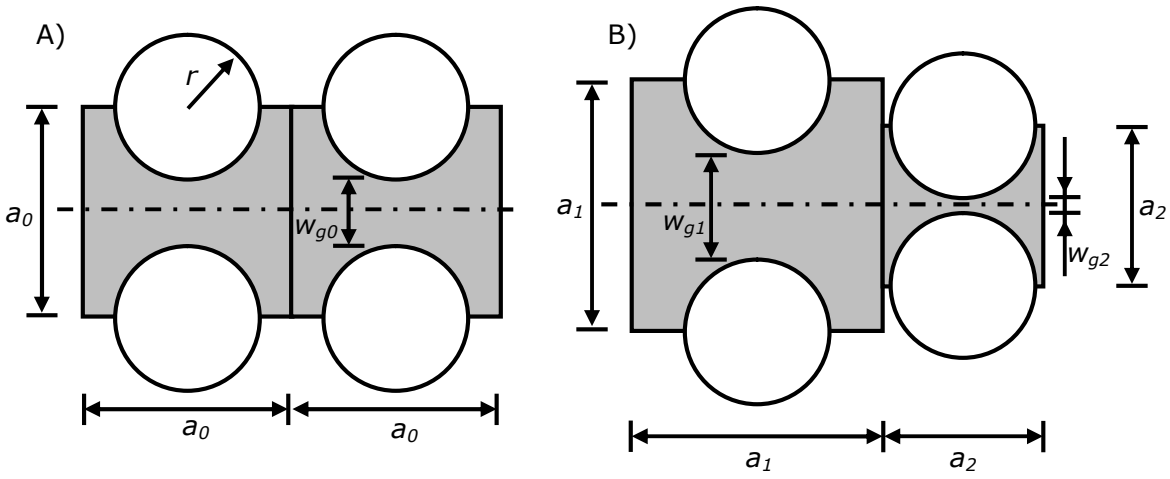

Figure 85: A) Two unit cells connected in series with constant and B) two unit cells connected in series with variable side length. The global V_f = 0.37 is identical in both cases.

The distance between two filaments in a square arrangement is defined by:

$$w_{gi} = a_i - 2r \qquad \text{Eq. 77}$$

Due to the presumed identical V_f (Eq. 76) of the series of unit cells in Figure 85A and Figure 85B it can be shown that:

$$a_1 = \sqrt{2a_0^2 - a_2^2} \qquad \text{Eq. 78}$$

The change of the inter-filament gap width as a result of the changing geometry can be expressed as

$$w_{g1} - w_{g0} = a_1 - a_0 \qquad \text{Eq. 79}$$

for the quadratic unit cell with increased dimension and

$$w_{g0} - w_{g2} = a_0 - a_2 \qquad \text{Eq. 80}$$

for the unit cell with a decrease in dimension compared to the periodic arrangement. Due to the non-linear relationship of the resulting pressure drop as a function of the gap between fibres (Eq. 74) the change in resulting inter-filament gaps has to be analysed. The hypothesis of a reduced permeability in the case of a random arrangement can be validated if the increase in width of one gap leads to an identical or larger decrease in the other gap width compared

to the original periodic arrangement. Hence, the following inequality has to be proven:

$$a_o - a_2 \geq^{?} a_1 - a_0 \qquad \text{Eq. 81}$$

substituting Eq. 78 in Eq. 81 leads to:

$$a_o - a_2 \geq^{?} \sqrt{2a_0^2 - a_2^2} - a_0 \qquad \text{Eq. 82}$$

adding a_0 and squaring the equation, it can be shown that

$$(a_o - a_2) > 0 \qquad \text{Eq. 83}$$

which is true. Therefore, the decrease in gap width, w_{g2}, is larger than the increase in w_{g1}. This larger decrease in gap width leads to a larger increase in pressure drop (Δp_2 - Δp_0) than the decrease in pressure drop (Δp_0 - Δp_1) due to the increased gap width of the other inter-filament gap (Figure 86). Therefore, the total pressure drop for the complete system will always be larger for a random arrangement compared to a periodic arrangement at identical V_f. Hence,

$$2\Delta p_0 < \Delta p_1 + \Delta p_2 \qquad \text{Eq. 84}$$

which implies that the permeability of the random system is lower than the permeability of the periodic system.

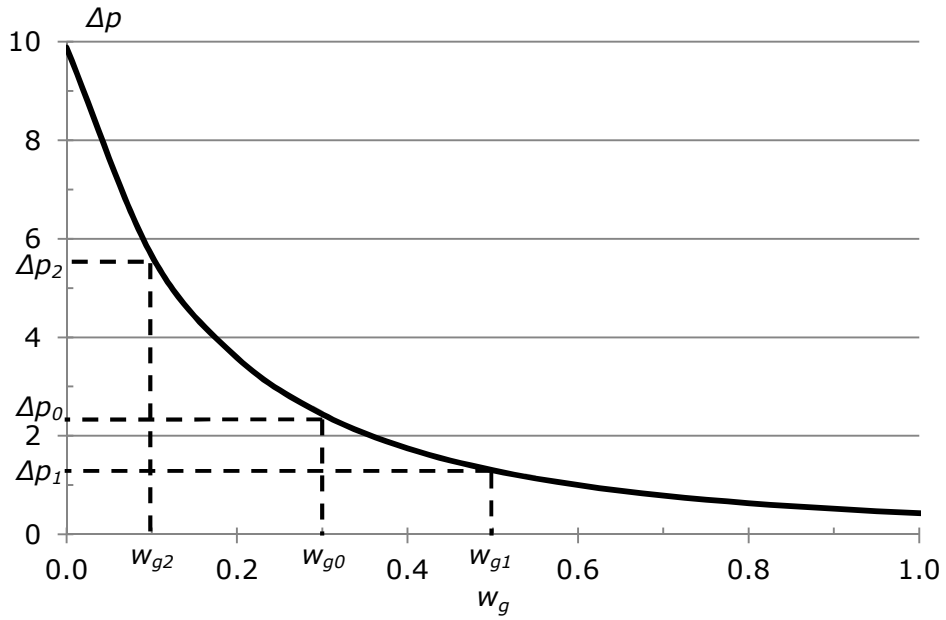

Figure 86: Pressure drop, Δp_i, in transverse flow through a filament pair as function of a gap, w_{gi}, formed between two filaments following Gebart [49]. The values shown are dimensionless to illustrate the trend.

I. Flow velocity distributions of a larger model

For steady-state transverse flow simulations as described in Chapter 4, the maps of fluid flow velocity show a few major flow channels, indicated by a high flow velocity (Figure 87A). The difference of fluid velocity in these channels and the surrounding material is significant. This leads to a right stewed distribution of the velocity data of the elements (Figure 87B), weighted by the element size (Section 4.3.3).

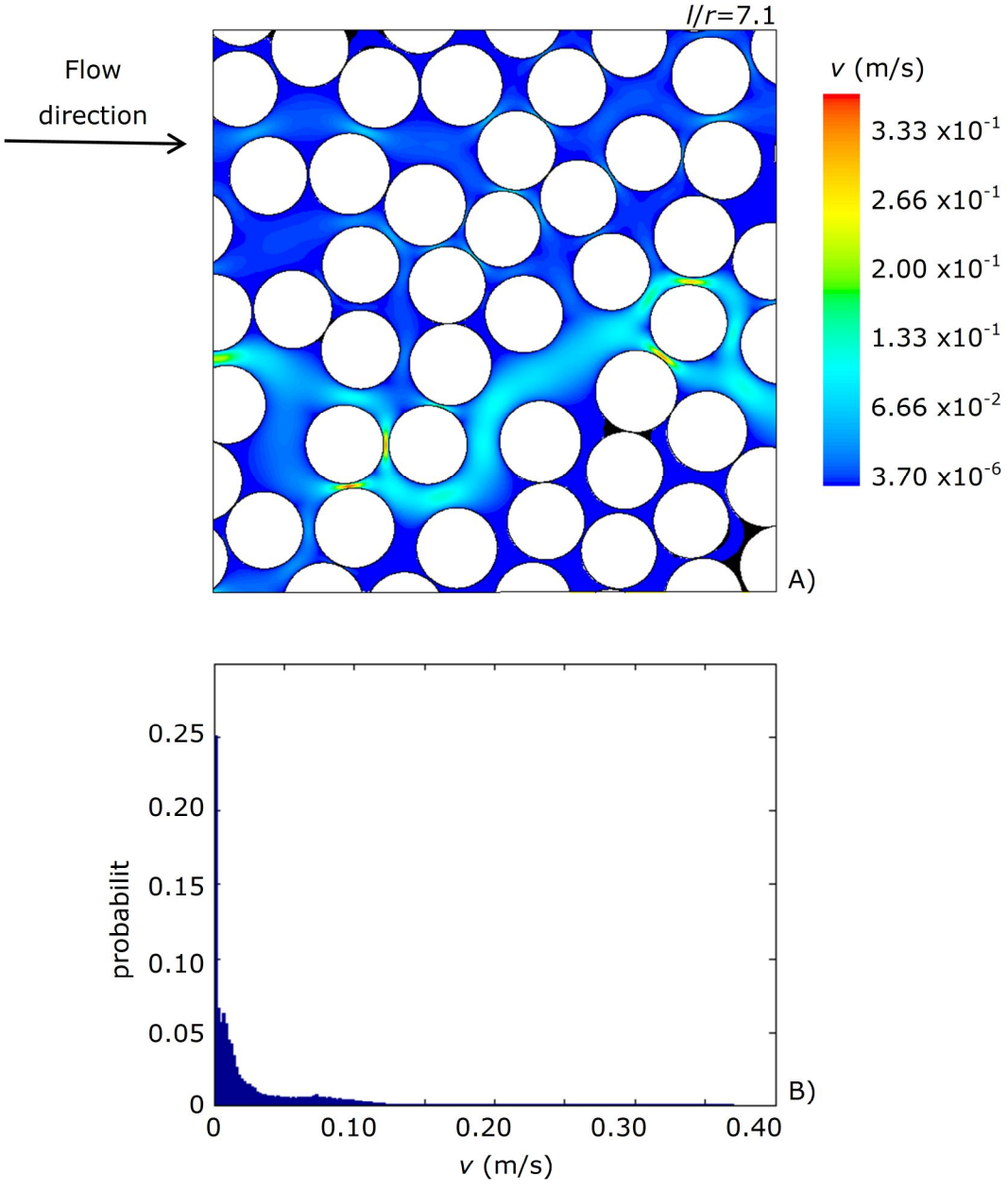

Figure 87: A) Map of the fluid flow velocities, v, of transverse flow through a random filament arrangement. B) The histogram of the distribution of the flow velocity, normalised by the minimum observed fluid velocity, v_{min}.

A log transform of these flow velocities enables to indicate peaks in the distributions (Figure 88B) which coincide with distinct areas in the map of fluid velocities in the micro-structure (Figure 88A). It was speculated that zones which exhibit low flow velocities in steady-state flow may indicate probable zones of void formation in the case of impregnating transient flow (Section 5.4.4). The larger model domain here results in more peaks of the histograms of the fluid flow distributions. With an increase in model size, the distribution is thought to converge in a similar way as the permeability values presented in Section 4.3. This indicates that this analysis may be valuable for small domains only.

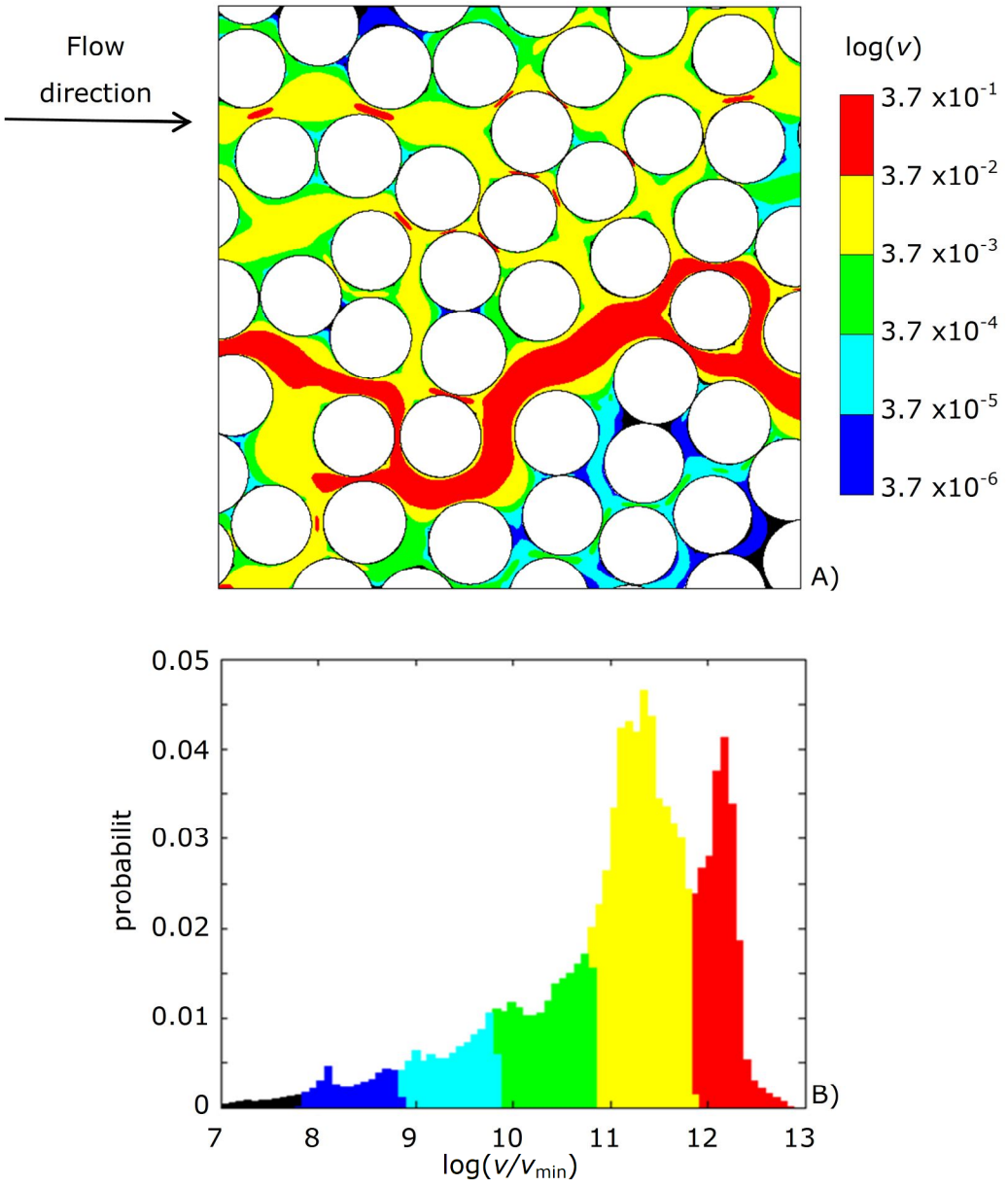

Figure 88: A) Map of the fluid flow velocities, v, of transverse flow through a random filament arrangement on a logarithmic scale. B) The histogram of the distribution of the flow velocity, normalised by the minimum observed fluid velocity, v_{min}.

J. Outline void detection code in Matlab

The void content presented in Section 5.2 was determined following the procedure outlined below implemented in Matlab®.

Retile images

The micrograph overlap was determined in the same way as described in Appendix B.

Detect fibre bundle boundary

Single tiles of the fibre bundle are subsequently loaded and analysed. The boundary of the complete fibre bundle is determined by:

1) Image enhancement
   - greyscale erosion and dilation
2) Determine the boundary
   - thresholding with empirical threshold
   - determine the maximum and minimum (upper and lower) boundary

Determine void content

Single tiles of the fibre bundle are subsequently loaded and analysed.

3) Image enhancement
   - Greyscale erosion and dilation
   - Increase contrast (unsharp)
4) Determine voids
   - Thresholding with empirical threshold
   - Fill holes in detected objects to account for bright areas due to debris or shallow sized voidage (Figure 67)
   - Remove noise
   - Remove long and slender objects which correspond to shading around local fibre clusters. These shades stem from the polishing process due to differences in stiffness of the fibres and surrounding matrix.

Assemble data

Assemble all data to determine the spatial position of the voidage within the fibre bundle.

K. Measured void distributions

This appendix presents the distributions for the measurement data presented in Section 5.2.2. The histograms for the measurements of flow longitudinal (Section K.1) and transverse (Section K.2) to the fibre bundle axis are presented.

K.1 Longitudinal flow

Void content measured in samples with flow longitudinal to the bundle axis.

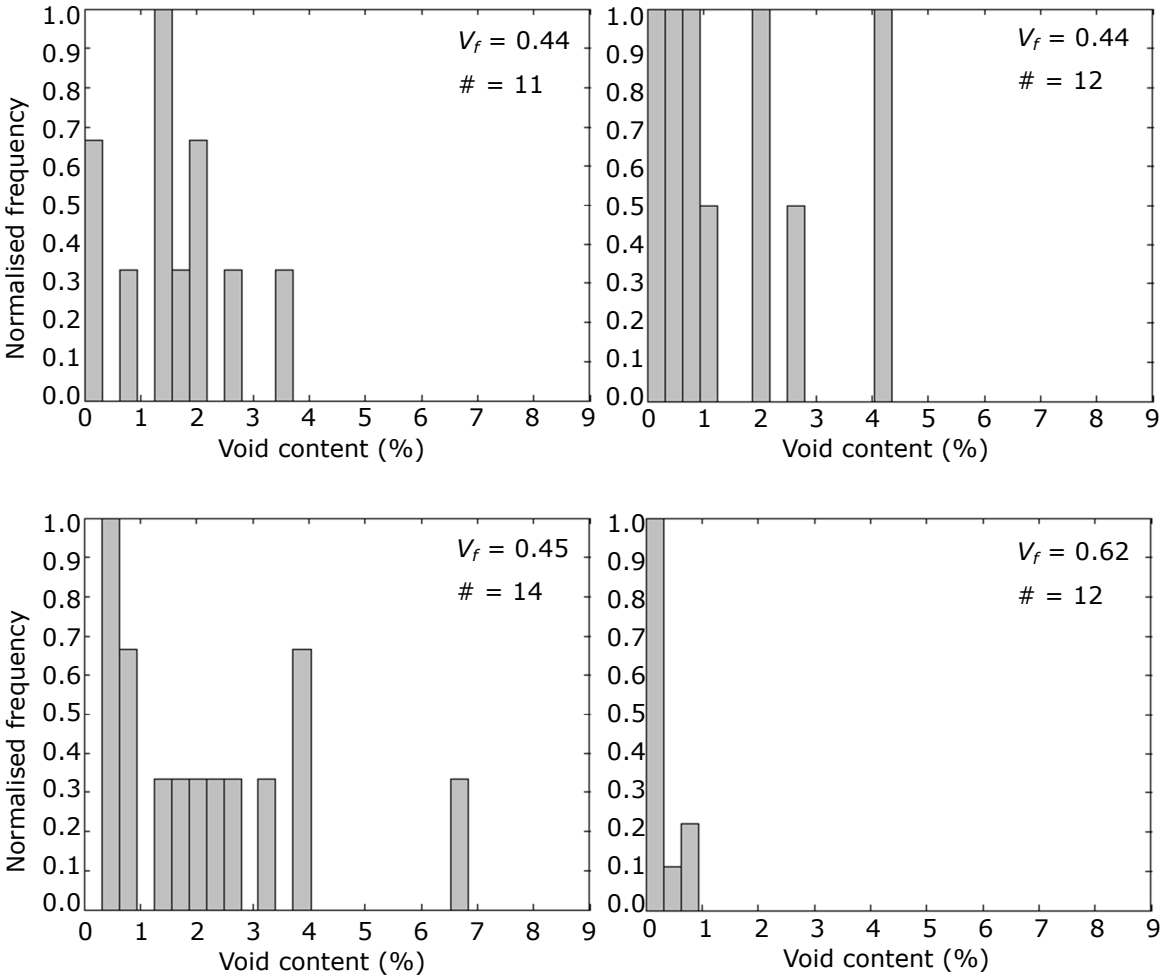

Figure 89: Histograms of void contents measured on samples produced by longitudinal flow. The frequencies are normalised by the maximum count. The analysed fibre volume fraction, V_f, and number of samples analysed, #, are shown. The histograms reflect the measurements presented in Section 5.2.

K.2 Transverse flow

Void content measured in samples with flow transverse to the bundle axis.

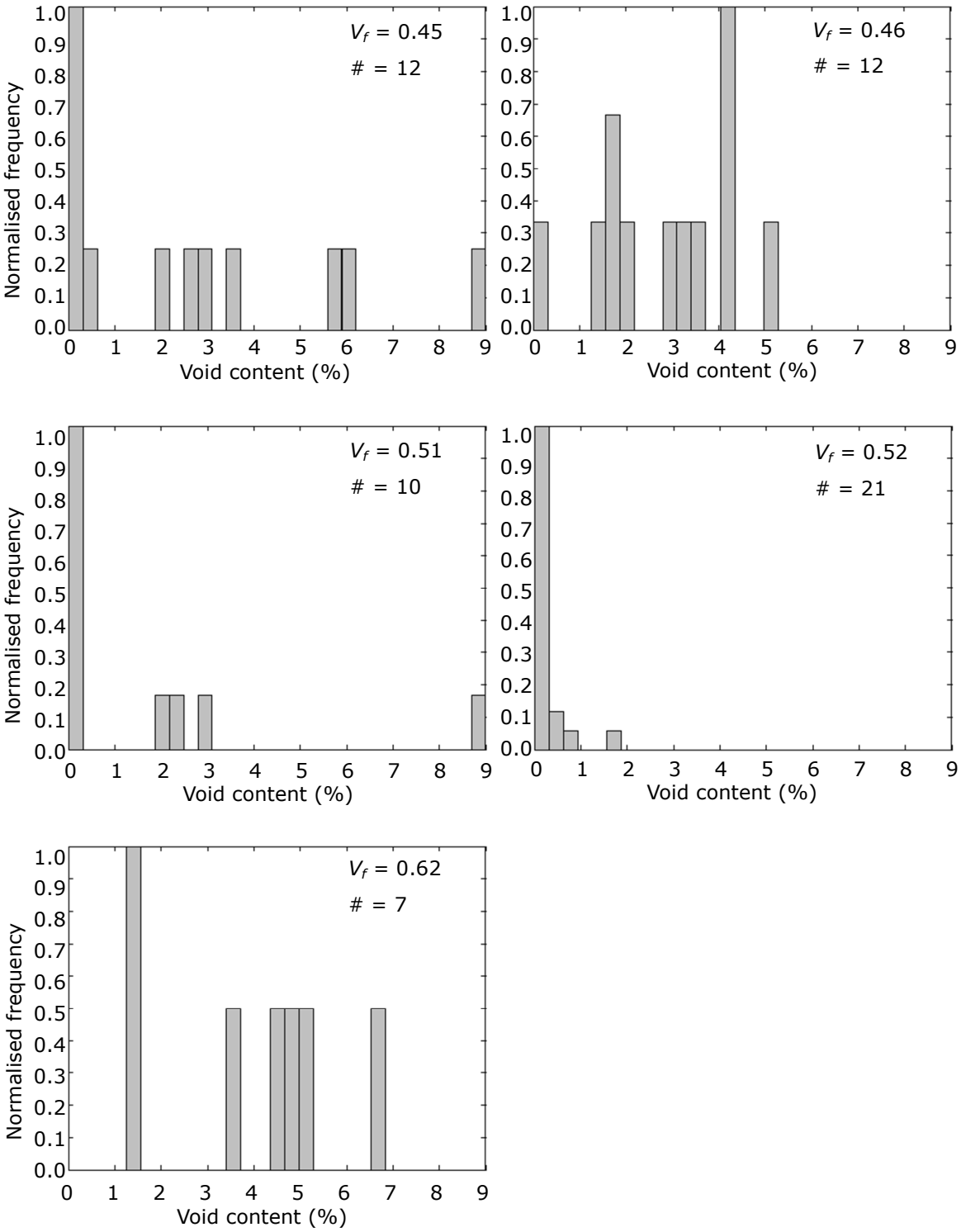

Figure 90: Histograms of void contents measured on samples produced by transverse flow. The frequencies are normalised by the maximum count. The analysed fibre volume fraction, V_f, and number of samples analysed, #, are shown. The histograms reflect the measurements presented in Section 5.2.

L. Transient flow Fluent® journal file

The data below is a typical Fluent® journal file (.jou) used in the analysis of transient flow in Section 5.4. Loading and executing the file enables automated analysis of a two-dimensional model domain.

The following denotations are used:

- left = velocity inlet (left) boundary
- right = pressure outlet (right) boundary
- top and bottom = symmetry (top and bottom) boundaries
- Input parameters as described in Chapter 5 are utilised

If the explicit modelling scheme is desired lines coloured in yellow should be removed in the journal file below. For the implicit modelling scheme, the corresponding grey highlighted lines should be removed.

```
;start journal file:
;****** import mesh ********************************************
;read mesh
file import abaqus input "Folder/FilaName.inp" yes
;scale to μm and smooth mesh
mesh scale 1e-006 1e-006
;****** define materials ********************************************
;define materials:
define materials copy fluid water-liquid
;change viscosity
define materials change-create water-liquid , , , , yes constant 0.1 , , ,
;set fluid cell zone condition to water:
define boundary-conditions modify-zones zone-type 1 fluid
define boundary-conditions fluid , yes air , , , , , , ,
;****** define transient model ********************************************
define models unsteady-2nd-order? yes
define models multiphase model vof
define models multiphase volume-fraction-parameters explicit 0.25 no no no
define models multiphase volume-fraction-parameters implicit no no
;****** define phases: ********************************************
;define wall adhesion and surface tension parameters:
define phases interaction-domain yes 0 yes constant 0.042
;****** define boundary conditions: ********************************
```

```
mesh modify-zones zone-type left velocity-inlet
mesh modify-zones zone-name velocity-inlet-1 left ,
mesh modify-zones zone-type right pressure-outlet
mesh modify-zones zone-name pressure-outlet-2 right ,
mesh modify-zones zone-type top symmetry
mesh modify-zones zone-name symmetry-4 top ,
mesh modify-zones zone-type bottom symmetry
mesh modify-zones zone-name symmetry-3 bottom ,
;set initial fluid velocity at inlet:
define boundary-conditions velocity-inlet left mixture yes yes no 4.5e-005 no 1
        no 0
;set initial volume fration phase-2 at inlet to 1
define boundary-conditions velocity-inlet left phase-2 n 1
;set initial volume fraction phase-2 at outlet to 0
define boundary-conditions pressure-outlet right phase-2 n 0
;define fluid wall contact angle
define boundary-conditions wall ,default_exterior-5 , , , , 61
;****** pressure-velocity coupling **********************************
;set pressure-velocity coupling to: 20=SIMPLE; 21=SIMPLEC; 22=PISO
; 24=coupled
solve set p-v-coupling 22
;disable skewness-neighbour coupling
solve set p-v-controls 1 1 no
;****** set discretisation schemes **********************************
;activate all discretisation schemes:
solve set expert no no yes
define beta-feature-access yes
;change gradient scheme to "Green-Gauss cell based"
solve set gradient-scheme no no
;set pressure discretization scheme to: 14=PRESTO!, 12=2nd-order
solve set discretization-scheme pressure 14
;set momentum discretization scheme to: 1= 2nd-oder-upwind
solve set discretization-scheme mom 1
;set volume fraction discretisation scheme to: 8=CICSAM, 1=2nd-order,
28=compressive
solve set discretization-scheme mp 28
solve set numerics , , , yes , ,
;****** set URFs ****************************************************
```

```
;set under relaxation factors
solve set under-relaxation pressure 0.6
solve set under-relaxation mom 0.6
;****** set monitors ********************************************
;set monitor convergence criteria:
solve monitors residual convergence-criteria 0.001 0.001 0.001 0.001
;only monitor volume phase-2
solve monitors residual check-convergence? no yes yes yes
;****** initialise and run job ***************************************
;start solution initialization with 0 Pa gauge pressure:
solve initialize set-defaults mixture pressure 0
solve initialize initialize-flow
;set-up auto safe
file auto-save data-frequency 1000
file auto-save root-name "Folder/FileName"
;reorder mesh
mesh reorder reorder-domain
mesh reorder reorder-domain
mesh reorder reorder-domain
mesh reorder reorder-domain
;variable time stepping
solve set variable-time-stepping yes no 1 1000 1E-07 0.01 0.5 2 1
solve set time-step 1E-05
solve set time-step 1e-006
;number of time steps , iteration per time step
solve dual-time-iterate 1000000 20
solve dual-time-iterate 1000000 25
; ************************************************************
;end of journal file
```